Technical Physics, Vol. 46, No. 12, 2001, pp. 1489–1493. Translated from Zhurnal Tekhnicheskoĭ Fiziki, Vol. 71, No. 12, 2001, pp. 1–5.

THEORETICAL AND MATHEMATICAL PHYSICS

Methods for Calculating the Spectral Properties of Multilayer Anisotropic Structures Based on Crossed Polarizing Gratings

A. V. Arzhannikov and S. A. Kuznetsov

Budker Institute of Nuclear Physics, Siberian Division, Russian Academy of Sciences, pr. Akademika Lavrent'eva 11, Novosibirsk, 630090 Russia

e-mail: sakuzn@inp.nsk.su

Received February 27, 2001

Abstract—Methods for calculating the spectral properties of multilayer anisotropic structures are described. The structures comprise plane-parallel polarizing gratings made of linear conductors. The conductors in adjacent gratings are arbitrarily directed. The methods employ mathematical approaches used in the interference optics of multilayer isotropic structures. *© 2001 MAIK "Nauka/Interperiodica".*

INTRODUCTION

Optical Fabry–Perot interferometers employ semitransparent mirrors based on continuous metal films. For measurements in the long-wavelength range (including millimeter and submillimeter waves), one cannot use multibeam interferometers and interference filters with the reflectors made of continuous films, since such films exhibit a high absorption of electromagnetic waves in the skin layer [1]. Fabry–Perot interferometers designed for measurements in the microwave range use the reflectors representing periodic gratings made of linear conductors to minimize the absorption [2–7].[1] As a rule, such gratings operate in the long-wavelength approximation, when the period of the conductors l is much smaller than the wavelength of the incident beam λ. If $l/\lambda \ll 1$, the grating represents an effective polarizer, since it reflects the E wave and nearly completely transmits the H wave.[2] In microwave Fabry–Perot interferometers of high spectral resolution, the incident electromagnetic wave must be the E wave for both gratings.

Conventional multilevel microwave interferometers usually use polarizing gratings with identically directed conductors. The general theory of diffraction by multilayer gratings [8, 9] also considers only systems with the identical orientation of the grating conductors. However, it is expedient to consider multilayer interference structures (systems) in which the conductors of neighboring gratings make an angle with each other. Figure 1 shows such a structure containing N plane-parallel gratings. The advantage of the systems with nonparallel (crossed) conductor gratings is the possibility of gradually varying the spectral properties of the multilayer structure by merely varying the crossing angle without replacing the gratings.

The purpose of this work was to present two rather general methods for calculating the spectral properties of the multilayer anisotropic structures with crossed gratings operating in the long-wavelength approximation. The consideration is restricted to the normal incidence of the radiation.

STATEMENT OF THE PROBLEM AND PRELIMINARY REMARKS

Consider the general case of a multilayer anisotropic structure consisting of N arbitrarily crossed plane-parallel gratings with linear conductors (Fig. 1). Assume, for simplicity, that the gratings reside in a homogeneous isotropic medium with a refractive index of 1. Let us number the gratings from left (first) to right (Nth). The $X0Y$ plane of the Cartesian coordinates XYZ coincides with the plane of the first grating and the $0Z$ axis is directed to the Nth grating. Let $\alpha_n \in [0, \pi]$ be the counterclockwise-counted angle between the $0X$ axis and the direction of the nth grating conductors and d_n be the spacing between the nth and $(n + 1)$th gratings (in the latter case, the subscript n varies from 1 to $N - 1$). Finally let τ_n^E and τ_n^H (ρ_n^E and ρ_n^H) be the amplitude transmission (reflection) coefficients of the nth grating for the E- and H-polarized waves, respectively. If the nth grating operates in the long-wavelength approximation, these coefficients represent the amplitudes of the fundamental undamped harmonics of the infinite diffraction spectrum of the grating. The relationships between the coefficients are as follows: $\tau_n^E = 1 + \rho_n^E$

[1] Along with the term "grating," one can also use the term "one-dimensional grid," which is a matter of the production technology.

[2] It is generally accepted that the incident wave is $E(H)$ polarized if the electric (magnetic) field strength vector is aligned with the conductors.

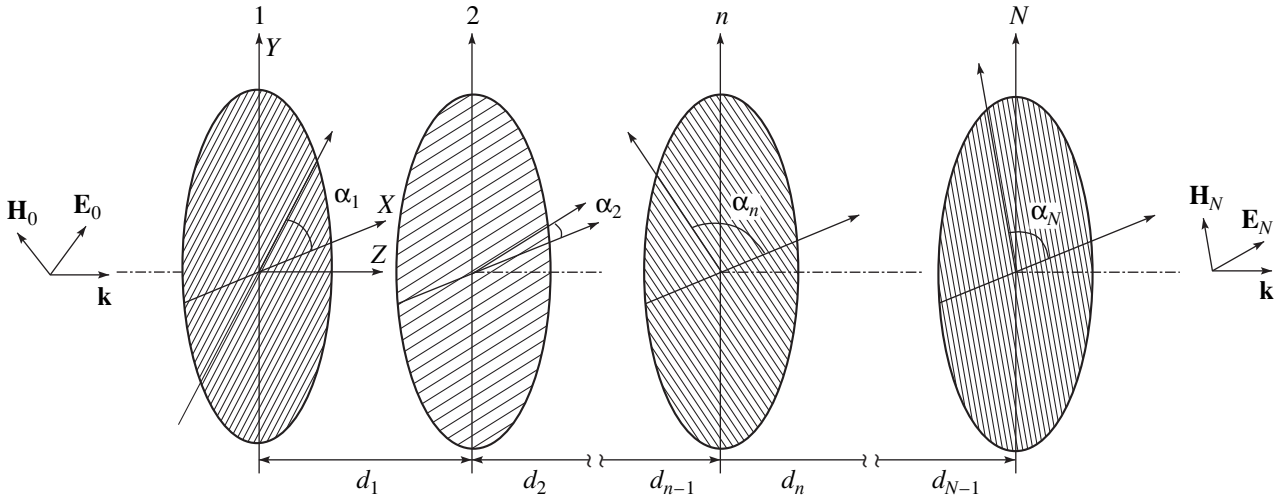

Fig. 1. Multilayer structure with *N* arbitrarily crossed gratings.

and $\tau_n^H = 1 + \rho_n^H$. Below, we will not specify the geometry and the transverse dimensions of the conductors, which govern (at a given wavelength) the explicit form of the coefficients [7–10] and consider the problem for the general case.

Let a plane monochromatic linearly polarized electromagnetic wave be incident from the left ($Z < 0$) on the multilayer structure. The amplitude of the electric field $\mathbf{E}_0$ of the wave has nonzero *x* and *y* components, and the wave vector is **k**. We assume that the aperture of the gratings and the width of the incident wave front are much larger than the wavelength λ, which allows us to neglect the diffraction effects. We are looking for the amplitude of the electric field $\mathbf{E}_N$ of the wave transmitted through the multilayer structure.

In what follows, we will present two independent but physically equivalent computing methods and begin with the method of direct summation of multiple reflections. We extend the Vlasov–Caballero method of recurrence formulas [11–13] to our anisotropic structures. Then, we will consider the method of boundary conditions for interfering fields, which generalizes the (direct) matrix methods that are applied for analyzing multilayer isotropic coatings [11–13].

Prior to describing the methods, note that in interference optics, a wave incident on a multilayer isotropic structure at an arbitrary angle is represented as the superposition of mutually orthogonal *TE* and *TM* components (or, in other words, *s* and *p* polarizations) that interfere independently. The independent interference of the *TE* and *TM* waves is inherent in isotropic media. This statement in terms of *E*- and *H*-polarized components apparently applies also to multilayer anisotropic structures based on identically oriented gratings. However, an arbitrarily oriented polarizing grating is characterized by the transmission and reflection matrices (Jones matrices [14]), which are generally off-diagonal.

In our coordinate system *XYZ*, the explicit form of the Jones matrices for the *n*th grating in an *N*-grating structure can be derived in the following way. First, we consider the grating in a new coordinate system *X'Y'Z'* obtained by rotating the initial system around the 0*Z* axis through an angle α_n so that the conductors become parallel to the 0*X'* axis. In the new coordinates, the Jones matrices of the grating are

$$\mathcal{J}'_N = \begin{pmatrix} \tau_n^E & 0 \\ 0 & \tau_n^H \end{pmatrix} \quad \text{(transmission matrix)}$$

and

$$\mathcal{R}'_N = \begin{pmatrix} \rho_n^E & 0 \\ 0 & \rho_n^H \end{pmatrix} \quad \text{(reflection matrix).}$$

Under such a rotation, the Jones matrices transform as

$$\mathcal{J}'_N = P_n^{-1}\mathcal{J}'_N P_n, \quad \mathcal{R}'_N = P_n^{-1}\mathcal{R}'_N P_n,$$

where

$$P_n = \begin{pmatrix} \cos\alpha_n & \sin\alpha_n \\ -\sin\alpha_n & \cos\alpha_n \end{pmatrix}$$

is the rotation matrix. With this in mind, the transmission matrix $\mathcal{J}_n$ of the *n*th grating in the *XYZ* coordinates is explicitly represented as

$$\mathcal{J}_n = \left\{ \begin{array}{c|c} \tau_n^E \cos^2\alpha_n + \tau_n^H \sin^2\alpha_n & (\tau_n^E - \tau_n^H)\cos\alpha_n \sin\alpha_n \\ \hline (\tau_n^E - \tau_n^H)\cos\alpha_n \sin\alpha_n & \tau_n^E \sin^2\alpha_n + \tau_n^H \cos^2\alpha_n \end{array} \right\}. \quad (1)$$

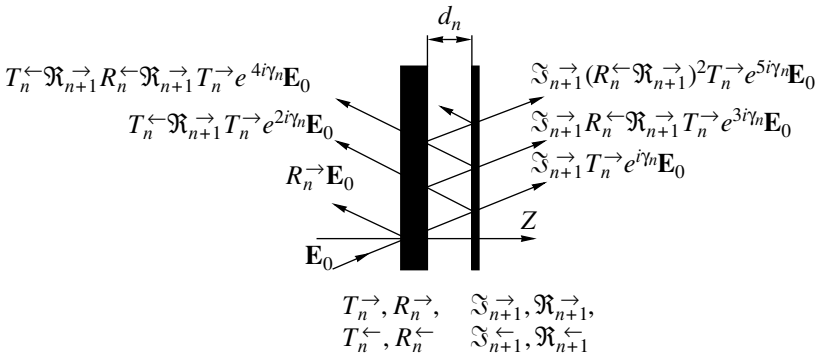

Fig. 2. To the method of recurrence formulas. For clearness, off-normal incidence of the wave is shown.

The reflection matrix $\mathcal{R}_n$ is derived from $\mathcal{J}_n$ by substituting ρ_n^E for τ_n^E and ρ_n^H for τ_n^H.

It follows from expression (1) that the off-diagonal elements of the matrices $\mathcal{J}_n$ and $\mathcal{R}_n$ equal zero only at $\alpha_n = 0$, $\pi/2$, and π (recall that $\tau_n^E \neq \tau_n^H$, since $|\tau_n^E| \ll 1$ and $|\tau_n^H| \approx 1$ in the long-wavelength limit). Therefore, multilayer anisotropic structures based on arbitrarily crossed polarizing gratings, where at least one of the equalities $\alpha_1 = \alpha_2 = \ldots = \alpha_n = \ldots = \alpha_N$ does not hold, do not allow one to reduce the vector problem of interference to corresponding independent scalar problems. The reason is the interrelation between the mutually orthogonal components of the transmitted and reflected fields. Hence, the computing methods for multilayer structures can be extended to crossed polarizing gratings if the transmission and reflection matrices of the gratings are correctly applied instead of the scalar Fresnel reflection and transmission coefficients used in the conventional methods of multibeam interference optics.

THE METHOD OF RECURRENCE FORMULAS (SUMMATION OF MULTIPLE REFLECTIONS)

Separate a subsystem of a multilayer N-grating system (Fig. 1) containing gratings with the numbers from 1 to n. Let us denote the transmissions and reflection matrices of the isolated n-grating subsystem as $T_n^{\rightarrow}$ and $R_n^{\rightarrow}$ for a wave incident from the left ($k_z > 0$) and $T_n^{\leftarrow}$ and $R_n^{\leftarrow}$ for that incident from the right ($k_z < 0$).[3] Apparently, in the general case, $T_n^{\rightarrow} \neq T_n^{\leftarrow}$ and $R_n^{\rightarrow} \neq R_n^{\leftarrow}$. Now the subsystem is supplemented by the $(n+1)$th grating characterized by the transmission and reflection matrices $\mathcal{J}_{n+1}^{\rightarrow}$, $\mathcal{R}_{n+1}^{\rightarrow}$, $\mathcal{J}_{n+1}^{\leftarrow}$, and $\mathcal{R}_{n+1}^{\leftarrow}$. Below, we use leftward and rightward arrows as the superscripts of the grating matrices for generality, assuming that $\mathcal{J}_{n+1}^{\rightarrow} = \mathcal{J}_{n+1}^{\leftarrow} \equiv \mathcal{J}_{n+1}$ and $\mathcal{R}_{n+1}^{\rightarrow} = \mathcal{R}_{n+1}^{\leftarrow} \equiv \mathcal{R}_{n+1}$ at normal incidence [see (1)]. To determine the transmission, $T_{n+1}^{\rightarrow}$ and $T_{n+1}^{\leftarrow}$, and reflection, $R_{n+1}^{\rightarrow}$ and $R_{n+1}^{\leftarrow}$, matrices of the new subsystem, which contains $(n+1)$ gratings and is considered independently of the remaining $(N-n-1)$ gratings of the initial system, we represent it as a multibeam (Fabry–Perot) interferometer with two anisotropic mirrors (Fig. 2). The n-grating subsystem and the $(n+1)$th grating act as the first and the second anisotropic mirrors, respectively.

Let a wave with an amplitude $\mathbf{E}_0$ be incident on the interferometer from the left. First, we calculate the vector amplitude of the transmitted wave $\mathbf{E}_{tr}$. It obviously represents the superposition of the vector amplitudes of the partial transmitted waves formed by multiple reflections from the mirrors. For the case of normal incidence and the infinite number of the partial waves, we perform the summation of the field amplitudes (as for the interferometer with isotropic mirrors) in view of their matrix transformation. Using the scheme shown in Fig. 2 and assuming that the phase factor is given by $\exp(ik_z z)$, we arrive at

$$\begin{aligned}
\mathbf{E}_{tr} &= \mathcal{J}_{n+1}^{\rightarrow}T_n^{\rightarrow}e^{i\gamma_n}\mathbf{E}_0 + \mathcal{J}_{n+1}^{\rightarrow}R_n^{\leftarrow}\mathcal{R}_{n+1}^{\rightarrow}T_n^{\rightarrow}e^{3i\gamma_n}\mathbf{E}_0 \\
&\quad + \mathcal{J}_{n+1}^{\rightarrow}(R_n^{\leftarrow}\mathcal{R}_{n+1}^{\rightarrow})^2T_n^{\rightarrow}e^{5i\gamma_n}\mathbf{E}_0 \\
&\quad + \ldots + \mathcal{J}_{n+1}^{\rightarrow}(R_n^{\leftarrow}\mathcal{R}_{n+1}^{\rightarrow}e^{2i\gamma_n})^mT_n^{\rightarrow}e^{i\gamma_n}\mathbf{E}_0 \\
&+ \ldots = \mathcal{J}_{n+1}^{\rightarrow}[I + R_n^{\leftarrow}\mathcal{R}_{n+1}^{\rightarrow}e^{2i\gamma_n} + (R_n^{\leftarrow}\mathcal{R}_{n+1}^{\rightarrow}e^{2i\gamma_n})^2 \\
&\quad + \ldots + (R_n^{\leftarrow}\mathcal{R}_{n+1}^{\rightarrow}e^{2i\gamma_n})^m + \ldots]T_n^{\rightarrow}e^{i\gamma_n}\mathbf{E}_0 \\
&= \mathcal{J}_{n+1}^{\rightarrow}\left[I + \sum_{m=1}^{\infty}(R_n^{\leftarrow}\mathcal{R}_{n+1}^{\rightarrow}e^{2i\gamma_n})^m\right]T_n^{\rightarrow}e^{i\gamma_n}\mathbf{E}_0,
\end{aligned} \tag{2}$$

where $\gamma_n = k_z d_n$ and I is the identity matrix.

[3] The term "isolated" means that the subsystem is bounded on both sides by a semi-infinite space so that there are no gratings with numbers exceeding n.

One can transform the infinite matrix sum in (2) based on the theorem for the expansion of the resolvent of a linear bounded operator in the Neumann series. According to this theorem, the following formula is valid for an operator A with a norm $\|A\| < 1$:

$$(I - A)^{-1} = I + \sum_{m=1}^{\infty} A^m.$$

We consider the product $R_n^{\leftarrow}\mathcal{R}_{n+1}^{\rightarrow}e^{2i\gamma_n}$ as the operator A and assume that the above condition for the norm is met.[4] Then, expression (2) can be rewritten as

$$\mathbf{E}_{tr} = \mathcal{J}_{n+1}^{\rightarrow}[I - R_n^{\leftarrow}\mathcal{R}_{n+1}^{\rightarrow}e^{2i\gamma_n}]^{-1}T_n^{\rightarrow}e^{i\gamma_n}\mathbf{E}_0. \quad (3)$$

The expression preceding the vector $\mathbf{E}_0$ in the right-hand side of (3) is nothing but the transmission matrix of the subsystem consisting of $(n + 1)$ gratings for the wave incident from the left.

Repeating the above procedure for the amplitude of the reflected wave and also for the case of incidence direction reversal ($k_z \longrightarrow -k_z$), we obtain the matrix expressions

$$T_{n+1}^{\rightarrow} = \mathcal{J}_{n+1}^{\rightarrow}[I - R_n^{\leftarrow}\mathcal{R}_{n+1}^{\rightarrow}e^{2i\gamma_n}]^{-1}T_n^{\rightarrow}e^{i\gamma_n},$$
$$R_{n+1}^{\rightarrow} = R_n^{\rightarrow} + T_n^{\leftarrow}\mathcal{R}_{n+1}^{\rightarrow}[I - R_n^{\leftarrow}\mathcal{R}_{n+1}^{\rightarrow}e^{2i\gamma_n}]^{-1}T_n^{\rightarrow}e^{2i\gamma_n}; \quad (4)$$

$$T_{n+1}^{\leftarrow} = T_n^{\leftarrow}[I - \mathcal{R}_{n+1}^{\rightarrow}R_n^{\leftarrow}e^{2i\gamma_n}]^{-1}\mathcal{J}_{n+1}^{\leftarrow}e^{i\gamma_n},$$
$$R_{n+1}^{\leftarrow} = \mathcal{R}_{n+1}^{\leftarrow} + \mathcal{J}_{n+1}^{\rightarrow}R_n^{\leftarrow}[I - \mathcal{R}_{n+1}^{\rightarrow}R_n^{\leftarrow}e^{2i\gamma_n}]^{-1}\mathcal{J}_{n+1}^{\leftarrow}e^{2i\gamma_n}. \quad (5)$$

Thus, we derived the recurrence relationships for multilayer anisotropic structures containing an arbitrary number of crossed polarizing gratings. The recurrence process for an N-grating structure involves $N - 1$ steps, at each of which the number of the polarizers n is increased by unity from 2 to N and the intermediate variants of the n-grating system are calculated with formulas (4) and (5). Note that the expressions obtained do not admit the rearrangement of the matrices, since, in the general case, the commutative law of multiplication here fails.

THE METHOD OF BOUNDARY CONDITIONS (DIRECT MATRIX METHOD)

Consider another approach to analyzing the interference of the waves in the multilayer system. Let the apertures of the mirrors and the width of the incident wave front be infinitely large. Then, the field between neighboring gratings can be represented as the field of two waves propagating in the opposite directions along the $0Z$ axis (Fig. 3). In this case, the field strengths of all the waves are related through the boundary conditions written as the continuity conditions for the total field vector crossing the surfaces of the gratings. We can represent the above conditions for the nth grating in terms of the transmission and reflection matrices:

$$\mathbf{E}_n e^{-i\gamma_n} = \mathcal{J}_n^{\rightarrow}\mathbf{E}_{n-1} + \mathcal{R}_n^{\leftarrow}\mathbf{E}'_n e^{i\gamma_n},$$
$$\mathbf{E}'_{n-1} = \mathcal{R}_n^{\rightarrow}\mathbf{E}_{n-1} + \mathcal{J}_n^{\leftarrow}\mathbf{E}'_n e^{i\gamma_n}, \quad (6)$$

where $\gamma_n = k_z d_n$.

Equation (6) allows a clear physical interpretation: the wave field $\mathbf{E}_n$ is the superposition of the field transmitted through the nth grating, $\mathbf{E}_{n-1}$, and the field reflected from the grating, $\mathbf{E}'_n$ (the same also holds for the wave $\mathbf{E}'_{n-1}$). Here, we assume that the phases of the waves propagating between the nth and the $(n + 1)$th gratings are reckoned from the surface of the latter. Expression (6) can conveniently be rewritten in the matrix form

$$\begin{pmatrix}\mathbf{E}_n\\ \mathbf{E}'_n\end{pmatrix} = M_n\begin{pmatrix}\mathbf{E}_{n-1}\\ \mathbf{E}'_{n-1}\end{pmatrix}, \quad (7)$$

where the matrix M_n is given by

$$M_n = \left(\begin{array}{c|c} [\mathcal{J}_n^{\rightarrow} - \mathcal{R}_n^{\leftarrow}(\mathcal{J}_n^{\leftarrow})^{-1}\mathcal{R}_n^{\rightarrow}]e^{i\gamma_n} & \mathcal{R}_n^{\leftarrow}(\mathcal{J}_n^{\leftarrow})^{-1}e^{i\gamma_n} \\ \hline -(\mathcal{J}_n^{\leftarrow})^{-1}\mathcal{R}_n^{\rightarrow}e^{-i\gamma_n} & (\mathcal{J}_n^{\leftarrow})^{-1}e^{i\gamma_n} \end{array}\right).$$

By sequentially applying boundary conditions (7) to the surface of each of the gratings in the N-grating structure, we obtain the relationship between the amplitudes of the incident, $\mathbf{E}_0$; reflected, $\mathbf{E}'_0$; and transmitted, $\mathbf{E}_N$, waves:

$$\begin{pmatrix}\mathbf{E}_N\\ 0\end{pmatrix} = \prod_{n=N}^{1} M_n\begin{pmatrix}\mathbf{E}_0\\ \mathbf{E}'_0\end{pmatrix} = M_N M_{N-1} M_{N-2}\ldots M_1\begin{pmatrix}\mathbf{E}_0\\ \mathbf{E}'_0\end{pmatrix} \quad (8)$$

(note that for $n = N$, one must formally put $\gamma_N = 0$). Introducing the notation

$$\tilde{M} = \begin{pmatrix}\tilde{M}_{11} & \tilde{M}_{12}\\ \tilde{M}_{21} & \tilde{M}_{22}\end{pmatrix} = \prod_{n=N}^{1} M_n,$$

we find the solution of the initial problem:

$$\mathbf{E}_N = [\tilde{M}_{11} - \tilde{M}_{12}\tilde{M}_{22}^{-1}\tilde{M}_{21}]\mathbf{E}_0.$$

As in the case of the isotropic structures, the direct matrix method possesses the advantage over the method of recurrence formulas: according to (7) and (8), a change in the parameters of any nth grating or in the distance d_n does not necessitate the recalculation of

[4] The condition $\left\|R_n^{\leftarrow}\mathcal{R}_{n+1}^{\rightarrow}e^{2i\gamma_n}\right\| < 1$ means that two successive reflections (respectively, from the left and right mirrors of the interferometer) lead to a decrease in the modulus of the wave amplitude, which is physically evident.

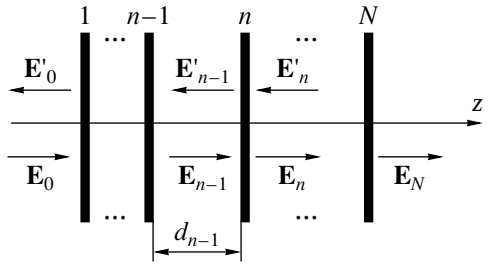

Fig. 3. To the method of boundary conditions.

the partial products $\prod_{j=n-1}^{1} M_j$ and $\prod_{j=N}^{n+1} M_j$, which saves the computation time. Unfortunately, the matrix method operates on 4×4 M_n matrices, whereas the recurrence method employs 2×2 matrices.

CONCLUSION

We considered two approaches to calculating the spectral properties of multilayer anisotropic structures based on crossed polarizing gratings. The solution methods proposed can also be applied to other anisotropic structures, since our methods do not use the explicit form of the transmission and reflection matrices of the polarizers. Note that the methods are valid only in the plane monochromatic wave approximation. If the spacing between the gratings is comparable to the period of the conductors, the interference pattern is affected by higher harmonics and the methods become inapplicable.

Finally, it should be noted that the general formalism of the approaches makes it possible to consider small-angle incidence (one can neglect the finiteness of the apertures of the gratings in this case, which reduces the effective number of interfering beams). Strictly speaking, the dependence of the elements of the transmission and reflection matrices on the angle of incidence should then be taken into account. However, for small angles, such a dependence introduces a correction factor on the order of φ into the amplitude transmission coefficient of the anisotropic structure (φ is the angle between the wave vector and the normal to the grating) and a correction factor on the order of φ^2 into the energy transmission coefficient. Thus, if $\varphi \ll 1$, the calculations can be performed in the same way as for normal incidence, with the z component of the wave vector being equal to $|\mathbf{k}|\cos\varphi$.

REFERENCES

1. A. E. Kaplan, Radiotekh. Élektron. (Moscow) **4**, 1781 (1964).
2. F. A. Korolev and V. A. Gridnev, Opt. Spektrosk. **16**, 335 (1964).
3. A. V. Chernetskiĭ, O. A. Zinov'ev, and O. V. Kozlov, *Apparatuses and Methods for Plasma Investigation* (Atomizdat, Moscow, 1965).
4. E. A. Vinogradov, E. M. Dianov, and N. A. Irisova, Pis'ma Zh. Éksp. Teor. Fiz. **2**, 323 (1965) [JETP Lett. **2**, 205 (1965)].
5. V. Ya. Balakhanov, V. D. Rusanov, and A. R. Striganov, Zh. Tekh. Fiz. **35**, 127 (1965) [Sov. Phys. Tech. Phys. **10**, 96 (1965)].
6. A. A. Bagdasarov, V. V. Buzankin, N. L. Vasin, *et al.*, in *Diagnostics of Plasma: Collection of Articles* (Énergoatomizdat, Moscow, 1981), Vol. 4 (1), pp. 141–146.
7. B. Walker, E. A. M. Baker, and A. E. Costley, J. Phys. E **14**, 832 (1981).
8. V. P. Shestopalov, L. P. Litvinenko, S. A. Masalov, and V. G. Sologub, *Wave Diffraction by Gratings* (Kharkovsk. Univ., Kharkov, 1973).
9. V. P. Shestopalov, *Method of the Riemann–Gilbert Problem in the Theory of Electromagnetic Wave Diffraction and Propagation* (Kharkovsk. Univ., Kharkov, 1971).
10. I. E. Tarapov, Zh. Vychisl. Mat. Mat. Fiz. **5**, 883 (1965).
11. P. G. Karg, *Analysis and Synthesis of Multilayer Interference Films* (Valgus, Tallinn, 1971).
12. G. V. Rozenberg, *Optics of Thin-Film Coatings* (GIFML, Moscow, 1958).
13. *Physics of Thin Films: Advances in Research and Development*, Ed. by G. Hass (Academic, New York, 1963; Mir, Moscow, 1967), Vol. 1.
14. R. M. Azzam and N. M. Bashara, *Ellipsometry and Polarized Light* (North-Holland, Amsterdam, 1977; Mir, Moscow, 1981).

Translated by A. Chikishev

Technical Physics, Vol. 46, No. 12, 2001, pp. 1494–1500. Translated from Zhurnal Tekhnicheskoĭ Fiziki, Vol. 71, No. 12, 2001, pp. 6–12.

THEORETICAL AND MATHEMATICAL PHYSICS

Magnetic Properties of Degenerate Atomic Fermi Gases

E. V. Orlenko, B. G. Matisov, and G. T. Ketiladze

St. Petersburg State Technical University, ul. Politekhnicheskaya 29, St. Petersburg, 195251 Russia

e-mail: quark@citadel.stu.neva.ru

Received 13 March, 2001

Abstract—Magnetic effects in a degenerate atomic Fermi gas, such as the exchange enhancement of the paramagnetic susceptibility and the existence of the phase transition to the ferromagnetic state with the spontaneous polarization of the atomic spins, are discussed. The propagation of spin waves in the atomic system is considered. © *2001 MAIK "Nauka/Interperiodica".*

INTRODUCTION

A degenerate atomic Fermi gas is a unique object for experimentally simulating perfect Fermi gas and studying its quantum statistic. Unlike an electron Fermi gas in metals or in a plasma, where strong interaction effects cause nonideality, the atomic gas, where Van der Waals interaction alone is present, seems to be an excellent model of perfect quantum gas.

Once atomic Bose systems had been successfully cooled and the Bose condensate had been obtained [1], experiments on cooling Fermi systems, specifically, K^{40}, were performed. A total of 7×10^5 K^{40} atoms were cooled down to the degeneracy temperature, i.e., below 300 nK [2]. Ultracold atoms produce a low-density ensemble where interparticle interaction is weak and can be controlled via the so-called magnetic-field Feishbach resonance [3]. Such behavior of cooled Fermi atoms is also observed in Bose systems [4]. Among new features predicted for Fermi systems are the flaky structure of the spatial distribution [5], the suppression of elastic and inelastic collisions [6, 7], and the existence of zero sound at low temperatures [8]. Finally, the possibility of the phase transition to the superfluid state for Cooper pairs is discussed [9].

However, we should bear in mind magnetic phenomena in atomic gases that are far from degeneracy ($T \approx 4$ K) but in which quantum effects are appreciable, providing the basis for the quantitative characterization of a physical event having no classical analog. Boltzmann gases where macroscopic quantum effects are observed have been called "quantum gases" [10]. The term "quantum" as applied to a Boltzmann gas merely means that the thermal de Broglie wavelength λ much exceeds the atomic size a and at the same time is much less than the mean interparticle spacing; that is,

$$n^{-1/3} \gg \lambda \gg a,$$

where n is the density of a spin-polarized atomic gas.

For such gases, in particular for spin-polarized hydrogen and $^3He^{\uparrow}$, collective magnetic phenomena like spin waves have been observed [11–14]. The magnetic effects in spin-polarized Boltzmann gases have been treated *ab initio* [15], as well as within the phenomenological theory of Fermi liquid [10]. In the former case, not only a term taking into account atom spin correlation was introduced into the quantum kinetic equation but also the exchange interaction constant was derived in a natural way. In addition, the fundamental reason for the Heisenberg-type term appearing in the equation was elucidated.

The magnetic effects remain appreciable for colder systems as well. Moreover, they may be a basic mechanism violating the ideality of an atomic gas. Therefore, these effects should be considered in detail even in a degenerate atomic gas. In fact, strong Coulomb interaction, observed in an ensemble of charged particles, is absent in atom systems; hence, weak effects of spin correlation begin to play a more significant part. The spin correlation effects arise because of exchange interaction, which is a consequence of the interference redistribution of the atomic gas density when Van der Waals interaction is weak. Thus, the spin correlation effects and collective excitations, which have been observed in quantum Boltzmann gases at $T \approx 4$ K, will show up more vividly in a degenerate Fermi gas. Moreover, they may give rise to even more intriguing magnetic effects, such as the second-order phase transition to the ferromagnetic state.

EXCHANGE INTERACTION

Consider the interaction of two neutral atoms at temperatures such that the thermal de Broglie wavelength of the atom is comparable to the mean interparticle spacing: $\hbar/\sqrt{2mT} \sim n^{-1/3}$, where m is the mass of the atom and the temperature is expressed in units of energy. In this case, the atom indistinguishability principle should be taken into account in the quantum mechanical calculation of the interaction energy. Since Van der Waals interaction is weak, the perturbation theory basically applies. However, the wave properties of

the atoms will substantially affect the resulting interference redistribution of the atom concentration in the space. Therefore, it is more appropriate to invoke the exchange perturbation theory (EPT), which has been specially tailored for such systems [16]. According to the EPT, the first-order correction to the energy is given by

$$\varepsilon^{(1)} = \langle \Phi | \hat{V} | \Psi \rangle, \tag{1}$$

where $\langle \Phi|$ is the nonsymmetrized wave function of an ensemble of noninteracting particles, which is merely the product of the wave functions of individual particles; $|\Psi\rangle$ is the antisymmetrized wave function (or the coordinate part of the antisymmetrized wave function if a perturbation does not contain spin operators in the explicit form); and $\hat{V}$ is the interaction operator.

In our case, the interaction operator is taken in the form of the Suserland potential

$$\hat{V} = \begin{cases} -\dfrac{c}{r^6}, & r > a \\ +\infty, & r < a, \end{cases} \tag{2}$$

where c is the Van der Waals constant, a is the range of repulsion forces between the atoms ($a \sim 10^{-8}$ cm), and r is the center-to-center distance of the atoms.

In the center-of-mass coordinate system, the wave function for two noninteracting atoms is written as

$$|\Phi(r)\rangle = e^{ik_z z} + f(\theta)\frac{e^{i\mathbf{kr}}}{r},$$

where $z = r\cos\theta$ is the coordinate along the z axis, connecting the nuclei; f is the scattering amplitude, which depends on the direct interaction of the atoms (that is, $\hat{V}$); $\mathbf{k} = \mathbf{p}/\hbar$ is the wave number; $\mathbf{p}$ is the momentum of the relative motion of the nuclei.

The wave function including the permutation of the atom centers is given by

$$|\Phi'(\mathbf{r})\rangle = e^{-ik_z z} + f(\pi - \theta)\frac{e^{i\mathbf{kr}}}{r}.$$

Then, the coordinate part of the diatomic function is either symmetric or antisymmetric,

$$\Psi(\mathbf{r}) = e^{ik_z z} \pm e^{-ik_z z} + (f(\theta) \pm f(\pi - \theta))\frac{e^{i\mathbf{kr}}}{r}, \tag{3}$$

since the associated spin part is either symmetric or antisymmetric. In the experiments, K^{40} atoms have only two spin states:

$$\left| j = \frac{9}{2};\ j_z = \frac{9}{2} \right\rangle \quad \text{and} \quad \left| j = \frac{9}{2};\ j_z = \frac{7}{2} \right\rangle \text{ [2]},$$

where j is the total atom spin and j_z is the projection of the total atom spin onto the z axis. Therefore, the associated symmetric or antisymmetric function will correspond to two possible states with a total spin of the diatomic system $J = 9$ or $J = 8$, respectively:

$$|\chi_{s,a}\rangle = \frac{1}{\sqrt{2}}\left\{ \left| j = \frac{9}{2};\ j_z = \frac{9}{2} \right\rangle_{\mathrm{I}} \left| j = \frac{9}{2};\ j_z = \frac{7}{2} \right\rangle_{\mathrm{II}} \right.$$
$$\left. \pm \left| j = \frac{9}{2};\ j_z = \frac{9}{2} \right\rangle_{\mathrm{III}} \left| j = \frac{9}{2};\ j_z = \frac{7}{2} \right\rangle_{\mathrm{I}} \right\}, \tag{4}$$

where the subscripts I and II are atomic numbers, $|\chi_s\rangle = |J = 9;\ J_z = 8\rangle$, and $|\chi_a\rangle = |J = 8;\ J_z = 8\rangle$. Thus, in expression (3), the upper and lower signs correspond, respectively, to the $|\chi_a\rangle$ and $|\chi_s\rangle$ states.

Let the probability of the interatomic spacing being r in a Boltzmann gas be defined by the function

$$W(r) = N^{-1}\exp\left(-\frac{V(r)}{T}\right),$$

where N is the normalizing factor.

Then, the averaged correction to the interaction energy is found by modified formula (1),

$$\varepsilon^{(1)}(r) = \langle \Phi | \hat{V}(r) W(r) | \Psi \rangle, \tag{5}$$

which is equivalent to averaging using the density matrix in the coordinate representation. The correction to the energy will then have the well-known form

$$\varepsilon^{(1)} = K \pm A, \tag{6}$$

where K is the direct contribution and A is the exchange contribution. The latter term specifies the energy split due to the Van der Waals potential and at the same time depends on the atom spin orientation. For A, we find

$$A = \frac{bT}{2kN}\mathrm{Im}(I_5(k) + 2\bar{f} I_6(k)), \tag{7}$$

where $b = c/T$, $I_n(k)$ are the integrals taken by the saddle-point method, $\bar{f}$ is the amplitude averaged over the angular variables ($\bar{f}$ and a are of the same order of magnitude),

$$N = \int_a^\rho \exp\left(\frac{b}{r^6}\right) r^2 dr,$$

and ρ is the mean interatomic spacing ($\rho > n^{-1/3}$).

For a given temperature T_0 at $ka > 1$ and $\rho \gg a$, we, using the approximate values of the integrals, obtain

$$A = -\frac{2}{3}\pi T_0 \frac{3b}{a^6}\left(\frac{r_0}{a}\right)^3 \left(\frac{\pi}{7kr_0}\right)^{1/2}$$
$$\times \sin\left(\frac{4\pi}{7} + \frac{7kr_0}{3}\right)\left(1 + \frac{2f}{r_0} - \frac{1.5}{ak}\right). \tag{8}$$

Here, $(6b/k)^{1/7} = r_0$ is the effective radius of exchange interaction. Since the superscripts and the subscripts in (3) and (6) stand for the antisymmetric spin part $|\chi_a\rangle = |J = 8; J_z = 8\rangle$ and the symmetric spin part $|\chi_s\rangle = |J = 9; J_z = 8\rangle$, respectively, expression (6) can be recast using the explicit form of the spin operators. Since the eigenvalue of the operator $\hat{j}_I\hat{j}_{II}$ is

$$\overline{\hat{\mathbf{j}}_I \cdot \hat{\mathbf{j}}_{II}} = \frac{1}{2}(J(J+1) - j_I(j_I+1) - j_{II}(j_{II}+1)) \quad (9)$$

and takes two values: $\overline{\hat{\mathbf{j}}_I\hat{\mathbf{j}}_{II}} = 81/4$ at $J = 9$ and $45/4$ at $J = 8$, one can conventionally introduce the operator

$$\hat{P}_{I,II} = \frac{1}{18}(63 - 4\overline{\hat{\mathbf{j}}_I\hat{\mathbf{j}}_{II}}),$$

whose eigenvalues are +1 and –1 for the antisymmetric and symmetric functions, respectively. Then, this operator can replace ±1 in expression (6):

$$\hat{\varepsilon} = K + \frac{A}{18}(63 - 4\hat{\mathbf{j}}_I\hat{\mathbf{j}}_{II})$$

or

$$\hat{\varepsilon} = \varepsilon_0 - \frac{2A}{9}\hat{\mathbf{j}}_I\hat{\mathbf{j}}_{II}, \quad (10)$$

where

$$\varepsilon_0 = K + \frac{7}{2}A.$$

Thus, the spin-interaction-related addition to the energy operator for the atomic gas can be introduced:

$$\hat{H} = -\frac{2}{9}A\sum_{i<j}\hat{\mathbf{j}}_i\hat{\mathbf{j}}_j. \quad (11)$$

Evaluations of the exchange interaction constant will be given for temperatures below $T_0 = 1/2 \times 10^{-16}$ erg. The point is that the mechanism of exchange interaction in gases may be very effective at certain relationships between the basic scattering parameters (thermal de Broglie wavelength, Van der Waals constant, and atom concentration) unlike condensed media where the exchange interaction depends on the thermal motion of interacting atoms only slightly. The constant b equals $5 \times 10^4 c$, where $c = 6E_B(a_B^2)^6$, $k \cong 1/a_B$, and a_B is the Bohr radius. The radius of the potential barrier in the Suserland model is usually taken near the Van der Waals minimum: $a \cong 5a_B$, where $r_0 = 8a_B$. At such values of the parameters, we obtain $A \approx$ several T_0 from (8). When the temperature increases by one order of magnitude, the saddle-point in the integrals entering into (7) turns out to be lower than the potential barrier height ($r_0 < a$) and the calculation becomes invalid. The exchange integral vs. temperature dependence can be approximated as

$$A \approx T_0 x^{3/2} e^{-x},$$

where x is the Van der Waals-to-thermal energy ratio.

It is obvious that the interaction is the most effective at $x = 3/2$. Thus, in the temperature interval considered, the exchange interaction of two atoms splits the energy according to the alignment of the atom spins, the state with the parallel spins being energetically more favorable. Therefore, spontaneous magnetization or at least the enhancement of the paramagnetic susceptibility of the atom ensemble in a magnetic field could be expected.

THE EFFECT OF EXCHANGE INTERACTION ON THE FERMI ENERGY AND ON THE TOTAL ENERGY OF AN ENSEMBLE OF DEGENERATE GAS ATOMS

Exchange interaction in an ensemble of degenerate gas atoms acts in two opposing directions. First, spontaneous polarization in an atomic gas changes the Fermi level position, thus increasing the mean kinetic energy of the atoms. Second, as was shown, exchange interaction, which causes the alignment of the spins, decreases the system energy. Thus, the equilibrium polarization of the spins results from two competing processes: nonforce exchange, or the interference redistribution of the atomic concentration, and exchange interaction as such. The former is due to the Pauli exclusion principle and sets the antiparallel spin orientation. The latter decreases (increases) the energy if the spins are parallel (antiparallel) by a value $\Delta E = A$. This is taken into account in the Landau theory of Fermi liquid as applied to electrons in metals by introducing the Landau phenomenological function [17].

Let us estimate first the change in the Fermi energy in the presence of the spontaneous polarization of power α:

$$n^+ - n^- = \alpha n, \quad n^+ + n^- = n, \quad (12)$$

where n is the atom concentration.

The Fermi energy including the polarization is given by

$$\varepsilon_F^+ = \varepsilon_F(1 \pm \alpha)^{2/3}, \quad \varepsilon_F = \frac{\hbar^2}{2m}(3\pi^2 n)^{2/3}. \quad (13)$$

The kinetic energy without the temperature corrections is

$$T = \frac{3}{5}n\varepsilon_F(1-\alpha)^{5/3} + \frac{3}{5}n\varepsilon_F\frac{1}{2}((1+\alpha)^{5/3} - (1-\alpha)^{5/3}). \quad (14)$$

Then, the total energy with regard for the exchange

interaction is given by

$$U = \frac{3}{5}n\frac{\varepsilon_F}{2}\{(1+\alpha)^{5/3} + (1-\alpha)^{5/3}\} + \frac{A}{2}n(1-2\alpha). \quad (15)$$

The minimum of (15) in the weak interaction approximation $2A \ll \varepsilon_F$ is at

$$\alpha_{min} \approx \frac{1}{4}\left(\frac{2A}{\varepsilon_F}\right)^3; \quad (16)$$

at $A > \varepsilon_F$, the potential energy is minimal if $\alpha = 1$. Thus, the exchange interaction between free atoms may cause spontaneous polarization in a degenerate atom system.

ENHANCED PARAMAGNETISM IN THE PRESENCE OF EXCHANGE INTERACTION

Exchange interaction results in spontaneous polarization, which affects the Fermi level position. Substituting the operator $\hat{P}_{I,II}$ for ± 1 in (13) yields

$$\varepsilon_F^{\pm} = \varepsilon_F\left(1 - \frac{7}{2}\alpha + \frac{2}{9}\alpha\hat{\mathbf{j}}_I\hat{\mathbf{j}}_{II}\right)^{2/3}. \quad (17)$$

The exchange correction to the energy is given by (10). Thus, the density matrix in the spin variable is

$$\hat{n} = \frac{1}{\exp\left(\dfrac{\varepsilon - \frac{2}{9}A\hat{\mathbf{j}}\cdot\hat{\mathbf{j}}' - \varepsilon_F^{\pm}}{T}\right) + 1}. \quad (18)$$

Expanding (18) in the small parameter, we obtain

$$\hat{n} = n_0 + \frac{\partial n_0}{\partial\varepsilon}\hat{f}, \quad (19)$$

where

$$\hat{f} = -\frac{1}{n}\left\{\frac{\alpha}{3}\varepsilon(p) + \left(\frac{4\alpha}{27}\varepsilon(p) + \frac{2}{9}A(p,p')\right)\hat{\mathbf{j}}\hat{\mathbf{j}}'\right\},$$

and n_0 is the Fermi function.

Consider the effect of an applied magnetic field on the atom system. In this case, the total change in the system energy can be written as [16]

$$\delta E = -\beta_1(\mathbf{p})\hat{\mathbf{j}}\mathbf{H}. \quad (20)$$

This change has two components. First, the magnetic field acts on the magnetic moment of the atom, which gives the contribution

$$-2\mu_0^*\mathbf{H}\hat{\mathbf{j}}, \quad (21)$$

where

$$\mu_0^* = \frac{e\hbar}{2m_{am}c}.$$

Second, the energy spectrum is affected by the change in the distribution function. The associated change in the energy is expressed as

$$\begin{aligned}
&Sp_{j'}\int f(\mathbf{p},\mathbf{j},\mathbf{p}',\mathbf{j}')\delta n(\mathbf{p}',\mathbf{j}')\frac{d^3p'}{(2\pi\hbar)^3} \\
&= Sp_{j'}\int f(\mathbf{p},\mathbf{j},\mathbf{p}',\mathbf{j}')\frac{\partial n_0}{\partial E}(\mathbf{p}',\mathbf{j}')\frac{d^3p'}{(2\pi\hbar)^3} \\
&= -Sp_{j'}\int f(\mathbf{p},\mathbf{j},\mathbf{p}',\mathbf{j}')\frac{\partial n_0}{\partial E}\beta_1(p')\mathbf{j}'\mathbf{H}\frac{d^3p'}{(2\pi\hbar)^3} \\
&= -Sp_{j'}\int\frac{d^3p'}{(2\pi\hbar)^3 n} \\
&\times\left[\frac{\alpha}{3}\varepsilon(p') + \left(\frac{4\alpha}{3}\varepsilon(p') + 2A(p,p')\right)\frac{\hat{\mathbf{j}}\hat{\mathbf{j}}'}{9}\right] \\
&\times\left(-\frac{\partial n_0}{\partial E'}\right)\beta_1(p')(\hat{\mathbf{j}}'\mathbf{H}) \\
&= -\frac{1}{(2\pi\hbar)^3 n}\frac{\hat{\mathbf{j}}\mathbf{H}}{9}\int\left[\frac{4\alpha}{3}\varepsilon(p') + 2A(p,p')\right] \\
&\times\left(-\frac{\partial n_0}{\partial E'}\right)\beta_1(p')d^3p',
\end{aligned} \quad (22)$$

where $(\hat{\mathbf{j}}\mathbf{H})$ is the scalar product.

In view of (20)–(22), we come to

$$\begin{aligned}
\beta_1(p) &= 2\mu_0^* + \frac{(2m)^{3/2}}{9n2\pi^2\hbar^3 2}\int\left(-\frac{\partial n_0}{\partial E}\right)\beta_1(p') \\
&\times\left[\frac{4\alpha}{3}\varepsilon(p') + 2A(p,p')\right]\sqrt{\varepsilon'}d\varepsilon',
\end{aligned}$$

$$\beta_1(p) \approx 2\mu_0^* + \frac{1}{12\varepsilon_F^{3/2}}\left\{\frac{4\alpha}{3}\varepsilon_F^{3/2} + 2A(p)\sqrt{\varepsilon_F}\right\}\beta_1(p')$$

or

$$\beta_1(p) = \frac{2\mu_0^*}{1 - \frac{1}{6}\left(\frac{2}{3}\alpha + \frac{A(p)}{\varepsilon_F}\right)}. \quad (23)$$

The magnetic moment is

$$\mathbf{M} = 2\mu_0^* Sp_j\hat{j}\int\delta n(p,\hat{j}')\frac{d^3p'}{(2\pi\hbar)^3}$$

$$= 2\mu_0^* S p_j \hat{j} \int \delta n(p, \hat{j}) \frac{\partial n_0}{\partial \varepsilon} \delta\varepsilon(p, \hat{j}) \frac{d^3 p'}{(2\pi\hbar)^3}$$
$$= 2\mu_0^* S p_j \hat{j} (\hat{\mathbf{j}}\mathbf{H}) \int \frac{\partial n_0}{\partial \varepsilon} \beta_1(p) \frac{d^3 p'}{(2\pi\hbar)^3} \quad (24)$$
$$= \frac{2\mu_0^*}{1 - \frac{1}{6}\left(\frac{2}{3}\alpha + \frac{A(p)}{\varepsilon_F}\right)}.$$

Then, for the magnetic susceptibility, we have [17]

$$\chi = \frac{4\mu_0^{*2}}{1 - \frac{A}{6\varepsilon_F}\left(\frac{1}{6}\left(\frac{A}{\varepsilon_F}\right)^2 + 1\right)}. \quad (25)$$

It is seen that if the ratio A/ε_F is not small, the magnetic susceptibility may have a singularity related to the transition to the spontaneous magnetization state. In other words, the paramagnetic–ferromagnetic phase transition is a possibility. This situation deserves special consideration.

ON THE POSSIBILITY OF THE FERROMAGNETIC STATE OF ATOMIC FERMI GAS

If a system has spontaneous polarization of the spins, one can comment on the spontaneous magnetic moment of the entire Fermi system. Let **m** be the unit vector in the direction of the spontaneous magnetic moment. Then, the particle binding energy depends on the mutual orientation of the spin and **m**:

$$\varepsilon(\mathbf{p}, \mathbf{j}) = \varepsilon_0(\mathbf{p}) - \kappa \hat{\mathbf{j}}\mathbf{m}. \quad (26)$$

According to this formula, the energy of the atom with the spin parallel to **m** is $\varepsilon_0 - \kappa$; accordingly, the equilibrium distribution function is $n_F(\varepsilon_0 - \kappa) = n^+$. The energy of the atom with the oppositely directed spin is $\varepsilon_0 + \kappa$, and the equilibrium distribution function has the form $n_F(\varepsilon_0 + \kappa) = n^-$. The eigenvalues of n^+ and n^- are obtained under the action of the operator

$$\hat{n}_0(\mathbf{p}, \mathbf{j}) = \frac{1}{2}(n^+ + n^-) + (n^+ - n^-)\hat{\mathbf{j}}\mathbf{m}, \quad (27)$$

which can be viewed as the equilibrium density matrix. For excited states ($\varepsilon > \varepsilon_F$), we can put

$$n^+ - n^- = n_F^0 \frac{e^{\frac{\kappa}{T}} - e^{-\frac{\kappa}{T}}}{e^{\frac{\kappa}{T}} + e^{-\frac{\kappa}{T}}}, \quad (28)$$

where n_F^0 is the Fermi distribution function.

Now let us see how the electron energy changes when **m** rotates through an angle $\delta\theta$. In this case, $\delta\mathbf{m} = [\delta\boldsymbol{\theta} \times \mathbf{m}]$, and we have from (26)

$$\delta\boldsymbol{\sigma} = -\kappa[\mathbf{m} \times \hat{\mathbf{j}}]\delta\theta. \quad (29)$$

On the other hand, when **m** changes, so do equilibrium distribution function (27),

$$\delta\hat{n}_0(\mathbf{p}, \mathbf{j}) = (n^+ - n^-)[\mathbf{m} \times \hat{\mathbf{j}}]\delta\theta,$$

and hence the energy:

$$\delta\varepsilon = S p_j \int \hat{f} \delta n_0 \frac{d^3 p}{(2\pi\hbar)^3}$$
$$= S p_j \int \hat{f}(n^+ - n^-)[\mathbf{m} \times \hat{\mathbf{j}}]\delta\theta \frac{d^3 p'}{(2\pi\hbar)^3}. \quad (30)$$

Equating (29) to (30) at an arbitrary $\delta\theta$, we obtain

$$-\kappa[\mathbf{m} \times \hat{\mathbf{j}}] = S p_{j'} \int \hat{f}(n^+ - n^-)[\mathbf{m} \times \hat{\mathbf{j}}] \frac{d^3 p'}{(2\pi\hbar)^3}. \quad (31)$$

Substituting (19) into (31) yields

$$-\kappa[\mathbf{m} \times \hat{\mathbf{j}}] = -\frac{\sinh\frac{\kappa}{T}}{\cosh\frac{\kappa}{T}}\left(\frac{4\alpha}{3}\varepsilon_F + 2A\right)[\mathbf{m} \times \hat{\mathbf{j}}],$$

since

$$\alpha \approx \frac{1}{4}\left(\frac{2A}{\varepsilon_F}\right)^3,$$

$$\frac{\kappa}{T}\frac{T}{\frac{4\alpha}{3}\varepsilon_F + 2A} = \tanh\frac{\kappa}{T}, \quad (32)$$

$$\frac{\kappa}{T}\frac{T}{2A\left(\left(\frac{2A}{\varepsilon_F}\right)^2 + 1\right)} = \tanh\frac{\kappa}{T}. \quad (33)$$

At

$$\frac{T}{2A\left(\left(\frac{2A}{\varepsilon_F}\right)^2 + 1\right)} < 1, \quad (34)$$

transcendental equation (33) has a nontrivial solution corresponding to the phase transition to the state with a uncompensated magnetic moment.

The above condition holds in the temperature range where the degeneracy of the atomic gas is observed. Note, however, that the phase transition to the ferromagnetic state may take place at much higher temperatures.

SPIN WAVES IN A DEGENERATE FERMI GAS

In the ferromagnetic state, a new type of spin waves may occur in an atomic Fermi system. For the density matrix with respect to the spin variable, the associated kinetic equation has the form

$$\frac{\partial \hat{n}}{\partial t} = \frac{i}{\hbar}[\hat{H}, \hat{n}].$$

The coordinate and momentum operators for the atoms are considered to be classical. Taking into account that only the spin variables are noncommutative, we come to

$$\frac{\partial n}{\partial t} + \frac{i}{\hbar}[\hat{\varepsilon}, \hat{n}] + \mathbf{v}\frac{\nabla n}{\partial \mathbf{r}} + \dot{\mathbf{p}}\frac{\partial n}{\partial \mathbf{p}} = 0.$$

We will seek the distribution $\hat{n} = \hat{n}_0 + \delta\hat{n}$, where $\hat{n}_0$ is equilibrium function (27) and $\delta\hat{n} \sim \exp[i(\mathbf{kr} - \omega t)]$, and represent $\delta\hat{n}$ as the sum of two terms, one of which depends on the spin and the other is spin-independent:

$$\delta\hat{n} = \nu(\mathbf{p}) + \boldsymbol{\nu}(\mathbf{p})\sigma.$$

Leaving the terms linear in δn, we obtain the sets of equation for ν and $\boldsymbol{\nu}$.

The first set describes the oscillations of the atom density and the related oscillations of the spin projections onto the direction of the magnetic field: $\nu_z = \boldsymbol{\nu}\mathbf{m}$. Note that in the case of the electron density oscillations, which are accompanied by the oscillations of the charge density, it is necessary to consider the resulting electric fields, which causes high-frequency excitations: $\omega = \mu/\hbar$ [18]. For an atomic system, the oscillations of the spin projection lead to the same effect but are not considered in this work. The second set of equations describes the oscillations of the transverse components and, after introducing the cyclic variables, gives for $\nu_+ = \nu_x + i\nu_y$ [18]

$$-\omega\nu_+ + \mathbf{kv}\boldsymbol{\nu}_+ + [\mathbf{k}(\mathbf{v} - \mathbf{u})\delta(\varepsilon_0 - b - \mu)$$

$$+ \mathbf{k}(\mathbf{v} + \mathbf{u})\delta(\varepsilon_0 + b - \mu)]\int\left(\frac{4}{3}\alpha\varepsilon(p) + j(p, p')\right)$$

$$\times \nu_+(p')\frac{d^3p'}{(2\pi\hbar)^3} - \frac{2b}{\hbar}\nu_+ - \frac{2}{\hbar}(n_+ - n_-)$$

$$\times \int\left(\frac{4}{3}\alpha\varepsilon(p) + j(p, p')\right)\nu_+(p')\frac{d^3p'}{(2\pi\hbar)^3} = 0,$$

where $\mathbf{v} = \partial\varepsilon_0/\partial p$, $\mathbf{u} = \partial b/\partial p$, and $2A = J$.

Solving this equation by the method of successive approximations, we obtain the dispersion relation for the second-order terms in k [17]:

$$\omega = \left\{\int\hbar(\mathbf{kv})^2(n_+ - n_-)\frac{d^3p}{(2\pi\hbar)^3}\right.$$

$$\left. - \hbar b\int(\mathbf{kv})^2\frac{ds}{(2\pi\hbar)^3\nu_{\varepsilon_0 = \mu + b}} - \hbar b\int(\mathbf{kv})^2\frac{ds}{(2\pi\hbar)^2\nu_{\varepsilon_0 = \mu - b}}\right\}$$

$$\times\left[2b\int(n_+ - n_-)\frac{d^3p}{(2\pi\hbar)^3}\right]^{-1}.$$

It turns out that $\omega \sim \hbar k^2\nu^2 b/\mu$. This relationship is also valid for a degenerate atomic Fermi gas, where transverse wave may propagate. In essence, this result is consistent with those obtained in [10, 15], where similar effects have been considered in Boltzmann atomic gases (or, more precisely, in nondegenerate quantum gases).

CONCLUSION

The analysis of magnetic effects taking place in heavily cooled atomic Fermi systems is of importance for at least two reasons. First, the process of cooling and confining the atoms proceeds in the magnetic traps with rather complex configurations of magnetic fields. Therefore, the behavior of the atomic gas confined by such a trap in many ways depends on its response to an applied nonuniform field (paramagnetic effects), as well as on the ability of the gas to generate the magnetic self-field (ferromagnetism). Second, the interaction by itself, causing the spontaneous magnetization of the atomic gas, may result in nonideality. Consequently, the atomic gas cannot be considered as an adequate model of a perfect Fermi system at temperatures lower than some critical temperature.

In this work, we did not strive to give a comprehensive electrodynamic analysis of macroscopic magnetic fields in the trap with allowance for the generation of magnetic fields by an atom system (although such a description would be of interest). Here, we tried to macroscopically describe the behavior of near-degenerate interacting atoms and outline possible quantum effects, like exchange effects in solids, that cause ferromagnetism in an atomic gas. In more rarefied gases, at least the exchange enhancement of paramagnetism may be observed. We also showed that the exchange interaction constant calculated *ab initio* is not small compared with the thermal energy.

Having found the fundamental possibility of the spontaneous spin polarization of a degenerate atomic gas in the presence of exchange interaction, we came to conclusion that force exchange dominates over nonforce exchange, which gives rise to the antiparallel spin alignment, and that the partial polarization of the spin may set in the system. Statistically, this circumstances means that the phase transition of the atomic gas to the

ferromagnetic state is a possibility. With the atom spins aligned ferromagnetically, the excitations (spin waves) observed earlier in Boltzmann gases may propagate.

ACKNOWLEDGMENTS

The authors are indebted to Christoph Ehricht for his encouragement.

This work was financially supported by the Russian Foundation for Basic Research (grant no. 99-02-17076), Program "Universities of Russia" (grant no. 015.01.04), and the Ministry of Education of the Russian Federation (grant no. E00-3-12).

REFERENCES

1. M. H. Anderson, Science **269**, 198 (1995); K. B. Davis, Phys. Rev. Lett. **75**, 3969 (1995); C. C. Bradley, Phys. Rev. Lett. **75**, 1687 (1995); C. C. Bradley, C. A. Sackett, and R. G. Hulet, Phys. Rev. Lett. **78**, 985 (1997).
2. B. De Marko and D. S. Jin, Science **285**, 1703 (1999).
3. S. Inouye, Nature **392**, 151 (1998); Ph. Coureille, R. S. Freeland, D. J. Heinzen, *et al.*, Phys. Rev. Lett. **81**, 69 (1998); J. L. Roberts, Phys. Rev. Lett. **81**, 5109 (1998); V. Vuletic, A. J. Kerman, C. Chin, and S. Chu, Phys. Rev. Lett. **82**, 1406 (1999).
4. E. A. Cornell, J. R. Enscher, and C. E. Wieman, http://lanl.gov/abs/condmat/9903109.
5. J. Schneider and H. Wallis, Phys. Rev. A **57**, 1253 (1998); G. M. Bruun and K. Burnet, Phys. Rev. A **58**, 2427 (1998).
6. J. M. V. A. Koelman, H. T. C. Stoof, B. J. Verhaar, and J. T. M. Walraven, Phys. Rev. Lett. **59**, 676 (1987).
7. G. Ferari, Phys. Rev. A **59**, R4125 (1999).
8. S. K. Yip and T. L. Ho, Phys. Rev. A **59**, 4653 (1999).
9. H. T. C. Stoof, M. Houbiers, C. A. Sackett, and R. G. Hulet, Phys. Rev. Lett. **76**, 10 (1996); M. Houbiers and H. T. C. Stoof, Phys. Rev. A **59**, 1556 (1999); M. A. Baranov and D. S. Petrov, Phys. Rev. A **58**, R801 (1998).
10. S. P. Bashkin, Usp. Fiz. Nauk **148**, 433 (1986) [Sov. Phys. Usp. **29**, 238 (1986)].
11. A. F. Silvera and J. Walraven, Sci. Am **246**, 56 (1982); Usp. Fiz. Nauk **139**, 701 (1983); I. F. Silvera, Physica B (Amsterdam) **109–110**, 1499 (1982).
12. M. Leduc, P. J. Nacher, S. B. Crampton, and F. Lalé, J. Phys. Lett. **45**, L441 (1984).
13. B. R. Johnson, J. S. Denker, N. Bigelow, *et al.*, Phys. Rev. Lett. **52**, 1508 (1984); B. R. Johnson, J. S. Denker, and N. Bigelow, Phys. Rev. Lett. **53**, 302 (1984).
14. G. Tastevin, P. J. Nacher, M. Leduc, and F. Lalé, J. Phys. Lett. **45**, L249 (1985).
15. E. V. Orlenko and A. A. Rumyantsev, Fiz. Nizk. Temp. **15**, 485 (1989) [Sov. J. Low Temp. Phys. **15**, 272 (1989)].
16. E. V. Orlenko and A. A. Rumyantsev, Zh. Éksp. Teor. Fiz. **97**, 439 (1990) [Sov. Phys. JETP **70**, 244 (1990)]; E. V. Orlenko and T. Yu. Latyshevskaya, Zh. Éksp. Teor. Fiz. **113**, 2139 (1998) [JETP **86**, 1167 (1998)]; E. V. Orlenko and B. G. Matisov, Fiz. Tverd. Tela (St. Petersburg) **41**, 2127 (1999) [Phys. Solid State **41**, 1951 (1999)].
17. L. D. Landau, Zh. Éksp. Teor. Fiz. **30**, 1058 (1956) [Sov. Phys. JETP **3**, 920 (1956)].
18. A. A. Abrikosov, *Fundamentals of the Theory of Metals* (Nauka, Moscow, 1987; North-Holland, Amsterdam, 1988).

Translated by V. Isaakyan

Technical Physics, Vol. 46, No. 12, 2001, pp. 1501–1503. Translated from Zhurnal Tekhnicheskoĭ Fiziki, Vol. 71, No. 12, 2001, pp. 13–15.

On the Principle of Minimum Kinetic Energy Dissipation in the Nonlinear Dynamics of Viscous Fluid

V. A. Lyul'ka

Computing Center, Russian Academy of Sciences, ul. Vavilova 40, GSP-1, Moscow, 1179647 Russia

Received July 31, 2000

Abstract—By the direct numerical integration of the complete set of the Navier–Stokes equations, it is found that the minimum kinetic energy dissipation principle, or the Helmholtz principle, is realized in some internal flows of a viscous fluid. Studies are conducted for the Reynolds numbers from 2 to 20. A class of problems where this principle takes place is considered. © *2001 MAIK "Nauka/Interperiodica".*

In the slow viscous flow dynamics, for which the nonlinear terms in the Navier–Stokes equations may be neglected, the Helmholtz variational principle holds. This principle reads as follows: The mechanical energy dissipated during the real slow flow of a viscous incompressible fluid within some volume is less than that dissipated during the arbitrary motion of an incompressible fluid with the same velocity distribution on the surface of this volume [1]. In the nonlinear dynamics of viscous fluid, the principle thus stated does not take place.

The question arises of whether there are nonlinear flows where the principal of minimum kinetic energy dissipation is observed. It turns out that such flows do exist and their class is fairly wide. It is clear that these flows have been found by numerical methods, since it seems unrealistic to solve more or less significant problem with the aid of analytical methods.

Let us formulate the problem. A viscous incompressible fluid containing one or several rigidly bound cylindrical particles flows along an infinitely long circular cylindrical pipe. The pipe and particle axes coincide. The particle moves along the pipe axis with a constant velocity. This velocity will referred to as the velocity of particle entrainment. This is the velocity of the coordinate system related to the particle. The type of particles for which the entrainment problem is solved is shown in Fig. 1.

Let us write the Navier–Stokes equations in the cylindrical coordinate system using a stream function Ψ. We introduce the stream function with the equations

$$V_r = -\frac{1}{r}\frac{\partial\Psi}{\partial z}; \quad V_z = \frac{1}{r}\frac{\partial\Psi}{\partial r}.$$

Here, V_r and V_z are the velocities along the radius and the z axis, respectively. Having eliminated the pressure, we arrive at the following set of equations in terms of dimensionless variables:

$$\frac{\partial^2\Psi}{\partial r^2} - \frac{1}{\partial r}\frac{\partial\Psi}{\partial r} + \frac{\partial^2\Psi}{\partial z^2} = \omega,$$

$$\frac{\partial^2\omega}{\partial r^2} - \frac{1}{\partial r}\frac{\partial\omega}{\partial r} + \frac{\partial^2\omega}{\partial z^2} = \frac{\mathrm{Re}}{r^2}\frac{\partial\Psi}{\partial z}\omega + \frac{\mathrm{Re}}{2}\frac{1}{r} \tag{1}$$

$$\times\left(\frac{\partial\Psi}{\partial r}\frac{\partial\omega}{\partial z} - \frac{\partial\Psi}{\partial z}\frac{\partial\omega}{\partial r}\right).$$

Here,

$$\frac{\partial^2}{\partial r^2} - \frac{1}{r}\frac{\partial}{\partial r} + \frac{\partial^2}{\partial z^2} \equiv D$$

is the Stokes operator [2]; $\mathrm{Re} = (\rho R V_m)/\mu$, the Reynolds number; ρ, the fluid density; R, the pipe radius; V_m, the mean fluid velocity for $z \longrightarrow \pm\infty$; and μ, the fluid viscosity.

The Navier–Stokes set of differential equations has to be supplemented by boundary conditions. We specify them in the frame of references where the particle is at rest. In particular, $\Psi = -(1 - r^2)^2 - 0.5Vr^2$ (V is the particle velocity) and $\omega = -8r^2$ for $z \longrightarrow \pm\infty$. The other boundary conditions were listed in [3]. The boundary conditions for ω on solid surfaces involve the Thom-like conditions [4]. System (1) was approximated by the method of central differences. The resulting set of

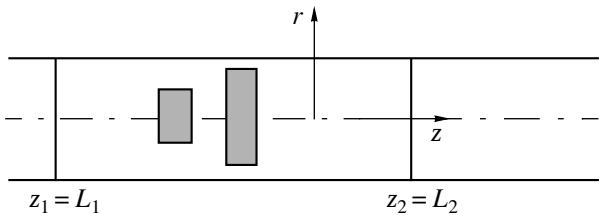

Fig. 1.

1063-7842/01/4612-1501$21.00 © 2001 MAIK "Nauka/Interperiodica"

difference equations was solved with the Zaidel method. In [5], the accuracy of numerical results as applied to this problem was considered in detail.

For reference, we present the expression for the dissipation energy in the axially symmetric problem in cylindrical coordinates:

$$E = \frac{2}{\mathrm{Re}}\int_{z_1}^{z_2} dz \int_0^1 \left[4\pi\left(\frac{\partial U_r}{\partial r}\right)^2 + 4\pi\left(\frac{U_r}{r}\right)^2 + 4\pi\left(\frac{\partial U_x}{\partial x}\right)^2 + \frac{2\pi}{r}\left(\omega - 2\frac{\partial^2 \Psi}{\partial z^2}\right)^2 \right] r\,\partial r, \quad (2)$$

where

$$U_r = -\frac{1}{r}\frac{\partial \Psi}{\partial z}, \quad U_z = \frac{1}{r}\frac{\partial \Psi}{\partial r},$$

and z_1 and z_2 correspond to the left and right pipe ends, respectively.

Consider an important issue that has not yet been discussed, namely, the numerical differentiation of a numerical solution of a differential equation. The resulting error of a numerical solution of a differential equation is the sum of a systematic error $O(h^k)$, the so-called approximation error, and an accidental error ε related to inaccurate solutions of difference equations by iteration. The differentiation of numerical results is made by dividing a difference of a certain order by h^l, where h is the step of the grid and l is the exponent. In this case, the error of the final result may become intolerably large. Such a situation would take place in our problem if the numerical results obtained by a scheme of second order of accuracy were doubly differentiated, squared, and summed up. The remarkable feature here is that the presence of the systematic and accidental errors in the numerical solution of a boundary problem results in acceptable accuracy of the derivatives. The author is also familiar with Volkov's theorem, which states that, in differentiating the numerical solution of the Laplace equation, any derivative has the same order of accuracy as the solution itself [6].

The entrainment problem was solved in the following way: particles are entrained by a viscous incompressible fluid flowing in a circular cylindrical pipe (Fig. 1). The system of coordinates is fixed and related to the particles. In this system, the flow of the viscous fluid at the solid particles is considered in the volume bounded by $z_1 = L_1$ and $z_2 = L_2$ (Fig. 1). At the ends of this pipe segment, the pressure gradient across the pipe cross section is equal to the Poiseuille gradient.

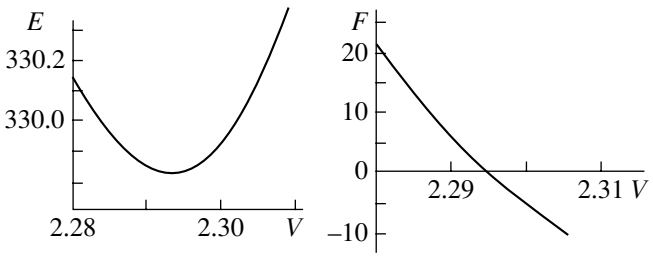

Fig. 2.

For various shapes of the particles, various Reynolds numbers Re, and various velocities of the particles, we calculated the dissipation energy by formula (2). In the left-hand side of Fig. 2, the dependence of dissipation energy on the velocity of the bodies shown in Fig. 1 is presented. The total force acting on the moving particle as a function of the particle velocity is shown in the right-hand side of Fig. 2. The curves were obtained for Re = 10. Consider the force behavior: at a certain value of the particle velocity, the total force acting on it is equal to zero. By definition, this velocity is the entrainment velocity. Note, however, that a minimum of the dissipation energy is also observed at a certain velocity in the left-hand plot. The velocities corresponding to the zero total force and to the minimal dissipation energy coincide within a relative error of 0.04%. The author perceives that a numerical calculation cannot serve as the proof of the principle stated in this paper. However, there is no doubt that this principle is correct, since the coincidence of the minimum of dissipation energy (2) and the zero of the total force acting on the bodies of certain configurations cannot occur accidentally, especially if it is taken into account that both very complex expressions are derived on the special ensemble of points (the numerical solution of the Navier–Stokes equations).

This study was carried out for Reynolds numbers from 2 to 20. The behavior of the dissipation energy and the total force acting on the bodies is the same throughout the range of Reynolds numbers and for various configurations of the bodies. It may appear that the Reynolds numbers selected are too small. However, the nonlinearity in this problem was observed even for Re = 1–3. This range of Reynolds numbers was chosen because the calculations were performed with the BÉSM-6 computer, whose performance is relatively low.

Note another fact of interest. As is shown in Fig. 3, in the Re range considered, the Re dependence of the dissipation energy is represented by the hyperbola $E = b/\mathrm{Re}$, where b is a certain constant depending on the shape of the particles. The deviation of the calculated data from the inverse proportionality does not exceed 0.1%. As follows from Fig. 3, the Re dependence of the dissipation energy for such flows obeys the similarity law.

Axisymmetric and plane problems are not the only ones for which the minimum energy dissipation principle is valid. Intuition suggests that this principle takes place for a viscous fluid flowing in an infinite straight cylinder of an arbitrary radius if the solid bodies entrained move with a constant velocity vector, which is referred to as an entrainment velocity vector, and sta-

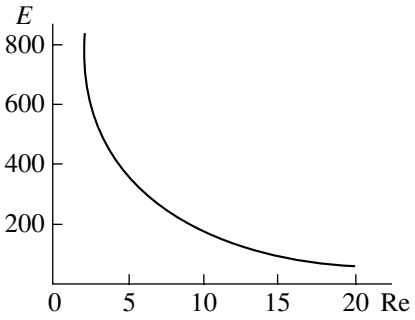

Fig. 3.

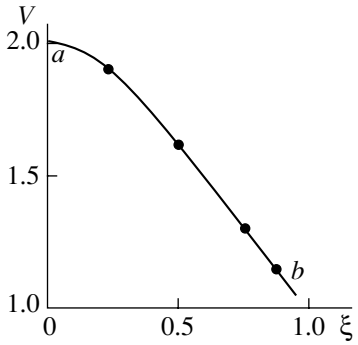

Fig. 4.

tionary boundary conditions are held at the ends of the cylinder. This fact is also correct for the entrainment of periodical structures.

Let us briefly describe the effect observed in [7]. In an infinitely long pipe containing a viscous fluid, an infinitely long rod (cylinder) of different radius is entrained by the fluid. The minimum energy dissipation principle has been used to find the velocity of the solid rod, and the exact formula has been derived for the velocity of entrainment of infinitely long cylinders of certain radii. The $V(\xi)$ curve (Fig. 4) shows the velocities of sufficiently long cylindrical bodies of the same radii; the dots indicate the velocities found by the direct numerical integration of the Navier–Stokes equations [8]. Therefore, an exact formula for the entrainment velocity may be obtained by applying the minimum energy dissipation principle to the case when an infinite circular cylinder is entrained by a viscous fluid flowing in another circular cylinder. This formula is written as

$$\frac{2}{V} = \frac{2\zeta}{a} = 1 + \zeta^2$$

$$+ b[(1 + \zeta^2)\zeta^2 \ln\zeta^2 + 2\zeta^2(1 - \zeta^2)]/8,$$

where b is determined from the equation $4b = (l + b)^2\zeta^2$ in view of the relationship $l(1 - \zeta^2) = 8 + b\zeta^2 \ln\zeta^2$ for l.

Applying the same principle to solving a similar problem of entrainment of an infinite cylinder in an axisymmetric wavy pipe would result in the correct result but for a nonlinear flow. As is seen, the use of the minimum energy dissipation principle is the only method to completely solve a number of problems. Since in the last two problems the force acting on an body entrained cannot be equal to zero, the minimum energy dissipation principle has to be applied to find the entrainment velocity for the solid body.

In [9], some problems related to the Stokes equation have been considered from the variational standpoint. In [10], much attention has been given to the viscous fluid dynamics and the question has been raised as to whether flows where the Helmholtz principle takes place exist. However, no answer has been provided. Both [9] and [10] were published much later than the author's papers; however, neither refers to his papers and results. The author therefore inferred that his early work "sank" in a number of other papers and decided to publish it once more after some revision.

REFERENCES

1. L. G. Loĭtsyanskiĭ, *Mechanics of Liquid and Gas* (Fizmatgiz, Moscow, 1959).
2. N. A. Slezkin, *Dynamics of Viscous Incompressible Liquid* (GITTL, Moscow, 1955).
3. V. A. Lyul'ka, Zh. Vychisl. Mat. Mat. Fiz. **13**, 1347 (1973).
4. P. J. Roach, *Computational Fluid Dynamics* (Hermosa, Albuquerque, 1976; Mir, Moscow, 1980).
5. V. A. Lyul'ka, Zh. Vychisl. Mat. Mat. Fiz. **13**, 135 (1983).
6. E. A. Volkov, Tr. Mat. Inst. im. V. A. Steklova, Akad. Nauk SSSR **128**, 1 (1972).
7. V. M. Borisov, V. G. Markov, and S. F. Palilova, Zh. Vychisl. Mat. Mat. Fiz. **11**, 785 (1971).
8. V. A. Lyul'ka and Yu. N. Pavlovskiĭ, Zh. Vychisl. Mat. Mat. Fiz. **9**, 238 (1969).
9. V. L. Berdichevskiĭ, *Variational Principles in Mechanics of Continuous Medium* (Nauka, Moscow, 1983).
10. Yu. L. Klimontovich, *Statistical Physics* (Nauka, Moscow, 1982; Harwood, Chur, 1986).

Translated by M. Fofanov

Technical Physics, Vol. 46, No. 12, 2001, pp. 1504–1513. Translated from Zhurnal Tekhnicheskoĭ Fiziki, Vol. 71, No. 12, 2001, pp. 16–25.

GASES AND LIQUIDS

Capillary Instability of the Cylindrical Interface between Ferrofluids in a Magnetic Field with Circular Field Lines

V. M. Korovin

Research Institute of Mechanics, Moscow State University, Michurinskiĭ pr. 1, Moscow, 119899 Russia
e-mail: korovin@imec.msu.ru

Received March 5, 2001

Abstract—Capillary breakup of a viscous magnetic fluid layer subjected to a gradient magnetic field under hydroweightlessness is studied within the linear theory. The cylinder surface of a current-carrying conductor serves as the inner boundary of the layer. The outer boundary of the layer is the coaxial interface with an immiscible nonviscous fluid of lower permeability. The particular subject of investigation is the effect of the relative thickness of the layer and that of the magnetic Bond number on the characteristic time of growth of the fastest-increasing harmonic and on the size of droplets forming under the ultimate conditions of capillary breakup (i.e., at large and small Ohnesorge numbers). © *2001 MAIK "Nauka/Interperiodica".*

INTRODUCTION

It is known that a liquid sheath covering a fine filament (one of natural objects having a similar structure, web [2], was considered by Rayleigh [1]) changes the initially cylindrical shape of its free surface because of capillary instability [1]. As a result, droplets regularly spaced along the filament like beads appear (see Fig. 37 in [2], where tiny satellites between the droplets are due to the nonlinear capillary breakup of the liquid sheath). A thin liquid film applied on a wettable solid substrate (quartz [2] or metallic [3] filaments, as well as synthetic fibers) behaves in a similar way if one of the principal radius of curvature of the substrate surface is sufficiently small. It should be stressed that the use of a fine filament (with a diameter on the order of 10^{-2} or 10^{-3} cm) and a rather viscous liquid (honey) [3] are necessary to provide the slow formation of droplets (with a diameter much less than the capillary constant [4] of the liquid). Such conditions prevent the droplets from being detached from the substrate due to the gravity force.

These experiments were modified by applying a magnetic fluid layer in the zero-gravity state on a cooled steel tube with an outer diameter of 2×10^{-1} cm through which direct current is passed [5, 6]. Under such conditions, researchers were able to observe (for a very long time) the final steady-state breakup of the layer that was much less viscous and much thicker than that used in [3]. Moreover, one could easily control the droplet size, varying solely the current, hence, the density of bulk magnetic forces directed to the axis of symmetry.

The perfect fluid model is usually used [see, e.g., [7–9] and Refs. therein) for analyzing the capillary breakup of both cylindrical layers and cylindrical columns of magnetic fluids placed in magnetic fields with various configurations. When applied to the problem of capillary breakup for a cylindrical liquid layer during rest in a magnetic field with circular field lines, such an approach has made it possible to introduce the critical magnetic Bond number Bo_m (equal to unity), which separates the stability ($\mathrm{Bo}_m > 1$) and instability ($\mathrm{Bo}_m < 1$) regions.

Within the linear theory of stability, the characteristic size of droplets due to the capillary breakup of a continuous layer depends on the wavelength λ_* of the fastest-growing harmonic of the initial perturbation of the outer cylindrical boundary of the layer. For a thin cylindrical layer of a nonviscous magnetic fluid surrounded by a stationary gas layer, the relationship between λ_* and Bo_m that neglects the gravity force has been obtained [6–8]. In [9], the capillary breakup of a thin film of a magnetic Newtonian liquid covering a current-carrying conductor and having the cylindrical free outer boundary has been considered. Based on the equations of the hydrodynamic theory of lubrication, the authors of [9] have inferred that the viscosity has an effect on the perturbation increment alone, while the value of λ_* remains the same as for a thin layer of a perfect liquid.

In this work, the capillary breakup of a cylindrical viscous magnetic fluid layer surrounded by a nonviscous fluid with a lesser permeability is studied in terms of the linearized equations of ferrohydrodynamics. The effect of Bo_m and the relative layer thickness on λ_* and on the characteristic time of growth of the fastest-increasing harmonic are studied for the extreme cases (large and small Ohnesorge numbers).

1063-7842/01/4612-1504$21.00

STARTING EQUATIONS AND STATEMENT OF THE PROBLEM

Let a cylindrical layer of an immiscible liquid with a density ρ and a magnetic susceptibility χ_2 be surrounded by a stationary magnetic fluid of infinitely large volume that has the same density and a magnetic susceptibility $\chi_2 < \chi_1$. Let also the layer completely cover a horizontal conductor of radius s and be held on its surface by bulk forces due to the magnetic field induced by a direct electric current I passing through the conductor. We assume that the magnetic susceptibilities depend on the magnetic field magnitude and introduce a cylindrical coordinate system (r, ϑ, z) such that the interface is described by the relationship $r = a$, where $a > s$. The azimuth ϑ will be reckoned from the direction of the gravity force ρg. The magnetic field is azimuth, $\mathbf{H} = (0, H, 0)$, and is defined as $H = I/(2\pi r)$ in both fluids. The densities of the bulk magnetic forces $\mathbf{f}_j = (f_j, 0, 0)$ in the inner ($j = 1$) and outer ($j = 2$) fluids are given by $\mathbf{f}_j = \mu_0 M_j \nabla H$, where $\mu_0 = 4\pi \times 10^{-7}$ H/m is the permeability and $\mathbf{M}_j = \chi_j(H)\mathbf{H}$ is the magnetization.

In hydrostatic equilibrium, the pressures P_1 and P_2 in the associated regions are given by

$$\frac{\partial P_j}{\partial r} = \mu_0 M_j \frac{dH}{dr} + \rho g \cos\vartheta,$$
$$\frac{1}{r}\frac{\partial P_j}{\partial \vartheta} = -\rho g \sin\vartheta; \quad j = 1, 2. \tag{1}$$

Taking into account that the pressure experiences a capillary jump $P_1(a, \vartheta) - P_2(a, \vartheta) = \alpha/a$ at the cylindrical interface $r = a$, we find from Eqs. (1)

$$P_1(r, \vartheta) = \frac{\alpha}{a} + \rho g r \cos\vartheta + \mu_0 \int_{H(a)}^{H(r)} M_1 dH,$$
$$P_2(r, \vartheta) = \rho g r \cos\vartheta + \mu_0 \int_{H(a)}^{H(r)} M_2 dH, \tag{2}$$

where α is the surface tension coefficient.

Now we will state the problem on the stability of hydrostatic state (2) against small axisymmetric perturbations. Let the equation $r = a + \zeta(z, t)$, where $|\zeta| \ll a$, describe the shape of the perturbed interface and the expressions $P_j(r, \vartheta) + p_j(r, z, t)$ represent the distribution of the perturbed pressures at a time instant t. As before, $j = 1, 2$ refers to the inner and outer fluids, respectively. It is assumed that the inner fluid is Newtonian (with a dynamic viscosity η_1), while the fluid surrounding it is perfect. In our case, the distribution of the initial magnetic field and the shape of the perturbed interface are axisymmetric; therefore, magnetic field lines do not intersect the interface during the development of capillary instability, so that the magnetic field $\mathbf{H}$ and the densities of the bulk magnetic forces $\mathbf{f}_j$ remain unperturbed. Because of this, the linearized equations of ferrodynamics (where it is assumed that $\eta_2 = 0$) are written as

$$\frac{\partial u_j}{\partial r} + \frac{u_j}{r} + \frac{\partial w_j}{\partial z} = 0, \tag{3}$$

$$\rho \frac{\partial u_j}{\partial t} = -\frac{\partial p_j}{\partial r} + \eta_j\left(\Delta u_j - \frac{u_j}{r^2}\right), \tag{4}$$

$$\rho \frac{\partial w_j}{\partial t} = -\frac{\partial p_j}{\partial z} + \eta_j \Delta w_j. \tag{5}$$

Here,

$$\Delta = \frac{\partial^2}{\partial r^2} + \frac{1}{r}\frac{\partial}{\partial r} + \frac{\partial^2}{\partial z^2};$$

and u_j, 0, and w_j are the components of the velocity vector $\mathbf{v}$. Hereafter, we will use η instead of η_1.

The impermeability condition, the condition that the tangential velocity component vanishes on the conductor surface, as well as the linearized kinematic and dynamic conditions at the viscous–nonviscous interface are written as

$$r = s: u_1 = 0, \quad w_1 = 0, \tag{6}$$

$$r = a: \frac{\partial \zeta}{\partial t} = u_2, \quad u_1 = u_2, \quad \frac{\partial u_1}{\partial z} + \frac{\partial w_1}{\partial r} = 0, \tag{7}$$

$$r = a: p_1 - p_2 = 2\eta \frac{\partial u_1}{\partial r} - \alpha\left(\frac{\zeta}{a^2} + \frac{\partial^2 \zeta}{\partial z^2}\right) + \frac{\mu_0 \zeta}{2\pi a^2} I(M_1 - M_2)\big|_{H = H(a)}. \tag{8}$$

Certainly, only those functions u_j, w_j, and p_j having a finite value at $r = 0$ and vanishing at $r \longrightarrow \infty$ have the physical meaning.

The magnetic field affects the development of the capillary instability of the initially cylindrical magnetic fluid layer only if the magnetic susceptibility experiences a jump at the interface. In this case, the magnetic forces contribute to balance (8) of normal stresses at the interface. For this contribution, the integral terms in Eqs. (2) for the unperturbed pressures are responsible. Physically, the reason for the nonstationary forces (induced by the gradient magnetic field that remains unchanged during the development of capillary instability) acting on the perturbed interface is straightforward: When the susceptibilities experience a jump, these forces appear as a result of the change in the magnetic field $H(a + \zeta) - H(a) \approx \zeta dH/dr|_{r = a}$ in response to the change in the interface position because of the axisymmetric deformation of its initially cylindrical shape. In this case, the last term in the right-hand side of linearized dynamic condition (8), which describes the magnetic-force-induced perturbation of the pressure, depends only on the perturbation $\zeta(z, t)$ of the

interface, whereas the pressure perturbation due to capillary forces (the second term) depends on both $\zeta(z, t)$ and $\partial^2\zeta/\partial z^2$.

As follows from experiments [5–8], capillary and magnetic forces are of the greatest importance among various physical forces considered in this problem. It is just their competition that causes a magnetic fluid layer either to retain its continuity ($\mathrm{Bo}_m > 1$) or to breakup into droplets ($\mathrm{Bo}_m < 1$). Recall that the magnetic Bond number $\mathrm{Bo}_m = \mu_0 I^2(\chi_1 - \chi_2)|_{H = H(a)}/(4\pi^2\alpha a)$, given by the ratio of the third term in the right-hand side of (8) to that part of the second term depending only on $\zeta(z, t)$, is the measure of the relative contribution of these forces.

To simplify the mathematics, we will rearrange the equations and the boundary conditions. Since the external forces are potential, the velocity field is continuous, and the system is initially at rest, there exists the velocity potential $\varphi_2(r, z, t)$ [10] in the range ($a + \zeta \le r < \infty$, $0 \le \vartheta \le 2\pi$, $-\infty < z < \infty$) such that

$$u_2 = \frac{\partial\varphi_2}{\partial r}, \quad w_2 = \frac{\partial\varphi_2}{\partial z}. \tag{9}$$

The motion of a nonviscous magnetic fluid is described by the Laplace equation

$$\Delta\varphi_2 = 0 \tag{10}$$

and the linearized Cauchy–Lagrange integral

$$p_2 = -\rho\frac{\partial\varphi_2}{\partial t}. \tag{11}$$

Naturally, the motion of the viscous fluid is vortical. In the range ($s \le r \le a + \zeta$, $0 \le \vartheta \le 2\pi$, $-\infty < z < \infty$), we introduce the velocity potential $\varphi_1(r, z, t)$ and stream function $\psi(r, z, t)$. Assuming that

$$u_1 = \frac{\partial\varphi_1}{\partial r} + \frac{1}{r}\frac{\partial\psi}{\partial z}, \quad w_1 = \frac{\partial\varphi_1}{\partial z} - \frac{1}{r}\frac{\partial\psi}{\partial r} \tag{12}$$

and following the procedure applied in the problem of viscous fluid vibration [11], we pass from set (3)–(5), which describes the vortical axisymmetric motion of the viscous liquid in the layer adjacent to the conductor surface, to the equations

$$\Delta\varphi_1 = 0, \quad \frac{\partial\psi}{\partial t} - \nu\left(\frac{\partial^2\psi}{\partial r^2} - \frac{1}{r}\frac{\partial\psi}{\partial r} + \frac{\partial^2\psi}{\partial z^2}\right) = 0, \qquad \nu = \frac{\eta}{\rho} \tag{13}$$

and to the representation of the pressure perturbation in the form

$$p_1 = -\rho\frac{\partial\varphi_1}{\partial t}. \tag{14}$$

In view of (9), (11), (12), and (14), boundary conditions (6)–(8) can be written as

$$r = s: \frac{\partial\varphi_1}{\partial r} + \frac{1}{s}\frac{\partial\psi}{\partial z} = 0, \quad \frac{\partial\varphi_1}{\partial z} - \frac{1}{s}\frac{\partial\psi}{\partial r} = 0,$$

$$r = a: \frac{\partial\zeta}{\partial t} = \frac{\partial\varphi_2}{\partial r}, \quad \frac{\partial\varphi_1}{\partial r} + \frac{1}{a}\frac{\partial\psi}{\partial z} = \frac{\partial\varphi_2}{\partial r},$$

$$2\frac{\partial^2\varphi_1}{\partial r\partial z} + \frac{1}{a}\left(\frac{\partial^2\psi}{\partial z^2} - \frac{\partial^2\psi}{\partial r^2}\right) + \frac{1}{a^2}\frac{\partial\psi}{\partial r} = 0, \tag{15}$$

$$\rho\left(\frac{\partial\varphi_2}{\partial t} - \frac{\partial\varphi_1}{\partial t}\right) = 2\eta\left(\frac{\partial^2\varphi_1}{\partial r^2} + \frac{1}{a}\frac{\partial^2\psi}{\partial r\partial z} - \frac{1}{a^2}\frac{\partial\psi}{\partial z}\right)$$

$$+ \frac{\mu_0\zeta}{2\pi a^2}I(M_1 - M_2)|_{H = H(a)} - \alpha\left(\frac{\zeta}{a^2} + \frac{\partial^2\zeta}{\partial z^2}\right).$$

In the subsequent derivation of the dispersion relation, the problem will be stated by (10), (13), and (15) (that is, in terms of ζ, φ_1, φ_2, and ψ).

INERTIAL AND VISCOUS CONDITIONS OF CAPILLARY BREAKUP

Within the problem stated, various ultimate conditions of the capillary breakup of the layer are possible. Physically, they differ by the relative contributions of the inertial and viscous forces to the growth of the perturbations. These conditions also have various characteristic velocities of the fluids and various time scales that characterize the linear stage of instability development.

Before proceeding to the discussion of the ultimate cases, we note that, irrespective of the instability condition, our problem has the specific time scale $\tau_d = d^2/\nu$. In essence, it is the characteristic diffusion time of the vorticity caused by the solid surface (due to liquid particle adhesion) and diffusing inward to the viscous fluid layer of thickness $d = a - s$.

In the theoretical articles available, the capillary breakup of a magnetic fluid layer is considered for the case when Eqs. (4) and (5) where $j = 1$, as well as boundary condition (8), ignore the contribution from viscous forces. In this case, according to (8), the pressure perturbation due to capillary forces is on the order of $p_* \sim \alpha\zeta_*/a^2$ at $\mathrm{Bo}_m < 1$, where ζ_* is the characteristic deviation of the interface from its initial cylindrical shape. With this estimate, we find from Eq. (4) the characteristic radial velocity of the viscous fluid $u_* \sim p_*\tau_i/(\rho d)$ and then, from continuity equation (3), the characteristic longitudinal velocity $w_* \sim u_*\lambda_*/d$. Here, τ_i is the characteristic time of the linear stage of instability growth and λ_* is the wavelength of the fastest-growing harmonic. On the other hand, from the kinematic condition at the interface [the first equation in

(7)], it follows that $u_* \sim \zeta_*/\tau_i$. Eventually, we have $\tau_i^2 \sim \rho a^2 d/\alpha$. Thus, the breakup due to the action of capillary and inertial forces has the time scale $\tau_i \sim a\sqrt{\rho d/\alpha}$.

To write this condition in terms of dimensionless criteria, let us turn to equations of motion (4) and (5) for the viscous fluid ($j = 1$) and to boundary condition (8), which involves viscous forces. Using our estimated, we obtain

$$\frac{\eta\left|\Delta u_1 - u_1/r^2\right|}{\rho\left|\frac{\partial u_1}{\partial t}\right|} \sim \frac{\tau_i}{\tau_d}, \quad \frac{\eta|\Delta w_1|}{\rho\left|\frac{\partial w_1}{\partial t}\right|} \sim \frac{\tau_i}{\tau_d}, \quad \frac{\eta\left|\frac{\partial u_1}{\partial r}\right|}{\alpha|\zeta|/a^2} \sim \frac{\tau_i}{\tau_d}, \quad \frac{\tau_i}{\tau_d} \sim \frac{a}{d}\frac{\eta}{\sqrt{\rho\alpha d}}. \tag{16}$$

Thus, with the condition $Z \ll \delta$, where $Z = \eta/\sqrt{\rho\alpha d}$ and $\delta = d/a$ ($0 < \delta < 1$) is the relative thickness of the viscous layer, fulfilled, the effect of viscous forces on the capillary instability development is negligible. The dimensionless criterion Z (Ohnesorge number) seems to be first introduced in [12], where experimental data for the capillary breakup of liquid cylindrical streams of diameter d injected into a gaseous medium were processed. In the modern literature concerned with the capillary breakup of fine filaments of viscous fluids, the criterion Z^2 is usually meant by the Ohnesorge number (see, e.g., [13]).

In this work, we concentrate on the other ultimate case: the capillary breakup of a cylindrical viscous fluid layer when inertial forces are small. Let τ_ν be the characteristic time of the linear stage of perturbation growth under these conditions. As above, we have $p_* \sim \alpha\zeta_*/a^2$, $u_* \sim \zeta_*/\tau_\nu$, and $w_* \sim u_*\lambda_*/d$. According to Eq. (4), the order of the characteristic radial velocity is governed by the balance between viscous forces and pressure forces. From this condition, we obtain $u_* \sim p_* d/\eta$ and then $\tau_\nu \sim \eta a/(\alpha\delta)$, so that the ratio τ_i/τ_d in the right-hand sides of expressions (16) should be replaced by $\tau_\nu/\tau_d \sim (Z/\delta)^2$. Thus, for $Z^2 \gg \delta^2$, the effect of inertial forces on the capillary breakup of a cylindrical viscous layer is negligible.

Using the dimensionless parameters $Z = \eta/\sqrt{\rho\alpha d}$ and $\delta = d/a < 1$, one can easily check that

$$\tau_d = \frac{\tau_0}{Z}, \quad \tau_i \sim \frac{\tau_0}{\delta}, \quad \tau_\nu \sim \frac{Z}{\delta^2}\tau_0, \tag{17}$$

where $\tau_0 = \sqrt{\rho d^3/\alpha}$ is some characteristic time of the problem considered.

From representations (17), it follows that at $Z \approx 1$ and $\delta \approx 1$, the scales of τ_d, τ_i, and τ_ν are the same by the order of magnitude, whereas at $Z \ll \delta$ (inertial conditions) and $Z \gg \delta$ (viscous conditions), $\tau_\nu \ll \tau_i \ll \tau_d$ and $\tau_d \ll \tau_i \ll \tau_\nu$, respectively.

DISPERSION RELATION

Let us examine the behavior of the partial solutions having the form

$$[\zeta(z,t), \varphi_j(r,z,t), \psi(r,z,t)] = \exp[i(kz - \omega t)][\zeta_0, \Phi_j(r), \Psi(r)]; \quad i = \sqrt{-1}, \quad j = 1, 2 \tag{18}$$

with time. Here, ζ_0 is a constant and k is a specified real-valued parameter (wave number). Note that the linear theory of stability of homogeneous states in continuous media is aimed at finding the function $\omega = W(k)$ and analyzing its behavior in dependence of dimensionless parameters characterizing a phenomenon studied.

Substituting expressions (18) into Eqs. (10) and (13) yields

$$\Phi_j'' + \frac{1}{r}\Phi_j' - k^2\Phi_j = 0, \quad \Psi'' - \frac{1}{r}\Psi' - m^2\Psi = 0, \quad m = \sqrt{k^2 - i\frac{\omega}{\nu}}, \quad \mathrm{Re}\, m > 0, \tag{19}$$

and boundary conditions (15) take the form

$$\Phi_1'(s) + \frac{ik}{s}\Psi(s) = 0, \quad ik\Phi_1(s) - \frac{1}{s}\Psi'(s) = 0,$$

$$i\zeta_0\omega + \Phi_2'(a) = 0, \quad \Phi_1'(a) - \Phi_2'(a) + \frac{ik}{a}\Psi(a) = 0,$$

$$2ik\Phi_1'(a) - \frac{1}{a}[k^2\Psi(a) - \Psi''(a)] + \frac{1}{a^2}\Psi'(a) = 0, \tag{20}$$

$$i\rho\omega[\Phi_2(a) - \Phi_1(a)] + 2\eta\left\{\Phi_1''(a) + \frac{ik}{a}\left[\Psi'(a) - \frac{1}{a}\Psi(a)\right]\right\} + \frac{\alpha\zeta_0}{a^2}[\mathrm{Bo}_m - 1 + (ka)^2] = 0.$$

As follows from the last expression in (20), if the cylindrical interface experiences a harmonic perturbation with some wave vector k, $\zeta = \zeta_0\exp[i(kz - \omega t)]$, the contribution of magnetic surface forces into the balance between the normal stresses at the interface (hence, the effect of the magnetic forces on the evolution of this harmonic) does not depend on k; in other words, this contribution is the same for any of the harmonics at a given $\mathrm{Bo}_m \neq 0$. Thus, by varying the current passing through the conductor, one can effectively control the evolution of the harmonics throughout the wave number interval $0 < k < \infty$.

Table 1. Dimensionless matrix of the coefficients involved in Eq. (22) for the viscous conditions of capillary breakup

0	$I_1(x)$	$-K_1(x)$	0	$iI_1(y)$	$iK_1(y)$
0	$ixI_0(x)$	$ixK_0(x)$	0	$-yI_0(y)$	$yK_0(y)$
$i\Omega\delta$	0	0	$-\kappa K_1(\kappa)$	0	0
0	$I_1(\kappa)$	$-K_1(\kappa)$	$K_1(\kappa)$	$iI_1(\sigma)$	$iK_1(\sigma)$
0	$2i\kappa^2 I_1(\kappa)$	$-2i\kappa^2 K_1(\kappa)$	0	$-(\kappa^2+\sigma^2)I_1(\sigma)$	$-(\kappa^2+\sigma^2)K_1(\sigma)$
c_{61}	c_{62}	c_{63}	$-i\varepsilon\Omega K_0(\kappa)$	$-2i\kappa\sigma I_1'(\sigma)$	$-2i\kappa\sigma K_1'(\sigma)$

Table 2. Dimensionless matrix of the coefficients involved in Eq. (22) for the inertial conditions of capillary breakup

0	$I_1(x)$	$-K_1(x)$	0	$iI_1(y_1)$	$iK_1(y_1)$
0	$ixI_0(x)$	$ixK_0(x)$	0	$-y_1I_0(y_1)$	$y_1K_0(y_1)$
$i\Omega_1$	0	0	$-\kappa K_1(\kappa)$	0	0
0	$I_1(\kappa)$	$-K_1(\kappa)$	$K_1(\kappa)$	$iI_1(\sigma_1)$	$iK_1(\delta_1)$
0	$2i\kappa^2 I_1(\kappa)$	$-2i\kappa^2 K_1(\kappa)$	0	$-(\kappa^2+\sigma_1^2)I_1(\sigma_1)$	$-(\kappa^2+\sigma_1^2)K_1(\sigma_1)$
s_{61}	s_{62}	s_{63}	$-i\Omega_1 K_0(\kappa)$	$-2iZ\kappa\sigma_1 I_1'(\sigma_1)$	$-2iZ\kappa\sigma_1 K_1'(\sigma_1)$

From (19), we have

$$\Phi_1 = A_1 I_0(kr) + BK_0(kr), \quad \Phi_2 = A_2 K_0(kr), \quad \Psi = r[C_1 I_1(mr) + C_2 K_1(mr)], \tag{21}$$

where $I_l(x)$ and $K_l(x)$ ($l = 1, 2$) are the modified Bessel functions and A_1, A_2, B, C_1, and C_2 are arbitrary constants.

The solutions obtained must satisfy boundary conditions (20). Substituting expressions (21) into (20) and using the recurrence formulas for the Bessel functions [14], we come to the set of linear homogeneous equations for $\zeta_0, A_1, A_2, B, C_1$, and C_2:

$$\begin{gathered}
I_1(x)A_1 - K_1(x)B + iI_1(x_1)C_1 + iK_1(x_1)C_2 = 0,\\
ixI_0(x)A_1 + ixK_0(x)B + x_1I_0(x_1)C_1 - x_1K_0(x_1)C_2 = 0,\\
i\omega a\zeta_0 - \kappa K_1(\kappa)A_2 = 0,\\
I_1(\kappa)A_1 - K_1(\kappa)B + K_1(\kappa)A_2\\
+ iI_1(\kappa_1)C_1 + iK_1(\kappa_1)C_2 = 0,\\
2i\kappa^2 I_1(\kappa)A_1 - 2i\kappa^2 K_1(\kappa)B - (\kappa^2+\kappa_1^2)I_1(\kappa_1)C_1\\
-(\kappa^2+\kappa_1^2)K_1(\kappa_1)C_2 = 0,\\
\alpha\zeta_0(1-\mathrm{Bo}_m-\kappa^2) + [i\rho\omega a^2 I_0(\kappa) - 2\eta\kappa^2 I_1'(\kappa)]A_1\\
+ [i\rho\omega a^2 K_0(\kappa) + 2\eta\kappa^2 K_1'(\kappa)]B - i\rho\omega a^2 K_0(\kappa)A_2\\
-2i\eta\kappa\kappa_1 I_1'(\kappa_1)C_1 - 2i\eta\kappa\kappa_1 K_1'(\kappa_1)C_2 = 0,
\end{gathered} \tag{22}$$

where $x = \kappa(1-\delta)$, $x_1 = \kappa_1(1-\delta)$, $\kappa = ka$, and $\kappa_1 = \sqrt{\kappa^2 - i(a^2/\nu)\omega}$, $\mathrm{Re}\,\kappa_1 > 0$.

Let the matrix of the coefficients of algebraic set (22) be designated as $\|a_{ij}\|$. The condition

$$\det\|a_{ij}\| = 0 \tag{23}$$

for the existence of the nontrivial solution of problem (19), (20) is the dispersion relation from which the function $\omega = W(k)$ can be found.

From (23), it readily follows that the matrix $\|a_{ij}\|$ can be represented in the dimensionless form by multiplying and dividing its columns by some dimensional coefficients that are defined by the statement of the problem. In so doing, we do not lose the generality in subsequent computations of $\omega = W(k)$.

For τ_ν taken as the time scale, the dimensionless form $\|c_{ij}\|$ of the matrix $\|a_{ij}\|$ is given in Table 1, where

$$\begin{gathered}
\Omega = \omega\tau_\nu, \quad \varepsilon = Z^{-2}, \quad y = \sigma(1-\delta),\\
\sigma = \sqrt{\kappa^2 - i\varepsilon\Omega}, \quad \mathrm{Re}\,\sigma > 0,\\
c_{61} = 1 - \mathrm{Bo}_m - \kappa^2, \quad c_{62} = i\varepsilon\Omega I_0(\kappa) - 2\kappa^2 I_1'(\kappa),\\
c_{63} = i\varepsilon\Omega K_0(\kappa) + 2\kappa^2 K_1'(\kappa).
\end{gathered} \tag{24}$$

For τ_i taken as the characteristic time, the dimensionless form $\|s_{ij}\|$ of the initial matrix $\|a_{ij}\|$ is given in Table 2, where

$$\begin{gathered}
\Omega_1 = \omega\tau_i, \quad y_1 = \sigma_1(1-\delta),\\
\sigma_1 = \sqrt{\kappa^2 - i\Omega_1/(Z\delta)}, \quad \mathrm{Re}\,\sigma_1 > 0,\\
s_{61} = 1 - \mathrm{Bo}_m - \kappa^2, \quad s_{62} = i\Omega_1 I_0(\kappa) - 2Z\kappa^2 I_1'(\kappa),\\
s_{63} = i\Omega_1 K_0(\kappa) + 2Z\kappa^2 K_1'(\kappa).
\end{gathered}$$

If $Z \approx 1$ and $\delta \approx 1$, any of the matrices $\|c_{ij}\|$ and $\|s_{ij}\|$ can be used in the analysis of the dispersion relation $\det\|a_{ij}\| = 0$. On the other hand, for $Z \gg 1$ ($Z \ll \delta$), Table 1 (Table 2) should be employed.

Let $Z \gg 1$, i.e., the perturbation development be governed primarily by the inertial forces. It is easy to check that the expressions in the matrix $\|c_{ij}\|$ that contain the factor ε are due to the inertial forces involved in Stokes equations (4) and (5) for the viscous ($j = 1$) fluid. Therefore, if the problem is stated in terms of quasi-stationary Stokes equations (that is, the time derivatives in Eqs. (4) and (5) where $j = 1$ are rejected), the elements of the matrix $\|c_{ij}\|$ lose terms containing ε. In this case, the second column of the matrix becomes proportional to the fifth one and the third column, to the sixth one, so that $\det\|c_{ij}\| = 0$ at any Ω, κ, and δ. Thus, although the inertial forces are small (at $Z \gg 1$), they must necessarily be taken into account, because, as follows from the above considerations, no dispersion relation exists if the problem is stated in terms of the quasi-stationary Stokes equations. This situation is akin to the well-known paradox: if both the linear and nonlinear parts of the inertial term are rejected from the equation of motion, the problem of transverse flow around an infinite cylinder moving in a viscous fluid (filling the entire space) becomes insoluble in the sense that there is no solution that satisfies the boundary conditions on the cylinder surface and vanishes at infinity [15, 16].

ULTIMATE CONDITIONS OF CAPILLARY INSTABILITY

In the general case, dispersion relation (23) is very cumbersome and the physically meaningful roots can be obtained only numerically, whereas the ultimate conditions admit analytical examination. We will start with the case $Z \gg 1$ (or $\varepsilon \ll 1$) and designate $\det\|c_{ij}\|$ as $F(\Omega, \kappa; \varepsilon, \delta)$. It is easy to see that $F(0, \kappa; \varepsilon, \delta) = 0$, since at $\Omega = 0$ the second column of the matrix $\|c_{ij}\|$ is proportional to the fifth one and the third column, to the sixth one. Having calculated $F'_\Omega(\Omega, \kappa; \varepsilon, \delta)$, we find that each of the determinants involved in the expression for $F'_\Omega(0, \kappa; \varepsilon, \delta)$ as an individual term has two columns proportional to each other; hence, $F'_\Omega(0, \kappa; \varepsilon, \delta) = 0$. With the MAPLE suite for symbolic computation, we have established that the condition $F''_{\Omega\Omega}(0, \kappa; \varepsilon, \delta) \neq 0$ is met for any κ, ε, and δ admitted by the statement of the problem. Thus, the dispersion relation $\det\|c_{ij}\| = 0$ has the two-fold root $\Omega = 0$. The trivial root is no physical interest.

We can show in a similar way that the equalities $F(\Omega, \kappa; 0, \delta) = 0$ and $F'_\varepsilon(\Omega, \kappa; 0, \delta) = 0$ hold for any Ω, κ and $\delta \neq 0$. Because of this, the expansion of $F(\Omega, \kappa; \varepsilon, \delta)$ in ε begins with the quadratic term. Thus, at $\varepsilon \ll 1$, the existence condition for a nontrivial solution of set (22) can be written, in the first approximation, as

$$F''_{\varepsilon\varepsilon}(\Omega, \kappa; 0, \delta) = 0. \tag{25}$$

Expanding $\det\|c_{ij}\|$ in the first column, we have

$$F(\Omega, \kappa; \varepsilon, \delta) = i\Omega\delta C_{31} + (1 - \mathrm{Bo}_m - \kappa^2)C_{61},$$

where $C_{31}(\Omega, \kappa; \varepsilon, \delta)$ and $C_{61}(\Omega, \kappa; \varepsilon, \delta)$ are the algebraic supplements for the elements c_{31} and c_{61}.

In view of this equality and with the condition $\delta \neq 0$ met, we find, from (25), the approximate expression for the root of the dispersion relation:

$$\omega = \frac{i\alpha}{\eta a} q(\kappa, \delta)(1 - \mathrm{Bo}_m - \kappa^2),$$
$$q(\kappa, \delta) = \left.\frac{d^2 C_{61}}{d\varepsilon^2}\right|_{\varepsilon = 0} \left(\left.\frac{d^2 C_{31}}{d\varepsilon^2}\right|_{\varepsilon = 0}\right)^{-1}. \tag{26}$$

This expression will also be used in the subsequent analysis of the effect of the dimensionless parameters Bo_m and δ on the capillary breakup of the layer.

Note that in the limit case (Bo_m when $\delta \longrightarrow 0$), expression (26) yields

$$\omega = \frac{i\alpha}{2\eta a} \frac{(1 - \kappa^2) I_1^2(\kappa)}{\kappa^2 I_0^2(\kappa) - (\kappa^2 + 1) I_1^2(\kappa)}.$$

This result follows from the theory of capillary instability of fine filaments of very viscous liquids and has been known since the Rayleigh's time [1, 17–19].

Formula (26) is the principal term in the expansion of ω in ε for $\kappa \geq 0$ and $0 < \delta < 1$. From (26), the principal term in the expansion of ω in δ cannot be found in principle, since the function $q(\kappa, \delta)$ is undefined at $\delta = 0$. To solve this problem, one must set the ordering relationship between $\det\|c_{ij}\| = 0$ and ε and, when constructing the approximate solution of the equation $\det\|c_{ij}\| = 0$, use the expansion of $F(\Omega, \kappa; \varepsilon, \delta)$ in the asymptotic sequence of functions containing the products $\varepsilon^m\delta^n$ (m, $n = 1, 2, \ldots$). Using the MAPLE suite for $\varepsilon \ll 1$ and $\delta \sim \varepsilon$, we obtained

$$F(\Omega, \kappa; \varepsilon, \delta) = \varepsilon^2\delta[P(\Omega, \kappa) + \delta Q(\Omega, \kappa) + \delta^2 R(\Omega, \kappa)], \tag{27}$$

where

$$P(\Omega, \kappa) = \frac{1}{2}\left.\frac{\partial^3 F}{\partial\varepsilon^2\partial\delta}\right|_{\varepsilon = 0, \delta = 0} = \frac{i}{\kappa}\Omega^3 K_1(\kappa),$$

$$Q(\Omega, \kappa) = \frac{1}{4}\left.\frac{\partial^4 F}{\partial\varepsilon^2\partial\delta^2}\right|_{\varepsilon = 0, \delta = 0} = \frac{i}{\kappa}\Omega^3 K_1(\kappa),$$

$$R(\Omega, \kappa) = \frac{1}{12}\frac{\partial^5 F}{\partial\varepsilon^2\partial\delta^3}\bigg|_{\varepsilon=0,\,\delta=0} = \frac{1}{3\kappa}\Omega^2 K_1(\kappa)$$
$$\times[\kappa^2(1-\mathrm{Bo}_m-\kappa^2)+3i\Omega(1+2\kappa^2)].$$

Equating the right-hand side of expression (27) to zero, we find in the first approximation:

$$\omega = \frac{i\alpha\delta^3}{3\eta a}\kappa^2(1-\mathrm{Bo}_m-\kappa^2). \qquad (28)$$

Note that the denominator of the same formula in [9], which was derived within the hydrodynamic theory of lubrication, has the numerical coefficient 2 instead of 3. Unlike [9], our numerical analysis made it possible to find the applicability condition for formula (28), namely, $\delta \sim \varepsilon \ll 1$.

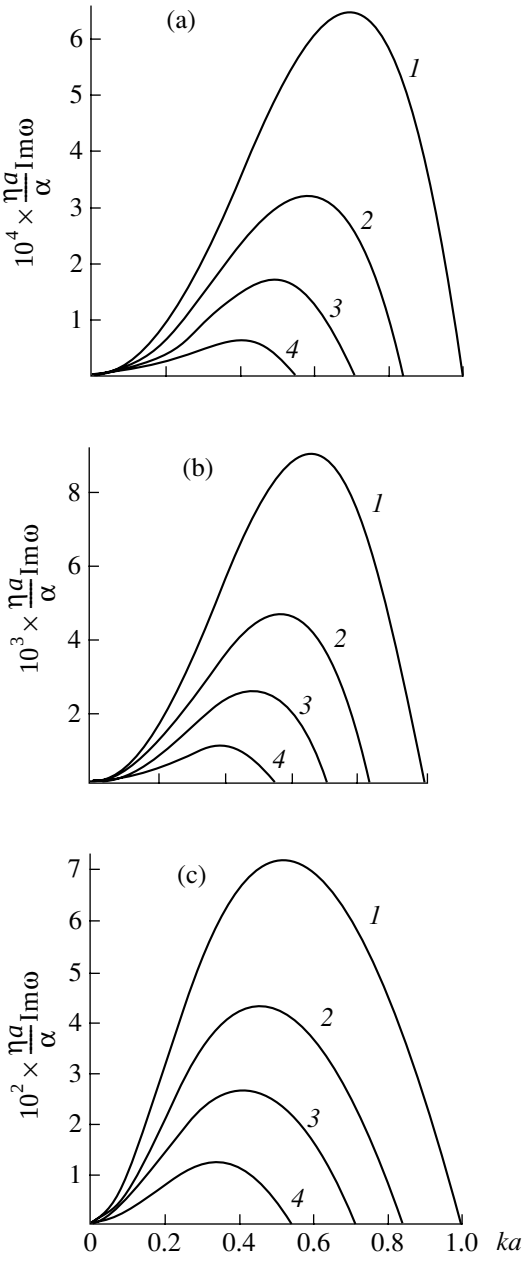

Fig. 1. Dimensionless increment vs. dimensionless wave number for the viscous capillary breakup. δ = (a) 0.2, (b) 0.5, and (c) 0.99. Bo_m = (*1*) 0, (*2*) 0.3, (*3*) 0.5, and (*4*) 0.7.

At $\mathrm{Bo}_m > 1$, expression (28) yields $\mathrm{Im}\omega < 0$; that is, the layer is stable. If $\mathrm{Bo}_m < 1$, $0 < \kappa < \sqrt{1-\mathrm{Bo}_m}$. In this case, the layer is unstable, because $\mathrm{Im}\omega > 0$, but the magnetic field still stabilizes the range of harmonics with wave numbers $\sqrt{1-\mathrm{Bo}_m} < \kappa < 1$, which is unstable at $\mathrm{Bo}_m = 0$. Thus, the value $\mathrm{Bo}_m = 1$ should be considered as critical in accordance with the data available in the literature.

One can easily show that the harmonic with the wave number $ka = \sqrt{(1-\mathrm{Bo}_m)/2}$ is the fastest-growing at $\mathrm{Bo}_m < 1$. The wavelength and the growth increment of this harmonic are respectively given by

$$\lambda_*^0 = 2\pi a\sqrt{\frac{2}{1-\mathrm{Bo}_m}}, \quad \mathrm{Im}\omega_*^0 = \frac{\alpha\delta^3}{12\eta a}(1-\mathrm{Bo}_m)^2. \qquad (29)$$

Consider the inertial conditions ($Z \ll \delta$) of the capillary breakup of the layer. From dispersion relation (23) and with regard for Table 2, we have

$$\Omega_1 = i(1-\mathrm{Bo}_m-\kappa^2)T(\Omega_1, \kappa; Z, \delta),$$
$$T(\Omega_1, \kappa; Z, \delta) = S_{61}S_{31}^{-1},$$

where $S_{31}(\Omega_1, \kappa; Z, \delta)$ and $S_{61}(\Omega_1, \kappa; Z, \delta)$ are the algebraic supplements to the elements s_{31} and s_{61}.

With the MAPLE suite, we found that

$$\lim_{Z\to 0} T = \frac{i\kappa^2 K_1(\kappa)}{\Omega_1 K_1[\kappa(1-\delta)]}$$
$$\times\{I_1(\kappa)K_1[\kappa(1-\delta)] - I_1[\kappa(1-\delta)]K_1(\kappa)\}.$$

Thus, if the effect of viscosity is completely neglected (i.e., within the perfect fluid model), the dispersion relation takes the form

$$\omega^2 = \frac{\alpha}{\rho a^2 d}\frac{\kappa^2 K_1(\kappa)}{K_1[\kappa(1-\delta)]}(\mathrm{Bo}_m - 1 + \kappa^2) \qquad (30)$$
$$\times\{I_1(\kappa)K_1[\kappa(1-\delta)] - I_1[\kappa(1-\delta)]K_1(\kappa)\}.$$

At $\kappa > 0$ and $0 < \delta < 1$, the brace in (30) is positive, so that the sign of ω^2 as a function of κ, Bo_m, and δ depends on that of the expression $(\mathrm{Bo}_m - 1 + \kappa^2)$. It is easy to check that $\omega^2 < 0$ at $\mathrm{Bo}_m < 1$ (the layer is unstable) and $\omega^2 > 0$ at $\mathrm{Bo}_m > 1$ (the layer is stable). In the limit cases $\delta \longrightarrow 1$ and $\delta \longrightarrow 0$, we respectively obtain from (30):

$$\omega^2 = \frac{\alpha}{\rho a^3}\kappa^2 I_1(\kappa)K_1(\kappa)(\mathrm{Bo}_m - 1 + \kappa^2), \qquad (31)$$

$$\omega^2 = \frac{\alpha}{\rho a^3}\kappa^2(\mathrm{Bo}_m - 1 + \kappa^2). \quad (32)$$

Note that in the previous works, dispersion relations (30) and (31) have not been derived and, accordingly, have not been used in the analysis of the effect of Bo_m and δ on the wavelength of the fastest-growing harmonic, although a formula similar to (30) follows from expression (3.88) in [8] (for other dimensionless ω and layer thickness). In the absence of the magnetic field, expression (31) differs greatly from the dispersion relation derived in [20] for the capillary breakup of a perfect fluid cylindrical column surrounded by a stationary gas and used in [8] for the analysis of capillary breakup of a cylindrical fluid column under weightlessness.

With (32), one can show that, at $\delta \ll 1$, the wavelength of the fastest-growing harmonic is given by the first formula in (29) and the growth increment for this harmonic is

$$\mathrm{Im}\omega_* = \sqrt{\frac{\alpha}{4\rho a^3}}(1 - \mathrm{Bo}_m).$$

Thus, droplets forming under ultimate (viscous and inertial) conditions of capillary breakup of two different thin ($\delta \ll 1$) layers have the same characteristic sizes if $\mathrm{Bo}_m < 1$. The growth increments for the two harmonics that characterize the breakup process under these conditions are conversely much different.

Figures 1 (viscous conditions of capillary breakup) and 2 (inertial conditions) illustrate how Bo_m (or, roughly speaking, the current passing through the conductor) and the relative thickness of the layer affect the dependence of the imaginary parts of ω (in the dimensionless form) on the dimensionless wave number *ka*. The curves in Figs. 1a–1c plot function (26) at the fixed δ and various Bo_m, while curves *1–3* in Fig. 2 are constructed by formulas (30)–(32) for various Bo_m. It follows from Figs. 1 and 2 that at the fixed value of δ and various Bo_m, the characteristic growth time $(\mathrm{Im}\omega_*)^{-1}$ of the fastest growing harmonic (responsible for the peak in the associated curve) increases with Bo_m. If Bo_m is fixed, this time decreases with increasing δ. This means that the capillary breakup of a thicker layer proceeds faster under both ultimate conditions for the same current passing through the conductor of a given diameter. Comparing Figs. 1a–1c, one can see that the value of $(\mathrm{Im}\omega_*)^{-1}$ under the viscous conditions is much more sensitive to δ than to Bo_m; in other words, the characteristic growth time of the fastest-growing harmonic depends primarily on the relative thickness of the layer, while the effect of the current is significantly weaker. Under the inertial breakup conditions (Fig. 2), the situation is reverse: the value of $(\mathrm{Im}\omega_*)^{-1}$ depends largely on the current and the relative thickness of the layer is of minor importance.

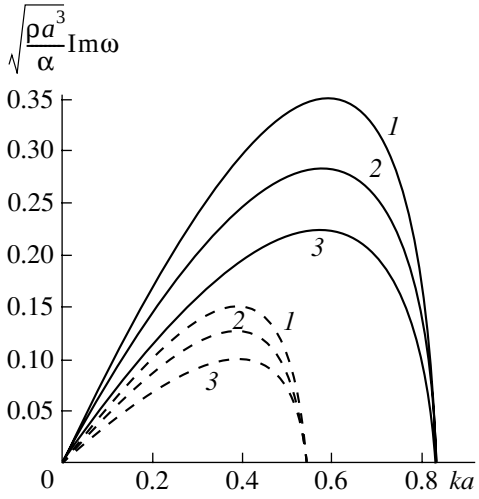

Fig. 2. The same as in Fig. 1 for the inertial breakup. δ = (*1*) 1, (*2*) 0.5, and (*3*) $\ll$ 1. Bo_m = 0.3 (continuous curves) and 0.7 (dashed curves).

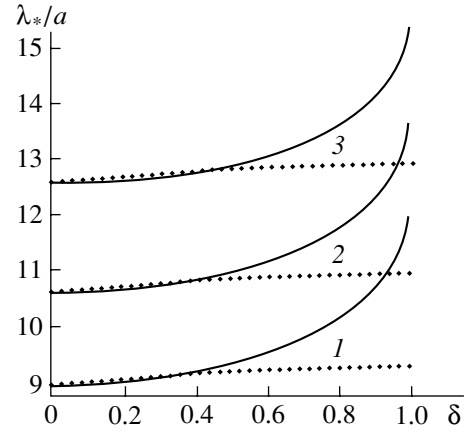

Fig. 3. Dimensionless wavelength of the fastest-growing harmonic vs. relative thickness of the layer. Bo_m = (*1*) 0, (*2*) 0.3, and (*3*) 0.5. Continuous curves, viscous conditions of breakup; dotted curves, inertial conditions of breakup.

Figure 3 and 4 allow us to compare the effects of Bo_m and δ on the characteristic size λ_*/a of the droplets forming under the ultimate conditions of the breakup. As follows from Fig. 3, at $\delta \le 0.4$ and fixed Bo_m, the difference between the size of the droplets appearing under the two conditions is insignificant and the value of λ_*/a depends largely on Bo_m, increasing with it. Under the viscous conditions at $\mathrm{Bo}_m \le 0.5$, the rise in λ_*/a due to the increase in the current is comparable to that due to the increase in the relative thickness of the layer (in the entire interval $0 < \delta \le 1$). For the inertial conditions, however, the characteristic droplet size grows with δ insignificantly and depends for the most part on the magnetic Bond number. Figure 3 shows that the droplets forming under the viscous conditions are much larger than those produced under the inertial ones

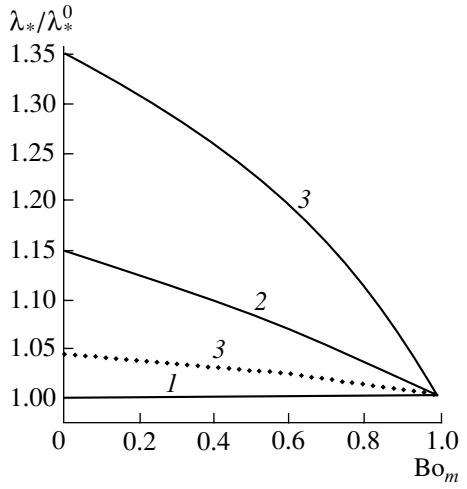

Fig. 4. Normalized wavelength of the fastest-growing harmonic vs. magnetic Bond number. δ = (*1*) 0.01, (*2*) 0.8, and (*3*) 0.99. Continuous curves, viscous conditions of breakup; dotted curves, inertial conditions of breakup.

when $Bo_m \le 0.5$ and the layer is thick (δ is close to unity).

Figure 4 refers to both conditions and shows the deviation of the $\lambda_*(Bo_m)$ dependences from the analytical curve described by the first expression in (29). From curve *1* and dashed line *3*, it follows that the maximal increase in λ_*/a for $Bo_m = 0$ and the relative thickness varying from $\delta \ll 1$ to the limit case $\delta = 1$ (continuous cylindrical column of the fluid) is no more than 5% under the inertial conditions. For the viscous conditions, the increase in λ_*/a at $Bo_m = 0$ (continuous curves *1* and *3*) is 35%. Note for comparison that at $Bo_m = 0$, $\lambda_*/(2\pi a) = \sqrt{2}$ under both ultimate conditions of the capillary breakup of a thin ($\delta = 0.01$) layer. On the other hand, for $Bo_m = 0$ and $\delta = 0.99$, $\lambda_*/(2\pi a) = 1.477$ for the inertial conditions and 1.912 for the viscous ones.

CONCLUSION

Within the linear theory, we studied the capillary instability of a viscous magnetic fluid layer covering a long cylindrical direct-current-carrying conductor. The outer boundary of the layer is in contact with an immiscible perfect liquid of density equal to that of the layer and of magnetic susceptibility lower than that of the layer. The phenomenon is characterized by three dimensionless parameters: magnetic Bond number Bo_m, Ohnesorge number *Z*, and relative layer thickness δ.

Two ultimate conditions of the capillary breakup of the layer were considered: viscous ($Z \gg 1$) and inertial ($Z \ll \delta$). It was shown that in the former case, one must include inertial forces in the equation of motion for the viscous fluid, although they are negligibly small compared with viscous forces; otherwise, the dispersion relation is absent. Such a situation is akin to the well-known paradox that arises when the problem of transverse flow around an infinite cylinder moving with a constant velocity in a viscous liquid that occupies the entire space is solved in terms of the Stokes equations.

For $Z \gg 1$, the approximate root of the dispersion relation was found. At $Bo_m = 0$ and $\delta = 1$, this root transforms into the classical expression for capillary instability of a fine viscous fluid filament immersed in a perfect liquid. It was shown that the thickness of the layer has a noticeable effect on the characteristic growth time of the fastest-growing harmonic under both ultimate conditions. This effect is most pronounced at $Z \gg 1$. As the layer thickens, the breakup goes faster. At $Z \ll \delta$, the characteristic size of resulting droplets depends largely on Bo_m and is weakly dependent on δ; however, at $Z \gg 1$ and small Bo_m, the difference in the droplet size as δ varies from $\ll 1$ to values close to unity grows and may exceed 30%. For thin layers ($\delta \ll 1$), the characteristic droplet size is independent of the ultimate breakup conditions and is controlled by Bo_m.

ACKNOWLEDGMENTS

This work was supported by the Russian Foundation for Basic Research (project no. 99-01-01057).

REFERENCES

1. Lord Rayleigh, Philos. Mag. **34**, 145 (1892).
2. C. V. Boys, *Soap Bubbles and the Forces with Mould Them* (E. & J. B. Young, London, 1900; Nauchnoe Knigoizdatel'stvo, Petrograd, 1919).
3. S. L. Goren, J. Fluid Mech. **12**, 309 (1962).
4. L. D. Landau and E. M. Lifshitz, *Course of Theoretical Physics*, Vol. 6: *Fluid Mechanics* (Pergamon, New York, 1987; Nauka, Moscow, 1988).
5. V. I. Arkhipenko, Yu. D. Barkov, V. G. Bashtovoĭ, *et al.*, Dokl. Akad. Nauk BSSR **23**, 341 (1979).
6. V. I. Arkhipenko, Yu. D. Barkov, V. G. Bashtovoĭ, *et al.*, Izv. Akad. Nauk SSSR, Mekh. Zhidk. Gaza, No. 4, 3 (1980).
7. R. Rosensweig, *Ferrohydrodynamics* (Cambridge Univ. Press, Cambridge, 1985; Mir, Moscow, 1989).
8. B. M. Berkovsky, V. F. Medvedev, and M. S. Krakov, *Magnetic Fluids: Engineering Applications* (Khimiya, Moscow, 1989; Oxford, 1993).
9. É. Ya. Blums, M. M. Maĭorov, and A. O. Cebers, *Magnetic Fluids* (Zinatne, Riga, 1989; Walter de Gruyter, Berlin, 1997).
10. L. I. Sedov, *A Course in Continuum Mechanics* (Wolters-Noordhoff, Groningen, 1971; Nauka, Moscow, 1984, 3rd ed.), Vol. 2.
11. N. N. Moiseyev and V. V. Rumyantsev, *Dynamics Stability of Bodies Containing Fluid* (Nauka, Moscow, 1965; Springer, Berlin, 1968).

12. W. von Ohnesorge, Z. Angew. Math. Mech. **16**, 355 (1936).
13. J. R. Lister and H. A. Stone, Phys. Fluids **10**, 2758 (1998).
14. *Handbook of Mathematical Functions*, Ed. by M. Abramowitz and I. A. Stegun (Dover, New York, 1971; Mir, Moscow, 1979).
15. H. Lamb, *Hydrodynamics* (Cambridge Univ. Press, Cambridge, 1932; Gostekhizdat, Moscow, 1947).
16. O. A. Ladyzhenskaya, *The Mathematical Theory of Viscous Incompressible Flow* (Nauka, Moscow, 1970; Gordon & Beach, New York, 1969).
17. S. Tomotika, Proc. R. Soc. London, Ser. A **150**, 322 (1935).
18. S. Chandrasekhar, *Hydrodynamic and Hydromagnetic Stability* (Clarendon Press, Oxford, 1961).
19. W.-K. Lee and R. W. Flumerfelt, Int. J. Multiphase Flow **7**, 363 (1981).
20. J. W. Strutt (Lord Rayleigh), *The Theory of Sound* (Macmillan, London, 1896; Gostekhizdat, Moscow, 1955), Vol. 2.

Translated by V. Isaakyan

Technical Physics, Vol. 46, No. 12, 2001, pp. 1514–1517. Translated from Zhurnal Tekhnicheskoĭ Fiziki, Vol. 71, No. 12, 2001, pp. 26–29.

Determination of the Magnetic Fluid Parameters from the Microwave Radiation Reflection Coefficients

D. A. Usanov, Al. V. Skripal, An. V. Skripal, and A. V. Kurganov

Chernyshevsky State University, ul. Astrakhanskaya 83, Saratov, 410026 Russia

e-mail: UsanovDA@info.sgu.ru

Received March 5, 2001

Abstract—The interaction of microwave radiation with a magnetic fluid that completely fills a waveguide and is bounded by a dielectric insertion is studied at frequencies between 20 and 40 GHz. The frequency dependence of the alternating interference maxima and minima that are associated with the reflection from the front and back walls of the dielectric insertion is found. The reason for such a dependence is the variation of the complex magnetic susceptibility of the magnetic fluid. The inverse problem, i.e., the determination of the ferromagnetic particle diameter and the volume content of the solid phase in the magnetic fluid, is solved based on the frequency dependence of the reflection coefficient. © *2001 MAIK "Nauka/Interperiodica"*.

INTRODUCTION

The interaction of microwave radiation with a magnetic fluid has been considered in a number of papers. The subject of investigation was the dispersion of the magnetic susceptibility [1, 2] and how the magnetic induction dependence of the imaginary component of the magnetic fluid susceptibility affects the ferromagnetic resonance characteristics [3, 4]. However, in [3, 4], the magnetic induction dependence of the real component of the magnetic susceptibility was ignored. Such an approach may result in the inadequate treatment of experimental data, particularly, when the magnetic fluid parameters are determined with microwave techniques.

This paper studies the reflection of microwave radiation from a magnetic fluid layer in a waveguide in the presence of an external steady-state magnetic field. Experimental data are compared with theoretical analysis that takes into account the magnetic induction dependence of both the real and imaginary components of the fluid magnetic susceptibility. The possibility of determining the magnetic fluid parameters from the results obtained is discussed.

THEORETICAL ANALYSIS

We consider the propagation of the $TE_{10}(H_{10})$ wave in a waveguide and its reflection from semi-infinite magnetic fluid layer *3* bounded by dielectric insertion *2* (Fig. 1).

Under these conditions, the expression for the complex reflection coefficient can be written in the form [5]

$$R^* = \frac{\exp(2\gamma_d L)(\gamma_d - \gamma_0)(\gamma + \gamma_d) + (\gamma_0 + \gamma_d)(\gamma - \gamma_d)}{-\exp(2\gamma_d L)(\gamma_d + \gamma)(\gamma_0 + \gamma_d) + (\gamma_0 - \gamma_d)(\gamma - \gamma_d)}, \quad (1)$$

where

$$\gamma_1^2 = \frac{\pi^2}{a^2} - \omega^2 \varepsilon_0 \mu_0 \varepsilon \mu^*;$$

γ_0 and γ_1 are the propagation constants in the empty and filled parts of the waveguide, respectively; γ_d is the propagation constant of the wave in the dielectric; a is the size of the wide wall of the waveguide; ε_0 and μ_0 are the electric and magnetic constants, respectively; ε and $\mu^* = 1 + \chi_m' - j\chi_m''$ are the permittivity and the permeability of the medium that fills the waveguide cross section, respectively; and χ_m' and χ_m'' are the real and imaginary parts of the magnetic susceptibility, respectively [6]:

$$\chi_m' = \frac{\gamma\varphi ML(\sigma)}{\omega H_n} \frac{(1+\eta^2)^2 H_n^4 + (\eta^2 - 1)H_n^2}{(1+\eta^2)^2 H_n^4 + 2(\eta^2 - 1)H_n^2 + 1},$$

$$\chi_m'' = \frac{\gamma\varphi ML(\sigma)}{\omega H_n} \frac{\eta H_n^2 (1 + H_n^2(1+\eta^2))}{(1+\eta^2)^2 H_n^4 + 2(\eta^2 - 1)H_n^2 + 1}, \quad (2)$$

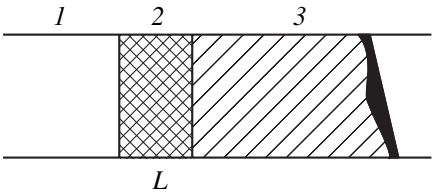

Fig. 1. Waveguide filled by the magnetic fluid: *1*, unfilled region of the waveguide; *2*, dielectric insertion of thickness L; and *3*, semi-infinite magnetic fluid layer.

1063-7842/01/4612-1514$21.00 © 2001 MAIK "Nauka/Interperiodica"

$$\eta = \xi\left(\frac{1}{L(\sigma)} - \frac{1}{\sigma}\right), \quad \sigma = \frac{\mu_0 M_d V}{kT} H.$$

In (2), $L(\sigma)$ is the Langevin function; H_n is the reduced magnetic field, $H_n = \gamma H/\omega$; σ is the combined parameter of the magnetic fluid; M_d is the saturation magnetization of the solid magnetic; $V = \pi d^3/6$ is the volume of a ferromagnetic particle; ξ is the damping constant of the electromagnetic wave in the magnetic fluid; d is the diameter of the ferromagnetic particles; and φ is the volume content of the solid phase in the magnetic liquid. For spherical ferromagnetic particles, it is assumed that the dielectric properties of the magnetic fluid are independent of the magnetic field.

Figure 2 shows the analytic dependence of the absolute value of the reflection coefficient $R = |R^*|$ on the frequency of the incident microwave radiation for different external magnetic fields. The magnetic fluid parameters used in the calculations were $M_d = 0.48$ T, $\varphi = 0.1$, and $d = 5.5$ nm. For the dielectric insertion, $\varepsilon = 2.1$ and $L = 37$ mm.

As follows from Fig. 2, the $R(f)$ dependence exhibits alternate interference maxima and minima (curve *1*) caused by the reflection from the front and back walls of the dielectric insertion.

In the presence of the magnetic field, both the frequency position and the absolute value of the reflection minima change. The frequency shift of the reflection minima is defined mainly by the magnetic induction dependence of the real part of the fluid magnetic susceptibility, whereas the absolute value of the reflection minima varies according to the magnetic induction dependence of the imaginary component of the magnetic susceptibility.

EXPERIMENT

Experiments were carried out with the setup shown in Fig. 3. The microwave radiation from panoramic VSWR meter *1* was directed to magnetic fluid *3*, which completely fills the cross section (7.2×3.4 mm) of a 70-mm-long waveguide. The fluid was bounded by a dielectric Teflon insertion. The thickness of the fluid was such that the electromagnetic wave reflected largely from the its front (adjacent to the dielectric layer) wall. The microwave radiation reflected passed through a directional coupler to detector *4*. The signal from the detector was applied to indicator *5* and then to recorder *6*. The fluid-filled part of the waveguide was placed between the poles of electromagnet *7*, fed by dc source *8*. As a magnetic fluid, we used a kerosene-based liquid with magnetite particles stabilized by olein acid. The parameters of the system were $M_d = 0.48$ T, $\varphi = 0.25$, and $\varepsilon = 3$.

The experimental $R(f)$ dependences are presented in Fig. 4 for the different values of the external steady-state magnetic field applied to the magnetic liquid at

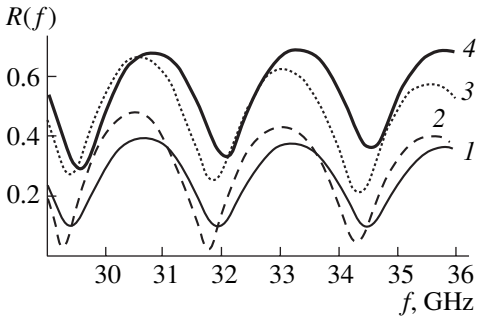

Fig. 2. Reflection coefficient of the microwave signal vs. frequency. The magnetic induction B = (*1*) 0, (*2*) 0.5, (*3*) 0.75, and (*4*) 1.0 T.

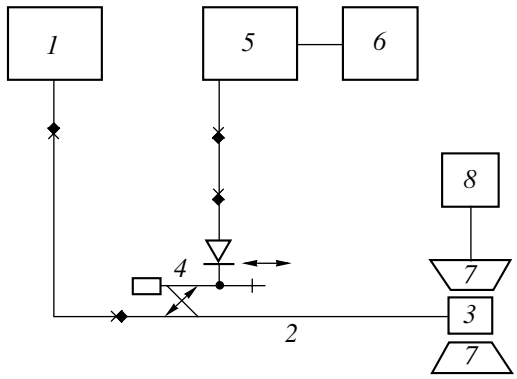

Fig. 3. Setup for taking the magnetic field dependence of the reflection coefficient: *1*, generator; *2*, waveguide; *3*, magnetic fluid; *4*, detector; *5*, indicator; *6*, recorder; *7*, electromagnet; and *8*, dc source.

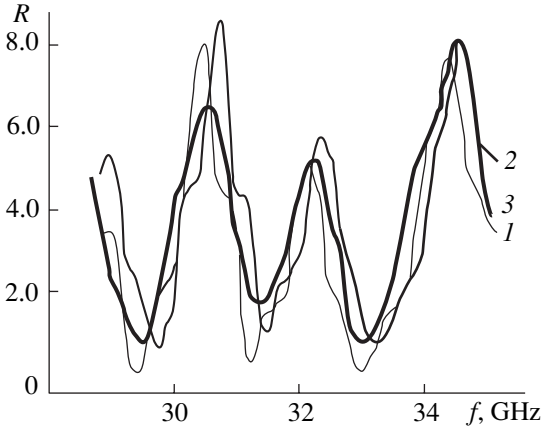

Fig. 4. Experimental frequency dependences of the reflection coefficient. The magnetic field induction B = (*1*) 0, (*2*) 0.25, and (*3*) 0.5 T.

$T = 293$ K. The alternate interference maxima and minima are observed, as follows from curve *1*.

In the presence of the magnetic field, the reflection minima change their position and absolute value, which agrees closely with the theoretical predictions. The pos-

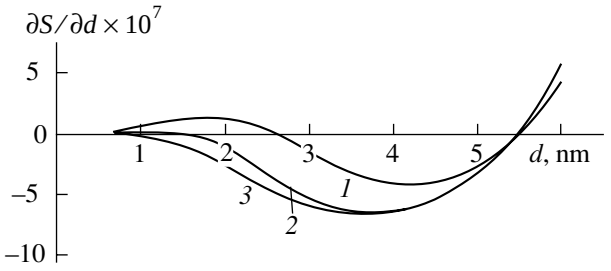

Fig. 5. Partial derivative $\partial S/\partial d$ vs. particle diameter. The number n of the model points in the dependence $R_{\text{theor}}(f_i, d, \varphi)$ is (*1*) 5, (*2*) 10, and (*3*) 15.

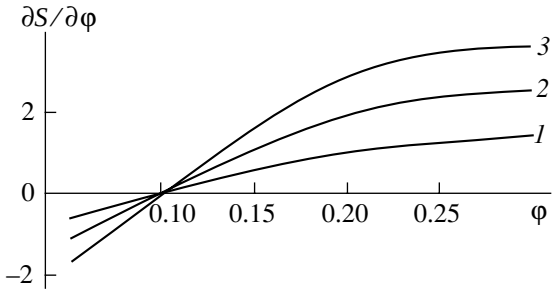

Fig. 6. Partial derivative $\partial S/\partial\varphi$ vs. volume fraction of the solid phase in the fluid. The number n of the model points in the dependence $R_{\text{theor}}(f_i, d, \varphi)$ is (*1*) 5, (*2*) 10, and (*3*) 15.

sibility of theoretically constructing the dependence of R on f, as well as of measuring this dependence, gives us the chance to solve the inverse problem, namely, to determine the magnetic fluid parameters from this dependence.

SOLUTION TO THE INVERSE PROBLEM

To solve the inverse problem, the reflection coefficient was measured at different values of the microwave frequency f. Then, the sum of the squares of the differences between the experimental values of the reflection coefficient, $R_{\text{ex}}(f)$, and the theoretical values, $R_{\text{theor}}(f)$, was constructed:

$$S = \sum_{i=1}^{n} [R_{\text{theor}}(f_i, d, \varphi) - R_{\text{exp}}(f_i)]^2. \qquad (3)$$

Here, the diameter d of the ferromagnetic particles and the volume content φ of the solid phase in the magnetic liquid are the desired parameters of the inverse problem. Our goal is to find such values of the desired parameters that minimize the sum S. At the point of minimum of the sum S, its partial derivatives vanish. Differentiating S with respect to d and φ and equating the partial derivatives $\partial S/\partial d$ and $\partial S/\partial\varphi$ to zero, we come to the system of two equations

$$\frac{\partial S}{\partial d} = 2\sum_{i=1}^{n} [R_{\text{theor}}(f, d, \varphi) - R_{\text{exp}}(f)]\frac{\partial R(f, d, \varphi)}{\partial d} = 0,$$
$$\frac{\partial S}{\partial \varphi} = 2\sum_{i=1}^{n} [R_{\text{theor}}(f, d, \varphi) - R_{\text{exp}}(f)]\frac{\partial R(f, d, \varphi)}{\partial \varphi} = 0, \qquad (4)$$

where $R_{\text{theor}}(f, d, \varphi)$ are obtained from Eqs. (1) and (2). Solving system (4), we find the desired parameters d and φ.

The numerical simulation of the solution to the inverse problem was performed for a magnetic fluid with $d = 5.5$ nm and $\varphi = 0.1$. With these values and Eqs. (1)–(3), we constructed the sum S where, instead of data points for the dependence $R_{\text{exp}}(f_i)$, a set of model points $R_{\text{theor}}(f_i, d, \varphi)$ calculated for the magnetic liquid with the specified parameters d and φ was used. Then, for different numbers n of the model points, the partial derivatives $\partial S/\partial d$ and $\partial S/\partial\varphi$ were calculated. Figures 5 and 6 present the dependences $\partial S/\partial d$ on the particle diameter d and $\partial S/\partial\varphi$ on the volume content φ of the solid phase in magnetic liquid, respectively, for different numbers n of the model points $R_{\text{theor}}(f_i, d, \varphi)$. As evident from Fig. 5, the partial derivative $\partial S/\partial d$ vanishes at two values of the parameter d; specifically, at $n = 5$, we have $d = 5.5$ nm and $d = 2.56$ nm. However, as the number of the points increases, the smaller (spurious) root of the equation $\partial S/\partial d = 0$ shifts to the left along the d axis and eventually disappears. The convergence of the parameters d and φ is observed even at $n = 2$, and the spurious root disappears at $n = 12$.

Next, we studied how a random deviation of the reflection coefficient influences the error in determining the desired parameters. To do this, a random quantity from the random-number generator of the computer was added to the theoretical value of the reflection coefficient. For a 5% deviation of the reflection coefficient R from its theoretical value, the error involved in the parameters d and φ recovered did not exceed 5%.

Using this procedure, the experimental results presented in Fig. 4 were processed. The solutions of system (4) with a set of 12 experimental points yielded the average diameter of the ferromagnetic particles $d = 47$ nm and the volume content of the solid phase in the magnetic liquid $\varphi = 0.249$.

CONCLUSION

Thus, we experimentally and theoretically studied the reflection of microwave radiation from a magnetic fluid layer in a waveguide in the presence of an external steady-state magnetic field. The position and the absolute value of the alternating maxima and minima in the $R(f)$ curve were found to vary. The shift of the reflection minima is due to the magnetic field dependence of the real component of the fluid magnetic susceptibility, whereas the absolute value of the reflection coefficient

varies because of the magnetic field dependence of the imaginary component of the fluid magnetic susceptibility.

Our measuring approach can be applied to solving the inverse problem, i.e., to determine the real and imaginary components of the magnetic susceptibility of a magnetic fluid, as well as to find magnetic fluid parameters, such as the diameter of ferromagnetic particles and the volume content of the solid phase in the fluid.

REFERENCES

1. Yu. L. Raikher and M. I. Shliomis, Zh. Éksp. Teor. Fiz. **67**, 1060 (1974) [Sov. Phys. JETP **40**, 526 (1975)].
2. P. C. Fannin, S. W. Charles, and T. Relihan, Meas. Sci. Technol. **4**, 1160 (1993).
3. Y. L. Raikher and V. I. Stepanov, Phys. Rev. B **50**, 6250 (1994).
4. Y. L. Raikher and V. I. Stepanov, Phys. Rev. B **51**, 16428 (1995).
5. D. A. Usanov, *Microwave Methods for Measuring Semiconductor Parameters* (Saratovsk. Univ., Saratov, 1985).
6. D. A. Usanov, A. V. Skripal', and S. A. Ermolaev, Magn. Gidrodin. **32**, 503 (1996).

Translated by M. Lebedev

Technical Physics, Vol. 46, No. 12, 2001, pp. 1518–1521. Translated from Zhurnal Tekhnicheskoĭ Fiziki, Vol. 71, No. 12, 2001, pp. 30–33.

Numerical Simulation of Asymmetric Non-Steady-State Turbulent Flows around Supersonic Sharp Cones

Yu. P. Golovachev and N. V. Leont'eva

Ioffe Physicotechnical Institute, Russian Academy of Sciences, Politekhnicheskaya ul. 26, St. Petersburg, 194021 Russia

e-mail: n.leont@pop.ioffe.rssi.ru

Received April 25, 2001

Abstract—Results are presented of a numerical simulation of turbulent flows around pointed circular supersonic cones at angles of attack $\alpha \geq 3\theta_c$, where θ_c is the cone half-angle. The problem is solved in the framework of a locally conical approximation of a set of Reynolds' equations written in terms of mass-averaged quantities with the use of a differential one-parametric turbulence model. The numerical solutions are obtained with the help of an implicit finite-difference unidirectional scheme, with the focus on violation of the symmetry and stationarity of the separated cross flow. © *2001 MAIK "Nauka/Interperiodica".*

INTRODUCTION

The flow of gas around sharp cones at large angles of attack is accompanied by a cross flow separation substantially influencing the aerodynamic characteristics of the cone. At moderate supersonic velocities and large Reynolds numbers the flow separated from the leeward surface of a slender body becomes asymmetric producing a considerable lateral force. Available theoretical and experimental data give evidence also of a non-steady-state character of the separated flow, which can feature oscillations in a wide frequency band from a few tens to several thousand hertz. Nonsteady processes in the gas flows around pointed slender cones at large angles of attack include low-frequency oscillations associated with the emergence of von Karman's vortex street, high-frequency oscillations caused by the instability of the free shear layer, and oscillations with intermediate frequencies caused by interaction between vortices in the cross flow.

Theoretical studies of the symmetry violation in separated flows were carried out earlier, mainly, for laminar flow regimes [1–9]. In works [1, 3, 5] the symmetry violation is explained by the convective instability, which is due to a distortion of the cone shape in the tip vicinity. This point of view is confirmed by results of numerical solution of 3-D Navier–Stokes equations and experimental data [10]. However, it does not explain asymmetry of locally conical solutions of the Navier–Stokes equations [4, 7, 9]. Therefore, the symmetry violation of the separated flow is also explained by an instability of the bifurcational kind related to nonuniqueness of the stationary solution of the Navier–Stokes equations [2]. This nonuniqueness for supersonic flows has been demonstrated in [8, 9] for the case of flows around sharp slender cones. Experimental and theoretical investigations of turbulent flows with an asymmetric cross flow separation were carried out for subsonic flow regimes [10, 11]. Results of the calculations performed with the use of an algebraic turbulence model are in qualitative agreement with available data for laminar flows. However, these results, in contrast to available data, do not demonstrate any noticeable nonsteadiness of the flow.

In this paper, the results of a numerical simulation of supersonic turbulent flows are presented. The calculations are performed in terms of a locally conical approximation with the use of a differential one-parametric turbulence model [12].

FORMULATION OF THE PROBLEM AND NUMERICAL METHOD

Formulation of the problem of supersonic flow around pointed bodies in the locally conical approximation is stated in detail in [13]. In this approximation, the calculation of a spatial gas flow around a body is reduced to solving a 2-D problem in a plane normal to the cone axis. The numerical study is carried out with the use of a set of Reynolds' equations written in terms of averaged characteristics of the turbulent flow, similarly to [14]. However, in distinction from [14], the calculations are performed without assuming flow symmetry relative to the plane containing the cone axis and the mainstream velocity vector. Along the curvilinear coordinate in the azimuthal direction, related to the contour of the cone transverse cross section, periodic boundary conditions are set. The outer boundary of the calculation region is placed in the undisturbed mainstream.

1063-7842/01/4612-1518$21.00

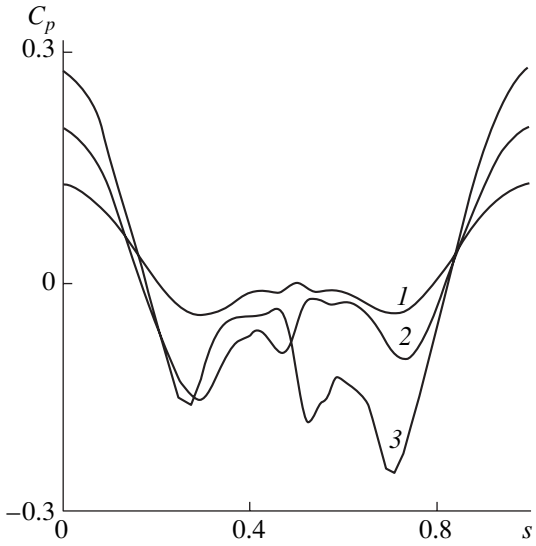

Fig. 1. Distribution of the pressure coefficient over the cone surface. $M_\infty = 1.8$; $\theta_c = 5°$; α: (*1*) 10°, (*2*) 15°, (*3*) 20°.

The numerical method of solving the problem coincides with that described in [9, 14], except for the procedure of introducing artificial dissipation in the azimuthal direction. In the present study, the coefficient of artificial dissipation σ decreases monotonously along the calculation path from the constant value σ_0 near the cone surface to zero in the undisturbed mainstream according to the formula

$$\sigma = \sigma_0 \begin{cases} 1 & \text{at} \quad \xi \le \xi_1 \\ 0.5[1 + \cos(A(\xi - \xi_1))] & \text{at} \quad \xi_1 \le \xi \le \xi_2 \\ 0 & \text{at} \quad \xi \le \xi_2, \end{cases}$$

where $0 \le \xi \le 1$ is the normalized transverse coordinate introduced in such a way that the bow shock wave is contained in the interval $\xi_1 \le \xi \le \xi_2$.

The calculation results discussed below have been obtained at $\xi_1 = 0.3$, $A = 10.0$, and $\xi_2 = \xi_1 + \pi/A$ with the use of a grid that is denser on the leeward side of the cone and near the cone surface. To construct the grid we use transformations of the azimuth-oriented curvilinear and transverse coordinates described in [13]. The distance between the body surface and the nearest inner grid node will then be of an order of the dynamic length of the turbulent boundary layer $l_* = \mu/\sqrt{\rho\tau_w}$, where μ is the gas viscosity coefficient and τ_w is the friction stress at the body surface.

The numerical algorithm, including the procedure for constructing the grid and introducing the artificial dissipation, is fully symmetrical relative to the plane containing the cone axis and the mainstream velocity vector. In the case of smooth solutions, the difference

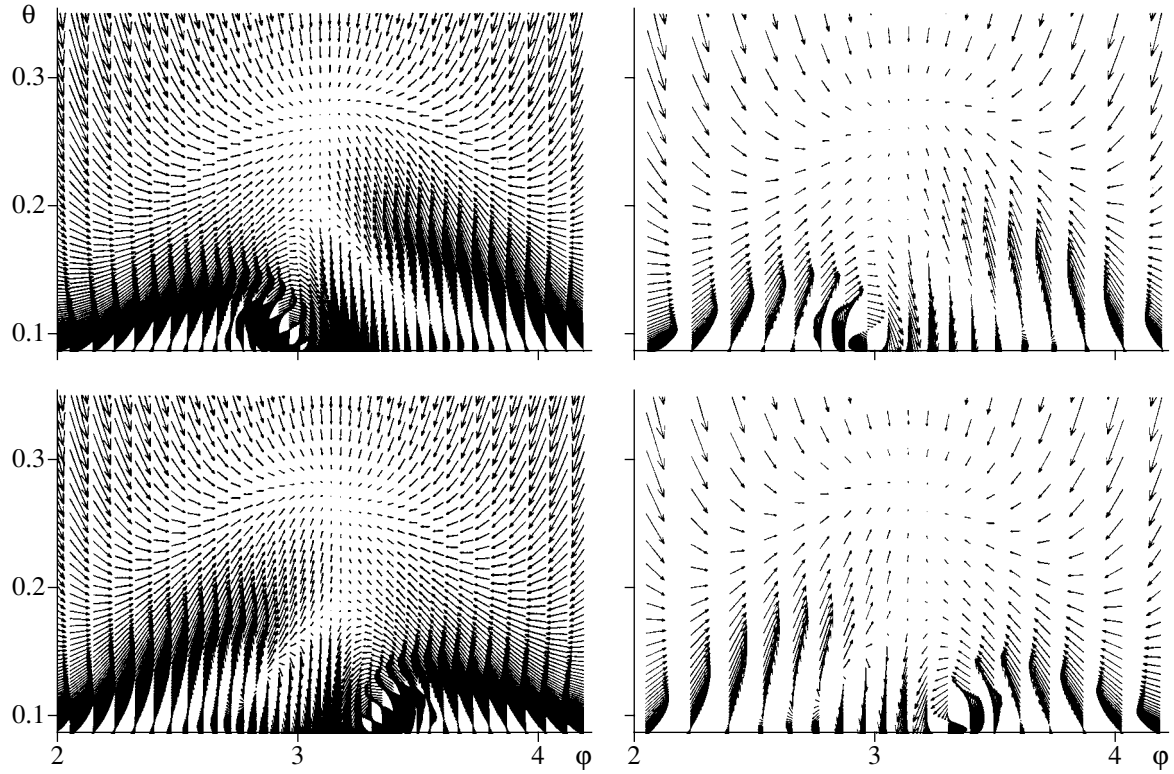

Fig. 2. Vector lines of the velocity field in the cross flow near the cone leeward side. $M_\infty = 1.8$; $\theta_c = 5°$; $\alpha = 18°$.

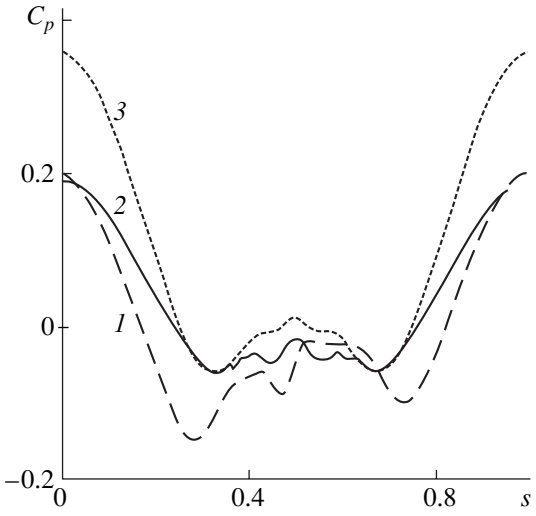

Fig. 3. Distribution of the pressure coefficient over the cone surface. $\alpha = 15°$; (*1*) $M_\infty = 1.8$; $\theta_c = 5°$; (*2*) $M_\infty = 3.5$, $\theta_c = 5°$; (*3*) $M_\infty = 1.8$, $\theta_c = 10°$.

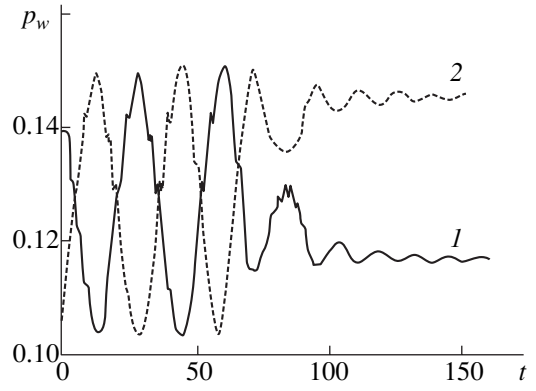

Fig. 4. Variation of the pressure at the cone leeward side. $M_\infty = 1.8$; $\theta_c = 5°$; $\alpha = 21.25°$; *s*: (*1*) 0.3; (*2*) 0.7.

scheme provides the second order of accuracy with respect to both spatial coordinates and the first order with respect to time. Most of the calculations were performed using a grid containing 60 rays with 150 nodes on each of them.

CALCULATION RESULTS

The calculation results pertain to the turbulent flow of a perfect gas with the specific heat ratio $\gamma = 1.4$ around sharp circular supersonic cones at a Prandtl number of Pr = 0.72. The coefficient of molecular viscosity of the gas is calculated using Sutherland's formula for air. The cone surface is assumed to be heat-insulated. Reynolds number calculated using parameters of the undisturbed mainstream and the distance from the cone vortex is $\mathrm{Re} = 2.5 \times 10^6$.

Figure 1 displays the pressure coefficient distributions over the cone surface with the cone half-angle $\theta_c = 5°$ for three angles of attack. Plotted on the abscissa are curvilinear coordinates in the azimuthal direction normalized to the cone cross section circumference length. It is seen that the solution is symmetrical at $\alpha = 10°$ and asymmetrical at $\alpha = 15°$ and 20°; besides, as the angle of attack increases the asymmetry changes into the opposite one. Here it should be emphasized that the asymmetry arises when no disturbance is present and an entirely symmetrical calculation algorithm is used. Similar to the laminar flow regime [9], the calculation results demonstrate the nonuniqueness of the stationary asymmetric solution which turns out to be dependent on the initial data. As an example, Fig. 2 shows velocity fields of the cross flow past the leeward side of the cone at an angle of attack of $\alpha = 18°$. The upper and lower plots correspond to two stationary solutions obtained by integration with respect to the time of solutions for $\alpha = 17°$ and 19°. The vector lines of the velocity field are plotted on a sphere with its center at the cone vertex; θ and φ are the spherical coordinates.

Figure 3 demonstrates the dependence of the character of numerical solution on the mainstream Mach number and the cone half-angle. In the figure, it is seen that the symmetry of the numerical solution is restored as M_∞ and θ_c increase.

The results presented above are in qualitative agreement with the available experimental data [10, 15] on the flow around an ogive cylinder. Comparison with the computation results for laminar flows [9] shows that in the turbulent flow the asymmetry of the separated flow arises at smaller angles of attack and persists to larger Mach numbers and cone half-angles.

Further increase of the angle of attack is accompanied by transition from the stationary asymmetric flow to a nonsteady-state periodic flow. This is illustrated in Fig. 4, where dependencies of the gas pressure on time are presented for two points on the leeward side of the cone symmetrically relative to the plane containing the cone axis and the mainstream velocity vector (the points are specified by the azimuth-directed curvilinear coordinate *s* expressed in terms of the cone cross section circumference length). The pressure and time are plotted in units of $\rho_\infty V_\infty^2$ and x/V_∞, respectively, where x is the distance from the cone vertex. Till the time instant $t = 60$ the integration is performed with the coefficient of artificial dissipation $\sigma_0 = 8$. After that, this coefficient was increased to 10. As seen from the figure, at a sufficiently weak artificial dissipation the pressure variation is featured by continuous oscillations at a frequency of $f \approx 0.03 V_\infty / x$ Hz. The calculations have shown that this frequency does not change if the time integration step is reduced or the grid mesh near the leeward cone side is made smaller. Qualitatively, the results in Fig. 4 fit experimental data [15] for a laminar subsonic flow around an ogive-cylinder. Increasing the artificial dissipation dampens the pressure oscillations

and leads to a stationary asymmetric solution. A more detailed analysis of the influence of artificial dissipation on the asymmetry of the numerical solution is given in [9].

CONCLUSION

The results of the numerical simulation of turbulent flows around supersonic pointed cones at high incidences demonstrate violation of the flow symmetry without any disturbance present although an entirely symmetrical computation algorithm is used. The results also demonstrate the nonuniqueness of the stationary asymmetric solution, restoration of the flow symmetry as the Mach number and the cone half-angle increase, and transition to a non-steady-state flow with increasing angle of attack.

ACKNOWLEDGMENTS

The work was supported by the Russian Foundation for Basic Research (project no. 99-01-00735).

REFERENCES

1. D. Degani, AIAA Pap., No. 90-0593 (1990).
2. M. J. Siclari, AIAA J. **30**, 124 (1992).
3. D. Degani, AIAA J. **29**, 560 (1991).
4. O. A. Kandil, T. C. Wang, and C. H. Liu, in *Proceedings of the AGARD Conference, 1990*, No. 0493.
5. K. J. Vanden and D. M. Belk, AIAA J. **31**, 1377 (1993).
6. Y. Levy, L. Hesselink, and D. Degani, AIAA J. **33**, 999 (1995).
7. R. Zheng and Z. Hanxin, in *Proceedings of the 7th International Symposium on Computational Fluid Dynamics* (International Academic Publ., Beiging, 1997), p. 602.
8. Yu. P. Golovachev, in *Proceedings of the 8th International Symposium on Computational Fluid Dynamics, Bremen, Germany, 1999*, CD-ROM.
9. Yu. P. Golovachev and N. V. Leont'eva, Zh. Vychisl. Mat. Mat. Fiz. **40**, 638 (2000).
10. P. J. Lamont, AIAA J. **20**, 1492 (1982).
11. D. Degani and Y. Levy, AIAA J. **30**, 2267 (1992).
12. P. R. Spalart and S. R. Allmaras, Rech. Aerosp., No. 1, 5 (1994).
13. Yu. P. Golovachev, *Numerical Simulation of Viscous Gas Flow in Shock Layer* (Nauka, Moscow, 1996).
14. Yu. P. Golovachev and N. V. Leont'eva, Izv. Akad. Nauk, Mekh. Zhidk. Gaza, No. 1, 99 (2000).
15. D. Degani and G. G. Zilliac, AIAA J. **28**, 642 (1990).

Translated by N. Mende

Technical Physics, Vol. 46, No. 12, 2001, pp. 1522–1529. Translated from Zhurnal Tekhnicheskoĭ Fiziki, Vol. 71, No. 12, 2001, pp. 34–42.

GAS DISCHARGES, PLASMA

On the Theory of Discharge in Crossed Fields

M. A. Vlasov†, A. V. Zharinov, and Yu. A. Kovalenko

State Scientific Center of the Russian Federation, Lenin All-Russia Electrical Engineering Institute, Moscow, 111250 Russia

e-mail: kjury@online.ru

Received April 11, 2000; in final form, March 29, 2001

Abstract—A model of a space charge layer that may form between cathode and anode plasmas in the presence of a transverse magnetic field is considered. Collisions are assumed not to affect the motion of electrons in the gas. It is shown that two solutions differing by cathode plasma parameters may take place. Conditions when the effect of collisions may be ignored are found. © *2001 MAIK "Nauka/Interperiodica".*

INTRODUCTION

The generation of intense charged particle fluxes is of great practical interest. Among the recent advances in magnetohydrodynamic methods for plasma acceleration, accelerators with a closed drift of electrons in an electrical discharge in crossed fields seem to be the most promising.

The theory of closed-drift accelerators that is based on the diffusion approximation has been comprehensively set forth in many articles [1, 2]. A review of the current status of the problem is beyond the scope of this paper. Its basic goal is to report novel theoretical results, which will probably help to outline ways for further improving the performance of these accelerators and find new areas for their application.

Closed-drift accelerators are based on the possibility of generating a strong electric field either in a quasi-neutral plasma or between plasma regions separated by a double electric field, the electric field generated being normal to the applied magnetic field. In both cases, an "electrodeless" $E \perp H$ layer is produced. The "electrodelessness" is a key feature that differentiates an $E \perp H$ accelerator from an electrostatic one and allows one to generate ion beams with a current density several hundreds of times higher than in the case of electrostatic acceleration. Apparently, the presence of a strong electric field in a quasi-neutral plasma has first been theoretically substantiated by Chapman and Ferraro [3]. They showed that the injection of a plasma into the region of a transverse magnetic field H_0 causes an ion-decelerating potential jump φ_a across a length $\approx \rho\alpha = \sqrt{\gamma_a^2 - 1}\, mc^2/eH_0$. This length far exceeds the size of the Langmuir space charge layer for given ion current density and kinetic energy of the ions ($\gamma_a = 1 + e\varphi_a/mc^2$). This result was obtained without considering electron diffusion. Therefore, the diffusion approximation seems to be rather inconsistent and sometimes inadequate. In this work, we assume that electrons emitted by the cathode plasma dominate in the generation of the $E \perp H$ layer and that collisions do not affect their motion.

Another important feature of these accelerators is that the ionization probability is so high that under certain conditions the ion current equals or even exceeds the consumption of the working medium. When passing through the $E \perp H$ layer with a velocity v_g, neutral atoms from the anode are ionized by electrons with a probability $P(z) = 1 - \exp(-\chi(z))$, where $\chi(z)$ satisfies the equation

$$\frac{d\chi}{dz} = -\frac{\sigma_i(\gamma_z)}{v_g} v(z) n(z). \qquad (1)$$

Here, $\sigma_i(\gamma_z)$ is the ionization cross section of the gas, $\gamma_z = 1 + e\varphi(z)/mc^2$, $\varphi(z)$ is the electric field potential, $v^2(z) = (1 - 1/\gamma_z^2)c^2$, and $n(z)$ is the electron concentration.

Using the continuity equation for electron current and averaging (1) over z, one can estimate the ionization probability $P = 1 - \exp(-I_H/I_g)$, where $I_H = J_i\bar{\rho}_i$ is the Hall current produced by the electrons [1]; J_i is the ion current density; and $\bar{\rho}_i$ is the mean Larmor radius of the accelerated ions, which depends on the mean strength of the magnetic field in the $E \perp H$ layer. $I_H = 1.5 \times 10^4$ A/m, $I_g = ev_g/\sigma_m = 915$ A/m, $P \cong 1 - \exp(-16)$ for xenon at $\varphi_a = 300$ V, $\bar{H} = 10^{-2}$ T, $\langle \sigma_i(\gamma_z) v(z) \rangle = \sigma_m v_a$, $v_a^2 = (1 - 1/\gamma_a^2)c^2$, and $J_i = 5 \times 10^3$ A/m^2. The very high ionization probability allows us to assume that the $E \perp H$ layer may contain a narrow region of strong atom ionization near the anode. Indeed, if the spread of the initial velocities of the electrons injected from the cathode plasma is neglected and it is assumed that collisions do not affect the motion of the electrons in the $E \perp H$ layer, the concentration of fast electrons goes

† Deceased.

into infinity on the magnetron cutoff surface. Therefore, all atoms coming from the anode will ionize within a thin sublayer near the magnetron cutoff surface The thickness of the sublayer depends on the electron temperature, which is much less than the potential difference across the layer.

Note that an $E \perp H$ accelerator is not strictly electrodeless. The power and the cross sizes of an ion beam are always limited, which inevitably causes the edge effect whose strength is proportional to the ratio of the layer thickness to the cross size of the beam. Because of this effect, the production of efficient low-power accelerators with a slightly diverging ion beam is difficult.

The magnetic field in the $E \perp H$ layer is the superposition of the applied field and the self-field of the Hall current. The layer may be paramagnetic or diamagnetic. Clearly, the ionization probability is the highest under complete demagnetization conditions, when the Hall current self-field coincides with the applied magnetic field. In this case, the edge effect shows up most vividly, so that the distortions of the magnetic field configuration and the beam geometry may be intolerable. Hence, one must find optimal conditions providing a desired angular divergence of the beam at a sacrifice in the ionization probability and/or an increase in the ion velocity spread at the cost of the demagnetization. Thus, two primary problems result from the aforesaid: One must (1) find the distribution of the potential, electric and magnetic fields, as well as space charge densities of the particles, in the $E \perp H$ layer and (2) study the ionization of the gas flow coming from the anode, using the solution to the former problem.

It should be emphasized that the two problems are by no means the only problems in the physics of $E \perp H$ accelerators. Points, such as the stability of the $E \perp H$ layer, the effect of the edge effects and of the magnetic field configuration on the formation of the ion beam, the electrostatic stability of the ion beam in the cathode plasma, etc., deserve further investigation.

In this work, we consider a stationary planar $E \perp H$ layer that is uniform and equipotential on any magnetic surface in the one-dimensional approximation. The electrons start from the cathode plasma surface ($z = 0$), are accelerated toward the anode plasma boundary ($z = z_d$), are reflected by the magnetic field from the magnetron cutoff surface ($z = z_c$), and return to the cathode plasma (Fig. 1). Collisions do not affect the motion of the electrons.

The cathode plasma consists of fast and slow ions generated by charge reversal. Its quasi-neutrality is provided by electrons due to gas ionization, secondary emission from the cathode cavity walls, or artificial injection.

The anodic side of the layer also contains the plasma because of the ionization of the gas penetrating through the anode. The thickness of the $E \perp H$ layer is specified by the magnetron cutoff distance z_c, which is usually

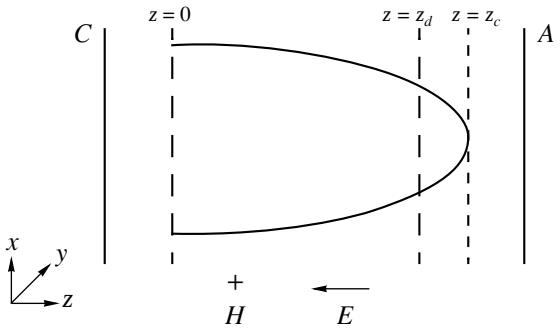

Fig. 1. *C*, cathode; *A*, anode; $z = 0$, cathode plasma boundary; $z = z_d$, anode plasma boundary; $z = z_c$, magnetron cutoff surface; and *H* and *E*, magnetic and electric field strength vectors.

several orders of magnitude larger than the Langmuir space charge layer for given ion current density and potential difference across the layer. Hence, the entire $E \perp H$ layer is quasi-neutral, but the occurrence of the double electrical layer with a potential jump of about φ_a in its interior must not be ruled out.

At $z \geq z_c$, the magnetic field $H_y(z)$ equals the applied field H_0 drops from the magnetron cutoff surface toward the cathode plasma because of the Hall current of the fast electrons accelerated in the layer.

Slow secondary electrons generated (at a positive potential) by the ionization of the gas penetrating through the anode may move only to the anode, their direction being perpendicular to the magnetic field. Therefore, because of the low transverse mobility of the electrons, a strong electric field that does not violate the quasi-neutrality may exist in the anode plasma. The detailed theoretical description of the problem is impossible within a single article. In what follows, we therefore will resort to several simplifications and perform the analysis on a qualitative basis.

MATHEMATICAL MODEL OF A DOUBLE ELECTRICAL LAYER IN A TRANSVERSE MAGNETIC FIELD

Consider a double electrical layer between plane-parallel electrodes to which the plasma layers are adjacent. The system is in a transverse magnetic field. The electric field in the plasma layers is assumed to be infinitesimal. Let us suppose that electrons coming to the layer from the cathode plasma have a current density j_0 and an initial energy $\gamma_n = 1 + e\varphi_n/mc^2$. Collisions do not affect their motion. We will look for stationary solutions; i. e., we assume that the settling time (transient period) is much greater than the magnetic diffusion time and that the electron current markedly affects the magnetic field distribution in the layer. It is also assumed that the magnetic field has an effect only on the motion of the electrons. The magnetic self-field of the current j_z (but not j_x!) is ignored. In this case, the

vector potential of the magnetic field has the single component $A_x(z)$. Ions enter the layer from the anode plasma. The ion current density J_0 and the electron current density j_0 are space-charge-limited. The electric field and the ion velocity both have the single component along the z axis. The thermal spread of the particle velocities is disregarded. After some rearrangements, the problem can mathematically be stated as [4]

$$\frac{d^2U}{d\xi^2} = \frac{\lambda(1+U+U_n)}{\sqrt{(U+U_n)^2+2(U+U_n)-W^2}} - \frac{\Lambda}{\sqrt{U_a-U}}, \quad (2a)$$

$$\frac{d^2W}{d\xi^2} = \frac{\lambda W}{\sqrt{(U+U_n)^2+2(U+U_n)-W^2}}. \quad (2b)$$

Here, $U = e\varphi/mc^2$, $U_n = e\varphi_n/mc^2$, $W = eA_x/mc^2$, $\xi = eH_y(0)z/mc^2$, c is the velocity of light, m and e are the mass and the charge of the electrons, M is the mass of the ions, $dA_x/dz = H_y(z)$, $\lambda = (8\pi e j_0)/(b^2mc^3)$, $\Lambda = (4\pi eJ_0\sqrt{M/m})/(b^2mc^3\sqrt{2})$, $b = eH_y(0)/mc^2$, $H_y(0) \neq H_0$, $A_x(0) = 0$, $\varphi_0(0) = 0$, $\varphi(d) = \varphi_a$, and φ_a is the anode plasma potential. The value of λ is other than zero in the range $0 \le z \le z_c$.

The boundary conditions have the form $U(0) = U'(0) = 0$ and $W(0) = W'(0) = 0$. At the point $\xi_c = eH_y(0)z_c/mc^2$, the condition $W'(\xi_c) = H_0/H_y(0)$ is valid. In addition, the conditions $U'(\xi_d) = 0$ and $U(\xi_d) = U_a = e\varphi_a/mc^2$ must be met at some point $\xi_d = eH_y(0)z_d/mc^2$. The point ξ_d is the anodic boundary of the space charge layer. The boundary conditions at the points ξ_c and ξ_d will be used to determine the parameters λ and Λ.

This problem has been studied for $U_n = 0$ and the magnetic flux retained in the layer [4]. It has been shown that the current ion density may exceed the current density in a bipolar diode only slightly if the magnetic field is absent. The ion current density is the highest when the size of the fast electron cloud coincides with that of the space charge layer.

The assumption that the electrons have some initial energy will allow us to find a new class of solutions to the problem. They are similar to the solution obtained in [3] but are found by directly solving the Poisson equation without neglecting electron inertia. Before presenting the results obtained, we will analyze the above set of equations and derive an important relationship that is an analog of the Child–Langmuir law for the layer in a transverse magnetic field.

Set (2) has the integral [4], which, by introducing $i = \lambda/\sqrt{2}\Lambda$ and $dW/d\xi = H_y(\xi)/H_y(0) = h$, can easily be transformed to the form

$$\left(\frac{dU}{d\xi}\right)^2 = h^2 - 1 + 4\Lambda\left[i\left(\sqrt{(U+U_n)+\frac{(U+U_n)^2-W^2}{2}} - \sqrt{\frac{U_n^2}{2}+U_n}\right) + \sqrt{U_a-U} - \sqrt{U_a}\right]. \quad (3)$$

With this integral, the problem is simplified and now one can use (3) together with (2a) or (2b). For $z_c > z_d$, it is more appropriate to use Eq. (2b) and exclude the divergence due to the space charge of the ions at the boundary with the anode plasma.

Now, three cases are possible: $z_c < z_d$ (i.e., $h(\xi) = h_c$ at $\xi_c < \xi$), $z_c = z_d$ (i.e., $h(\xi) = h_c$ and $U(\xi) = U_a$ at $\xi = \xi_c = \xi_d$), and $z_c > z_d$ (i.e., $U(\xi) = U_a$ at $\xi > \xi_d$). At the point $\xi = \xi_c$, the expression $(U(\xi) + U_n) + 0.5((U(\xi) + U_n)^2 - W^2(\xi)) = 0$ always holds. In the first case, $U(\xi_c) < U_a$ and from (3) at $\xi = \xi_c$ we have

$$(dU/d\xi)^2 = h_c^2 - 1 + 4\Lambda[\sqrt{U_a - U(\xi_c)} - \sqrt{U_a} - i\sqrt{0.5U_n^2 + U_n}].$$

In the range $\xi_c < \xi \le \xi_d$, only the ions exist. Their current is space-charge-limited; hence, integrating the Poisson equation from the anode yields $(dU/d\xi)^2 = 4\Lambda\sqrt{U_a - U(\xi_c)}$ at $\xi = \xi_c$. Joining together the derivatives, we come to

$$4\Lambda = \frac{h_c^2 - 1}{\sqrt{U_a} + i\sqrt{U_n + 0.5U_n^2}}. \quad (4)$$

In the second case, $dU/d\xi = 0$ at $\xi = \xi_c = \xi_d$. Using Eq. (3), we again arrive at Eq. (4) for Λ.

In the third case, the expression

$$h^2(\xi_d) + 4\Lambda[i(\sqrt{(U_a+U_n)+0.5((U_a+U_n)^2 - W^2(\xi_d))} - \sqrt{0.5U_n^2+U_n}) - \sqrt{U_a}] = 1 \quad (5)$$

holds for the point $\xi = \xi_d$.

Since $U = U_a$ at $\xi \ge \xi_d$, Eq. (2b) has an analytical solution

$$h_c^2 - h^2(\xi_d) = 2\lambda\sqrt{2(U_a+U_n) + (U_a+U_n)^2 - W^2(\xi_d)}.$$

Substituting $h^2(\xi_d)$ from this relationship into (5) also yields Eq. (4) for Λ.

Thus, irrespective of the sizes of the fast electron cloud and the space charge layer, the ion current density is given by Eq. (4). It is an analog of the Child–Langmuir law for the layer in a transverse magnetic field and a consequence of the momentum flux conservation law. Equation (4) implies that the electric fields at the boundaries of the cathode and anode plasmas are zero and the ions are accelerated by the "Ampére" force.

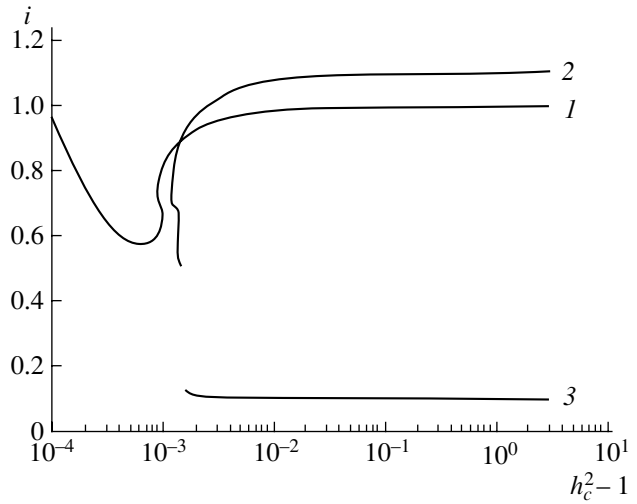

Fig. 2.

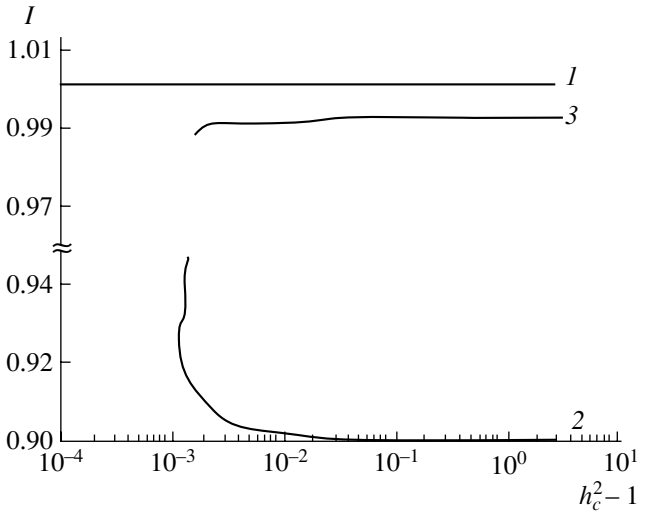

Fig. 3.

Given the "demagnetizing" parameter $H_0/H_y(0)$, applied magnetic filed H_0, and potential difference U_a, one can determine the ion current density at $U_n = 0$, using (4). In view of the definition of Λ and Eq. (4), it is easy to check that the ion current density is given by

$$J_0 = \frac{H_0^2 - H_y(0)^2}{8\pi M\sqrt{2e\varphi_a/M}(1 + i\sqrt{\eta_n + 0.5(\gamma_a - 1)\eta_n^2})} \quad (6)$$
$$= J_c I(1 - 1/h_c^2),$$

where

$$J_c = \frac{H_0^2}{8\pi M\sqrt{3e\varphi_a/M}}, \quad I = \frac{1}{1 + i\sqrt{\eta_n + 0.5(\gamma_a - 1)\eta_n^2}},$$

$$\eta_n = \frac{\varphi_n}{\varphi_a}.$$

It follows that the ion current density cannot exceed J_c even in the case of complete demagnetization (when $h_c \longrightarrow \infty$). Equation (4) allows the elimination of the parameter Λ from the equations and omit the numerical joining of the solutions at the interface, in contrast to (4).

E CONDITIONS IN THE DOUBLE ELECTRICAL LAYER UNDER A UNIFORM APPLIED MAGNETIC FIELD

A solution of set (2) along with expression (3) is conveniently sought in the functions $S(t) = (h(t)^2 - 1)/(h_c^2 - 1)$, $\eta(t) = \varphi(t)/\varphi_0$, $\vartheta(t) = A_x(t)/\varphi_0$, $d\vartheta/dt = h(t) = H_y(t)/H_y(0)$, $\eta(0) = 0$, $\vartheta(0) = 0$, and $S(0) = 0$, using $t = H_y(0)z/\varphi_0$ as an independent variable. The integral is taken from $t = 0$ until $\eta(t)$ and $S(t)$ reach unity. By varying i and h_c, we made the conditions $d\eta/dt = 0$ and $(\eta + \eta_n) + 0.5(\gamma_a - 1)((\eta + \eta_n)^2 - \vartheta^2) = 0$ be fulfilled at the points $\eta(t) = 1$ and $S(t) = 1$, respectively. To verify the solution algorithm and compare our results with those obtained previously, we first solved the problem for $\eta_n = 0$. From the definition of the parameter I, it follows that $I = 1$ and does not depend on i and that the ion current density depends only on the demagnetizing parameter $h_c^2 - 1$ in this case. Figures 2 and 3 plot, respectively, i and I vs. $h_c^2 - 1$ (curves *1*) for $\gamma_a = 1 + 4 \times 10^{-4}$. The curves coincide with those obtained in [4] and indicate the presence of an uncertainty in i in the range of solutions where the sizes of the fast electron cloud and the space charge layer are equal ($t_c \cong t_d$). For the given demagnetizing parameter and ion current density, there are three allowable values of the space charge layer thickness and the electron current density. Although the demagnetizing parameter is small in this range ($h_c^2 - 1 \cong 10^{-3}$), the assumption of the constancy of the magnetic field (see, e.g., [5]) is incorrect.

Figures 4 and 5 plot, respectively, t_c and t_d/t_c vs. $h_c^2 - 1$ (curves *1*). Even at $h_c^2 - 1 \geq 0.1$, $t_d/t_c < 0.1$; i.e., the space charge layer thickness becomes much smaller than the size of the fast electron cloud, or the cutoff length. Thus, if $J_0 \longrightarrow J_c$, the fast electron cloud is several orders of magnitude larger than the space charge layer between the anode and cathode plasmas ($z_d \ll z_c \approx \rho_a$). In this case, we can assume that the magnetic field does not affect the motion of the electrons in the layer; hence, the solution must coincide with the well-known solution for a bipolar diode if it is assumed that the electrons both to and from the anode. Then, the parameter i must be equal to unity. From Fig. 2 (curve *1*), we see that $i \longrightarrow 1$ when $h_c^2 - 1 \geq 0.1$.

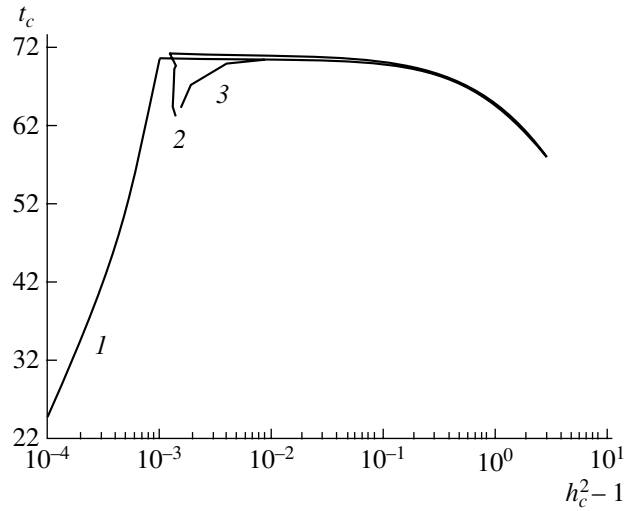

Fig. 4.

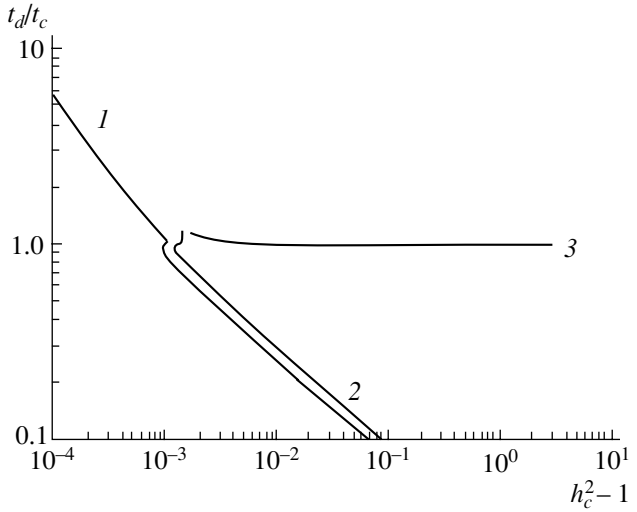

Fig. 5.

It is worth noting that when $h_c^2 - 1$ is large, the ions are accelerated in a narrow layer of a size much smaller than ρ_a. The majority of the ions form in the magnetic cutoff region at $z = z_c$, i.e., at a relatively large distance to the layer where the acceleration takes place. Therefore, when moving to the layer, some ions may reionize. The estimates of the potential drop across the anode plasma that take into account gas burning-out and the effect of the magnetic field on the motion of slow electrons of the anode plasma show that the layer–anode potential difference is on the order of the anode plasma electron temperature and is thus insignificant provided that the demagnetizing parameter is sufficiently large.

When solving the problem for $\eta_n = 0$, we failed to find solutions close to quasi-neutral. That is why we considered the problem where electrons enter the diode with some nonzero initial energy. For $T_c = 2$ eV and $\gamma_a = 1 + 4 \times 10^{-4}$, $\eta_n = 10^{-2}$. Let us evaluate the allowable range of the parameter i. Accelerated ions with a space charge density $\approx \Lambda/\sqrt{U_a}$ enter the cathode plasma from the layer. For the quasi-neutrality to be established, the electron space charge density in the cathode plasma must exceed this value. Hence,

$$i \geq \sqrt{\eta_n}\frac{\sqrt{1 + 0.5(\gamma_a - 1)\eta_n}}{1 + (\gamma_a - 1)\eta_n}. \qquad (7)$$

This problem was solved with the same algorithm, starting from relatively large values of $h_c^2 - 1$. Curves *2* in Figs. 2–5 represent, respectively, i, I, t_c, and t_d/t_c vs. $h_c^2 - 1$. At $h_c^2 - 1 \geq 0.1$, we have $i \longrightarrow 1.1$ (Fig. 2). As $h_c^2 - 1$ decreases, i sharply drops, the drop being even faster than in the case $\eta_n = 0$. At $t_c \cong t_d$, there are also three solutions for i but at somewhat higher $h_c^2 - 1$. At $h_c^2 - 1 \geq 0.1$, $I \approx 0.9$ (Fig. 3) and rapidly grows as $t_d \longrightarrow t_c$. At $t_c \cong t_d$, there also three solutions for I.

The attempt to solve the problem at $h_c^2 - 1 < 10^{-3}$ was a failure. This is associated with the fact that when $\eta_n \neq 0$, the electron momentum flux at the cathode changes. According to the momentum flux conservation law, this requires at least a slight difference in the magnetic field pressures at the anode and the cathode. The smaller η_n, the smaller the ultimate value of $h_c^2 - 1$.

A specific feature of this range of solutions is that the longitudinal electron velocity first increases with z, starting from the initial value $-v_n$, and then drops to zero, as in the case $\eta_n = 0$. In other words, the electric field strength turns out to be sufficient for the electrons to be accelerated in the longitudinal direction near the cathode. This class of solutions is hereafter referred to as the *E* layer. Figure 6 depicts typical distributions of the potential $\eta(t)$ (curve *1*); variable $S(t)$ (curve *2*), which characterizes the variation of the magnetic field; longitudinal electron velocity $v_z(t)/v_a$ (curve *3*), and electric field strength $(d\eta/dt)/(d\eta/dt)_{\max}$ (curve *4*).

H CONDITIONS IN THE DOUBLE ELECTRICAL LAYER UNDER A UNIFORM APPLIED MAGNETIC FIELD

The analysis of the problem for $\eta_n \neq 0$ showed that there is one more class of solutions that is radically different from the class considered above. If the parameter i is selected such that it exceeds the value defined by (7) only slightly, there exist solutions that admit a decrease in the longitudinal electron velocity with distance to the anode ($v_n > v_z \geq 0$; Fig. 7, curve *3*). In this case, throughout the layer, except for the vicinity of the anode, there exists a small excess negative space charge

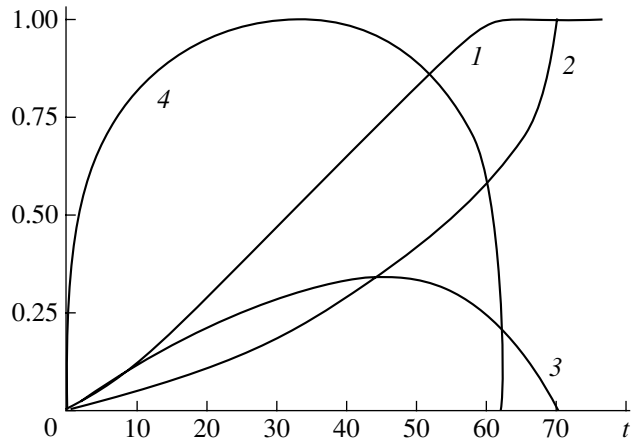

Fig. 6.

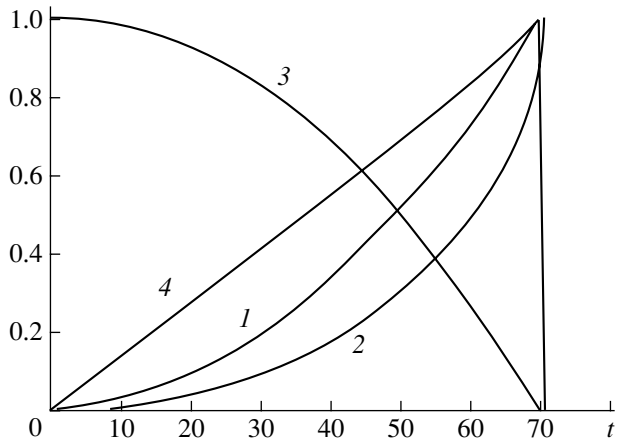

Fig. 7.

whose density is almost constant, as demonstrated by the electric field distribution (Fig. 7, curve *4*). Here, the size of the fast electron cloud approaches but never reaches that of the layer. In the narrow near-anode region, only ions that neutralize the excess negative charge and provide the fulfillment of the boundary conditions for the electric field exist. This class of solutions will hereafter be referred to as the *H* layer. This class, corresponding to the case considered in [3] and obtained directly from set (2) without neglecting electron inertia, shows that the existence of a quasi-neutral space charge layer is a possibility. Figures 2–5 (curves *3*) plot, respectively, i, I, t_c, and t_d/t_c vs. $h_c^2 - 1$ for the *H* layer at $\eta_n = 10^{-2}$. As $h_c^2 - 1$ decreases, i somewhat grows (Fig. 2), while I declines (Fig. 3). At $h_c^2 - 1 \geq 0$, the size t_c of the fast electron cloud nearly coincides with that of the layer (Fig. 5) and becomes smaller than the layer thickness when $h_c^2 - 1$ decreases. Figure 7 depicts typical variations of $\eta(t)$ (curve *1*) and $S(t)$ (curve *2*) over the layer.

Note that this model is not quite applicable to a discharge in crossed fields, since the ionization takes place within the cutoff region, while in the region $z > z_c$, the ions are absent. However, even if all the ions originate at the point z_c, the problem is hydrodynamically described with the same set of equations; as a result, the ion current density will grow insignificantly.

GAS IONIZATION IN DISCHARGES IN CROSSED FIELDS

The above solutions characterize the properties of the double layer in a uniform transversely applied magnetic field. It has been shown that the problem has only the two classes of solutions differing by cathode plasma parameters if the demagnetizing parameter is sufficiently large ($h_c^2 - 1 > 2 \times 10^{-3}$ for $\eta_n = 10^{-2}$ and $\gamma_a = 1 + 4 \times 10^{-4}$). The *E*-layer conditions are realized at a sufficiently large concentration of the cathode plasma ($i \cong 1$), while the *H*-layer conditions are observed when the cathode plasma concentration is much lower (at $\eta_n = 10^{-2}$, $i \approx 0.1$ or one order of magnitude lower). One can set one or the other conditions through the use of special cathodes, space charge neutralizers, which produce a cathode plasma with a desired concentration irrespective of the basic discharge. In this case, a controllable transition of the discharge from the *H*-mode to the *E*-mode is possible. To apply our results in designing closed-drift accelerators, it only remains to determine the gas ionization probability and to prove that the neglect of gas–electron collisions is valid.

Consider gas ionization in the *E* layer when the demagnetizing value is relatively large and $z_d \ll z_c$. In this case, $W(0) = 0$, $W(\xi_d) = 0$, and $h(\xi_d) = h(0) = 1$. Integrating Eq. (2b) yields the size of the fast electron cloud, or the cutoff length:

$$z_c = \frac{(\varphi_0 + \varphi_n)}{H_0}\sqrt{\frac{\gamma_a + 1}{\gamma_a - 1}}\int_0^1 \frac{dy}{\sqrt{1 - 2K^2\sqrt{1 - y^2}}}, \qquad (8)$$

where $2K^2 = (H_0^2 - H_y(0)^2)/H_0^2 = (1 - 1/h_c^2) = J_0/(J_c I)$.

For $2K^1 = 1$, the density of the ion current from the anode plasma $J_0 \longrightarrow J_c$ at $z_c \longrightarrow \infty$ and the magnetic field at the cathode $H_y(0) \longrightarrow 0$, as in [3]. Then, the problem does not have a stationary solution, which may cause instability.

At a sufficiently high demagnetization at $z_d \ll z_c$, Eq. (1) is easy to integrate with the use of the solution to set (2) and the definition of *K*. Eventually,

$$\chi(z_c) = \chi_0 2K^2\int_0^1 \frac{dy}{\sqrt{(1 - y^2)(1 - 2K^2\sqrt{1 - y^2})}} = \chi_0 2K^2\Psi_d(\alpha),$$

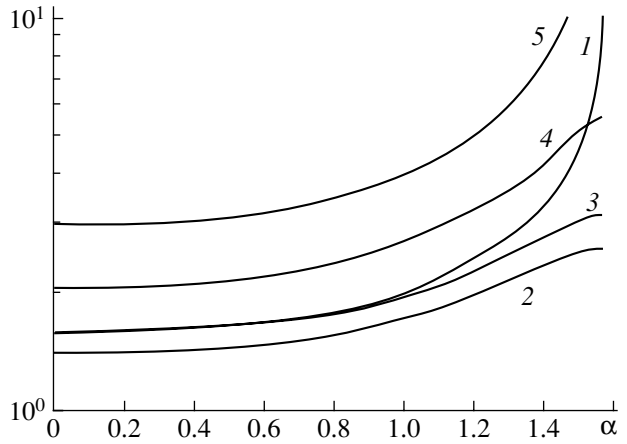

Fig. 8.

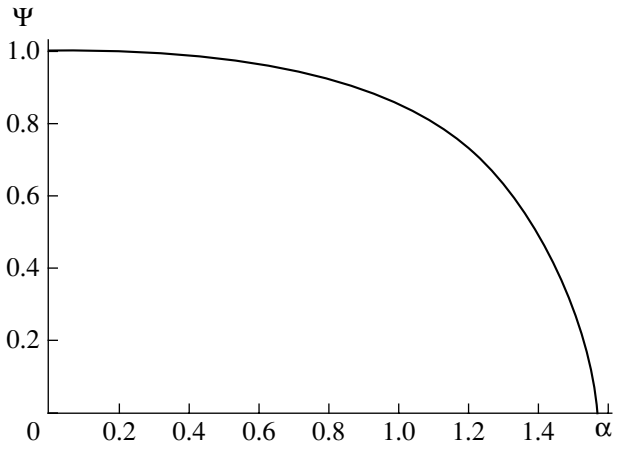

Fig. 9.

where

$$y = (A_x/\varphi_a)\sqrt{(\gamma_a - 1)/(\gamma_a + 1)}; \quad Z = \chi/\chi_0,$$

$$\chi_0 = (\sigma_i J_c \sqrt{M/m}\rho_a)/v_g, \quad \sigma_i = 4\sigma_m Ie(1 - Ie);$$

$$Ie = \varphi_i/(\varphi_a + \varphi_n);$$

$$\Psi_d(\alpha) = \sqrt{2}\sqrt{2 - \sin^2\alpha}(F(\alpha, \pi/2) - F(\alpha, \pi/4));$$

φ_i is the gas ionization potential, $F(\alpha, \Theta)$ is the elliptic integral of the first kind, and $\sin\alpha = 2K/\sqrt{1 + 2K^2}$. The function $\Psi_d(\alpha)$ is depicted in Fig. 8 (curve *1*).

For the ionization probability to be high, the following inequality must be met:

$$\chi(z_c) = \frac{\Psi_d(\alpha)\sigma_i J_0 \sqrt{M/m}\rho_a}{v_g I} > 3. \qquad (9)$$

This condition establishes a correlation between the minimal gas pressure at the discharge anode and the applied magnetic field. At small $2K^2 = J_0(J_c I)$, $\Phi_d(\alpha)$ tends to $\pi/2$. This means that the ionization length $\lambda_i = 1/\sigma_i n_g$ must be less than half the Larmor radius of the ions in the applied magnetic field ($J_0 \cong n_g v_g$, where n_g is the gas concentration at the anode, and $I \cong 1$). As $J_0 \longrightarrow J_c$, $2K^2 \longrightarrow 1$ and $\Psi_d(\alpha)$ substantially grows. For example, if $\alpha = 1.554(89°)$, $\Psi_d(\alpha) \approx 2\pi$, i.e., increases roughly fourfold. Hence, the gas pressure can be lower than in the case of small demagnetization.

Thus, we have found the conditions when the gas flow almost entirely ionizes near the cutoff. It is easy to check that they are consistent with the assumption that electron–electron collisions do not affect the motion of the electrons. Indeed, collisions with neutrals can be neglected if the condition $2\pi\rho_a < \lambda_0$ is met (λ_0 is the free path of the electrons) in the *E* layer at $h_c^2 - 1 > 10^{-2}$. Comparing this condition with (9), we see that both conditions hold simultaneously for most substances in the gaseous state, because the Larmor radius of the ions, not of the electrons, enters into condition (9) as the free path. At $\lambda_0 = 0.1\lambda_i$, both conditions are satisfied when $\sqrt{M/m} > 120$.

Consequently, our results adequately describe discharges with closed electron drift under the *E*-layer conditions. To find the characteristics of a specific discharge under these conditions, it is necessary first to determine from Eq. (6) the related demagnetization value h_c for given magnetic field and gas flow density that satisfy (9). Then, having determined h_c, one can find all the characteristic of the layer, using the above results of calculation.

For a cylindrical *E* layer, the situation is possible when the cathode radius r_{cath} lies in the applied magnetic field and the anode radius $r < r_{\text{cath}}$. Then, the electrons move toward smaller radii and the magnetron cutoff surfaces is located at $r < r_{\text{cath}}$. The azimuth current arising in the fast electron cloud is now paramagnetic, unlike the previous case, and enhances the magnetic field in the region of electron motion. One can readily show that the size of the fast electron cloud in the limit case of planar geometry is also given by expression (8) but with $2K^2 = (H_c^2 - H_0^2)/H_c^2 < 1$ (H_c is the magnetic field at the cutoff point z_c). Hence, the fast electron cloud has a finite size during any enhancement of the magnetic field. The ionization probability is then given by

$$\chi(z_c) = \chi_0\sqrt{1 - 2K^2}2K^2$$

$$\times \int_0^1 \frac{dy}{\sqrt{(1 - y^2)(1 - 2K^2\sqrt{1 - y^2})}} = \frac{\pi}{2}\chi_0\Psi(\alpha),$$

where $\Psi(\alpha) = (4/\pi)\cos\alpha(F(\alpha, \pi/2) - F(\alpha, \pi/4))$ and $F(\alpha, \Theta)$ is the elliptic integral of the first kind.

The curve $\Psi(\alpha)$ is depicted in Fig. 9. At $\alpha \longrightarrow \pi/2$, $\Psi(\alpha) \longrightarrow 0$ and $2K^2$ and $H_c/H_0 \longrightarrow \infty$. Yet, the ionization probability may be high if χ_0 is appreciable. With regard for gas burning-out, it can be easily checked that $\chi_0 = (4v_s/v_g)((q_0/j_\rho) - 1)$, where $j_\rho = (v_g/2\sigma_m\rho_a)\sqrt{m/M}$, $v_s = \sqrt{eT_e/M}$, $q_0 = n_g v_g/2$, and n_g is the initial density of the gas. Hence, $\chi_0 \approx 200$ and $\chi(z_c) = 10^2\pi\Psi(\alpha)$ for $4v_s/v_g \approx 20$ and $(q_0/j_\rho) \approx 10$.

Thus, even for $\Psi(\alpha)$ as small as 10^{-2}, the ionization probability remains high: $P(z_c) = 1 - \exp(-\chi(z_c)) = 0.95$. The magnetic field grows by several orders of magnitude in this case. Thus, it follows the supposition that an axial magnetic field may spontaneously be excited in hollow-cathode discharges. Such discharges may be used in promising inductive storage devices.

Consider now the gas ionization probability in the *H* layer. Strictly speaking, it is found by jointly integrating Eq. (1) and set (2). Since the solutions for the *H* layer are close to the solution obtained in [3], we can take advantage of the fact that the longitudinal velocity of the electrons is close to that of the ions in this case. In view of this, integrating Eq. (1) yields

$$\chi(z_c) = \frac{\chi_0 2K^2}{(1-Ie)}\int_0^1 \sqrt{\frac{1+\frac{m}{M}}{y^2+\frac{m}{M}}}\left(1-\frac{Ie\left(1+\frac{m}{M}\right)}{y^2+\frac{m}{M}}\right) \times \frac{dy}{\sqrt{(1-y^2)(1-2K^2\sqrt{1-y^2})}} = \chi_0 2K^2\Psi_d(\alpha).$$

The curves $\Psi_d(\alpha)$ for *Ie* = (*2*) 0.1, (*3*) 0.07, (*4*) 0.025, and (*5*) 0.004 are shown in Fig. 8. For *Ie* = 0.07, the ionization probability in the *H* layer coincides with that in the *E* layer for small values of the parameter $2K^2 = J_z/(J_c I)$. At higher values of *Ie*, the ionization probability in the *E* layer is larger than in the *H* layer and vice versa. This result is obvious, since the ionization cross section drops with increasing electron energy and the ionization within the layer becomes stronger than in the magnetron cutoff region.

The collisions with the neutrals can be neglected if the inequality $22\pi\rho_a/\sqrt{\eta_n} < \lambda_0$ is fulfilled within the electron path length in the *H* layer (this path is proportional to $2\pi\rho_a/\sqrt{\eta_n}$. Comparing this condition with (9), one can see that these conditions cannot simultaneously be met at $\eta_n \cong 10^{-2}$. Therefore, electron–neutral collisions may play a significant role in the *H* layer.

CONCLUSION

When studying the $E \perp H$ layer, we obtained the solutions for the one- and two-dimensional double layers subjected to a uniform magnetic field. It was shown that the problem has only two classes of solutions that differ by cathode plasma parameters if the demagnetization value is relatively large. Also, it was found that the *E*-layer conditions are realized when the cathode plasma density is large and that the collisions of the electrons does not affect their motion in this case.

The *H*-layer regime arises when the cathode plasma density is much lower. In this situation, electron–neutral collisions cannot be ignored. To qualitatively elucidate the effect of the collisions, one should bear in mind that the longitudinal electron velocity in the *H* layer decreases from its initial value to zero because of the force $F_z = e(E_z - (v_x/c)H_y)$ generated by the electric and magnetic fields. In the *H* layer, this force appears to be rather small, so that the approximation $E_z = (v_x/c)H_y$ applies. Due to collisions with the neutrals, the component v_x of the electron velocity changes and the above approximate equality becomes invalid. An electron experiences the action of a large accelerating force in the *z* direction and is thrown out of the layer to the anode, moving ballistically, because the thickness of the layer is much less than the free path of the electron. Therefore, electron transfer in the *H* layer is not a diffusion process in the conventional sense. Correct analysis of the *H* layer can be performed on assumption that some fast electrons are merely lost upon collisions.

This article is the last work carried out with the participation of Dr. Sci. (Phys.–Math.), Prof. M.A. Vlasov and is dedicated to his memory.

ACKNOWLEDGMENTS

We thank V.P. Shumilin for the valuable discussions and T. Sapronova for the help in the calculations.

REFERENCES

1. A. V. Zharinov and Yu. S. Popov, Zh. Tekh. Fiz. **37**, 294 (1967) [Sov. Phys. Tech. Phys. **12**, 208 (1967)].
2. *Reviews of Plasma Physics*, Ed. by M. A. Leontovich (Atomizdat, Moscow, 1974; Consultants Bureau, New York, 1980), Vol. 8.
3. F. Chapman and V. Ferraro, J. Geophys. Res. **57** (15), 227 (1952).
4. K. D. Bergeron, Appl. Phys. Lett. **28** (6), 306 (1976).
5. T. M. Antonsen and E. Ott, Phys. Fluids **19**, 52 (1976).

Translated by V. Isaakyan

Technical Physics, Vol. 46, No. 12, 2001, pp. 1530–1536. Translated from Zhurnal Tekhnicheskoĭ Fiziki, Vol. 71, No. 12, 2001, pp. 43–49.

SOLID-STATE ELECTRONICS

Nonlinear Excitation of the Second Harmonic in a Semiconductor Superlattice Placed into a Magnetic Field

A. A. Bulgakov and O. V. Shramkova

Usikov Institute of Radio Physics and Electronics, National Academy of Sciences of Ukraine, Kharkov, 61085 Ukraine

Received January 22, 2001

Abstract—The nonlinear interaction of waves in a periodic structure placed into a magnetic field is considered. The structure is comprised of alternate semiconducting and insulating layers. The three-wave interaction technique is applied to studying the nonlinear processes. It is shown that nonlinear phenomena in media with translational symmetry and in homogeneous media differ. Conditions for the resonant interaction between the first and second harmonics are analyzed. It is found that the second harmonic is generated when the interacting first spatial harmonics both co- and counterpropagate, which is possible only in periodic structures. Resonance events improving the generation efficiency are discussed. *© 2001 MAIK "Nauka/Interperiodica".*

INTRODUCTION

The method of second harmonic generation is used for the local diagnostics of structures. In the recent decade, extensive research on the second harmonic generation in crystals [1–5], thin films [[6–9], periodic structures [10–13], etc., has been carried out. One effect observed in inhomogeneous (in particular, periodic) media is the enhanced generation efficiency at frequencies near the transmission edge. The reasons for the anomalously high efficiency of the generation of pump radiation harmonics in a photoionized plasma have been considered in [14]. Ways to improve the generation efficiency for waves of different nature in periodic media have been discussed in [15]. In this work, we study the generation of the second harmonic in a superconductor superlattice placed into a magnetic field, using the three-wave interaction method [16–20]. The basic assumption in this method is the smallness of the nonlinear terms. Its advantage is taking account of the nonlinear terms acting in different layers of the structure. We report the method for finding coupling equations, discuss the nonlinear interaction of waves in a periodic structure, analyze conditions under which the first and second harmonics interact with each other, and explain the considerable enhancement of wave interaction due to three (cyclotron, Bragg, and nonlinear) resonances.

STATEMENT OF THE PROBLEM. COUPLING EQUATIONS

Consider a periodic structure where semiconductor layers of thickness d_1 and insulating layers of thickness d_2 alternate. Let the structure be placed into a magnetic field H_0 parallel to the $0Y$ axis. The $0Z$ axis runs perpendicularly to the boundaries of the layers. We will assume that the structure is homogeneous in the $0X$ and $0Y$ directions and put $\partial/\partial y = 0$, omitting the dependence on the coordinate y in the equations. Then, the Maxwell equations are split into equations for two polarizations. In this work, the polarization with the nonzero E_x, E_z, and H_y components is studied.

The object of our investigation is the nonlinear interaction of the waves in this superlattice. Using the method suggested in [18] for a homogeneous medium, one can reduce a set of nonlinear differential equations to an algebraic set. For an inhomogeneous structure, we obtain a set of differential equations that are solved with the Green function [21]

$$\int_a^b [\tilde{f}^*(\hat{L}f) - (\tilde{\hat{L}}\tilde{f})^* f]dV = f\tilde{f}\Big|_a^b. \qquad (1)$$

Here, $\hat{L}$ is the linear differential operator involving the terms of the linearized set of equations, $\tilde{\hat{L}}$ is the transposed operator $\hat{L}$, f and $\tilde{f}$ are the eigenfunctions of these operators, V is the coordinate space where the operators $\hat{L}$ and $\tilde{\hat{L}}$ act, and a and b are the limits of integration. Asterisk means complex conjugation, and the writing $\tilde{f}^*(\hat{L}f)$ denotes the scalar product.

This formula means that the eigenfunctions of the transposed linear differential operator are orthogonal to the right-hand side of the set of linear differential equations. This analytical method has been applied to studying nonlinear wave interactions in periodic structures in [19, 22, 23].

In our statement, the nonlinear mechanisms are related to current nonlinearity in the semiconductor layers. This nonlinearity appears as nonlinear terms in the equation of carrier motion and in the continuity

equation. The interaction of electromagnetic waves is described by the Maxwell equations, the continuity equation, and the equation of carrier motion:

$$\mathrm{curl}\mathbf{H}_1 = \frac{\varepsilon_{01}}{c}\frac{\partial \mathbf{E}_1}{\partial t} + \frac{4\pi}{c}\mathbf{j}_1,$$

$$\mathrm{curl}\mathbf{E}_1 = -\frac{1}{c}\frac{\partial \mathbf{H}_1}{\partial t},$$

$$\frac{\partial \mathbf{v}_1}{\partial t} + (\mathbf{v}_1\mathrm{grad})\mathbf{v}_1 = \frac{e}{m}\mathbf{E}_1 + \frac{e}{mc}[\mathbf{v}_1\mathbf{H}_0] + \frac{e}{mc}[\mathbf{v}_1\mathbf{H}_1], \quad (2)$$

$$\frac{\partial n_1}{\partial t} + \frac{1}{e}\mathrm{div}\mathbf{j}_1 = 0,$$

$$\mathbf{j}_1 = e(n_0 + n_1)\mathbf{v}_1,$$

where the bracketed vectors mean the vector product.

Set (2) is written for the semiconductor layers (hereafter, subscripts 1 and 2 will refer to the semiconducting and insulating layers, respectively). For the insulating layers, $\mathbf{j} = 0$ and ε_{01} should be replaced by ε_2. Set (2) can schematically be written as

$$\hat{L}f = \hat{H}(f, f), \quad (3)$$

where $\hat{H}$ is the bilinear column operator that involves the nonlinear terms of set (2).

According to the method developed in [18], the solution of set (2) can be represented in the form

$$\mathbf{E} = \sum_{k_x=-\infty}^{\infty} C_k(t)(\mathbf{e}(z) + \mathbf{e}^{(ad)})\exp(-i\omega_k t + ik_x t),$$
$$H_y = \sum_{k_x=-\infty}^{\infty} C_k(t)(h_y(z) + h_y^{(ad)})\exp(-i\omega_k t + ik_x t), \quad (4)$$

where $C_k(t)$ is the slowly varying amplitude of the kth wave; the components $\mathbf{e}$ and h_y depend on z, since the structure is inhomogeneous in the $0Z$ direction; and $\mathbf{e}^{(ad)}$ and $h_y^{(ad)}$ are the additional fields reflecting the action of the nonlinear mechanisms.

By virtue of the smallness of the nonlinear terms in (2), we will assume that the nonlinearity-induced time variation of the interacting wave amplitudes is slow; that is,

$$\omega \gg \frac{d\ln C}{dt}. \quad (5)$$

The operator $\hat{L}$ follows from linearized set (2) for the semiconducting and insulating layers. For the first layer ($Nd \le z < d_1 + Nd$),

$$\hat{L}f = \begin{pmatrix} i\frac{c}{\omega}\frac{\partial^2}{\partial z^2} + i\frac{\omega}{c}\varepsilon_0 - i\varepsilon_0\frac{\omega_p^2}{c}\frac{\omega}{\omega^2-\omega_H^2} & c\frac{k_x}{\omega}\frac{\partial}{\partial z} - \varepsilon_0\frac{\omega_p^2}{c}\frac{\omega_H}{\omega^2-\omega_H^2} \\ c\frac{k_x}{\omega}\frac{\partial}{\partial z} + \varepsilon_0\frac{\omega_p^2}{c}\frac{\omega_H}{\omega^2-\omega_H^2} & -i\frac{c}{\omega}k_x^2 + i\frac{\omega}{c}\varepsilon_0 - i\varepsilon_0\frac{\omega_p^2}{c}\frac{\omega}{\omega^2-\omega_H^2} \end{pmatrix} \quad (6)$$
$$\times \begin{pmatrix} C_k(e_{x1} + e_{x1}^{(ad)}) \\ C_k(e_{z1} + e_{z1}^{(ad)}) \end{pmatrix},$$

for the second layer ($d_1 + Nd \le z < (N+1)d$),

$$\hat{L}f = \begin{pmatrix} i\frac{c}{\omega}\frac{\partial^2}{\partial z^2} + i\frac{\omega}{c}\varepsilon_0 & c\frac{k_x}{\omega}\frac{\partial}{\partial z} \\ c\frac{k_x}{\omega}\frac{\partial}{\partial z} & -i\frac{c}{\omega}k_x^2 + i\frac{\omega}{c}\varepsilon_0 \end{pmatrix} \quad (7)$$
$$\times \begin{pmatrix} C_k(e_{x2} + e_{x2}^{(ad)}) \\ C_k(e_{z2} + e_{z2}^{(ad)}) \end{pmatrix}.$$

Equations for finding the function $C_k(t)$ (coupling equation) will be found with the Green formula. Consider integration in formula (1) in greater detail. Integrating dx and dt yields the product of the delta functions $\delta(\tilde{\omega} - \omega)\delta(\tilde{k}_x - k_x)$ in terms of linear operators. Integrating dz yields the difference in the related field components at the boundaries of the structure. Since the fields satisfy the boundary conditions, the integrals of the linear terms vanish. On the left-hand side of (1), only the terms involving the additional fields $\mathbf{e}^{(ad)}$ are left:

$$L(\delta/\delta z)C_k\varphi_k^{(ad)} = \frac{dC_k}{dt}\varphi_k$$
$$+ \sum_{k_x = k_x' + k_x''} C_{k'}C_{k''}\hat{H}_1(\varphi_{k'}, \varphi_{k''})e^{-i(\omega' + \omega'' - \omega)t},$$

where $\hat{H}_1$ is the operator consisting only of the nonlinear terms of the semiconducting layer, φ_k is the column vector involving the components of the field $\mathbf{e}$, and $\varphi_k^{(ad)}$ is the column vector involving the components of the field $\mathbf{e}^{(ad)}$.

This set of equation is inhomogeneous. For the semiconducting layer, the nonlinear terms have the form

$$H_1 = \frac{4\pi}{c} e n_0 \Big((\nabla \mathbf{v}_1)\mathbf{v}_1 + \frac{i}{\omega}\frac{e}{mc}(\omega_H^2 - \omega^2)[\mathbf{v}_1 \mathbf{H}] + i\omega(\mathbf{v}_1\nabla)\mathbf{v}_1 - \left(\frac{e}{mc}\right)^2 \mathbf{v}_1(\mathbf{H}_0\mathbf{H}_1) - [(\mathbf{v}_1\nabla)\mathbf{v}_1\mathbf{H}_0] \Big), \quad (8)$$

where the parenthesized vectors mean the scalar product.

To obtain the operator $\hat{H}_1$, it is necessary to express $\mathbf{v}_1$ and $\mathbf{H}_1$ through $\mathbf{E}_1$ and symmetrize the resulting expression. From equations (2) for the polarization studied, we find

$$\mathbf{v}_1 = \frac{-i\omega\frac{e}{m}\mathbf{E}_1 + \frac{e^2}{m^2 c}[\mathbf{E}_1\mathbf{H}_0]}{\omega_H^2 - \omega^2}, \qquad \mathbf{H}_1 = -i\frac{c}{\omega}[\nabla \mathbf{E}_1]. \quad (9)$$

When integrating dz in the nonlinear terms of (1), we split the integral $\int_{-\infty}^{\infty}$ into the sum of integrals over structure layers, separating a region of width $2\delta_i$ ($\delta_i \longrightarrow 0$) at each of the boundaries:

$$\int_{-\infty}^{\infty} = \lim_{\delta_i \to 0,\ i = 0, \pm 1, \ldots} \ldots + \int_{-\delta_0}^{\delta_0} + \int_{\delta_0}^{-\delta_1 + d_1} + \int_{-\delta_1 + d_1}^{\delta_1 + d_1} + \int_{\delta_1 + d_1}^{-\delta_2 + d} + \ldots,$$

where $d = d_1 + d_2$ is the period of the structure.

Since our structure is periodic, we apply the Floquet theorem and reduce the integrals of the nonlinear terms to those over the first period. Then, the periodicity of the structure will be reflected by the sum

$$\sum_{n=-\infty}^{\infty} \exp[i(\bar{k}' + \bar{k}'' - \bar{k} + 2\pi n/d)z]; \quad n = 0, \pm 1, \ldots,$$

which leads to the conservation law for the Bloch component of the wave vector:

$$\bar{k}' + \bar{k}'' - \bar{k} + 2\pi n/d = 0. \quad (10)$$

Here, $\bar{k}$ is the so-called Bloch wave number, which is the "average" of the transverse wave numbers k_{z1} and k_{z2} of the semiconducting and insulating layers.

Let us assume that the components of the additional field obey the same boundary conditions as the linearized ones. Then, if the resonance (synchronism) conditions

$$\omega' + \omega'' - \omega = 0, \quad k_x' + k_x'' - k_x = 0, \quad \bar{k}' + \bar{k}'' - \bar{k} + \frac{2\pi n}{d} = 0 \quad (11)$$

are met, the equation for the amplitude C_k takes the form [17–19]

$$\frac{dC_k}{dt} = W_{k,k',k''} C_{k'} C_{k''}, \quad (12)$$

where $W_{k,k',k''}$ is the matrix coefficient.

The equations for the amplitudes $C_{k'}$ and $C_{k''}$ are obtained by permuting the subscripts. It should be taken into account that, along with relationships (11) and (12), the parameters k, ω, and k_x are related by the dispersion relation for an infinite periodic medium placed into a magnetic field [24]:

$$\cos kd = \cos k_{z1}d_1 \cos k_{z2}d_2 - \frac{\varepsilon_{f1}\varepsilon_2}{2k_{z1}k_{z2}}\left[\left(\frac{k_{z1}}{\varepsilon_{f1}}\right)^2 + \left(\frac{k_{z2}}{\varepsilon_2}\right)^2 - k_x^2\left(\frac{\varepsilon_{\perp 1}}{\varepsilon_{\parallel 1}\varepsilon_{f1}}\right)^2\right]\sin k_{z1}d_1 \sin k_{z2}d_2, \quad (13)$$

where $k_{z1} = \sqrt{\frac{\omega^2}{c^2}\varepsilon_{f1} - k_x^2}$ and $k_{z2} = \sqrt{\frac{\omega^2}{c^2}\varepsilon_2 - k_x^2}$ are the transverse wave numbers for the semiconducting and insulating layers, $\varepsilon_f = \varepsilon_\parallel + \varepsilon_\perp^2/\varepsilon_\parallel$ is the Voigt permittivity, and $\varepsilon_\parallel$ and $\varepsilon_\perp$ are the components of the permittivity tensor:

$$\varepsilon_\parallel = \varepsilon_{xx} = \varepsilon_{zz} = \varepsilon_0\left\{1 - \frac{\omega_p^2(\omega + i\nu)}{\omega[(\omega + i\nu)^2 - \omega_H^2]}\right\}, \qquad \varepsilon_\perp = \varepsilon_{xz} = -\varepsilon_{zx} = -i\varepsilon_0\frac{\omega_p^2\omega_H}{\omega[(\omega + i\nu)^2 - \omega_H^2]}. \quad (14)$$

Here, ω_p is the plasma frequency, ε_0 is the lattice part of the permittivity, ω_H is the cyclotron frequency, and ν is the effective collision frequency.

In [24], dispersion relation (13) was obtained by using the transmission matrix that relates the fields at the beginning and at the end of the period.

For the subsequent discussion, we need expressions for the fields. Their derivation is straightforward and

here is omitted. For the first layer ($Nd \le z < d_1 + Nd$),

$$H_{y1} = A_1(\cos k_{z1} z + A_2 \sin k_{z1} z),$$

for the second layer ($d_1 + Nd \le z < (N+1)d$),

$$H_{y2} = A_1(B_1 \cos k_{z2} z + B_2 \sin k_{z2} z).$$

The coefficients A_2, B_1, and B_2 are found from the continuity condition for the tangential field components at the interfaces and the Floquet theorem:

$$B_1 = \cos k_{z1} d_1 \cos k_{z2} d_1 + \frac{\varepsilon_2}{k_{z2}\varepsilon_{f1}} \sin k_{z2} d_1 \times \left(k_{z1} \sin k_{z1} d_1 - i k_x \frac{\varepsilon_{\perp 1}}{\varepsilon_{\| 1}} \cos k_{z1} d_1 \right)$$

$$+ A_2 \left\{ \sin k_{z1} d_1 \cos k_{z2} d_1 - \frac{\varepsilon_2}{k_{z2}\varepsilon_{f1}} \sin k_{z2} d_1 \times \left(k_{z1} \cos k_{z1} d_1 + i k_x \frac{\varepsilon_{\perp 1}}{\varepsilon_{\| 1}} \sin k_{z1} d_1 \right) \right\},$$

$$B_2 = \cos k_{z1} d_1 \sin k_{z2} d_1 + \frac{\varepsilon_2}{k_{z2}\varepsilon_{f_1}} \cos k_{z2} d_1 \times \left(i k_x \frac{\varepsilon_{\perp 1}}{\varepsilon_{\| 1}} \cos k_{z1} d_1 - k_{z1} \sin k_{z1} d_1 \right)$$

$$+ A_2 \left\{ \sin k_{z1} d_1 \sin k_{z2} d_1 + \frac{\varepsilon_2}{k_{z2}\varepsilon_{f1}} \cos k_{z2} d_1 \times \left(k_{z1} \cos k_{z1} d_1 + i k_x \frac{\varepsilon_{\perp 1}}{\varepsilon_{\| 1}} \sin k_{z1} d_1 \right) \right\},$$

$$A_2 = i \frac{\omega \varepsilon_{f1}}{c} \frac{1}{k_{z1} m_{12}} \left\{ \cos k_{z1} d_1 \cos k_{z2} d_2 - \frac{k_{z1}\varepsilon_2}{k_{z2}\varepsilon_{f1}} \sin k_{z1} d_1 \sin k_{z2} d_2 + i \frac{k_x \varepsilon_2}{k_{z2}\varepsilon_{f1}} \frac{\varepsilon_{\perp 1}}{\varepsilon_{\| 1}} \cos k_{z1} d_1 \sin k_{z2} d_2 - e^{-ikd} \right\},$$

where m_{12} is the element of the transmission matrix:

$$m_{12} = -i \frac{\omega \varepsilon_{f1}}{c} \frac{1}{k_{z1}} \sin k_{z1} d_1 \cos k_2 d_2 - i \frac{\omega}{c} \frac{\varepsilon_2}{k_{z2}} \times \cos k_{z1} d_1 \sin k_{z2} d_2 - \frac{\omega}{c} \frac{\varepsilon_{\perp 1}}{\varepsilon_{\| 1}} \frac{k_x}{k_{z1} k_{z2}} \varepsilon_2 \sin k_{z1} d_1 \sin k_{z2} d_2. \quad (15)$$

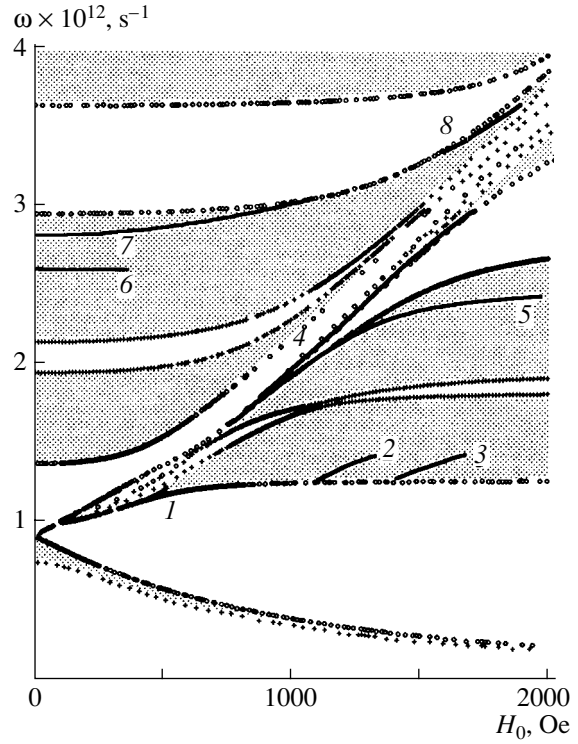

Fig. 1. Dispersion relation. $\varepsilon_0 = 17.8$, $d_1 = 0.01$ cm, $\varepsilon_2 = 2$, $d_2 = 0.015$ cm, and $k_x d = 2$.

The band structure of the spectrum with allowance for the finiteness of the velocity of light is depicted in Fig. 1 (curves *1–8*). The calculation was made for a superlattice where the first layer is InSb ($\varepsilon_{01} = 17.8$), the second layer is an insulator ($\varepsilon_2 = 2$), $d_1 = 0.01$ cm, $d_2 = 0.015$ cm, and $k_x d = 2$. The transmission bands are indicated by hatching.

The features of nonlinear interaction due to the periodicity of the structure are as follows.

(1) The matrix element and the synchronism condition are meaningful only in the transmission bands of the superlattice.

(2) The first two laws are similar to the synchronism conditions in a homogeneous medium. The third one represents the law for the Bloch components of the wave vector. The term $(2\pi n)/d$ reflects the periodicity of the structure. This relationship replaces the law for the z components of the wave vector in homogeneous media.

(3) The matrix element $W_{k,k',k''}$ is complex for a periodic (inhomogeneous) medium and imaginary for a homogeneous one.

Schematically, the matrix element can be represented as the sum of four terms of type

$$f_s \frac{\cos k_s d_1 - 1 + i \sin k_s d_1}{k_s}, \quad (16)$$

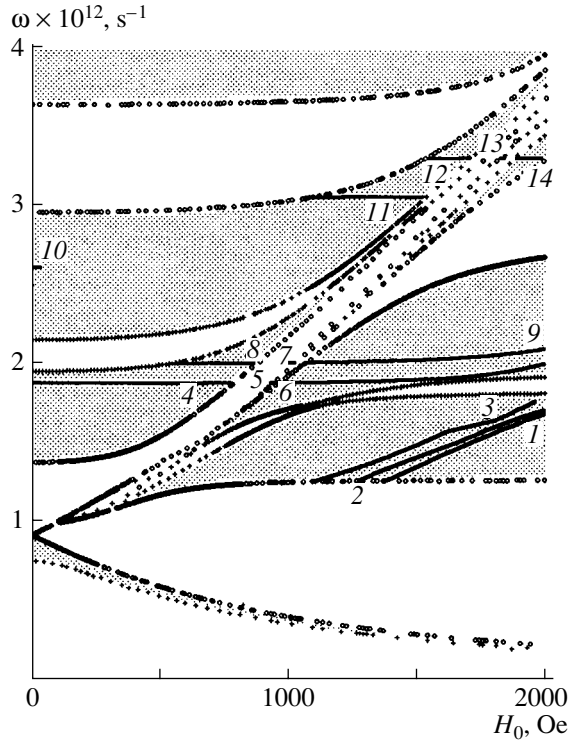

Fig. 2. Dispersion relation.

where $k_s = k_{z1} \pm k'_{z1} \pm k''_{z1}$ and f_s is a coefficient depending on the amplitudes of the interacting waves.

The coupling equations have been studied in [20]. It has been shown that the physical characteristics of the wave interaction can be obtained by investigating the dependences of the coefficients $W_{k, k', k''}$ on the parameters of the structure.

INTERACTION BETWEEN THE FIRST AND SECOND HARMONICS

Let us analyze the interaction of the first and second harmonics with frequencies ω = 2ω and ω'. In this case, the synchronism conditions are as follows:

$$\omega = 2\omega', \quad k_x = 2k'_x, \quad k = 2k'. \tag{17}$$

To determine k'_x and ω', we use the set of dispersion relations

$$\begin{aligned}\cos k'd &= \cos k'_{z1}d_1 \cos k'_{z2}d_2 - \frac{\varepsilon'_{f1}\varepsilon_2}{2k'_{z1}k'_{z2}}\left[\left(\frac{k'_{z1}}{\varepsilon'_{f1}}\right)^2\right.\\ &\left.+\left(\frac{k'_{z2}}{\varepsilon_2}\right)^2 - k_x'^2\left(\frac{\varepsilon'_{\perp 1}}{\varepsilon'_{\parallel 1}\varepsilon'_{f1}}\right)^2\right]\sin k'_{z1}d_1 \sin k'_{z2}d_2,\\ \cos kd &= \cos k_{z1}d_1 \cos k_{z2}d_2 - \frac{\varepsilon_{f1}\varepsilon_2}{2k_{z1}k_{z2}}\left[\left(\frac{k_{z1}}{\varepsilon_{f1}}\right)^2\right.\\ &\left.+\left(\frac{k_{z2}}{\varepsilon_2}\right)^2 - k_x^2\left(\frac{\varepsilon_{\perp 1}}{\varepsilon_{\parallel 1}\varepsilon_{f1}}\right)^2\right]\sin k_{z1}d_1 \sin k_{z2}d_2.\end{aligned} \tag{18}$$

Since $\varepsilon_{f1} \neq \varepsilon'_{f1}$, $k_{z1} \neq 2k'_{z1}$. Because of this, this set of equation cannot be solved analytically. The numerical solution of this set is depicted in Fig. 1 by continuous curves *1–8*. The curves lie in the transmission band. They all break at $k' = \pi/2$, since at $k' > \pi/2$, $k > \pi$; that is, the second harmonic falls into the opaque band.

Since the sign of the Bloch wave number cannot be found from the dispersion relation, the specific law for the Bloch numbers yields the new type of interaction:

$$\omega = 2\omega', \quad k_x = 2k'_x, \quad k \pm \frac{2\pi n}{d} = \bar{k}' - \bar{k}', \tag{19}$$

that is, the second harmonic is excited as a result of the interaction between two first harmonics counterpropagating along the 0*Z* axis.

Continuous curves *1–14* in Fig. 2 depict the numerical solution of the dispersion relations for the first harmonics in view of synchronism condition (19).

Now consider the frequency and field dependences of the matrix coefficient *W*. Figure 3a shows the *W*'(ω) and *W*'(*H*) dependences for curve *7* in Fig. 1; Fig. 3b, the *W*(ω) and *W*(*H*) dependences for the second harmonic of curve *7*; and Fig. 3c, *W*'(ω) and *W*'(*H*) dependences for curve *5*. The curves are normalized to the maximal values. The matrix coefficient depends on cyclotron, nonlinear, and Bragg resonances.

(i) At ω' = ω_H (ω = $2\omega_H$) or ω = ω_H (ω' = $2\omega_H/2$), we are dealing with the cyclotron resonance for the first or the second harmonic, which leads to infinite values of *W* and *W*'. The divergence of the *W*'(ω') and *W*'(*H*) dependences in Fig. 3c stems from the increase in the carrier velocity $\mathbf{v}_1$ at ω = ω_H [see (9)]. It is apparent that the divergence is associated with the disregard of dissipation processes. With the dissipation taken into account, $1/(\omega_H^2 - \omega^2)$ in (9) should be replaced by $1/(\omega_H^2 - \omega^2 - 2i\nu\omega + \nu^2)$ ([see (14)].

(ii) The value of *W* also grows if one of the values of k_s vanishes [see (16)]. The situation when k_s vanishes can be considered as the condition for nonlinear resonance. Note that the real part of the second factor in (16) vanishes and the imaginary part equals d_1 in the limit $k_s \longrightarrow 0$. Therefore, either Re*W*' (Re*W*) or Im*W*' (Im*W*) may solely have a maximum. The physical reason for the enhanced wave interaction is that the energy of the interacting waves turns out to be small at $k_x = 0$.

(iii) Bragg resonance is the resonance associated with the structure period. Its essence is that the field amplitudes take infinite values at points where

$$m'_{12} = 0 \quad \text{or} \quad m_{12} = 0. \tag{20}$$

Solutions for these relationships lie in the forbidden bands for the first or the second harmonic (since $(m'_{11} + m'_{22})/2 > 1$ or $(m_{11} + m_{22})/2 > 1$, where the synchronism

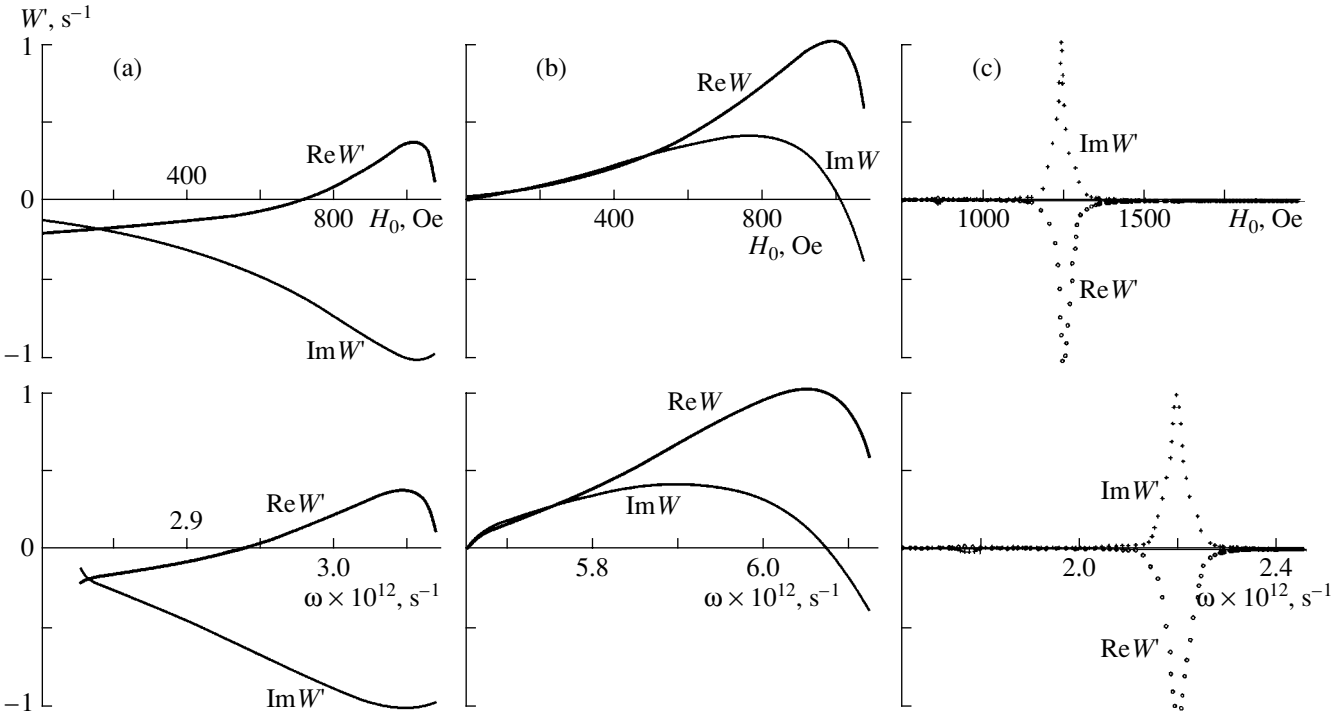

Fig. 3. Frequency and field dependences of the nonlinear coefficients: (a) for curve *7* (first harmonic) in Fig. 1, (b) for the second harmonic of curve *7* in Fig. 1, and (c) for curve *5* in Fig. 1.

conditions fail. Therefore, the condition for Bragg resonance cannot strictly be fulfilled. At the same time, the field amplitudes within the allowed bands are finite and depend on how much close the resonance points are to those meeting synchronism conditions (17) and lying at the boundary of the bands. Thus, the considerable increase in the matrix element W at the boundary of the transmission band is explained by Bragg resonance.

For the curves in Fig. 3, the maxima of $\mathrm{Im}\,W(\omega)$ and $\mathrm{Im}\,W(H)$ and the minima of $\mathrm{Im}\,W'(\omega')$ and $\mathrm{Im}\,W'(H)$ are due to the resonance for the first harmonic (Fig. 3b). Bragg resonance (Fig. 3c) leads to the increase in $\mathrm{Re}\,W(\omega)$, $\mathrm{Re}\,W(H)$, $\mathrm{Re}\,W'(\omega')$, and $\mathrm{Re}\,W'(H)$. The run of the curves at the high-frequency edges is explained by the competition between Bragg and nonlinear resonances.

CONCLUSION

We studied the nonlinear interaction of the waves in a periodic semiconductor–insulator superlattice placed into a magnetic field. The nonlinearity is due to the nonlinear free-carrier current in the semiconductor. We used the three-wave method, which applies to periodic structures. It was assumed that the nonlinearity is small, i.e., that the energy of nonlinear interaction is lower than the energy of the interacting waves. The features of the nonlinear interaction that arise from the periodicity of the structure were discussed. The generation of the second harmonic was considered for the co- and counterpropagating first harmonics. It was demonstrated that the amplitudes of the first and second harmonic change because of cyclotron, Bragg, and nonlinear resonances. The competition between these resonances gives rise to the complex frequency and field dependences of the nonlinear coefficients. Of special importance is the fact that for the semiconductor superlattice placed into the magnetic field, the efficiency of harmonic generation depends on the magnetic field: the wave interaction is markedly enhanced at the point of cyclotron resonance.

REFERENCES

1. V. N. Moiseenko, T. Z. Grechuk, A. E. Nosenko, and M. M. Antonenko, Fiz. Tverd. Tela (St. Petersburg) **38**, 3343 (1996) [Phys. Solid State **38**, 1823 (1996)].
2. L. Kador, M. Braun, K. R. Allakhverdiev, and E. Yu. Salaev, Opt. Commun. **143**, 62 (1997).
3. K. R. Allakhverdiev, F. Ismailov, L. Kador, and M. Braun, Solid State Commun. **104**, 1 (1997).
4. J. Martorell, R. Vilaseca, and R. Corbalan, Appl. Phys. Lett. **70**, 702 (1997).
5. Yoo Jeong-Geun, Choi Suk-Won, Hoshi Hajime, *et al.*, Jpn. J. Appl. Phys. **36**, L1168 (1997).
6. O. A. Aktsipetrov, K. A. Vorotilov, D. A. Klimkin, *et al.*, Fiz. Tverd. Tela (St. Petersburg) **38**, 3101 (1996) [Phys. Solid State **38**, 1696 (1996)].
7. I. L. Lyubchanskiĭ, Fiz. Tverd. Tela (St. Petersburg) **37**, 1812 (1995) [Phys. Solid State **37**, 987 (1995)].

8. H. Hoshi, T. Manaka, K. Ishikawa, and H. Takezoe, Jpn. J. Appl. Phys., Part 1 **36**, 6403 (1997).
9. A. Zayats, E. Vinogradov, O. Keller, *et al.*, Proc. SPIE **2801**, 115 (1996).
10. V. Scalora, M. J. Bloemer, A. S. Manka, *et al.*, Phys. Rev. A **56**, 3166 (1997).
11. N. A. Azarenkov, I. B. Denisenco, and K. N. Osticov, Surf. Rev. Lett. **2**, 579 (1995).
12. S. Tomaru, T. Watanabe, M. Hikita, *et al.*, Appl. Phys. Lett. **68**, 1760 (1996).
13. R. Vilaseca, J. Trull, J. Martorell, and R. Corbalan, Proc. SPIE **2801**, 108 (1996).
14. V. P. Silin, Zh. Éksp. Teor. Fiz. **117**, 926 (2000) [JETP **90**, 805 (2000)].
15. V. É. Pozhar and L. A. Chernozatonskiĭ, Fiz. Tverd. Tela (Leningrad) **27**, 682 (1985) [Sov. Phys. Solid State **27**, 421 (1985)].
16. N. Bloembergen, *Nonlinear Optics: A Lecture Note and Reprint Volume* (Benjamin, New York, 1965; Mir, Moscow, 1966).
17. J. Weiland and H. Wilhelmsson, *Coherent Nonlinear Interaction of Waves in Plasmas* (Pergamon, Oxford, 1976; Énergoizdat, Moscow, 1981).
18. A. A. Galeev and V. I. Karpman, Zh. Éksp. Teor. Fiz. **44**, 592 (1963) [Sov. Phys. JETP **17**, 403 (1963)].
19. A. A. Bulgakov, S. A. Bulgakov, and L. Vazquez, Phys. Rev. E **58**, 7887 (1998).
20. A. A. Bulgakov and O. V. Shramkova, Fiz. Tekh. Poluprovodn. (St. Petersburg) **35**, 578 (2001) [Semiconductors **35**, 557 (2001)].
21. P. Hartman, *Ordinary Differential Equations* (Wiley, New York, 1964; Mir, Moscow, 1970).
22. A. A. Bulgakov, S. I. Kharkina, and V. M. Yakovenko, Fiz. Tverd. Tela (Leningrad) **22**, 2536 (1980) [Sov. Phys. Solid State **22**, 1483 (1980)].
23. F. G. Bass, A. A. Bulgakov, and A. P. Tetervov, *High-Frequency Properties of Semiconductors with Superlattices* (Nauka, Moscow, 1989).
24. A. A. Bulgakov and O. V. Shramkova, Radiotekh. Élektron. (Moscow) **46**, 236 (2001).

Translated by V. Isaakyan

Technical Physics, Vol. 46, No. 12, 2001, pp. 1537–1544. Translated from Zhurnal Tekhnicheskoĭ Fiziki, Vol. 71, No. 12, 2001, pp. 50–57.

SOLID-STATE ELECTRONICS

Film Carriers for Super-High-Density Magnetic Storage

G. I. Frolov

Kirenskiĭ Institute of Physics, Siberian Division, Russian Academy of Sciences, Akademgorodok, Krasnoyarsk, 660036 Russia

Received February 27, 2001

Abstract—The problem of increasing the recording density in magnetic storage devices is considered. It is shown that nanograined magnetic film media are candidate materials for magnetic data carriers. For these materials to completely meet the requirements for super-high-density magnetic carriers, appropriate structure ordering must be set in the films. To this end, it is suggested to take advantage of the high adsorbability of 3*d* metal nanoparticles on high-molecular compounds. To produce the carriers based on these materials with a recording density of as high as 10^{10} bit/cm^2, nanoparticles of size ≤ 5 nm should be embedded in a polymer matrix. To do this, it is necessary to combine chemical and physical methods for nanocomposite production. © *2001 MAIK "Nauka/Interperiodica".*

INTRODUCTION

It seems quite realistic that science and technology of the 21st century will deal with nanometer- or even angström-size (quantum) objects, since many of the conventional microelectronic technologies are approaching or have already reached the fundamental (classical) limits of miniaturization. This stimulates the search of alternative lines of attack. Since the properties of a solid depend on its chemical composition, atomic structure, and dimensionality, the transition from a 3D (massive) body to an object whose dimensions in one, two, or three directions are as small as several interatomic spacings leads to a change in the physicochemical properties of the material. The specific properties of materials structured on the nanolevel (hereafter called nanostructured materials) provide the basis for the development of new-generation electron devices as microelectronics is now steadily passing from the micro- to the nanometer scale. An example is the breakthrough in the recording density of magnetic storage devices.

THE TRANSITION FROM MAGNETOOPTIC RECORDING TO LONGITUDINAL MAGNETIC RECORDING

In 1983, the US Commission on Magnetic Materials was established with the aim to judge the worldwide and national levels of research in the field of magnetism and outline directions of further development. The brief report of the Commission was issued in 1985 [1]. It was stated, in particular, that fundamental research on the physics of magnetic phenomenon is of great importance, since magnetic materials are "perfect systems for studying and verifying the basic concepts of the physics of solids." On the other hand, it was reported that the market of devices based on magnetic materials progressively expands. Among new promising applications of magnetic materials, emphasis was placed on external magnetooptic computer memories.

This direction is closely related with further advances in computer technology, whose potentialities depend on the performance of data writing, storage, and processing devices. At that time, optical technology was considered as a very promising way of increasing the RAM capacity. As alternative materials (carriers for regenerative magnetooptic storage devices), film alloys of rare-earth and transition metals were brought to the fore. The parameters of these films met the requirements of RAM designers completely [2, 3]. In these devices, data writing and reading are carried out with a laser beam. The recording density is restricted by the diffraction limit of optical radiations used and amounts to $\approx 10^8$ bit/cm^2 [4]. The predictions of RAM designers were to a great extent realized: early in the 1990s, magnetooptic memory devices filled their niche in the computer market [5].

Next item on the agenda was to devise still denser memories. In 1990, the idea of developing magnetic memory with a record density of $\approx 1.5 \times 10^8$ bit/cm^2 based on longitudinal recording was put forward [6]. In 1992, the technology of a magnetic memory with a record density of $\approx 1.5 \times 10^9$ bit/cm^2 was elaborated [7]. The new high technologies required novel materials whose properties depend on appropriately arranged structural nanoblocks. Let us consider the requirements for a magnetic carrier of recording density 1.5×10^9 bit/cm^2.

As is known, magnetically ordered materials consist of uniformly magnetized regions (domains) and transition regions (domain walls), where the magnetization varied from point to point. For a magnetic medium to be utilized for recording to the maximal extent, domain walls should be as thin as possible. The wall width W is

1063-7842/01/4612-1537$21.00

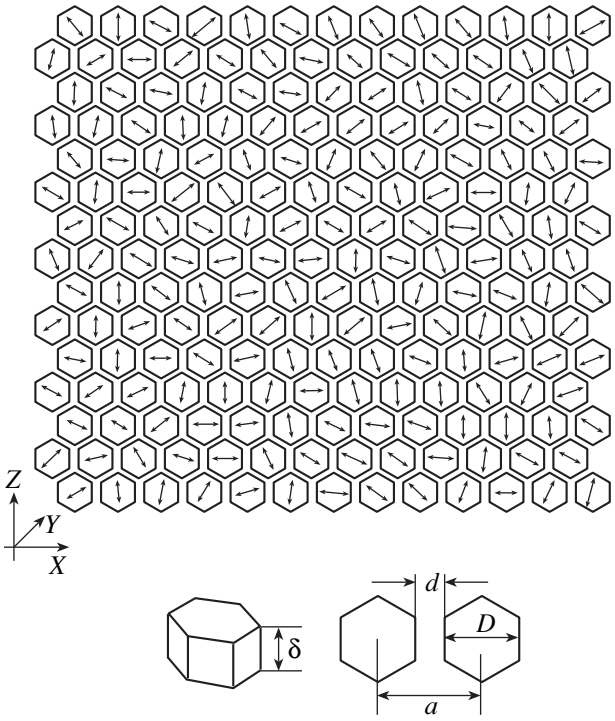

Fig. 1. Distribution of hexagonal grains in the *ZX* plane. The arrows indicate the directions of the easy axes of uniaxial anisotropy.

defined as $W = (A/K)^{1/2}$, where A is the exchange parameter and K is the anisotropy constant. The simplest way to make the wall thinner is to decrease A. This is easy to do in nanograined film materials where magnetic particles are separated from each other by a nonmagnetic spacer. Here, the particle size D is of great importance, since it specifies the signal-to-noise (S/N) ratio upon reading data. The value of D is calculated by the formula [8]

$$S/N = 10\log S/D^2,$$

where S is the area per bit. For a record density of 1.5×10^9 bit/cm^2 and S/N = 30–40 dB, D = 10–15 nm.

Now let us determine the basic magnetic parameters (coercive force H_c, remanent magnetization M_r, and the shape of hysteresis loop) of the nanograined films with the particles of the nanometer size. Since in longitudinal magnetic media the magnetization vector lies in the carrier plane, a large demagnetizing field arises. The value of H_c should therefore be selected as a trade-off: on the one hand, it must exceed this demagnetizing field; on the other hand, the capabilities of the read head must be taken into account. For the given recording density, $H_c \approx 3000$ Oe. The value of M_r is determined by the formula [9]

$$a = [M_r\delta(h + \delta/2)/\pi H_c]^{1/2},$$

where a is the width of the transition region between bits, h is the head–carrier spacing, and δ is the width of the magnetic layer of the carrier.

For a = 13 nm, h = 20 nm, δ = 10 nm, M_r = 500 G. The carrier also must have a rectangular hysteresis loop with a high ratio M_r/M_s, where M_s is the saturation magnetization. The feasibility of producing nanograined films with such magnetic parameters has been discussed by Zhu and Bertram [10]. They estimated the effect of the magnetic film microstructure on magnetization reversal and the hysteresis shape. The thin-film medium is represented as the planar arrangement of hexagonal nanograins shown in Fig. 1. Here, δ is the width of the film, which coincides with that of the grains; D is the grain size in the ZX plane; d is the intergranular spacing; and $a = d + D$ is the lattice constant. Each of the grains is a single-domain particle where the magnetization is reversed by the coherent rotation of the magnetic moment. The calculation involves the coupled dynamic equations with the Landau–Lifshitz phenomenological damping parameter. In this model, the effect of the microstructure on magnetic hysteresis shows up through exchange and dipole–dipole interactions between the particles (Fig. 2). The inclusion of both interactions leads to an increase in the ration M_r/M_s and a decrease in H_c. If, however, the dipole–dipole interaction is significant, magnetization reversal causes a vortical domain structure to appear and the quadratic shape of the hysteresis loop becomes distorted. Strong exchange interaction between particles widens the transition region between the domains. Thus, it has been shown that the nanograined films with an appropriate microstructure can have parameters necessary for high-density memory applications.

Subsequently, such devices have been created. Figure 3 shows a typical structure of the carrier used in advanced memories with longitudinal writing [11]. The carrier consists of several layers of which we are interested primarily in the Cr underlayer and the Co magnetic layer. The grain size in the magnetic layer depends on the microstructure of the underlayer (Fig. 4). The underlayer is usually made of Cr and NiAl. As the magnetic layer, Co-based alloys with Cr, Ta, Pt, etc. admixtures are employed. With such carriers, a recording density of 3–4 $\times 10^3$ bit/cm^2 [12, 13] has been attained. Memories with a recording density of up to 1.5×10^6 bit/cm^2 are predicted to appear in the former half of the current decade [14]. Several years ago, the problem of creating memory devices with a recording density as high as $\geq 10^{10}$ bit/cm^2 has been posed [15, 16].

REQUIREMENTS FOR MAGNETIC CARRIERS WITH A RECORDING DENSITY OF $\geq 10^{10}$ bit/cm^2

As a carrier for super-high-density memories, quantum magnetic disks have been suggested [15]. In these

disks, bits are single-domain particles in the form of a column or a strip that are evenly spaced in a nonmagnetic matrix. The shape and the form of each of the bits are selected such that their magnetic moments have only two oppositely directed quantum states of the same amplitude. The idea of quantum magnetic disks is by far very promising but requires much investigation into writing and reading processes and the development of the reliable technology.

It therefore seems logical to consider the potentialities of nanograined magnetic films as a medium for super-high-density ($\geq 10^{10}$ bit/cm^2) devices. Consider the requirements for the parameters of the films. Since the bit size decreases as the recording density grows, the demagnetizing field in longitudinal-writing media naturally increases; hence, H_c must be no less than 5000 Oe [16]. To keep the ratio S/N at a high level during data reading, the size of the magnetic particles must not exceed 5 nm. This raises the question as to whether there is a possibility of obtaining the desired parameters in the films considered.

It is known that the properties of the nanograined films depend on the properties of the nanoparticles and on the interactions between them. Let us see how the magnetic properties (M_s, H_c, and the Curie temperature T_C) vary as the particle size decreases. The variation of M_s in nanoparticles was discussed as early as in the 1960s [17]. By comparing the exchange energy, which is the energy of magnetic ordering, with the energy of zero-point oscillation, it has been found that the ferromagnetic properties of 3*d* metal particles of size ≤1 nm disappear at any temperature. Later, the magnetization of free 3*d* metal clusters containing from 10 to 300 atoms was measured. The < 1-nm clusters were found to be magnetized at temperatures between 100 and 200 K [18], and the magnetization may even exceed M_s of the bulk material [19]. This effect is related to the increased number of localized 3*d* electrons in the nanoparticles [20].

In the 1980s, works where the effect of the particle size on the Curie temperature was considered appeared. Although T_c of the nanoparticles is lower than in the bulk material, it was estimated at 500–600 K even for particles of size 1.0–1.5 nm [21].

As the magnetic particle size decreases, the coercive force becomes more difficult to measure. A typical H_c vs. D dependence is shown in Fig. 5 [22]. As the particle size diminishes from 40 to 20 nm, H_c grows, because the particles pass into the single-domain state. On further decreasing D, the coercive force sharply drops. This is associated with growing thermal fluctuations in the directions of the magnetic moment M of the particle. The magnetic moment M tends to align with the direction of easy magnetization, which is defined by the magnetic anisotropy of the particle. For M to deviate from this direction, it is necessary to overcome the energy barrier KV (V is the particle volume). The magnetic moment direction starts to noticeably fluctuate when the mean thermal energy k_BT (k_B is the Boltzmann constant) becomes comparable to the energy of anisotropy. At $k_BT_b = KV$ (T_b is the blocking temperature), a magnetic particle ensemble subjected to an external magnetic field and temperature behaves as a paramagnetic molecular gas with the only exception that the directions of the magnetic moment of the particles, not molecules, vary in the particle ensemble. This phenomenon has been called superparamagnetism [17]. In this case, the temperature dependence of the coercive

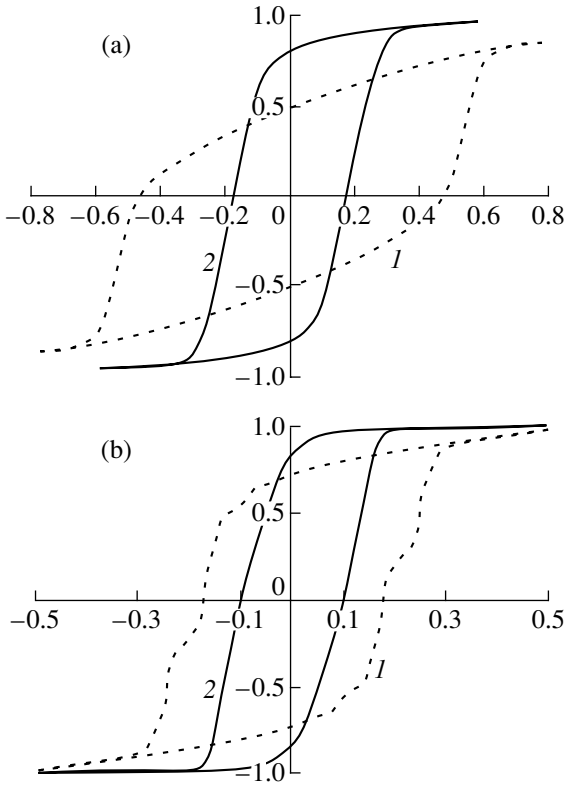

Fig. 2. Hysteresis loop for volume-disordered anisotropy axes. (a) Exchange interaction between the grains is absent, $\delta/a = 0.5$, dipole–dipole interaction $M/H_k = (1)$ 0 and (2) 0.4 (H_k is the anisotropy field); (b) $M/H_k = 0.4$, $\delta/a = 0.75$, exchange interaction is (1) 0 and (2) 0.15.

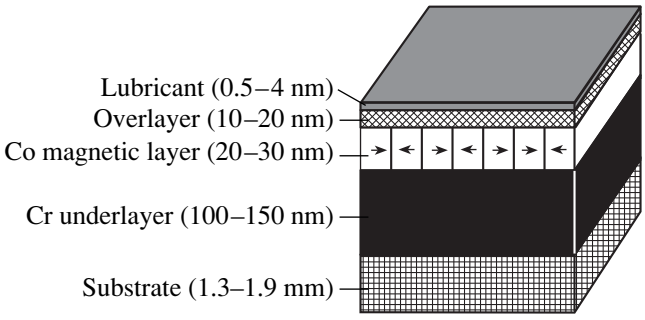

Fig. 3. Carrier for longitudinal writing.

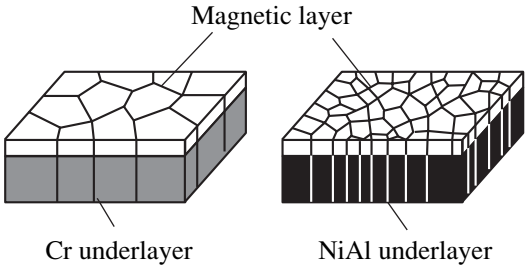

Fig. 4. Effect of the underlayer structure on the magnetic layer structure.

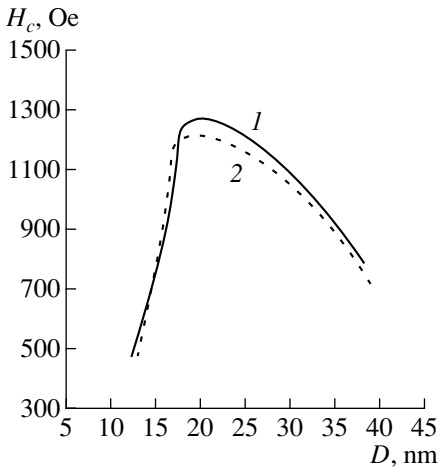

Fig. 5. Coercive force vs. Fe grain size. The particles were deposited in the (*1*) O_2 and (*2*) N_2 atmosphere.

force is given by [11]

$$H_c = H_{c0}[1 - (T/T_b)^{1/2}].$$

As follows from this expression, the coercive force can be increased by increasing the temperature of transition to the superparamagnetic state. To do this, one must raise the magnetic anisotropy constant of the particles. This can be done in three ways: (1) by using materials with a high crystallographic anisotropy (Co–Sm, Co–Pt, and like alloys), (2) by varying the shape of the particles (from spherical to elongated [23]), and (3) by inducing the anisotropy in a particle ensemble via exchange and dipole–dipole interactions. While the first two approaches have already been applied in producing novel magnetic carriers, the last one has not yet been implemented. For example, the effect of exchange and dipole–dipole interactions on the hysteresis loop has been considered only for the case of a one-layer nanostructured film [10]. At the same time, the interaction between magnetic particles has received much attention. Let us address ourselves to the results obtained in [24].

In [24], the conditions for ferromagnetic ordering in a set of single-domain particles interacting with each other are found in the mean field approximation. The set is comprised of spherical ferromagnetic particles of radius $D/2$ embedded in a solid nonmagnetic matrix. The distribution of the particles in the matrix is simulated under the assumption that their centers occupy (with a probability p) the sites of the tetragonal lattice having the periods d_1 (along the X and Y axes) and d_2 (along the Z axis, which is the tetrad axis). It is assumed that the interaction between the particles is magnetic dipole, the particles are uniaxial, their axes of easy magnetization are perpendicular to the XY plane, and the dynamics of the magnetic moment for any of the particles is described by the stochastic Landau–Lifshitz equation.

It has been established the ferromagnetic ordering in this system takes place at $d_2/d_1 < 1$. As the radius of the particles grows, the superparamagnetic–ferromagnetic phase transition temperature T_l rapidly approaches the Curie temperature of the bulk material. For example, for a set of single-domain Co particles ($p = 1$, $d_2/d_1 = 0.5$, and $d_2 = 3D/2$), the ratio T_b/T_C changes from 0.25 to 0.7 with $D/2$ varying from 2.5 to 3.5 nm.

The physical reason for the presence (at $d_2/d_1 < 1$) or absence ($d_2/d_1 \geq 1$) of ferromagnetic ordering in this system is the competition between magnetic dipole interactions between the particles. The particles surrounding some arbitrary chosen one can be subdivided into two groups according to their positions. Those of the first group produce a mean magnetic dipole field at the central particle chosen, this field being parallel to the magnetization vector, while the particles of the other group produce an antiparallel field. Ferromagnetic ordering occurs when the particles of the first group make a major contribution to the total dipole field, which takes place at $d_2/d_1 < 1$.

The result obtained indicates that a certain structure ordering in a set of interacting magnetic particle substantially raises the superparamagnetic–ferromagnetic phase transition temperature. With the beneficial effects due to the first and second approaches added, one may expect a significant rise in this temperature even for ≤5 nm particles.

From the aforesaid, it can be concluded that nanograined magnetic films with an ordered arrangement of the nanoparticles can meet the requirements for longitudinal recording carriers with a recording density above 10^{10} bit/cm^2.

FORMATION OF AN ORDERED STRUCTURE IN NANOGRAINED MAGNETIC FILMS

Ways for tackling the problem should be looked for in the new field of chemistry, so called supramolecular chemistry [25]. The subject of supramolecular chemistry is the synthesis and study of molecular ensembles (including clusters) with the self-organization properties. While conventional chemistry deals largely with reactions that break or produce valence bonds, supramolecular chemistry studies almost exclusively

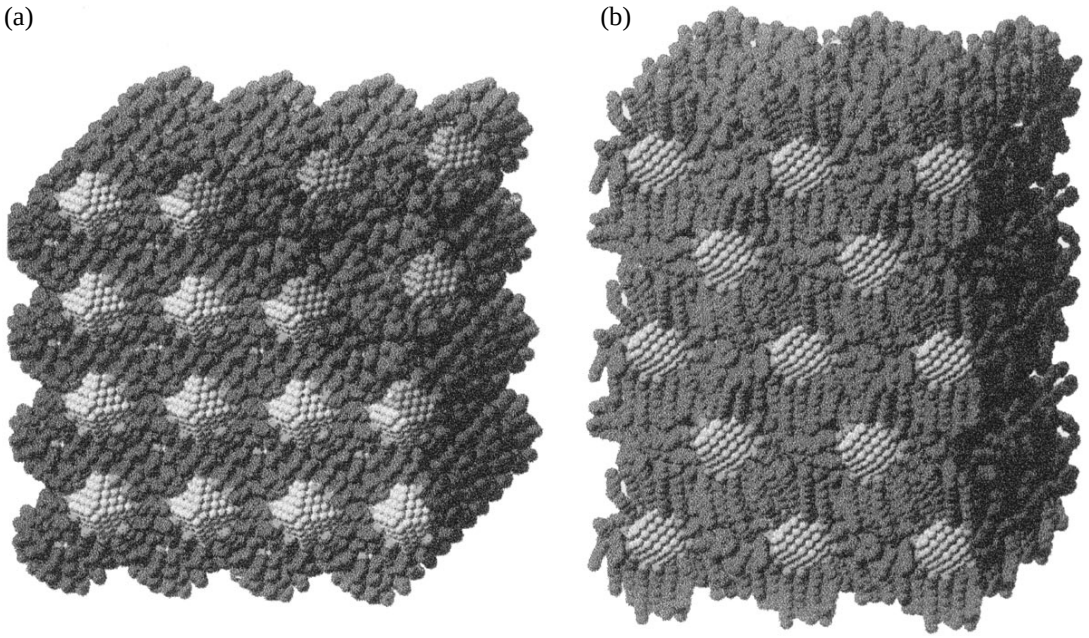

Fig. 6. Au nanoparticles are assembled into the (a) bcc and (b) *t*-fcc lattice.

nonvalent interactions, such as weak hydrogen bonds, electrostatic interaction, etc. The energy of these bonds are one to two orders of magnitude lower than the energy of valence ones; however, when combined, many such bonds may produce associates that are stable and at the same time readily change their structure.

Metal nanoparticles are highly reactive and have the developed surface. Accordingly, they are involved in a variety of spontaneous processes. To improve their stability is a basic challenge. For this purpose, various stabilizers are employed. One widely used approach is to stabilize metal nanoparticles with high-molecular compounds. The result is composites where ultradisperse particles or clusters are randomly distributed in a polymer matrix [26].

In recent years, the ensembles of passivated metal nanoparticles with the self-assembly properties have received much attention. Luedtke and Landman [27] studied the structure, dynamics, and thermal dynamics of ensembles of alkyl siloxane–passivated gold nanoparticles. The position and the concentration of the monolayers passivating the faces of the gold nanograins indicated that the monolayers are assembled like molecular packets of preferred orientation. On heating, this ordered state reversibly passes to the random intermolecular distribution. The equilibrium arrangement of adsorbed nanograins depends on the length of a molecular chain involved in passivation. If passivation is through a chain of $Au_{140}(C_4H_9S)_{62}$ molecules, the bcc superlattice forms at room temperature (Fig. 6a), which transforms into the fcc one on heating. At T = 300 K, the equilibrium superlattice of $Au_{140}(C_{12}H_{25}S)_{62}$ nanograins represents the tetragonally distorted fcc structure (*t*-fcc in Fig. 6b). The strength of the superlattices is due to the interaction between packet molecules. The superlattice parameters are $a \approx 2.9$ nm for the bcc and $a = b \approx 4.3$ nm, $c \approx 5.1$ nm for the *t*-fcc. Such ordered structures may be stable up to T = 800–900 K [28].

Subsequently, Yin and Wang [29] produced superlattices based on 3*d* metal nanograins. However, their technology concealed the danger of oxidizing 3*d* metal nanoparticles. To refine the resulting mixture, the metal particles were extracted by magnetic separation. Therefore, superlattices based on CoO nanoparticles were studied. The particles had the form of a tetrahedron (the edge length ≈4.4 nm) and form the fcc superlattice (with the parameter $a \approx 12$ nm). On heating to 600°C, the ordered structure breaks down, and a mixture of Co_2C and Co_3C nanograins instead of CoO results.

The materials described above were produced by the chemical method (the solution reduction of the metal compounds in the presence of stabilizers). This method is inappropriate for producing purely magnetic materials. Therefore, the need for physical methods (phase transitions of the first order in the absence of chemical reactions) to obtain nanograined magnetic films has emerged. Here, condensation methods have received the widest acceptance. Their essence is the assembly of the nanoparticles from individual metal atoms with the use of molecular or cluster beams. The atoms are then grouped together to produce a cluster that becomes a nucleus of the new phase once it has reached a certain size and exhibited the clear-cut physical interface.

At first glance, the cluster beam technology seems to be the most adequate solution to this problem. Mate-

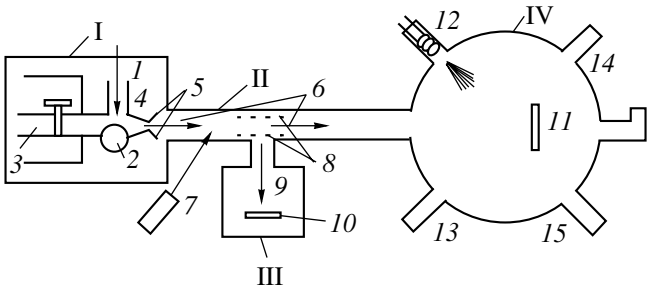

Fig. 7. Setup for evaporative deposition of the films from a neutral cluster beam. I, cluster generation chamber; II, cluster transport tube; III, chamber of cluster ion detector; IV, deposition chamber; *1*, pulsed laser; *2*, target; *3*, tube and valve for pulsed injection of helium; *4*, nozzle; *5*, skimmer; *6*, cluster flux; *7*, excimer laser; *8*, accelerating grids; *9*, cluster ion flux; *10*, detector; *11*, substrate; *12*, evaporator of matrix material; *13*, ion beam for cleaning the substrate; *14*, Auger spectrometer; and *15*, diffractometer.

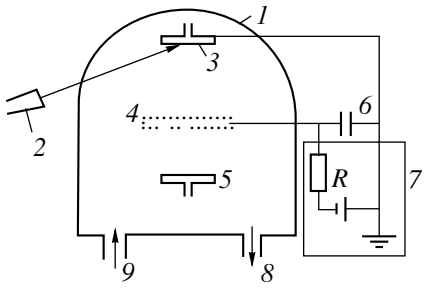

Fig. 8. Setup for evaporative deposition of the films from an atomic beam. *1*, Vacuum chamber; *2*, pulsed laser; *3*, target (cathode); *4*, circular electrode (anode); *5*, substrate; *6*, capacitor bank; *7*, bank charger; *8*, to pump; and *9*, working gas inlet.

rials thus obtained are thin films where clusters are embedded in an inert matrix. This technology has been applied by Perez *et al*. [30, 31]. They used a low-energy cluster beam to deposit nanograined films (including films of 3*d* metals). The associated setup is depicted in Fig. 7.

The generation of clusters is the most effective under nonequilibrium conditions, when the gas condenses into the bulk phase by cooling and the process ceases at the intermediate stage. Such conditions are the easiest to set when the gas or vapor freely flows out of a nozzle and expands to form a cluster beam. The target material is evaporated by a laser shot. Atoms evaporated are mixed with a buffer gas flow, and the subsequent expansion of the mixture into a vacuum through a nozzle leads to the formation of clusters. The mass of the clusters is measured with a time-of-flight mass spectrometer. Before the measurements, the clusters are irradiated by an excimer laser, ionized, accelerated, and directed to the measurement chamber. The neutral cluster flux strikes the substrate placed in the evaporation chamber.

The character of cluster–substrate interaction depends on the particle energy [32]. If the energy is low (<1 eV/atom), the cluster, when touching the surface, behaves as a liquid drop: initially, it adheres to the surface and produces a planar contact. Then, the surface (outer) atoms of the cluster spread over the surface due to diffusion, forming a thin film. When the cluster energy is high, the collision with the surface causes an appreciable shift of adjacent atoms, which results in the erosion of the surface material, followed by its evaporation. Therefore, low-energy cluster beams are used for depositing thin films. If several materials are sputtered simultaneously, a complex ensemble of solid clusters embedded in the matrix will condense. With this approach, nanograined films of various materials have been obtained in [30, 31, 33, 34].

However, the condensation of low-energy cluster beams to obtain nanograined films of 3*d* metals is a very complicated technology. Moreover, it does not have any obvious advantages over other simpler processes. The point is that the nanograin size in the resulting film depends largely on thermodynamic conditions under which the condensate forms rather than on the vapor flux type (atomic or cluster) [30, 31]. As a result, the nanograins have the same size when the films are deposited from atomic and cluster beams, all other things been equal.

To obtain nanograined magnetic films, we have suggested the method of pulsed plasma evaporation at a pressure of 10^{-6} torr [35–40]. Our setup is shown in Fig. 8. The method features a high condensation rate (~10^4 nm/s) at a pulse duration of ~10^{-4} s and at a cooling rate as high as ~10^8 K/s. This approach has turned out to be very efficient, since high vapor overcooling is the necessary condition for obtaining nanocrystalline systems [32]. In our method, a plasma is generated between the water-cooled anode and a 3*d* metal target being sputtered when a high-capacitance capacitor bank is discharged in the target vapor. An initial small amount of the vapor is produced by the laser evaporation of the target. The pulsed radiation of an LTI-207 solid-state laser partially evaporates the cathode material, producing the medium through which an electric current passes. The atoms evaporated are ionized in the discharge plasma. The resulting ions of the target atoms bombard the cathode, knocking out a new portion of the atoms. The evaporation process lasts for a time exceeding the pulse width by three or four orders of magnitude.

The novelty of our method is the proper choice of the ultimate dispersion of the crystalline structure when the number of originating nuclei is large and the radius of a critical nucleus coincides with that of coalescence. Films obtained with this method grow continuous, starting from thicknesses of 2 to 3 nm, and are comprised of nanograins of approximately the same size. This stems from the *in situ* measurements of the resistivity and the examination of the structures in tunnel

and high-resolution transmission electron microscopes. The parameters of the 3*d* metal films obtained with our method are similar to those of the films produced by the cluster beam technology: the grain sizes are equal, the local anisotropy constant is large, and the exchange parameter is relatively low.

Note, however, that the nanograined films of 3*d* metals obtained by the condensation of cluster and atomic beams have a low coercive force obviously because of the superparamagnetic effect. To rise the temperature of this transition, the films must be appropriately ordered. The ordering may be accomplished by taking advantage of the high adsorbability of the nanoparticles on high-molecular compounds. For example, one may deposit the metal nanoparticles in an appropriate atmosphere or sputter the metal and the polymer in parallel.

In this case, the new phase forms through the phase transition, but the synthesis of the final product involves chemical reactions [26]. Thin composite films may be prepared under conditions when the polymerization of related compounds and the vacuum evaporation of metals proceed concurrently. For example, the metallic target is sputtered in the glow discharge plasma of a polymer or compounds that will be used as matrices are sputtered in metal vapors. There can be versions where the vapors of a metal and of an organic solvent are codeposited onto a cooled substrate and the resulting condensate is heated to a certain temperature. In most of these cases, the material grows disordered. It becomes clear that the synthesis of structurally homogeneous nanocomposites is impossible if the matrix is not specially prepared. Therefore, a number of problems related to the vacuum condensation of the metallopolymeric phase and to the examination of its structure should be solved before the reliable technology of nanograined magnetic films with orderly arranged nanoparticles that combines physical and chemical methods is developed.

CONCLUSION

Thus, we showed that nanograined magnetic film media with nanoparticles of size ≤5 nm are competitive with magnetic quantum disks in the production of high-density magnetic memory devices.

The temperature of transition to the superparamagnetic state can be increased if certain structure ordering is established in these materials. To do this, one can take advantage of the high adsorbability of the nanoparticles on high-molecular compounds. In principle, the problem can be solved by chemical methods; however, dry (solution-free) processes for the formation of nanograined structurally ordered magnetic fields seem to be more appropriate for applications. Therefore, it is suggested to use technologies of vacuum deposition that combine physical and chemical methods.

Note, in conclusion, that ordered nanocomposites are not only of applied interest but also offer considerable scope for fundamental research.

REFERENCES

1. R. M. White, J. Appl. Phys. **57**, 2996 (1985).
2. L. V. Burkova and G. I. Frolov, Zarubezhn. Élektron., No. 9, 3 (1987).
3. G. I. Frolov, in *Magnetic Properties of Crystalline and Amorphous Media* (Nauka, Novosibirsk, 1989), pp. 218–234.
4. K. S. Aleksandrov, G. P. Berman, G. I. Frolov, and V. A. Seredkin, Proc. SPIE **1621**, 51 (1991).
5. M. D. Stoun, PC Magazine (USSR), No. 2, 11 (1991).
6. T. Yogi, C. Tsang, T. A. Nguyen, *et al.*, IEEE Trans. Magn. **26**, 2271 (1990).
7. E. S. Murdock, R. F. Simmons, and R. Davidson, IEEE Trans. Magn. **28**, 3078 (1992).
8. J. C. Mallinson, IEEE Trans. Magn. **5**, 182 (1969).
9. M. H. Kryder, W. Messner, and L. K. Garley, J. Appl. Phys. **79**, 4485 (1996).
10. J. G. Zhu and H. N. Bertram, J. Appl. Phys. **63**, 3248 (1988).
11. M. E. McHenry and D. E. Laughlin, Acta Mater. **48** (1), 223 (2000).
12. D. N. Lambeth, E. M. Velu, G. H. Bellesis, *et al.*, J. Appl. Phys. **79**, 4496 (1996).
13. H. Kisker, E. N. Abara, Y. Yamada, *et al.*, J. Appl. Phys. **81**, 3937 (1997).
14. I. Okamoto, I. Kaitsu, H. Akimoto, *et al.*, in *Digests of Intermag Conference, Korea, 1999*, AA-03.
15. S. Y. Chou, M. S. Wei, P. R. Kraus, and P. B. Fischer, J. Vac. Sci. Technol. B **12**, 3695 (1994).
16. E. S. Murdock, P. J. Ryan, J. F. Casto, *et al.*, in *Digests of Intermag Conference, Korea, 1999*, BA-02.
17. S. V. Vonsovskiĭ, *Magnetism* (Nauka, Moscow, 1971; Wiley, New York, 1974).
18. W. A. Heer, P. Milani, and A. Chatelain, Phys. Rev. Lett. **65**, 488 (1990).
19. J. P. Bucher, D. C. Douglass, and L. A. Bloomfield, Phys. Rev. Lett. **66**, 3052 (1991).
20. G. Gantefor and W. Eberhardt, Phys. Rev. Lett. **76**, 4975 (1996).
21. K. Kimura, Phys. Lett. A **158**, 85 (1991).
22. C.-M. Hsu, H.-M. Lin, and K.-R. Tsai, J. Appl. Phys. **76**, 4793 (1994).
23. H. Aharon, J. Appl. Phys. **41**, 5891 (1994).
24. S. I. Denisov, Fiz. Tverd. Tela (St. Petersburg) **41**, 1822 (1999) [Phys. Solid State **41**, 1672 (1999)].
25. A. F. Pozharskiĭ, Sorosov. Obraz. Zh., No. 9, 32 (1997).
26. A. D. Pomogaĭlo, A. S. Rozenberg, and I. E. Uflyand, *Nanoparticles of Metals in Polymers* (Khimiya, Moscow, 2000).
27. W. D. Luedtke and U. Landman, J. Phys. Chem. **100**, 13323 (1996).
28. S. A. Harfenist and Z. L. Wang, J. Phys. Chem. **103**, 4342 (1999).

29. J. S. Yin and Z. L. Wang, J. Phys. Chem. B **101**, 8979 (1997).
30. J. P. Perez, V. Dupuis, J. Tuaillon, *et al.*, J. Magn. Magn. Mater. **145**, 74 (1995).
31. A. Perez, P. Melinon, V. Dupuis, *et al.*, J. Phys. D **30**, 709 (1997).
32. B. M. Smirnov, Usp. Fiz. Nauk **167**, 1169 (1997) [Phys. Usp. **40**, 1117 (1997)].
33. J. Tuaillon, V. Dupuis, P. Melinon, *et al.*, Philos. Mag. A **76**, 493 (1997).
34. V. Dupuis, J. Tuaillon, B. Prevel, *et al.*, J. Magn. Magn. Mater. **165**, 42 (1997).
35. G. I. Frolov, V. S. Zhigalov, S. M. Zharkov, and I. R. Yarullin, Fiz. Tverd. Tela (St. Petersburg) **36**, 970 (1994) [Phys. Solid State **36**, 526 (1994)].
36. G. I. Frolov, O. A. Bayukov, V. S. Zhigalov, *et al.*, Pis'ma Zh. Éksp. Teor. Fiz. **61**, 61 (1995) [JETP Lett. **61**, 63 (1995)].
37. G. I. Frolov, V. S. Zhigalov, A. I. Pol'skiĭ, and V. G. Pozdnyakov, Fiz. Tverd. Tela (St. Petersburg) **38**, 1208 (1996) [Phys. Solid State **38**, 668 (1996)].
38. V. S. Zhigalov, G. I. Frolov, and L. I. Kveglis, Fiz. Tverd. Tela (St. Petersburg) **40**, 2074 (1998) [Phys. Solid State **40**, 1878 (1998)].
39. V. S. Zhigalov, G. I. Frolov, V. G. Myagkov, *et al.*, Zh. Tekh. Fiz. **68** (9), 136 (1998) [Tech. Phys. **43**, 1130 (1998)].
40. G. I. Frolov, V. S. Zhigalov, L. I. Kveglis, *et al.*, Fiz. Met. Metalloved. **88** (2), 85 (1999).

Translated by V. Isaakyan

Technical Physics, Vol. 46, No. 12, 2001, pp. 1545–1548. Translated from Zhurnal Tekhnicheskoĭ Fiziki, Vol. 71, No. 12, 2001, pp. 58–61.

RADIOPHYSICS

The Simulation of a Free-Electron Laser Amplifier with a Ribbon Relativistic Electron Beam

N. S. Ginzburg, R. M. Rozental', N. Yu. Peskov, A. V. Arzhannikov, and S. L. Sinitskiĭ

Institute of Applied Physics, Russian Academy of Sciences, ul. Ul'yanova 46, Nizhni Novgorod, 603600 Russia
e-mail: ginzburg@appl.sci-nnov.ru

Received March 19, 2001

Abstract—An amplifier based on a high-power free-electron planar laser operating at a wavelength of 4 mm is simulated. The system is built around the U-3 accelerator, which forms a ribbon relativistic electron beam with an energy of up to 1 MeV and a total operating current of up to 2 kA. The simulation uses various approaches, including the direct numerical simulation of the Maxwell equations and particle motion equations by means of the PIC-code KARAT. The approaches are shown to give close results. © *2001 MAIK "Nauka/Interperiodica".*

INTRODUCTION

The provision of a relatively high integral radiation power at a moderate energy density (the energy divided by the cross section) is one obvious advantage of using high-current ribbon relativistic electron beams (REBs) for the generation and amplification of microwave radiation [1–3]. The challenge here is the spatial coherency of radiations from different parts of the beam. For oscillatory circuits, this problem can be solved by applying two-dimensional distributed feedback based on planar Bragg structures with the double-period corrugation of the side walls [4, 5].

It has been shown [6] that two-dimensional Bragg arrays are also appropriate for introducing the radiation into an amplifier fed by an REB. In this case, the energy can be uniformly distributed over the cross section of the beam and the phase front of the output radiation can be made almost plane. The amplifier simulated is now being developed on the basis of the U-3 accelerator (Institute of Nuclear Physics, Siberian Division, Russian Academy of Sciences), which forms a ribbon REB with an energy of up to 1 MeV and a total operating current of up to 2 kA.

In this work, the amplification process is simulated with various approaches. In Section 1, we consider the complete unaveraged set of self-consistent equations that describe the interaction of the particles moving in the field of a planar undulator and in the guiding magnetic field with the TEM mode of a planar waveguide. In Section 2, these equations are averaged under the undulator resonance condition and the linear and nonlinear stages of the amplification process are studied based on these equations. Good agreement with the simulation with the unaveraged equations is demonstrated. In Section 3, we simulate a system whose geometry is close to the real geometry of the amplifier being developed, using the two-dimensional version of the PIC-code KARAT. All the approaches are shown to give similar results.

1. BASIC MODEL AND EQUATIONS

Let us assume that a ribbon electron beam having an initial velocity $\mathbf{v}_0 = v_0\mathbf{z}_0$ is transported in the field of a planar undulator and in a uniform guiding magnetic field $\mathbf{H}_0 = H_0\mathbf{z}_0$ through a planar waveguide made by two parallel metallic planes that are a apart along the y axis. The system is assumed to be homogeneous along the x coordinate. We also assume that the electron beam excites the TEM mode of the waveguide. The periodic undulator field and the field of the operating mode are defined by the vector potentials

$$\begin{aligned}\mathbf{A}_u &= \mathrm{Re}\{A_u\cosh(\bar{h}y)e^{i\bar{h}z}\mathbf{x}_0\},\\ \mathbf{A}_s &= \mathrm{Re}\{A_s(z)e^{i(\omega t-kz)}\mathbf{y}_0\},\end{aligned} \tag{1}$$

where $A_s(z)$ is the slowly varying amplitude of the signal wave; $\bar{h} = 2\pi/d$, d is the undulator period; $k = \omega/c$; and $\mathbf{x}_0$, $\mathbf{y}_0$, and $\mathbf{z}_0$ are the unit vectors of the Cartesian system.

Using the excitation equations and the equations for electron motion, we can obtain the self-consistent set of equations that describes electron–wave interaction in a one-way transmission-type amplifier:

$$\frac{da_s}{dZ} = iJ_0\int_0^{2\pi}\frac{P_y}{P_z}e^{-i(\tau-Z)}d\tau_0, \tag{2a}$$

$$\frac{dP_x}{dZ} = -\frac{P_y}{P_z}(\tilde{H}_u^z + \tilde{H}_0) + \tilde{H}_y^u, \tag{2b}$$

$$\frac{dP_y}{dZ} = -\frac{\gamma}{P_z}\tilde{E}_y^s - \frac{P_x}{P_z}(\tilde{H}_z^u + \tilde{H}_0) + \tilde{H}_x^s,$$
$$\frac{d\gamma}{dZ} = -\frac{P_y}{P_z}\tilde{E}_y^s, \quad \frac{dY}{dZ} = \frac{P_y}{P_z}\frac{d\tau}{dZ} = \frac{\gamma}{P_z}, \tag{2c}$$

$$P_z = \sqrt{\gamma^2 - 1 - P_x^2 - P_y^2} \tag{2d}$$

with the boundary conditions $a_s|_{Z=0} = a_0$, $P_x|_{Z=0} = P_y|_{Z=0} = 0$, $\gamma|_{Z=0} = \gamma_0$, $Y|_{Z=0} = ky_0$, and $\tau|_{Z=0} = \tau_0 \in [0, 2\pi)$. Here, $Z = kz$ and $Y = ky$ are the longitudinal and transverse coordinates, respectively; y_0 is the coordinate of beam injection into the interaction space; $\tau = \omega t$ is time; $P_{x,y,z} = p_{x,y,z}/m_0c$ are the normalized components of the electron momentum;

$$\tilde{E}_y^s = -\tilde{H}_x^s = \mathrm{Im}\{a_s e^{i(\tau - Z)}\},$$
$$\tilde{H}_y^u = -\mathrm{Im}\{\tilde{h}_k a_u \cosh(\bar{h}_k Y) e^{i\bar{h}_k Z}\},$$
$$\tilde{H}_z^u = -\mathrm{Re}\{\bar{h}_k a_u \sinh(\bar{h}_k Y) e^{i\bar{h}_k Z}\},$$
$$\tilde{H}_0 = eH_0/m_0c\omega$$

are the normalized field components; $\bar{h}_k = \bar{h}/k$ and $a_{u,s} = eA_{u,s}/m_0c^2$ are the amplitudes of the undulator field and signal wave field; $J_0 = 2ej_0/m_0c\omega^2 a$ is the current parameter; and j_0 is the linear current density.

In the equations of motion, time differentiation is replaced by differentiation with respect to the longitudinal coordinate: $d/dt = v_z d/dz$.

The derivation of set (2) requires neither the synchronism conditions nor conditions far away from cyclotron resonance; hence, set (2) has a fairly general character but averaging over fast oscillations in it is absent. This complicates the analysis, in particular, the elaboration of a linear theory. However, these equations may help to check the accuracy of results obtained with the averaged equations. Set (2) is intermediate in accuracy between the direct numerical simulation of the Maxwell equations (for example, using the PIC-code KARAT; see Section 3) and the approach based on the averaged equations (Section 2).

2. AVERAGED EQUATIONS

To obtain the averaged equations, we will consider the interaction of the electrons with the operating wave under the undulator synchronism conditions

$$\omega - h v_\parallel \approx \Omega, \tag{3}$$

where $\Omega = \bar{h} v_\parallel$ is the oscillation frequency of the electrons in the undulator field (bounce frequency).

We assume that the signal electromagnetic wave and the undulator field are far from cyclotron resonance with the electrons:

$$|\omega - h v_\parallel - \omega_H| T \gg 2\pi,$$
$$|\bar{h} v_\parallel - \omega_H| T \gg 2\pi, \tag{4}$$

where $\omega_H = eH_0/m_0c\gamma_0$ is the gyrofrequency, $v_\parallel$ is the longitudinal velocity of the electrons, and T is the characteristic time of interaction.

Approximately integrating equations of motion (2b) and (2c) under these assumptions, we find the amplitude of transverse electron oscillations in the resulting field of the signal wave and the undulator:

$$p_+ = \frac{e}{2c}\left\{\frac{k}{\bar{h}}\frac{iA_s(1/\beta_\parallel - 1)e^{i(\omega t - hz)}}{1 - u - g} + \frac{k}{\bar{h}}\frac{iA_s^*(1/\beta_\parallel - 1)e^{-i(\omega t - hz)}}{1 - u + g} - \frac{A_u \cosh(\bar{h}y)e^{i\bar{h}z}}{1 - u - g} + \frac{A_s^* \cosh(\bar{h}y)e^{-i\bar{h}z}}{1 - u + g}\right\}, \tag{5}$$

where $p_+ = p_x + ip_y$, $g = \omega_H/\Omega$ is the cyclotron-to-bounce frequency ratio, and $u = 1 - \gamma/\gamma_0$ is the relative change in the electron energy. Asterisk means complex conjugation.

Substituting (5) into excitation equation (2a) and energy variation equation (2d) and averaging over fast oscillations, we get

$$\frac{d\alpha_s}{dZ} = I_0\alpha_u \int_0^{2\pi}\left(\frac{1}{1 - \tilde{u} - g} - \frac{1}{1 - \tilde{u} + g}\right)e^{-i\tilde{\theta}}d\theta_0,$$
$$\frac{d\tilde{u}}{dZ} = \left(\frac{1}{1 - \tilde{u} - g} - \frac{1}{1 - \tilde{u} + g}\right)\mathrm{Re}\{\alpha_u^* \alpha_s e^{i\tilde{\theta}}\}, \tag{6}$$

where $\alpha_s = a_s/2\gamma_0$ is the amplitude of the operating wave, $\alpha_u = a_u \cosh(\bar{h}y_0)/2\gamma_0$ is the normalized field of the undulator, $I_0 = J_0/4\gamma_0$ is the current parameter, and $\theta = \omega t - (k + \bar{h})z$ is the phase of the electrons relative to the combinational wave. Tilde means averaging.

Writing the equation for the electron phase in the form

$$\frac{d\theta}{dz} = \frac{\omega}{v_z} - (k + \bar{h}) \tag{7}$$

and putting $1/\beta_z \approx 1 + 1/2\gamma^2 + \beta_\perp^2/2$ in the ultrarelativistic limit, we use expression (5) for transverse electron oscillations and average over fast electrons. Eventually, we come to the self-consistent set of equations (tilde is

omitted later on)

$$\frac{d\alpha_s}{dZ} = I_0\alpha_u\int_0^{2\pi}\left(\frac{1}{1-u-g}-\frac{1}{1-u+g}\right)e^{-i\theta}d\theta_0,$$

$$\frac{du}{dZ} = \left(\frac{1}{1-u-g}-\frac{1}{1-u+g}\right)\mathrm{Re}\{\alpha_u^*\alpha_s e^{i\theta}\},$$

$$\frac{d\theta}{dZ} = \frac{1}{\gamma_0^2}\frac{u(2-u)}{2(1-u)^2}+\frac{\beta_\perp^2}{2}-\Delta, \qquad (8)$$

$$\beta_\perp^2 = (|\alpha_s|^2+|\alpha_u|^2)\left(\frac{1}{(1-u-g)^2}+\frac{1}{(1-u+g)^2}\right)$$

$$-2\mathrm{Im}\{\alpha_u^*\alpha_s e^{i\theta}\}\left(\frac{1}{(1-u-g)^2}+\frac{1}{(1-u+g)^2}\right)$$

with the boundary conditions $\alpha_s|_{Z=0} = \alpha_0$, $u|_{Z=0} = 0$, $\theta|_{Z=0} = \theta_0 \in [0, 2\pi)$. Here, $\Delta = (1 + \bar{h}_k) - 1/\beta_0$ is the undulator synchronism detuning.

Linearizing set (8) in the small-signal approximation and representing a solution in the form $e^{-i\Gamma CZ}$, we arrive at the dispersion relation

$$\Gamma^3 - \tilde{\Delta}\Gamma^2 + b\Gamma + 1 = 0, \qquad (9)$$

where $\tilde{\Delta} = (\Delta - \beta_{\perp 0}^2/2)C^{-1}$, $b = 4C/\mu(1-g^2)$,

$$C = \left(4\pi I_0|\alpha_u|^2\mu\frac{g^2}{(1-g^2)^2}\right)^{1/3} \qquad (10)$$

is the Pierce parameter, and

$$\mu = \frac{1}{\gamma_0^2}+2|\alpha_u|^2\frac{1+3g^2}{(1-g^2)^3} \qquad (11)$$

is the inertial grouping parameter.

In the range of parameters that meets the condition of the designed experiment, the cyclotron frequency exceeds the bounce frequency and b is negative. Figure 1 plots the optimal detuning and the maximal increment against b. The increase in the absolute value of b decreases the maximal increment and shifts the optimal detuning toward negative values.

The nonlinear stage of the interaction was simulated for the parameters close to the conditions of the designed experiment based on the U-3 accelerator. A 12-cm-wide ribbon electron beam with an energy of about 900 keV and a total current of 2 kA is to be injected through a 1 × 20-cm rectangular waveguide into the field of a planar undulator with a field period of 4 cm and an amplitude of the transverse magnetic field component of 1.5 kOe. The strength of the guiding magnetic field is 11 kOe. It is assumed that the beam will interact with one of the lower H modes. At the point of beam injection, the field configuration of this

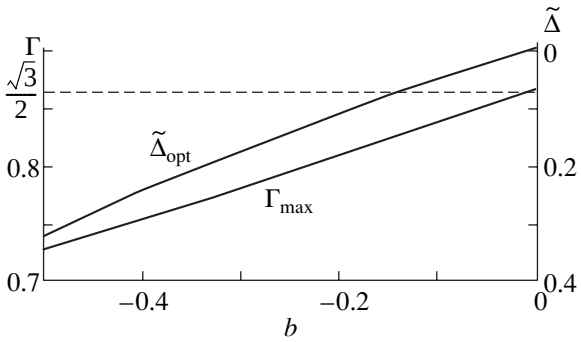

Fig. 1. Optimal detuning and maximal increment vs. b.

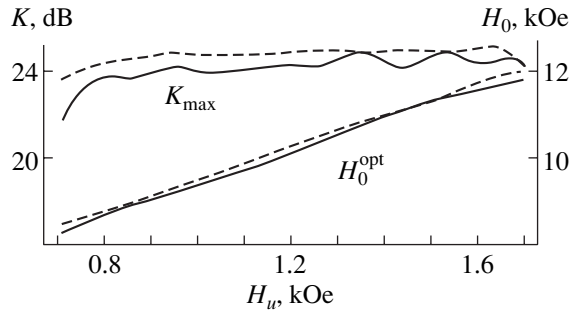

Fig. 2. Optimal relationships between the guiding and undulator magnetic fields and the dependence of the maximal gain on the undulator field under the optimal conditions. Continuous curves, unaveraged equations; dashed curves, averaged equations.

mode is close to that of the TEM mode of the planar waveguide. A 1-MW 75-GHz gyrotron is used as an external signal source.

Figure 2 shows the optimal (in terms of gain) relationship between the magnetic fields at the nonlinear stage of the interaction for the averaged and unaveraged equations. Here, the dependences of the maximal gain on the undulator magnetic field under the optimal conditions are also depicted. It is seen that the simulations using the averaged and total equations give nearly the same results. The gain is maximal throughout the entire length of the interaction space, 90–100 cm, reaching 24–25 dB, which corresponds to the output power 250–300 MW and the efficiency 14–17%.

3. SIMULATION OF THE AMPLIFICATION PROCESS WITH PIC-CODE KARAT

We additionally simulated the planar model of the ubitron–amplifier with the two-dimensional version of the PIC-code KARAT. This code allows us to directly solve the Maxwell equations jointly with the equations of macroscopic particle motion.

Figure 3 demonstrates the gain vs. longitudinal coordinate dependences obtained from the solutions of the averaged and unaveraged equations, also by the

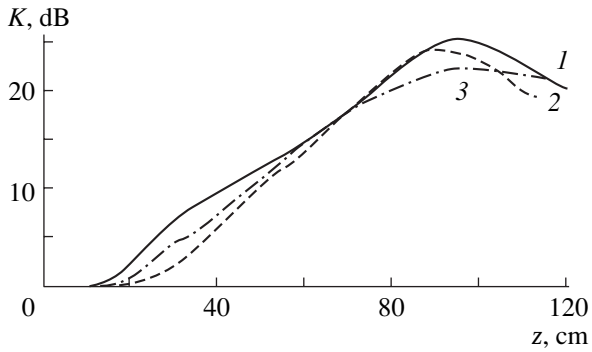

Fig. 3. Variation of the gain with the longitudinal coordinate: *1*, averaged equations; *2*, unaveraged equations; and *3*, KARAT code.

KARAT simulation. In the last case, the gain reaches 22 dB, which corresponds to an output power of 160–170 MW and an efficiency of 9%. The lower gain compared with the other approaches can be explained by the effect of low-frequency (static) and high-frequency space charges. Specifically, the static space charge must cause the separation of the electrons by longitudinal velocity. Moreover, the analysis of the averaged and unaveraged equations shows that the gain markedly drops when the relationship between the magnetic fields is not optimal. One can suppose that the same sensitivity takes place in simulating with the KARAT code. In this case, the exact optimal values of the fields are very difficult to find.

ACKNOWLEDGMENTS

The authors used the PIC-code KARAT by the courtesy of V.P. Tarakanov.

This work was supported by the Russian Foundation for Basic Research (grant no. 00-02-17232).

REFERENCES

1. A. V. Arzhannikov, S. L. Sinitskiĭ, and M. V. Yushkov, Preprint No. 91-85, IYaF SO RAN (Budker Institute of Nuclear Physics, Siberian Division, Russian Academy of Sciences, Novosibirsk, 1991).
2. A. V. Arzhannikov, N. S. Ginzburg, V. S. Nikolaev, *et al.*, in *Proceedings of the 14th International Free Electron Laser Conference, Kobe, Japan, 1992*, p. 214.
3. S. Cheng, W. W. Destler, V. L. Granatstein, *et al.*, IEEE Trans. Plasma Sci. **24**, 750 (1996).
4. N. S. Ginzburg, N. Yu. Peskov, and A. S. Sergeev, Pis'ma Zh. Tekh. Fiz. **18** (9), 23 (1992) [Sov. Tech. Phys. Lett. **18**, 285 (1992)].
5. N. S. Ginzburg, N. Yu. Peskov, A. S. Sergeev, *et al.*, Phys. Rev. E **60**, 935 (1999).
6. N. S. Ginzburg, N. Yu. Peskov, A. S. Sergeev, *et al.*, Pis'ma Zh. Tekh. Fiz. **25** (19), 87 (1999) [Tech. Phys. Lett. **25**, 796 (1999)].

Translated by V. Isaakyan

Technical Physics, Vol. 46, No. 12, 2001, pp. 1549–1552. Translated from Zhurnal Tekhnicheskoĭ Fiziki, Vol. 71, No. 12, 2001, pp. 62–65.

ELECTRON AND ION BEAMS, ACCELERATORS

Achromatic Deflectors with Combined Electrodes and Poles

L. P. Ovsyannikova*, T. Ya. Fishkova*, and I. A. Petrov**

** Ioffe Physicotechnical Institute, Russian Academy of Sciences, Politechnicheskaya ul. 26, St. Petersburg, 194021 Russia*

e-mail: L.Ovsyannikova@pop.ioffe.rssi.ru

*** Applied Materials, GEM Business Unit, 74103 Nes-Ziona, Israel*

Received March 23, 2001

Abstract—A combined electromagnetic deflector consisting of four or eight electrodes that simultaneously act as poles is proposed. The distribution of the potential in such systems is obtained, and the parameters of the base beam trajectory under achromatic operating conditions are calculated. New (nonclassic) relationships between the electrostatic and magnetic components of the field that provide a lower residual chromatic aberration and a higher deflection linearity are found. © *2001 MAIK "Nauka/Interperiodica".*

In scanning electron microscopes, electron-beam tubes, secondary-ion and atomic mass spectrometers, etc., a raster on the sample surface is produced mostly by electrostatic systems with colocated deflection centers, which are called deflectors. The deflectors do not defocus (in the first approximation) the charged particle beam (i.e., they do not affect the beam divergence). An electrostatic deflector is made as a cylinder or a cone split along its generatrix [1, 2] into an even number of planar electrodes placed on the sides of a rectangular (square) box [3] or as a split plane capacitor [4].

Many devices and installations must provide the same deflection for nonmonoenergetic beams. As is known, achromatic systems employ mutually orthogonal electrostatic and magnetic fields. We will write the achromatism condition in the first approximation for the general form, starting from the trajectory equation without specifying the types of the fields. The constraints are the following: (i) the electrostatic and magnetic fields exert the same action (deflection, focusing, or aberration correction) on the charged particle beam, (ii) the mutually orthogonal transverse (with respect to the particle motion) electrostatic and magnetic fields occupy the same space, and (iii) the longitudinal particle velocity within the field region is constant. Then we come to the first-order nonrelativistic achromatism condition by differentiating the right-hand sides of the projections of the trajectory equation on the *xz* and *yz* planes with respect to energy and equating the resulting expressions to zero:

$$v/c = 2E_x/H_y = -2E_y/H_x. \quad (1)$$

Here, v is the charged particle velocity, c is the velocity of light, and E and H are the intensities of the oppositely directed electrostatic and magnetic fields lying in the respective planes.

The purpose of this work is to theoretically study combined deflectors exhibiting a transverse chromatic aberration that can controllably be varied in magnitude and sign. Such deflectors are designed as a magnetic cylinder split along its generatrix into four or eight closely spaced parts. The electrodes simultaneously act as the pole tips of the magnet. Figure 1 shows the cross sections of the combined deflectors consisting of four or eight electrodes–poles. In the four-element system, only two pairs of the basic electrostatic ($\pm V_x$, $\pm V_y$) and magnetic ($\mp W_y$, $\pm W_x$) potentials are applied (Fig. 1a), while the eight-element system parts use additional potentials defined by the coefficient a (Fig. 1b) in order to improve the field uniformity. The coefficient a has been obtained in [1] from the condition that the coefficients of the third and fifth harmonics in the expansion of the potential vanish ($a = \sqrt{2} - 1$).

We obtained closed-form expressions for the distribution of the deflecting potential taking into account results from [5, 6]. For an infinite cylinder split into four identical parts along its generatrix (Fig. 1a), the

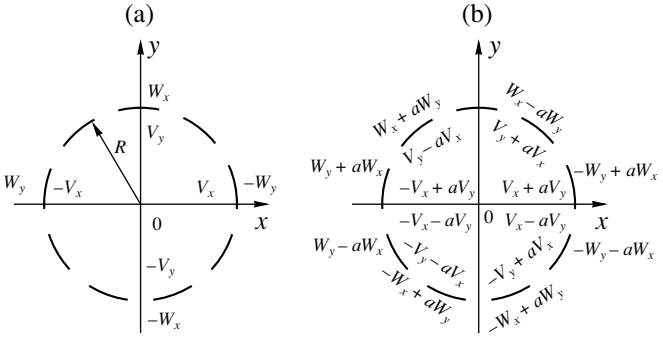

Fig. 1. Combined electromagnetic deflectors with (a) four and (b) eight identical electrodes–poles.

1063-7842/01/4612-1549$21.00

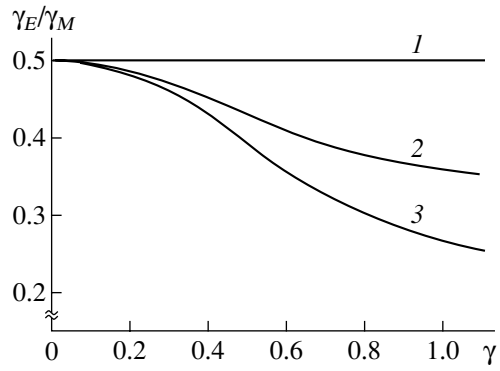

Fig. 2. Ratio of the electrostatic and magnetic power components versus field power of the combined deflector that provides (*1*) the first-order achromatism and (*2*, *3*) an expanded achromatism region.

distribution in the Cartesian coordinates has the form

$$\begin{aligned}\Phi(4) &= 1/\pi\{(V_x + V_y)\arctan[\sqrt{2}(x+y)/(1-x^2-y^2)] \\ &+ (V_x - V_y)\arctan[\sqrt{2}(x-y)/(1-x^2-y^2)]\}.\end{aligned} \quad (2)$$

Hereafter, the coordinates are normalized to the radius R of the cylinder. For an eight-electrode deflector (Fig. 1b), we have

$$\begin{aligned}\Phi(8) &= (1-a)\Phi(4) \\ &+ 2a/\pi\{V_x\arctan[2x/(1-x^2-y^2)] \\ &+ V_y\arctan[2y/(1-x^2-y^2)]\}.\end{aligned} \quad (3)$$

At $a = 0$, expression (3) turns to (2).

For a deflection system with combined electrodes and poles, expressions for the magnetic scalar potentials can be obtained from formulas (2) and (3) by changing V_x to $(-W_y)$ and V_y to W_x. In this case, the electrostatic and magnetic forces act in opposite directions.

Earlier [2], nonuniform electrostatic fields of the four- and eight-electrode deflectors were calculated as a function of distance to their axes with formulas (2) and (3). It should be noted that in magnetic systems with apparent poles, the nonuniformity of the magnetic fields is the same as that of the associated electrostatic fields. Since the deflection aberrations depend on the field, these data can be used to estimate the deflection angle, which is defined by the maximum admissible field nonuniformity.

In the plane of an object located outside the field, the distance from the base beam trajectory to the axis of the system; the angle of trajectory inclination to the axis; and the chromatic aberrations, which are the same in the horizontal and vertical planes in the first approximation, have the form

$$\begin{aligned}s_1 = \gamma g, \quad s_1' = \gamma, \quad \Delta s_1 = (\gamma_E - \gamma_M/2)g\Delta\varepsilon/\varepsilon_0, \\ \Delta s_1' = (\gamma_E - \gamma_M/2)\Delta\varepsilon/\varepsilon_0,\end{aligned} \quad (4)$$

where $\gamma = \gamma_M - \gamma_E$ is the power of the combined electromagnetic deflector field, which is equal to the tangent of the base beam trajectory inclination, and γ_E and γ_M are its electrostatic and magnetic components:

$$\begin{aligned}\gamma_E &= (K_{1E}eV/2\varepsilon_0)(L/R), \\ \gamma_M &= K_{1M}eWc^{-1}(2m\varepsilon_0)^{-1/2}(L/R).\end{aligned} \quad (5)$$

Here, ε_0 is the initial energy of the particles with a charge e and a mass m, $\Delta\varepsilon$ is the change in the particle energy, g is the distance from the deflector center to the object, L is the effective field length, and K_1 is the coefficient before the first harmonic in the expansion of the potential. For the deflectors with four electrodes–poles, $K_{1E} = K_{1M} = 2\sqrt{2}/\pi$; for the deflectors with eight electrodes–poles, $K_{1E} = K_{1M} = 8(\sqrt{2} - 1)/\pi$. Formulas (1) show that the chromatic aberration can controllably be varied in magnitude and sign. It is absent when the electrostatic power is half as large as the magnetic power.

The trajectory of the charged particle beam in the combined deflecting systems was calculated with the original program DEF. The program solves a system of second-order differential equations that contain the potentials and the field intensities determined from exact potential distributions (2) and (3). The field distribution along the deflector axis was specified by empirical formulas obtained in [2]. We studied short and long deflectors with four electrodes–poles, because they exhibit stronger aberrations than the deflectors with eight electrodes–poles (other factors being equal).

The conventional relationship between the electrostatic and magnetic power components, $\gamma_E/\gamma_M = 1/2$, provides achromatism only for small deflections (less than 7°). At larger deflections, the residual aberration sharply grows. We showed that the achromatism region can be expanded by choosing another value of γ_E/γ_M. Figure 2 plots the ratio of the electrostatic and magnetic components against the field power of the achromatic deflector that provides the same deflection at the exit from the field region as the electrostatic deflector. Interestingly, this dependence is the same for the deflectors of lengths $l = 2R$ and $4R$. Curve *2* in Fig. 2 refers to the case when the electrostatic component of the achromatic deflector field power is equal to the field power of the purely electrostatic deflector (conditions 2). Curve *3* was obtained by varying the electrostatic and magnetic components simultaneously (conditions 3). It is seen that, at large deflections, the ratio γ_E/γ_M is significantly different from the classical value (curve *1*, conditions 1). Note that, under achromatic conditions 2 and 3, the electrostatic and magnetic components of the deflector

field power are smaller and the deflections are larger than those under conventional conditions 1.

Figure 3 illustrates the chromatic aberration of the coordinate, Δs, and of the deflection angle, $\Delta s'$, for the short deflectors at an energy spread $\Delta\varepsilon/\varepsilon_0 = 5\%$. Curves *1* refer to the electrostatic deflector; curves *2*, to the magnetic deflector. The residual chromatic aberration for conditions 2 and 3 is illustrated by curves *4* and *5*, respectively. Figure 3 shows that the conditions suggested are much better than the conventional achromatic conditions (curves *3*). The new conditions also expand the achromatic region of the longer deflectors. In this case the residual aberrations, appearing with increasing deflection, are 4–10 times lower than those under the conventional conditions.

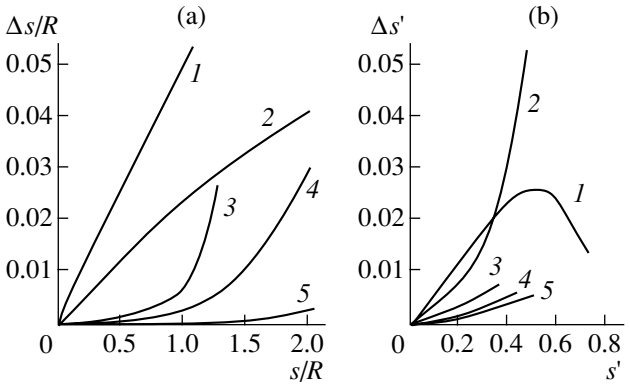

Fig. 3. Chromatic (a) coordinate and (b) angular aberrations of the shorter deflectors at the exit from the field region for the base beam trajectory: (*1*) electrostatic deflector, (*2*) magnetic deflector, and (*3–5*) achromatic deflectors.

Figure 4 plots the coordinates and deflection angles of the base beam trajectory in the horizontal and vertical directions at the exit from the field region for the shorter ($l = 2R$, $L = 2.56R$) and longer ($l = -4R$, $L = 4.34R$) electrostatic, magnetic, and achromatic deflectors versus their field powers for $\varepsilon_0 = \text{const}$. These plots are seen to be almost linear and identical for all types of the deflectors when the deflection angle is smaller than 7°. It should be noted that the maximum achievable deflection angle is approximately inversely proportional to the deflector length and is smaller in the longer deflector, because the beam reaches the electrodes faster. Furthermore, in the longer deflectors, the deflection nonlinearity under the weak (strong) conditions is higher (lower) than that in the shorter devices.

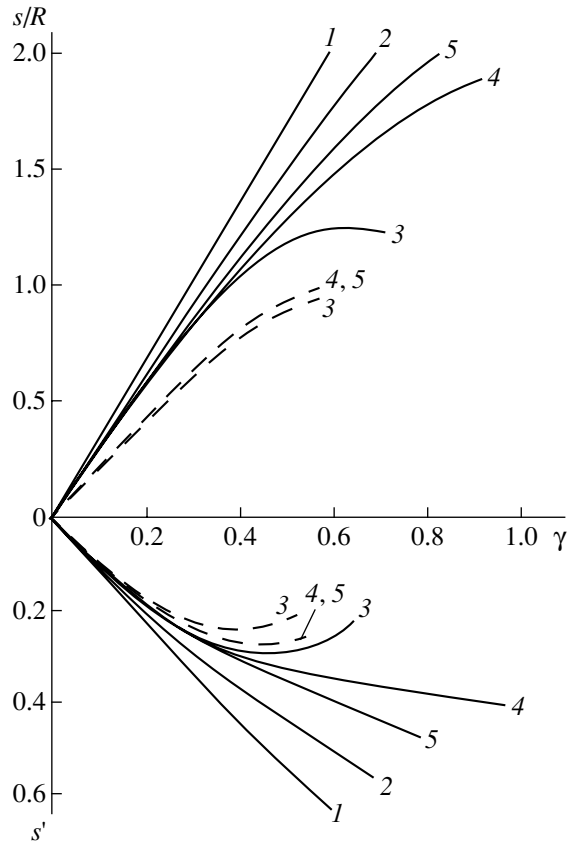

Fig. 4. Coordinates and deflection angles of the base beam trajectory versus field power of the shorter (solid lines) and longer (dashed lines) deflectors: (*1–5*) the same as in Fig. 3.

On the whole, the nonlinearity of angular and coordinate deflections in an achromatic deflector is lower than in electrostatic and magnetic deflectors. In a conventional achromatic deflector, the nonlinearity is so high that it limits the maximum achievable linear and angular deflections. In particular, in the shorter deflector, $s_{max} = 1.25R$ and $s'_{max} = 0.3$.

Generally speaking, the total deflection nonlinearity is the sum of the deflection aberrations due to the difference $s - s_1$ at $\varepsilon_0 = \text{const}$ and the chromatic aberrations. When $\Delta\varepsilon/\varepsilon_0 < 5\%$, the deflection aberrations are significantly higher. Therefore, when the raster is formed on the working area as large as 0.7 of the aperture or more, the four-electrode achromatic deflectors are inappropriate and the deflectors with eight electrodes–poles, in which the deflection aberrations are to a great extent corrected, should be used.

The achromatic conditions found are of interest in devices that scan an object not over the entire raster but over a small region at a large angle of incidence. As an example, consider the scanning of an object in the plane located parallel to the deflector axis at a distance $s = 1.2R$ with the field power varying in the range $\Delta\gamma = \pm 0.1$. The deflection nonlinearity is characterized by the ratio $\zeta = dz/d\gamma$ where dz is the change in the longitudinal coordinate at the extreme points of the above range of γ. The deflection is linear if $\zeta = 1$. In our calculations, the relative change in the initial energy was $\Delta\varepsilon/\varepsilon_0 = 5\%$. The results are summarized in the table, where Δz is the scan dimension.

As follows from the table, the deflectors with an expanded achromatic region (conditions 2 and 3) are

Table

Condition	γ	S	$\Delta z/R$	ξ
1	0.50	0.30	0.70	1.8
2	0.46	0.32	1.40	1.3
3	0.44	0.33	1.50	1.3

the best in terms of deflection nonlinearity and scan dimension.

CONCLUSIONS

(1) Achromatic systems that deflect the beam in arbitrary directions are suggested. They have the form of a cylinder split into an even number of parts that are used simultaneously as poles and electrodes.

(2) First-order achromatic conditions are written in the general form for deflecting, focusing, and correcting systems with transverse electromagnetic fields.

(3) A program for calculating the parameters of finite-length combined electromagnetic deflecting systems is developed. It involves exact potential distributions (in the two-dimensional approximation) and the edge-field model proposed.

(4) The base beam trajectory parameters, including the chromatic aberration, are calculated for a deflector with four electrodes–poles.

(5) A method for expanding the achromatic deflection region that uses an other-than-conventional relationship between the electrostatic and magnetic components of the combined deflecting field power is put forward.

(6) Operating conditions that expand the achromatic region and provide a deflection nonlinearity significantly lower than in a conventional first-order achromat are found numerically.

(7) It is shown that these conditions are appropriate for the discrete scanning of samples.

REFERENCES

1. J. Kelly, Adv. Electron. Electron Phys. **43**, 116 (1977).
2. L. P. Ovsyannikova and T. Ya. Fishkova, Zh. Tekh. Fiz. **70** (8), 104 (2000) [Tech. Phys. **45**, 1058 (2000)].
3. L. P. Ovsyannikova and T. Ya. Fishkova, Zh. Tekh. Fiz. **56**, 1348 (1986) [Sov. Phys. Tech. Phys. **31**, 791 (1986)].
4. L. P. Ovsyannikova and T. Ya. Fishkova, Zh. Tekh. Fiz. **58**, 1176 (1988) [Sov. Phys. Tech. Phys. **33**, 692 (1988)].
5. A. M. Strashkevich, in *Electron Optics of Electrostatic Systems* (Énergiya, Moscow, 1966), p. 141.
6. L. A. Baranova, S. G. Narylkov, and S. Ya. Yavor, Zh. Tekh. Fiz. **57**, 1872 (1987) [Sov. Phys. Tech. Phys. **32**, 1126 (1987)].

Translated by A. Khzmalyan

Technical Physics, Vol. 46, No. 12, 2001, pp. 1553–1557. Translated from Zhurnal Tekhnicheskoĭ Fiziki, Vol. 71, No. 12, 2001, pp. 66–70.

ELECTRON AND ION BEAMS, ACCELERATORS

Characteristics of Multipole Lenses with the Ideal Central Part of the Poles

V. V. Vecheslavov and O. V. Grigoryeva

Budker Institute of Nuclear Physics, Siberian Division, Russian Academy of Sciences, pr. akademika Lavrent'eva 11, Novosibirsk, 630090 Russia

e-mail:vecheslavov@inp.nsk.su

Received March 23, 2001

Abstract—A procedure for calculating the potential and field of multipole lenses in which the central part of the poles has the form of an ideal curve is presented. The procedure is based on the method of conformal mapping. The properties of these lenses are compared with those whose poles have a polygonal profile. It is shown that sufficiently wide ideal-center poles provide a better field quality than polygonal poles. © *2001 MAIK "Nauka/Interperiodica".*

INTRODUCTION

Modern techniques for the formation and transfer of charged particle beams widely use quadrupole (the number of pole pairs $P = 2$), sextupole ($P = 3$), and octupole ($P = 4$) lenses [1–3]. The quality of the lens field requirements for which have recently become much more stringent depend primarily on the pole geometry. For any P-lens, there exists a theoretical profile providing the "ideal" field: linear for a quadrupole, quadratic for a sextupole, and cubic for an octupole. The ideal profiles are however unfeasible, because they do not leave room for winding and flux closure, and real-lens fields always contain undesirable higher harmonics [2, 3].

In modern practice of searching for "good" profiles [2–4], there has appeared the tendency to construct lenses of two types: (1) the broken ideal profile is adequately approximated (for example, by a circular arc) and (2) the lens profile is polygonal (or admits the approximation by a polygon).

The early successful attempt to design lenses of the latter type has been undertaken in [4], where the planar profile of a quadrupole lens with the suppressed sixth (the first minor) harmonic of the potential has been found using conformal mapping. Note that the number of the vertices of a polygon to be determined was only two. The computing procedure applied in [4] has recently been extended [5], so that a lens sector (a part of the cross section belonging to one pole) could be approximated by a polygon with more than ten vertices.

In this work, we elaborate upon designing multipole lenses and consider lenses of the first type where the central part of the pole is a strictly ideal curve. The angular size of this part and the shim geometry are selected such that they provide the high quality of the field. In Section 3, lenses of both types are compared and their applicability domains are indicated.

It should be noted that the field quality is conventionally estimated by two parameters: the maximal (within the operating aperture) deviation of the field from the ideal one and/or the amplitude of the first minor harmonic of the potential. To date, it has remained unclear which of these parameters is of greater importance; therefore, we perform optimization by either parameter separately (Section 3). The conditions usually adopted for analytical methods are assumed to be met; that is, the lens is long and totally symmetric and iron does not saturate.

1. MAPPING OF A LENS SECTOR

Figure 1 exemplifies a quadrupole sector where the central part of the pole is an ideal hyperbola. This curve cannot be approximated by a polygon, as was done in [5], because a broken line with a relatively small number of vertices instead of the hyperbola will heavily distort the field configuration. We proceed as follows. It can be shown (see Appendix 3 in [5]) that the function

$$\delta(z) = \eta(z) + i\xi(z) = (z\exp(-i\alpha_P))^P, \quad \alpha_P = \pi(P-2)/4P \tag{1}$$

maps a sector of an ideal lens onto a band (digon) in the plane of an intermediate variable δ. The exponential in (1) makes the bisectrix $\varphi = \pi/4$ of the first quadrant on the z plane the line of symmetry of the sector for any number of pole pairs. With mapping (1) applied to a sector of any real P-lens, the δ plane will contain a closed figure whose central part is the exact map of the ideal portion of the profile, i.e., a straight horizontal segment (all other sections being curved in the general case (Fig. 2). This figure can be fairly accurately approximated by a polygon with the total number of vertices $2M + 1$, since such an approximation is tangible only at the periphery of the lens.

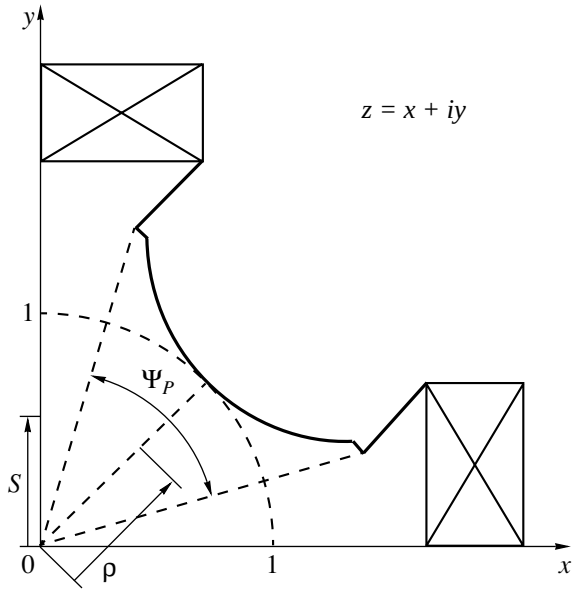

Fig. 1. Sector of a quadrupole with the ideal central part of a pole. The thickness of the lines indicates to the scalar potential distribution along the sector boundary.

The upper half-plane of the complex variable $\omega = u + iv$ is mapped onto this polygon with the Christoffel–Schwartz integral, which, in view of the symmetry of this domain, is written as [5, 6]

$$\delta(\omega) = C_0 \int_{\omega_0}^{\omega} \prod_{m=1}^{M} (\omega^2 - a_m^2)^{\beta_m} d\omega + C_1, \qquad (2)$$

where $\beta_m = \alpha_m - 1$, α_m are angles interior with respect to this domain (measured in terms of π), and a_m are points on the real axis u of the plane ω that are the maps of the vertices A_m of the polygon.

The conformal mapping procedure completely coincides with that employed in [5] for a polygonal profile and allows us to find all parameters entering into mapping (2). However, the construction of the potential and induction distributions, as well as of the potential spectrum (see the Appendix), is made in another way because of the presence of the intermediate mapping onto the δ plane.

2. MAGNETIC FIELD INDUCTION AND POTENTIAL DISTRIBUTIONS

The complex magnetic potential of a P lens on the intermediate δ plane can be represented in the form [5]

$$\mathcal{P}(\delta) = \mathcal{D}(\delta) + i\mathcal{F}(\delta) = p_0\delta\left(1 + \sum_{n}^{\infty} \tilde{p}_n \delta^{2n}\right), \qquad (3)$$

where $\mathcal{D}(\delta)$ and $\mathcal{F}(\delta)$ are the vector and scalar magnetic potentials, respectively [2].

We are dealing with the scalar potential $\mathcal{F}(\delta)$, the distribution of which over the lens sector is shown in Fig. 1. On the pole surface, $\mathcal{F} = 1$ (thick lines); near the winding, the potential falls to zero (variable-width line) and is zero along the remaining part of the sector boundary (thin lines). Expression (2) maps this distribution onto the real axis u of the plane ω. Calculations show that the winding region is small, so that the actual distribution $F(u)$ is well approximated by an equivalent rectangle (Fig. 3b in [5]):

$$\mathcal{F}(u) = 1, \quad -a_b \le u \le a_b; \quad \mathcal{F}(u) = 0, \quad |u| > a_b. \qquad (4)$$

Upon mapping the plane ω onto the intermediate plane δ, the imaginary axis $0 \le v < \infty$ transforms into the segment $0 < \chi < 1$ of the imaginary axis η; this segment, in turn, is the map of the unit segment from the lens center to the pole center $x = y = 1/\sqrt{2}$ on the z plane (Fig. 1).

In terms of the variables u and v, the potential $\mathcal{F}(u, v)$ at any point of the upper half of the plane ω and the potential distribution $\mathcal{F}(v)$ along the semiaxis $0 \le v < \infty$ are given by formulas (9) and (10) in [5]. The method of constructing the induction distribution along the lens bisectrix and along the boundary of the lens sector is also totally applicable to our case. However, the return to the initial plane z must include the variables of the intermediate plane δ; therefore, the induction distribution for the ideal central part of the pole somewhat differs from those obtained in [5] for the polygonal profile.

The dependence $v(\chi)$ entering into the potential distribution $\mathcal{F}(v(\chi))$ along the semiaxis $0 \le v < \infty$ is found from the equation

$$\frac{dv}{d\chi} = -\frac{1}{|C_0|} \prod_{m=1}^{M} (v^2(\chi) + a_m^2)^{-\beta_m}, \qquad (5)$$

which is obtained by substituting χ for $p \longrightarrow \chi$ in formula (12) in [5].

The induction distribution along the unit segment from the center of the lens to that of the pole on the initial plane z in view of the equality $\chi = \rho^P$ is given by

$$\mathcal{B}(\rho) = \frac{d\mathcal{F}}{d\rho} = \frac{d\mathcal{F}}{dv}\frac{dv}{d\chi}\frac{d\chi}{d\rho} = \frac{2}{\pi}\frac{a_b}{v^2(\chi) + a_b^2}\frac{P}{|C_0|}\prod_{m=1}^{M}[v^2(\chi) + a_m^2]^{-\beta_m}\rho^{P-1}. \qquad (6)$$

Essentially, the calculation of the $\mathcal{B}(\rho)$ along the bisectrix of the sector is performed by jointly using formulas (5) and (6). From (6), one can find the exact

induction value at the center of the pole, assuming that $\nu = 0$,

$$\mathcal{B}_{\rho=1} = \frac{2P}{\pi}\left(\frac{1}{a_b|C_0|}\right)\prod_{m=1}^{M} a_m^{-2\beta_m}, \quad (7)$$

and also determine the induction near the lens center from the conditions $\rho \longrightarrow 0$ and $\nu \longrightarrow \infty$,

$$\mathcal{B}_{p\to 0} = \frac{2Pa_b}{\pi|C_0|}\rho^{P-1}. \quad (8)$$

Comparing (8) and (3) in view of (1), one can find the exact value of the coefficient for the first potential harmonic:

$$p_0 = \frac{2}{\pi}\frac{a_b}{|C_0|}. \quad (9)$$

To construct the second distribution of the induction $\mathcal{B}(s)$, i.e., from the lens center along the sector boundary (Fig. 1), we must obtain relationships similar to (5) and (6) (the coordinate s is reckoned from the lens center; $s \equiv y$ for a quadrupole). The procedure is as follows. The left-hand boundary of the sector on the plane z is mapped onto the segment $A_M \le \sigma \le 0$ of the real axis ξ on the intermediate plane δ. This segment, in turn, is mapped onto the segment $a_M \le u < \infty$ of the real axis u on the plane ω, where only the ν component of the induction is nonzero. As in [5], we have

$$\mathcal{B}_\nu(u, 0) = -\lim_{\nu\to 0}\frac{\partial \mathcal{F}}{\partial \nu} = -\frac{2a_b}{\pi}\frac{1}{u^2 - a_b^2}.$$

The dependence $u(\sigma)$ entering into this expression is found from the equation

$$\frac{du}{d\sigma} = \frac{1}{|C_0|}\prod_{m=1}^{M}(u^2(\sigma) - a_m^2)^{-\beta_m}, \quad (10)$$

which is obtained by substituting $u(\sigma)$ for $s \longrightarrow \sigma$ in formula (20) in [5].

The final distribution of the induction along the sector boundary is given by

$$\mathcal{B}(s) = \mathcal{B}_\nu(u, 0)\frac{du}{d\sigma}\frac{d\sigma}{ds} = -\frac{2a_b}{\pi|C_0|}\frac{P}{u^2(\sigma) - a_b^2} \times \prod_{m=1}^{M}[u^2(\sigma) - a_m^2]^{-\beta_m} s^{P-1} \quad (11)$$

and is calculated together with (10). Note that the validity of formulas (8) and (9) can be confirmed from (11) in the limit $u(\sigma) \longrightarrow \infty$.

Of two distributions (6) and (11), we take into account that giving the greatest (within the working aperture) deviation of the field from the basic one.

It has been noted above that the parameter to be minimized can also be the relative amplitude of the first minor harmonic of the potential. In the appendix, we describe the recursive procedure for calculating the relative amplitudes of the higher harmonics $\tilde{p}_n$ ($n \le N$) appearing in (3) up to any order of N. For $N > 1$, this can be done only by invoking computer analysis tools [7]; for $N = 1$, however, the computations are simple and the exact expression for $\tilde{p}_1$ in our case has the form

$$\tilde{p}_1 = -\frac{1}{3C_0^2}\left(a_b^2 + \sum_{m=1}^{M}\beta_m a_m^2\right). \quad (12)$$

Note in pass that the similar characteristic for a polygonal profile (which is absent in [5]) is given by

$$\tilde{p}_1 = -(P|C_0|)^{-2P}\left(\frac{a_b^2}{3} - \frac{P}{2P+1}\sum_{m=1}^{M}\beta_m a_m^2\right).$$

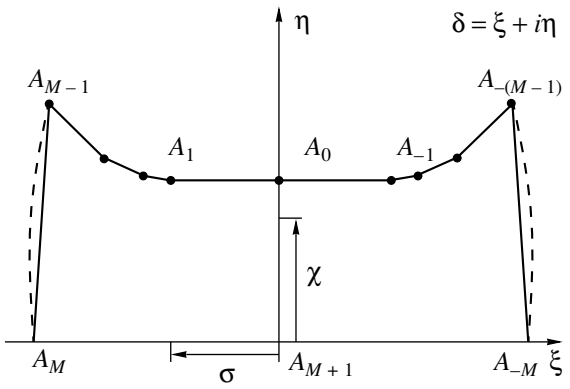

Fig. 2. Map of the lens sector (Fig. 1) on the intermediate plane δ. Dashed line, map obtained with function (1); continuous line, polygonal approximation of this map.

3. COMPARISON OF THE LENSES

Based on the algorithms used here and in [5], we have developed the MULTIPOL software suite, which makes it possible to interactively design and optimize lenses with any number of pole pairs. With this suite, we have gathered a large data array for designing quadrupoles and sextupoles whose profiles have both the ideal and polygonal central parts. One basic input parameter for the calculation is the total relative angle of a pole of a P lens (Fig. 1):

$$\tilde{\Psi}_P = P\Psi_P/\pi. \quad (13)$$

In all the cases, the program automatically (without the intervention of an operator) selected the shim length and slope so as to minimize either the maximal (within the working aperture $r_a \le 0.9$) deviation $\delta B/B$ of the field from the ideal one or the relative amplitude $\tilde{p}_1$ of the first minor harmonic. For polygonal profiles, the adjustable parameters T_φ and T_r were also automati-

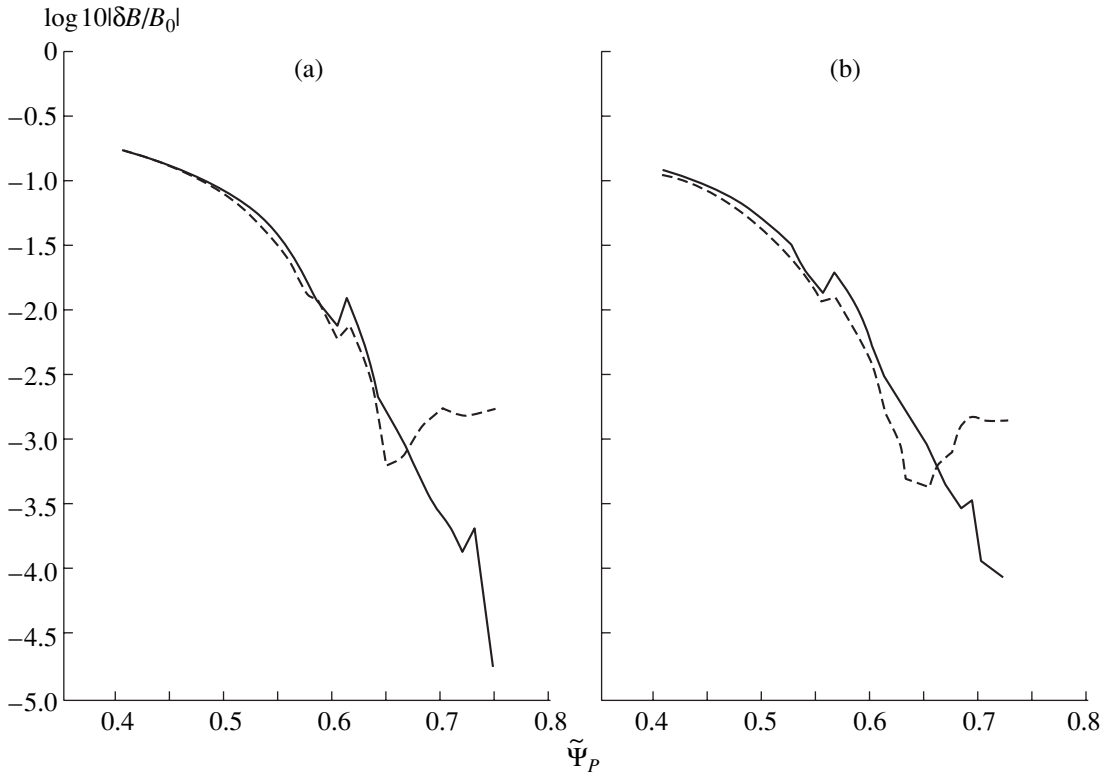

Fig. 3. Maximal relative deviation of the field from the ideal one for (a) quadrupoles and (b) sextupoles. Continuous line, profile with the ideal central part of a pole; dashed line, polygonal profile. $\tilde{\Psi}_P$ is the relative angle of the pole [see (13)].

cally selected in order to correct the radial and angular coordinates of the vertices (see Section 3 in [5]). The total number ($2M + 1$) of the vertices of the polygons approximating the sector of the second type [5, Fig. 2] was found to be 21 for both the quadrupoles and sextupoles.

CONCLUSION

For the optimization with respect to $\delta B/B$, the pole width is an important factor in deciding between the lenses, as follows from Fig. 3. The profiles with the ideal central part provide the better field quality when the poles are wide, $\tilde{\Psi}_P \gtrsim 0.65$, while the polygonal poles are better to use when the poles are narrow. For the optimization with respect to the amplitude of the first minor harmonic of the potential $\tilde{p}_1$, the situation is rather ambiguous; however, the presence of the profiles where this harmonic is suppressed is beyond question.

It should be also noted that the narrower the pole, the higher the fraction of the shim (the difference between the total angular size of a pole and that of its ideal or polygonal part). For example, at $\tilde{\Psi}_P \approx 0.75$, this fraction was about 10% in all the cases; for $\tilde{\Psi}_P \approx 0.4$, it grew to 30%. It appears that using shims of a shape more intricate than in Fig. 1 will improve the performance of narrow-pole lenses.

ACKNOWLEDGMENTS

The authors thank E.B. Levichev and V.N. Korchuganov for the valuable advices and discussion.

APPENDIX

The Potential Spectrum of a Lens with the Ideal Part of a Pole

With relationships (3) and (9), the relative distribution of the potential within a segment χ along the axis of symmetry of the lens (Fig. 2) can be represented in the form

$$\tilde{\mathcal{F}}(\mu) = \mathcal{F}/p_0 = \mu - \frac{(a_b/|C_0|)^2}{3}\mu^3 + \frac{(a_b/|C_0|)^4}{5}\mu^5 - \ldots. \quad \text{(A1)}$$

Here, the new variable

$$\mu(\chi) = \frac{|C_0|}{v(\chi)} \quad \text{(A2)}$$

is introduced and is assumed that the inequality $v > a_b$ is fulfilled [see (4)]. The dependence $\mu(\chi)$ is also found

in the form of a series:

$$\mu = \chi[1 + \theta(\chi)], \quad \theta(\chi) = \sum_{n=1}^{M} \tilde{\alpha}_n \chi^{2n}. \qquad \text{(A3)}$$

The second expression in (A3) is assumed to be a small correction: $|\theta(\chi)| \ll 1$.

From definition (A2), we find

$$\frac{d\mu}{d\chi} = -\frac{|C_0|}{\nu^2}\frac{d\nu}{d\chi} = \prod_{m=1}^{M}\left[1 + \left(\frac{\mu a_m}{|C_0|}\right)^2\right]^{-\beta_m}, \qquad \text{(A4)}$$

where $d\nu/d\chi$ is defined by formula (5) and the geometric equality $\sum_{m=1}^{M}\beta_m = -1$ is taken into account.

Using the binomial expansion of the right-hand side of (A4) with regard for (A3) and grouping the terms, one can obtain a series in χ with the coefficients containing the unknown quantities $\tilde{\alpha}_n$. On the other hand, the derivative $d\mu/d\chi$ in the form of series can be deduced directly from basic definition (A3):

$$\frac{d\mu}{d\chi} = 1 + 3\tilde{\alpha}_1\chi^2 + 5\tilde{\alpha}_2\chi^4 + \ldots. \qquad \text{(A5)}$$

Comparing the coefficients before the equal powers of χ in relationships (A4) and (A5) and using the exact values of p_0 and $|C_0|$, we can recurrently determine the parameters $\tilde{\alpha}_n$ ($n = 1, 2, \ldots$) appearing in (A3). This allows the construction of dependence (A2) for $\mu(\chi)$ in the explicit form and finding the amplitudes $\tilde{p}_n$ ($n = 1, 2, \ldots, N$) of the potential harmonics in series (3) through (A1).

REFERENCES

1. E. D. Courant *et al.*, Phys. Rev. **88**, 1190 (1952).
2. I. M. Kapchinskiĭ, *Particle Dynamics in Linear Resonant Accelerators* (Atomizdat, Moscow, 1966).
3. K. G. Steffen, *High-Energy Beam Optics* (Interscience, New York, 1965; Mir, Moscow, 1969).
4. V. K. Plotnikov, Prib. Tekh. Éksp., No. 2, 29 (1962).
5. V. V. Vecheslavov and O. V. Loginova, Zh. Tekh. Fiz. **70** (10), 81 (2000) [Tech. Phys. **45**, 1312 (2000)].
6. M. A. Lavrent'ev and B. V. Shabat, *Methods of the Theory of Functions of a Complex Variable* (Nauka, Moscow, 1973).
7. A. C. Hearn, *REDUCE User's Manual. Version 3.6* (RAND Pub. CP78 Rev. 7/95, 1995).

Translated by V. Isaakyan

Technical Physics, Vol. 46, No. 12, 2001, pp. 1558–1565. Translated from Zhurnal Tekhnicheskoĭ Fiziki, Vol. 71, No. 12, 2001, pp. 71–78.

EXPERIMENTAL INSTRUMENTS AND TECHNIQUES

A Simulation Study of the Cooling of an Isolated Metal Sphere in Aqueous Media (Quenching)

V. I. Aleshin*, N. A. Dolotova*, and V. S. Anisimov**

** Institute of High-Molecular Compounds, Russian Academy of Sciences, St. Petersburg, 199004 Russia*

*** St. Petersburg State Technical University, St. Petersburg, 195261 Russia*

Received January 26, 2001; in final form, June 4, 2001

Abstract—A quantitative study is carried of a metal cooling process in aqueous and water-polymer cooling liquids. In the study, an original spherical hot probe with a heat-insulated stem is used to simulate the cooling conditions of the operating part of the probe and to correspond to the cooling conditions of an isolated sphere. It has been shown that in this case the process consists of distinct consecutive stages, each of which can be studied separately in a quantitative way. The cooling process in all stages is described with a simple exponential relationship containing two parameters. One of these is the effective temperature of the cooling medium; the other is a time constant of the cooling process uniquely related to the heat dissipation coefficient. In the film boiling stage the effective temperature can be much lower than the nominal temperature; moreover, for cooling in cold water it is found to be lower than the absolute temperature, which indicates the dominant contribution of convection to the heat dissipation. The effective temperature of the medium is a monotonously increasing function of the nominal temperature and rises with rising liquid viscosity. Dependence of the cooling process time constant on the liquid temperature is influenced by two competing processes affecting convection, namely, by variations with temperature of the density and viscosity of a liquid. The effect of diminishing density becomes prevalent at temperatures of the liquid above ≈80°C. *© 2001 MAIK "Nauka/Interperiodica".*

INTRODUCTION

Quenching is one of the widely used technological procedures for imparting required mechanical properties to articles made of metal. Quenching in liquid cooling media is a very complicated process. It involves a large number of physical processes taking place in both the metal being quenched and the cooling liquid. In the metal various phase transitions can be taking place, as well as the fixation of metastable high-temperature crystal structures, microvolumetric deformations under the effect of internal micro- and macrostresses, and so on. For liquids typical processes are the phase transitions from liquid to steam state (boiling) and vice versa, chemical decomposition of organic components, and well-developed convective flows. During quenching, the cooling liquid becomes inhomogeneous and the temperature distribution becomes involved; locally, the liquid represents a two-phase system, namely, liquid/steam or liquid/gaseous decomposition products (quenching in organic oils). The liquid boiling can be of different types: bubble and film boiling or in the form of fronts of changing boil types moving along the surface of the item being quenched. The picture is further complicated by the fact that the articles to be quenched nearly always have a complex form, the cooling being strongly affected by their form; moreover, the same article will cool differently depending on the orientation, in which it is immersed in the liquid.

The complete study of such complex interrelated processes poses problems, to say the least, and is often practically impossible. In these circumstances it is expedient to resort to the opportunities offered by model investigations, in which a particular factor can be isolated and analyzed.

The present work is an experimental study of the cooling process under conditions simulating cooling of an isolated sphere in aqueous and water-polymer cooling liquids. With an article to be cooled having the form of a small sphere it is possible to ensure a maximally uniform cooling, such that the temperature gradient in the metal bulk can be neglected, and to have the various stages of the process occur one after another (film boiling, bubble boiling, and then the convective heat transfer).

EXPERIMENTAL

In this study we used a spherical polished hot probe 20 mm in diameter, with a heat-insulated stem and a central thermocouple made of nickel or an X18H9T stainless steel (Fig. 1) [1]. It can be seen that the design of the hot probe is standard except for its stem. Usually the stem is the element that causes nonuniform cooling of the hot probe because of enhanced heat dissipation from its surface (low heat conduction and large surface-to-volume ratio). In our case the surface of stem *3* is insulated from the cooling liquid *5* with a thin protective tube *4*. This simple design eliminates intensive heat dissipation by the stem surface and makes the cooling conditions of the (spherical) working part *1* of the hot

1063-7842/01/4612-1558$21.00

probe similar to those for an isolated sphere. The sphere surface was stabilized by keeping the hot probe in an oxidizing atmosphere at a temperature of 1100°C for 1 h. A chromel–alumel thermocouple with spaced junctions (*7*, *8* in Fig. 1) is used. The initial probe temperature in most experiments is 695°C.

The measurement setup scheme is also typical. The hot probe is heated in a tube heater to a temperature higher by 15°C than the initial temperature and then is positioned above the cuvette with the liquid under study. After cooling to the initial temperature of the experiment, the hot probe is lowered into the cuvette at a constant velocity of ≈50 mm/s. Variations of the hot probe temperature during cooling are registered by a KSP4 electronic recording potentiometer. The volume of the cuvette for a liquid under study is 800 ml; the liquid temperature is maintained with a fixed value by an electronic regulator with an accuracy of ±2°C. Immediately prior to measurements the magnetic stirrer maintaining uniform temperature field in the liquid is turned off and the measurements are carried out with the liquid at rest.

The simulative cooling media were distilled water, a 1% solution of sodium salt of carbomethylcellulose and dispersions of supermoistureabsorbent based on partially substituted cross-linked co-polymer of polyacrylic acid and polyacrylamide with a swelling index of 1000 g/g [2, 3] in various concentrations. The choice of these media is based on the following considerations. Carbomethylcellulose, as well as polyacrylic acid, their salts and co-polymers, are widely used as thickeners for water-polymer quenching liquids [4]. The use for thickeners of supermoistureabsorbents, sparsely linked copolymers (gels) of polyacrylic acid with a swelling index of up to 6000 g of water per 1 g of polymer, in the form of aqueous gel dispersions, makes it possible to lower the polymer concentration by more than an order of magnitude, down to 0.01% [5]. Advantages of the lower polymer concentrations in a quenching liquid are obvious and need not be explained. For quenching, an aqueous dispersion of ground gel with particle sizes in the swelled condition of a few millimeters or less is used. A large volume of such a dispersion has rheological properties similar to those of a viscous-flowing liquid; its viscosity is higher than that of a solution of a linear polymer of the same concentration by a factor of 10–100.

RESULTS AND DISCUSSION

Before presenting the measurement results we would like to consider qualitatively the process of cooling of the hot probe with a heat-insulated stem. If the bath temperature is higher than 10–15°C, then, as soon as the hot probe is immersed in the liquid, a steam layer of a thickness of about 1 mm forms around its spherical working part (in cold water, the formation of a stable steam layer does not take place). No contact between the liquid and the sphere takes place during immersion.

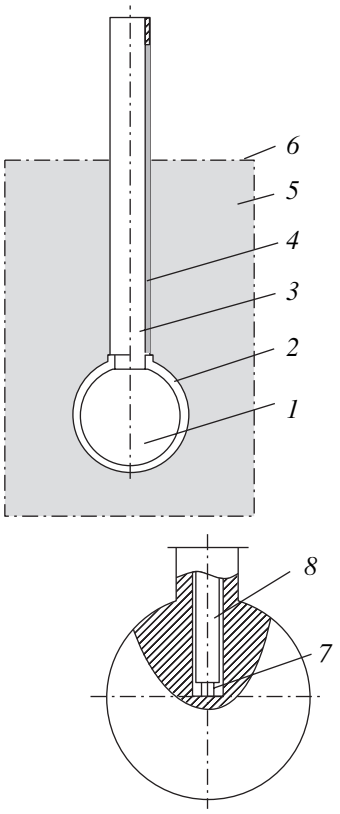

Fig. 1. Schematic of the hot probe: *1*—(spherical) working portion; *2*—spherical steam layer, surrounding the hot probe in the film boiling stage; *3*—stem of the hot probe; *4*—heat-insulating tube protecting from contacting the cooling liquid; *5*—cooling liquid; *6*—free surface of the liquid; *7*—electrode of the thermocouple; and *8*—ceramic tube.

Because the heat capacity of the heat-insulating tube protecting the stem from contacting the liquid and from cooling is low, its temperature drops significantly already during subcooling of the hot probe performed before starting the experiment. Therefore after immersion of the sphere the liquid contacts the heat insulation of the stem isolating the spherical steam layer from the atmosphere and no steam loss occurs. At water temperature above 40°C the steam layer is stable enough (life time more than 10 s), at the steam surface waves can be seen with naked eye. Destruction of the steam layer as a result of the hot probe cooling occurs explosively, practically simultaneously over the entire sphere surface, and is accompanied with a loud popping sound (a short intermediate stage is observed only under cooling in water at a temperature close to the boiling point or in solutions with a high concentration of polymer). Such a behavior is an evidence of the high uniformity of the cooling process. There is no intermediate stage between film and bubble boiling regimes. Duration of the bubble boiling stage is short, not exceeding a few seconds. Transition from the bubble boiling to convective heat exchange is slightly veiled, and for some time

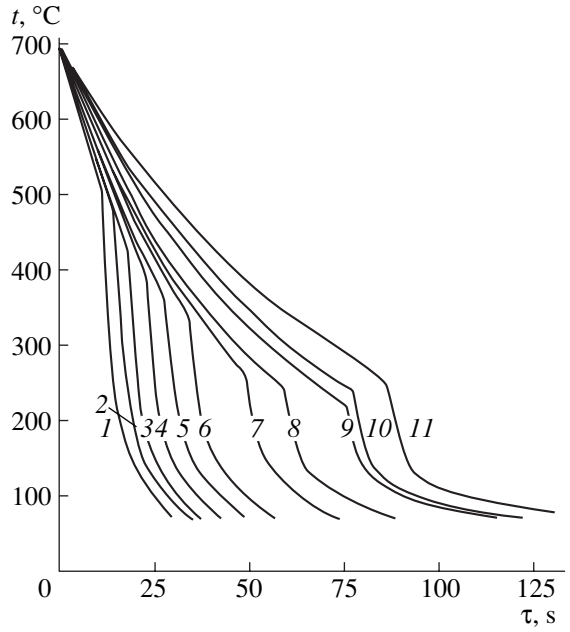

Fig. 2. Cooling curves of a hot probe for cooling in dispersions of supermoistureabsorbent of different concentrations at a temperature of 20 ± 0.2°C. Polymer concentrations in percent: *1*—0.1; *2*—0.08; *3*—0.07; *4*—0.06; *5*—0.05; *6*—0.045; *7*—0.04; *8*—0.035; *9*—0.03; *10*—0.025; *11*—0.02.

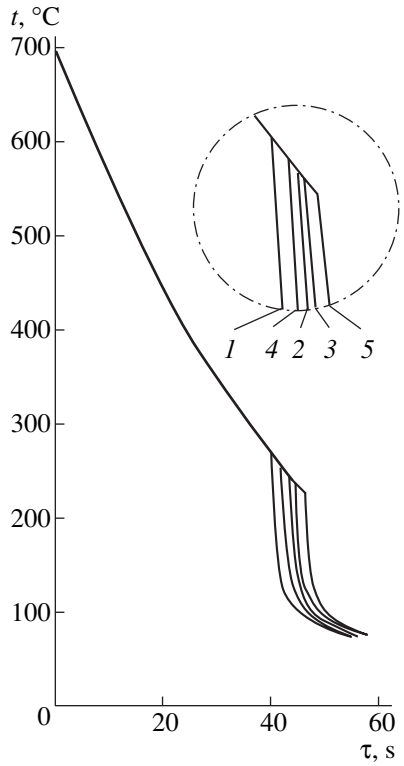

Fig. 3. Reproducibility of the cooling curves for distilled water at a temperature of 60 ± 0.1°C. Figures by the curves represent experiment numbers.

(1–2 s) regions of different cooling stages can exist on the hot probe surface. This is caused by different cooling conditions in the lower half of the sphere, which is washed by the upward flow of cool liquid, and in the upper half, which is washed by a slightly warmer liquid.

Examples of the hot probe cooling curves with dispersions of supermoistureabsorbent in distilled water at a nominal bath temperature of $t_0 = 20 \pm 0.2$°C with different polymer content are given in Fig. 2. Note the characteristic feature of the cooling curves: they have a kink corresponding to the explosive transition from film to bubble boiling. The only exception is curve *11* for a dispersion with maximum gel concentration, where the quantity of water in the space outside the particles is minimal, practically all water being bound by the gel particles. The slight spread of the kink is explained by the delayed temperature reading from thermocouple because of the temperature difference between the surface and the center of the spherical part. Figure 3 illustrates reproducibility of the cooling process in distilled water for a series of experiments at a bath temperature of $t_0 = 65 \pm 1$°C. It can be seen that the reproducibility of cooling curves in the film boiling stage is rather high, with some curves nearly coinciding. By shifting the curves along time axis regions of the bubble boiling and convective heat exchange can be aligned. Most of the scatter of the measurement results comes from the slightly stochastic nature of the transition from film to bubble boiling. Irreproducibility of the transition time is due to the whole complex of neglected experimental factors, the main factors being the state of the oxide film on the hot probe surface and concentration of gases dissolved in the water. This irreproducibility is fairly small; scatter in duration of the film boiling is usually within ±10%. Raising the bath temperature t_0 makes the cooling slower; the initial cooling rate in water in the region of film boiling drops by about half as t_0 is increased from 25 to 97°C. At the same time total cooling time of the hot probe from an initial temperature of 695 to 200°C rises by a factor of nearly 16, which is an evidence of the dominant role at high water temperatures of the film boiling stage duration and higher stability of the steam layer.

Variation with time of the hot probe temperature in all stages of the cooling process, namely, in the film and bubble boiling and convective heat exchange, can be approximated with high accuracy by an exponential relationship with constant parameters during stages

$$t = \Delta t^i_{\text{eff}} \exp(\tau/\tau_0) + t_{\text{eff}}. \quad (1)$$

Here, t_{eff} is an effective temperature of the medium; Δt^i_{eff} has a sense of an initial effective temperature difference between the hot probe and the liquid, $\Delta t^i_{\text{eff}} = (t_i - t_{\text{eff}})$, t_i being the hot probe initial temperature; we recall that in our experiments $t_i \approx 695$°C and τ_0 is a

parameter having the dimension of time. The difference between values calculated by Eq. (1) and the measured data usually do not exceed ±2°C; only rarely the difference exceeds ±3°C, which is also within the experimental error.

The obtained curves are scanned and digitized with the WINDIG program and then approximated using ORIGIN software. In this case the fitting is carried out using both parameters of Eq. (1), i.e., t_{eff} and τ_0. Some curves have been fitted manually using only one fitting parameter t_{eff}, choosing its value in such a way as to make the dependence of $\ln[(t - t_{eff})/(t_i - t_{eff})]$ on τ a straight line. Agreement between results of manual and computer approximations is good. Excluded from processing are small portion of the cooling curve near the kink point corresponding to transition from film to bubble boiling and a temperature region 105–100°C corresponding to transition from bubble boiling to convective heat exchange, when, as mentioned above, different stages of the cooling process coexist at the hot probe surface for 1–2 s.

As mentioned above, the cooling process in any of the stages is described with sufficient accuracy by relationship (1) with constant parameters over the stage duration. This statement does not mean that the heat exchange conditions remain actually the same from the beginning till the end of any of the stages. Rather, this means that the change of the conditions is fairly small and can be studied only after considerable improvement of the measurement accuracy, enough to make the error at least an order of magnitude less than in our experiments. Such a measurement accuracy is quite difficult to achieve.

Dependences of parameter τ_0 and the effective medium temperature t_{eff} on the nominal bath temperature t_0 for distilled water in different cooling regimes—film boiling, bubble boiling and convective heat exchange—are shown in Figs. 4–6.

It can be seen that the dependence of t_{eff} on t_0 for all cooling stages has a qualitatively similar character and represents a monotonically increasing function, as could be expected. A large difference is evident between t_{eff} and t_0 in the first two stages of the process; the values of these quantities come closer only at $t_0 \longrightarrow$ 100°C, i.e., as the cooling bath temperature approaches the boiling point. The equality of t_{eff} and t_0 is shown in Figs. 4–6 with dash-dot curves. The most significant difference between t_{eff} and t_0 is found in the film boiling stage under cooling in cold water.

Let us try to elucidate the physical nature of parameter t_{eff}, effective medium temperature, which is one of the two parameters in Eq. (1), and the nature of the difference between t_{eff} and t_0. For this purpose, consider schematically the temperature distribution around the hot probe for cooling, for example, in the film boiling stage (Fig. 7). It is natural to assume that the temperature at the steam–liquid interface is practically independent of the liquid temperature away from the hot probe (bath temperature t_0). It should be close to the boiling point, or, to be precise, to the maximum water overheating temperature t^*. The nominal liquid temperature in the bath controls the temperature lowering in the direction away from the steam layer surface. In the absence of convection the temperature lowering at some fixed moments of time can be tentatively represented by

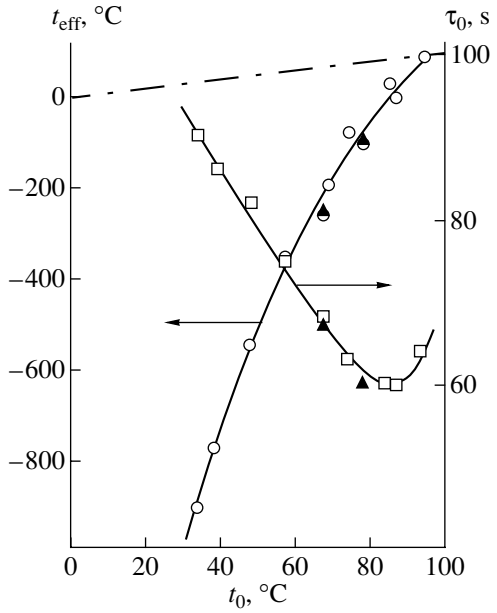

Fig. 4. Dependences of t_{eff} and τ_0 on the bath temperature t_0 for distilled water in the film boiling stage. Triangles—parameters calculated by cooling curves for a stainless steel probe. Dash-dot curve corresponds to equality of the effective and nominal bath temperatures.

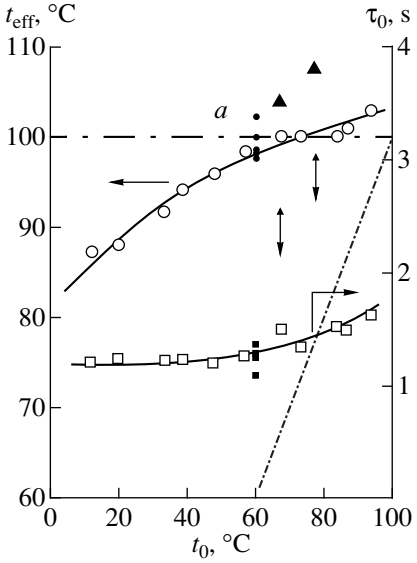

Fig. 5. Same as in Fig. 4, for the bubble boiling stage. Points and squares—parameters calculated from curves in Fig. 3. Dash-dot line *a*—water boiling point.

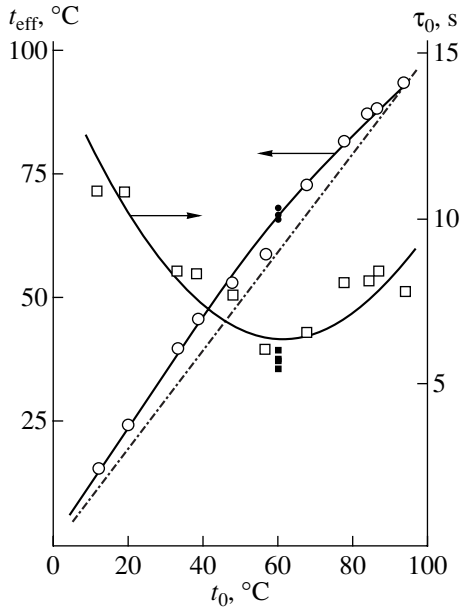

Fig. 6. Same as in Fig. 4, for the convective heat transfer stage.

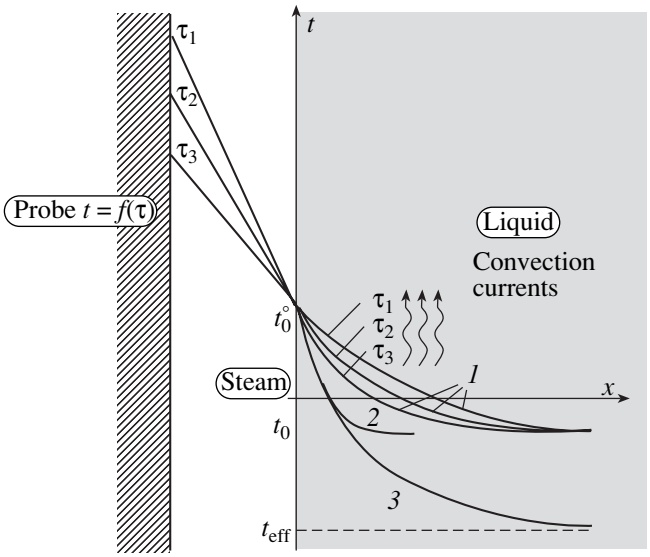

Fig. 7. Schematic temperature distribution in the zone close to the hot probe in the film boiling stage: *1*—temperature distributions without convection at successive moments of time; *2*—same with convection; *3*—temperature distribution without convection, in a medium at a temperature equal to t_{eff}.

curves *1*. Convection changes the temperature distribution, appreciably reducing the width of the zone of heated liquid (curve *2*). Of course, because of convection occurring in the form of jet flows, another effect of convection will be the emergence of nonuniform temperature distribution; but this effect will not be discussed here. It appears that in a fairly large region next to the steam layer surface curve *2* will be close to curve *3*, which is a temperature distribution in the liquid in the absence of convection but with the liquid at a temperature $t_{eff} < t_0$. So, it is reasonable to assume that the effect of the convective flows can be accounted for, in the first approximation, by introducing an effective temperature t_{eff} of the liquid. The more intensive the convection, the larger the difference should be $(t_{eff} - t_0)$. The driving force of convection is the lowering of the liquid density with rising temperature. The greater the density difference, which is uniquely related to the temperature gradient over the bulk of the liquid, the more intensive are the convective flows. Hence, the raising of liquid temperature t_0 should cause weakening of the convective flows and reduction of the difference between t_{eff} and t_0, which is observed in the experiment (Fig. 4). Extremely low values of t_{eff} at $t_0 \longrightarrow 0$°C attract attention. In this case $t_{eff} \ll 0$ K; i.e., below the absolute zero, which is an evidence of the dominant role of convection under cooling through the steam layer in cold water. The second factor determining development of the convective flows is the viscosity of the liquid. With rising temperature the viscosity of the liquid drops; so, this factor should counteract the rate of weakening of convection with rising temperature of the liquid.

For cooling under conditions of bubble boiling the temperature distribution near the probe is essentially different. The intensive movement of the steam bubbles and mixing of the liquid cause formation about the hot probe of a layer of hot liquid having a noticeably higher temperature than the nominal bath temperature. As a consequence, t_{eff} also rises (Fig. 5). For this reason in the bubble boiling regime $t_{eff} > t_0$ and at $t_0 \longrightarrow 100$°C the liquid near the hot probe is overheated and $t_{eff} > 100$°C. High values of t_{eff} do not signify that the role of convection in this stage is negligible. It should be emphasized once again that the actual temperature in the heated zone near the hot probe is higher than the effective temperature but the excess is not as high as in the film boiling stage. The water overheating above the boiling point near the hot probe in the bubble boiling regime can be observed directly using a thermocouple.

In the regime of convective heat exchange, as could be expected, the temperature in the area around the hot probe overheated in the previous stage drops down, t_{eff} diminishes, and over the entire temperature range exceeds the nominal bath temperature only by a few degrees (Fig. 6).

The second parameter in Eq. (1), τ_0, which has a dimension of time, is a time constant of the heat exchange process, and is directly related to the heat transfer coefficient of a sphere of small radius (the temperature difference over the sphere radius can be neglected) in accordance with the following equation [6]

$$\tau_0 = \frac{\rho c R}{3\alpha},$$

where α is the heat transfer coefficient, ρ is the material density, c is the specific heat, and R is the sphere radius.

As was already mentioned, in the zeroth-order approximation τ_0 and, correspondingly, the heat transfer coefficient in each regime can be considered as having some characteristic value which changes only weakly when t_0 is changed (Figs. 4–6). For the film boiling stage the characteristic values are in the range $\tau_0 = 60$–90 s and with rising t_0 the characteristic time of the process $\tau_0(t_0)$ first diminishes and then, near the water boiling point, has a slight minimum. These high values of τ_0 are explained by the relatively low rate of heat transfer through the steam layer. The decrease in τ_0 indicates that with increasing bath temperature the heat transfer coefficient becomes greater. This does not mean that the cooling rate is rising with the bath temperature. The increase in the heat transfer coefficient is by far overridden by the decrease in the effective temperature difference between the object and the cooling liquid. Presumably, the reason for this behavior of τ_0 is the decrease in the viscosity of water with temperature causing intensification of the convective flows. On the other hand, at higher water temperatures the maximum possible density differences of nonuniformly heated volumes are less. The experiment indicates that at temperatures below 80°C the overall effect is in favor of "viscosity" because the density of water has a relatively weak dependence on temperature. Analysis shows that the temperature dependence of τ_0 in the range of low temperatures follows the usual exponential relationship; estimates of the apparent activation energy are about half of the value for the temperature dependence of the density of water.

As could be expected, the lowest values of τ_0 have been observed in the bubble boiling regime, where mixing is intensive. Typical values for a nickel hot probe are in a range of 1–2 s and for a hot probe of stainless steel having low heat conduction 3–4 s. Note that the dependence of measured τ_0 values on the probe material is apparent only in the bubble boiling regime. In this regime $\tau_0(t_0)$ is a weakly increasing function, corresponding to some degree to the behavior of this function in the film boiling regime at high bath temperatures, $t_0 > 70$°C, because in the bubble boiling regime t_{eff} is also high, exceeding 80°C.

For cooling in the regime of the convective heat transfer typical values of τ_0 are intermediate, being equal to 6–11 s. Qualitatively, the dependence of τ_0 on t_0 shows the same behavior as in the stage of film boiling, with the relative growth of τ_0 starting at $t_0 > 70$°C.

The above data suggest the following *a priori* conclusions about the effect of thickeners added to water on the cooling curve parameters. From general considerations it is clear that any additive that increases viscosity and suppresses convective flows will cause localization of the heat transfer process and growth of local temperatures near the solid being cooled. This should lead among other things to higher t_{eff} values. It is also known that the thickening additives form two classes, solutions and dispersions. The main distinction of a dispersion is the availability in the space between disperse particles of pure water, which has low viscosity and is capable of transferring heat by convection.

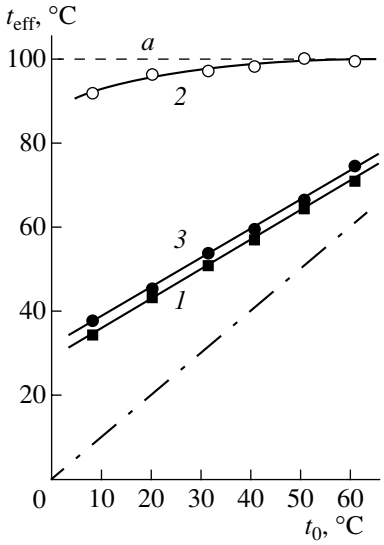

Fig. 8. Dependence of t_{eff} on the bath temperature t_0 for cooling in a 1%-solution of carbomethylcellulose: *1*—film boiling; *2*—bubble boiling; *3*—convective heat transfer. Dash-dot curve corresponds to equality of the effective and nominal bath temperatures. Dash line *a*—water boiling point.

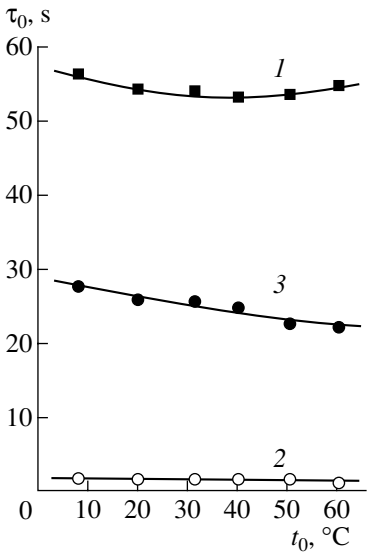

Fig. 9. Dependence of τ_0 on the bath temperature t_0 for cooling in a 1%-solution of carbomethylcellulose: *1*— film boiling; *2*—bubble boiling; *3*—convective heat transfer.

We studied the effect of an added linear polymer on parameters of the cooling curve for the case of 1%-solution of sodium salt of carbomethylcellulose

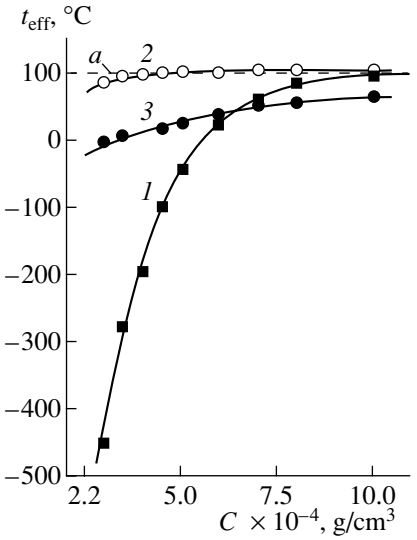

Fig. 10. Dependence of t_{eff} on *C*-concentration of polymer for aqueous dispersions of supermoistureabsorbent: *1*—film boiling; *2*—bubble boiling; *3*—convective heat transfer. Dash line *a*—water boiling point.

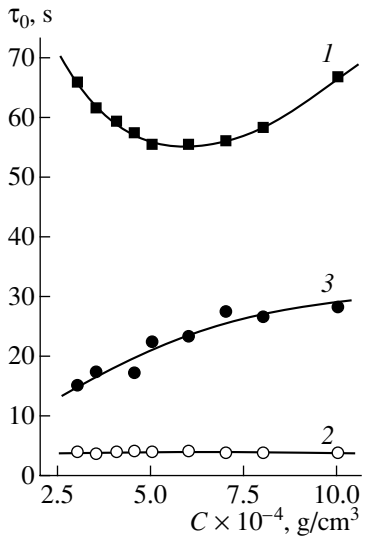

Fig. 11. Dependence of τ_0 on *C*-concentration for aqueous dispersions of supermoistureabsorbent: *1*—film boiling; *2*—bubble boiling; *3*—convective heat transfer.

(Figs. 8, 9). It can be seen (Fig. 8) that in this case for all cooling regimes $t_{eff} > t_0$, as expected. For the film boiling and convective heat transfer dependences of the effective temperature on bath temperature are practically straight lines. With increasing t_0 they tend to the boiling point of water and approach the straight line $t_{eff} = t_0$. In the bubble boiling regime $t_{eff} > 90$°C and weakly varies from t_0. This indicates a localized highly heated region, whose temperature does not depend on the nominal temperature of the cooling bath. Variation of τ_0 with t_0 is weak in all regimes (Fig. 9). In the film boiling a slight minimum in τ_0 is observed at 40–45°C. It corresponds to $t_{eff} \geq 60$°C, which is somewhat lower than in the case of distilled water (80°C). Absolute values of τ_0 are close to those observed for water at high bath temperatures, though lower by 5–6 s. This rather unexpected result is, evidently, related to the specific effect of the polymer additive on the characteristics of the steam layer surrounding the hot probe, due to which the higher viscosity of the liquid did not cause an increase in the thickness of the steam layer and growth of τ_0. Elucidation of the relation of this effect to physical characteristics of the solution requires a separate study. It is possible that a certain role can be played by different character of convective jet flows near walls of the spherical steam layer and lower turbulence in microscopic regions. It is remarkable that the growth of viscosity of the liquid did not cause any increase in τ_0 in the bubble boiling regime: $\tau_0 = 1.2$–1.5 s. The reason is probably the same as the noted above decrease in τ_0 in the film boiling regime and related to different conditions at the boundary of the steam layer. Also, in the convective heat transfer regime an almost two-fold increase of τ_0 is observed compared with values typical for pure water, which appears to be a natural consequence of the higher viscosity. With rising temperature τ_0 is decreasing as a consequence of the lowering of solution viscosity with temperature.

Consider now the effect on the cooling curve parameters of additions of supermoistureabsorbent in different concentrations (Figs. 10, 11). It is seen in these figures that increasing the polymer concentration causes changes in the cooling curve parameters similar to those resulting from changes brought about by raising the cooling bath temperature (cf. Figs. 10 and 4–6), which can be explained by gradual localization of the cooling process and by growth of the heated zone temperature near the hot probe. In the film boiling regime the time constant τ_0 is close to values typical of water at moderate temperatures, 55–65 s. It could be expected that at low concentrations of the polymer additive and a bath temperature of about 20°C, when the effective temperatures are very low, $t_{eff} < -200$°C, larger values of the time constant, $\tau_0 > 70$ s, characteristic of cooling in cold water will be observed. The possible reason for the difference in τ_0 may be the effect of polymer destruction products on the surface tension at the liquid–steam interface. Under convective heat transfer τ_0 values are close to the values for the linear polymer solution and increase with the concentration of the polymer additive. This means that the viscosity increase with concentration overrides the lowering of viscosity caused by the local temperature rise and, correspondingly, t_{eff}, because of gradual localization of the cooling process.

CONCLUSION

The data presented demonstrate the fruitfulness of the adopted simulation approach to the study of the cooling process. It has been shown that the cooling process at any stage can be described by a simple exponential relationship with two parameters. Such a relationship is characteristic of the heat transfer under conditions of convection [5]. It is essential that, with the accuracy of fitting the experimental data of ±3°C, the equation parameters can be considered constant over a stage. The first parameter has a dimension of time and is uniquely related to the heat transfer coefficient. The second parameter has a dimension of temperature and its physical meaning is that of the effective temperature of the cooling bath. Due to convection, the effective (apparent) temperature of the cooling bath is lower than the actual temperature of the liquid near the object being cooled. An especially large difference is observed in the film boiling stage, prior to formation of the zone of heated liquid. The intensive build up of this zone takes place in the bubble boiling stage.

When cooling proceeds under conditions of hardening of articles of complex shape, an important factor determining the course of the entire cooling process is the process inhomogeneity, i.e., coexistence at different regions of the surface of different stages: film boiling, bubble boiling, and convective heat transfer. It is natural to think that this general case can be considered in the first approximation as a sum of contributions from individual processes with weighting coefficients equal to a fraction of the surface, on which a process is dominant (not taking into account the fact that the temperature is nonuniform over the metal bulk).

To conclude, we note that on the basis of the performed experiments we were able to suggest an effective scheme for quantitative description of the cooling curves. Regrettably, no criterion could be found for transition from film to bubble boiling, the search being aggravated by the dependence of the temperature of this transition on many factors difficult to control. One of the most important among them is the state of the surface of the article being cooled, in particular, the thickness and fine structure of the oxide film. It is found that an increase of the film thickness makes the stability of film boiling lower and raises the break-up temperature.

REFERENCES

1. É. L. Aéro, V. S. Anisimov, V. I. Aleshin, and E. L. Gyulikhandanov, RF Patent No. 2039092 (1990), Byull. Izobret., No. 19 (1995).
2. A. L. Buyanov, L. G. Revel'skaya, and G. A. Petropavlovskiĭ, Zh. Prikl. Khim. (Leningrad) **62**, 1854 (1989).
3. A. L. Buyanov, L. G. Revel'skaya, and G. A. Petropavlovskiĭ, Zh. Prikl. Khim. (St. Petersburg) **65**, 181 (1992).
4. V. M. Ezhov, *Hardening Media for Heat Treatment of Metals. Technology, Industrial Organization and Management* (NIIÉ Informénergomash, Moscow, 1983).
5. A. L. Buyanov, L. G. Revel'skaya, V. S. Anisimov, *et al.*, RF Patent No. 1826527 (1992).
6. *Heat and Mass Exchange. Thermotechnical Experiment: Handbook*, Ed. by V. A. Grigor'ev and V. M. Zorin (Énergoizdat, Moscow, 1982).

Translated by B. Kalinin

Technical Physics, Vol. 46, No. 12, 2001, pp. 1566–1569. Translated from Zhurnal Tekhnicheskoĭ Fiziki, Vol. 71, No. 12, 2001, pp. 79–82.

EXPERIMENTAL INSTRUMENTS AND TECHNIQUES

The Stability of Mott Polarization Analyzers

V. N. Petrov, M. S. Galaktionov, and A. S. Kamochkin

St. Petersburg State Technical University, ul. Politekhnicheskaya 29, St. Petersburg, 195251 Russia

e-mail:galaktionov@tuexph.stu.neva.ru

Received April 9, 2001

Abstract—The stability of Mott conventional spherically symmetric and retarding-potential conical polarimeters are compared for the case when the position of the electron beam at their inputs is changed. The primary electron energies are 500 and 1600 eV. When the electron beam is shifted by 0.6 mm, the count rate of the former polarimeter remains unchanged, while for the latter, it changes by ≈7 and ≈18% for the energies 1600 and 500 eV, respectively. This instability may cause errors in measuring the degree of polarization of the electron beam. © *2001 MAIK "Nauka/Interperiodica".*

INTRODUCTION

Currently, the spin polarization of an electron beam is usually measured by sputtering high-energy electrons by gold films [1, 2]. In Mott polarimeters, the electron beam is accelerated to energies of 20–120 keV and the electrons sputtered are recorded with two (or four) detectors arranged at an angle of 120° to each other symmetrically about the beam. Because of the interaction of the electron spin with its orbital moment, the effective cross section of the interaction for the electrons with opposite spins is different. In other words, the spin-orbital interaction causes left–right asymmetry of scattering A_{LR}, which can be defined as the normalized difference between the signals of the left, N_L, and the right, N_R, detectors:

$$A_{LR} = (N_L - N_R)/(N_L + N_R). \quad (1)$$

Then, the beam polarization is given by the ratio

$$P_0 = A_{LR}/S_{\text{eff}}, \quad (2)$$

where S_{eff} is the effective Sherman function, i.e., the asymmetry that should be observed at 100% polarization of the electrons.

There are two types of high-voltage Mott electron polarization analyzers.

(1) A conventional Mott detector [3, 4] represents a linear accelerating column and a scattering chamber. The latter is under a high potential and includes the target and two (or four) silicon surface-barrier (SSB) or passivated implanted planar silicon (PIPS) detectors. When moving in the drift space, the electrons scattered are recorded and energy-selected by the detectors.

Another version of conventional polarimeters is a spherically symmetric field-free device [5, 6]. Here, the beam is accelerated between the spheres and the electrons scattered also move in the drift space and are energy-selected with SSB or PIPS detectors.

(2) Retarding-potential polarimeters [7–9]. The name of these devices reflects the essence of the method by which the electrons are selected by energy. When moving in a decelerating field, the particles scattered by a gold foil are recorded by electron multipliers or by microchannel plates that are under a near-ground potential.

At present, when interest in experiments on spin-polarized electron spectroscopy has significantly increased, there is no agreement among researchers regarding the advantages and disadvantages of one or the other type of the polarimeters. Such parameters of spin analyzers as efficiency, dimensions, design simplicity, cost, etc. are compared. Unfortunately, one more basic point, namely, the sensitivity of the count rate and the symmetry to a change in the electron beam position on the Au foil, as well as to changes in its diameter and density, is usually overlooked. It is however known that the position and the form of the beam do not remain constant during experiments, which may lead to false asymmetry (A_{LR}). For example, upon studying the magnetic properties of materials, it is often necessary to reverse the magnetization in opposite directions, which distorts the trajectories of both primary (if the excitation is due to electrons) and secondary beams. Next, the magnetization of the targets may change during temperature measurements, which also affects the electron trajectories. Moreover, if before entering a Mott detector, the electron beam passes through any energy analyzer, it may leave the analyzer at different angles and its density in the cross section will depend on its energy.

Note that the count rate stability is of primary importance in this case although the asymmetry is a normalized quantity. It may appear at first glance that a change in the count rate due to a change in the primary beam parameters will be compensated for if formula (1) is used to calculate the asymmetry of scattering. In practice, however, this is not always the case, since con-

1063-7842/01/4612-1566$21.00

Characteristics of the Mott polarimeters of two types

Parameters	Conventional spherically symmetric polarimeter	Retarding-potential conical polarimeter
Efficiency	2.5×10^{-4}	4.5×10^{-5}
Dimensions	450×250 mm Independent vacuum system. No high-voltage feedthrough required	135×100 mm It is necessary to place it inside the vacuum system or use a separate vacuum chamber. High-voltage feedthrough required
Maximal count rate	10^6 count/s at a detection efficiency of 80%. 4×10^5 count/s at a detection efficiency of 100%	5×10^4 count/s
Self-calibration capability (rather conditional)	By extrapolating to high discrimination level [10]	By extrapolating to the zero energy losses [13]

ditions for electron scattering into different detectors may change because of the uncontrollable variations in the angle of incidence onto the gold foil or because sites of beam–foil interaction alter.

Yet, the sensitivity of various Mott polarimeters to a shift of the electron beam on the target, as well as to the variation of its diameter and density, has not been explored.

In this work, we studied the count rate of two Mott detectors operating under identical conditions as a function of the beam shift at their entrance.

MOTT DETECTOR DESIGN

We have developed and studied two Mott polarimeters—conventional spherically symmetric and retarding-potential conical devices, which are currently used in basic research [10–12]. The table lists a number of their operating parameters that are the most important for the users.

Figure 1 shows the design of a spherically symmetric field-free polarimeter. Its basic components are two metallic polished semispheres with the center in common. The outer semisphere is under the ground or a near-ground potential. The inner one is under a potential of 60 kV. It is fixed by two series-connected cylindrical ceramic insulators that can withstand a voltage of ≈80 kV. An electron beam whose polarization is to be determined is directed to the intersphere region through a circular diaphragm. Then, being accelerated by the strong spherical field, it enters the inner sphere, inside which four large-area silicon detectors, an Au target, and guiding diaphragms are arranged. The scatterer is a 800-Å-thick Au layer deposited on a free thin Formvar (polyvinyl formal resin) film. The scattered electrons pass through holes in the diaphragms and are recorded by the detectors.

In this polarimeter, electron selection by energy is performed with the PIPS detectors. The pulse amplitude at their output is proportional to the electron energy. Once the pulses have been appropriately amplified and discriminated, their repetition rate can be assumed to be proportional to the number of elastically scattered electrons. For the PIPS detectors equipped with special charge-sensitive amplifiers, the energy resolution is ≈10 keV. To decrease the input capacitance, the spacing between the detectors and the amplifiers was minimized. The amplifiers are mounted in a specially designed cylindrical case and placed inside the polarimeter. The electrical feedthrough is in the vicinity of the detectors. The amplifiers are under an operating potential as high as ≈60 kV. For further processing, the signals are transferred to the input of driver amplifiers, which are under the ground potential, via a fiberoptic system. The amplifiers are fed with a specially designed 70-kV power supply measuring $300 \times 200 \times 150$ mm.

The design of a retarding-potential conical polarimeter is depicted in Fig. 2. The basic components of the analyzer are two metallic hollow polished truncated cones. The outer cone is under the ground potential, and the inner one is under a potential of 30 kV. The electron beam passes through a diaphragm with a circular hole, is accelerated by the strong field, and enters the region

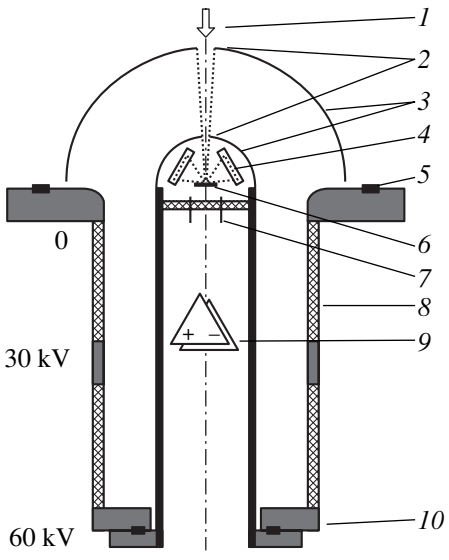

Fig. 1. Conventional spherically symmetric polarimeter: *1*, electron bean; *2*, input windows; *3*, semispheres; *4*, four PIPS detectors; *5*, CF-200 flange; *6*, gold foil; *7*, vacuum feedthrough; *8*, ceramic insulator; *9*, four amplifiers; and *10*, CF-63 flange.

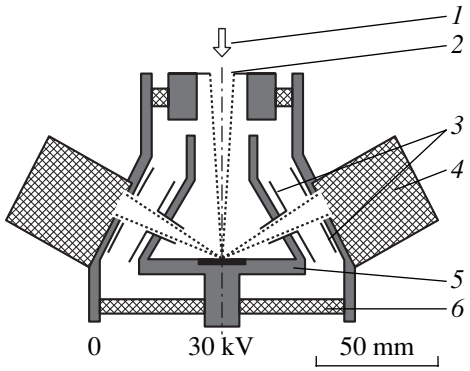

Fig. 2. Retarding-potential conical polarimeter: *1*, electron beam; *2*, input window; *3*, diaphragms; *4*, four channel electron multipliers; *5*, gold foil; and *6*, insulator.

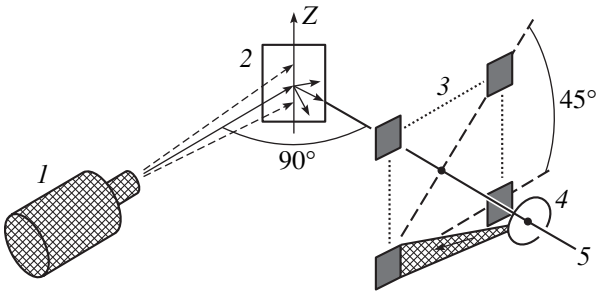

Fig. 3. Experimental scheme: *1*, electron gun; *2*, sample; *3*, detectors; *4*, gold foil; and *5*, polarimeter axis.

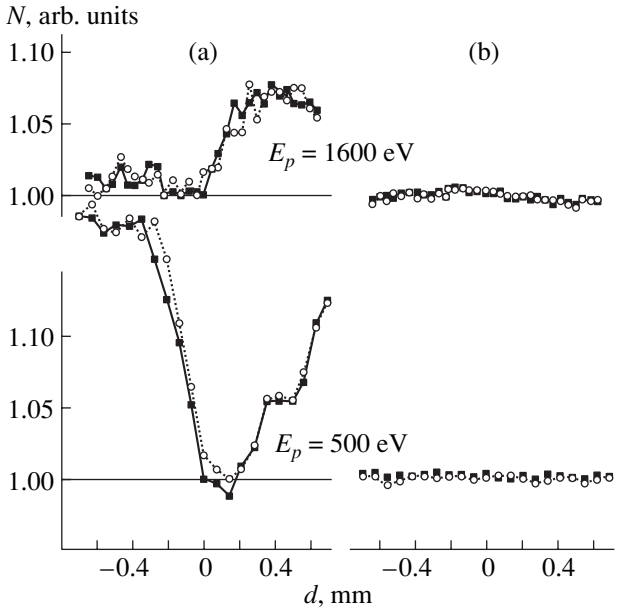

Fig. 4. Normalized count rate vs. electron beam shift *d* relative to the Mott polarimeter axis (the *Z* axis in Fig. 3) for energies of 1600 and 500 eV. (a) Retarding-potential polarimeter and (b) conventional polarimeter.

bounded by the smaller cone. A 100-μm-thick gold foil is placed inside the cone. Electrons scattered by the foil through an angle of ±120° leave the inner cone through symmetrically arranged diaphragms and fall into the decelerating electric field. Here, the scattered electrons slow down and those having lost a small amount of energy due to inelastic collisions pass through diaphragms located on the inner surface of the large cone and detected by channel electron multipliers. In our case, the range of energy losses ΔE due to inelastic collisions was 300 eV. The amplifiers were under the ground potential.

RESULTS AND DISCUSSION

The stability of the devices was checked with an experimental scheme shown in Fig. 3. The scattering geometry was typical of real experiments on spin-polarized electron spectroscopy. The excitation was carried out with an electron gun 60 mm distant from the Al sample. Polycrystalline Al was employed in order to exclude undesired effects associated with spin–orbital interaction and crystallographic ordering of the sample. Electrons scattered through 90° were detected by the Mott polarimeter. The experiments were performed with the devices of both types: first with one device and then with the other (the positions of the devices were the same). The polarimeters were placed in such a way that their input conditions were identical. When comparing their performance, we did not use any electron optics at the input. In both experiments, the potentials across the input elements were equal to zero. The energy selection of the Al-scattered electrons was absent. The arrangement of the polarimeters was such that the plane of second scattering (by the Au foil) made an angle of 45° with that of the initial scattering (by the Al sample).

The electron beam was scanned perpendicularly to the plane of initial scattering (along the *Z* axis, Fig. 3). The shift of the beam on the surface of the Al sample was ±1 mm.

The results of the experiments are shown in Fig. 4. Squares and circles correspond to the opposite scan directions. The results for the normalized count rates at primary beam energies of 500 and 1600 eV are presented, since they are the most typical. Similar measurements were made for many other energies. It is seen that, as the primary electron beam shifts by 0.6 mm, the count rate of the conventional spherical polarimeter remains fairly stable, while that of the retarding-potential device changes by ≈18 and ≈7% for the energies 500 and 1600 eV, respectively. It is also seen that the curves run in a different way. The curve corresponding to 500 eV is symmetric about the zero shift, while that corresponding to 1600 eV is asymmetric. It is not the goal of this work to comprehensively analyze the behavior of these dependences. We try merely to find an explanation for the low sensitivity of the conventional spherically symmetric polarimeter to the shift of the

electron beam at its input compared with the retarding-potential device.

In our opinion, the basic reasons for this difference are as follows (in order of increasing significance).

(1) The presence of a retarding potential may considerably affect the trajectories of electrons scattered by the Au foil, which is not the case in the conventional polarimeter, where the electrons scattered move in the drift space.

(2) The spherical accelerating field in a free-field polarimeter focuses the electron beam on the Au foil well unlike the analyzer of the other type.

Thus, when designing an experimental spin analyzer, one must be guided not only by such parameters as efficiency, dimensions, or design simplicity. It should also be taken into account that the count rate and, consequently, the asymmetry of scattering may sometimes change when the electron beam shifts at the input or when its diameter or density changes. Obviously, the electron beam polarization measured will be in error in this case.

REFERENCES

1. N. F. Mott, Proc. R. Soc. London **124**, 425 (1929).
2. J. Kessler, *Polarized Electrons* (Springer-Verlag, New York, 1985).
3. D. E. Nelson and R. W. Pidd, Phys. Rev. **114**, 728 (1959).
4. M. Kalisvaart, M. R. O'Neill, T. W. Riddle, *et al.*, Phys. Rev. B **17**, 1570 (1978).
5. M. Landolt, R. Allenspach, and D. Mauri, J. Appl. Phys. **57**, 3626 (1985).
6. M. Getzlaff, J. Bansmann, and G. Schönhense, J. Magn. Magn. Mater. **131**, 304 (1994).
7. L. G. Gray, M. W. Hart, F. B. Dunning, *et al.*, Rev. Sci. Instrum. **55**, 88 (1984).
8. F. B. Dunning, L. G. Gray, J. M. Ratliff, *et al.*, Rev. Sci. Instrum. **58**, 1706 (1987).
9. S. Qiao, A. Kimura, A. Harasawa, *et al.*, Rev. Sci. Instrum. **68**, 4390 (1997).
10. V. N. Petrov, M. Landolt, M. S. Galaktionov, *et al.*, Rev. Sci. Instrum. **68**, 4385 (1997).
11. Yu. Yashin, Yu. Mamaev, and A. Ambrazhei, in *Proceedings of the Low Energy Polarized Electron Workshop, 1998*, p. 27.
12. C. Stamm, F. Marty, A. Vaterlaus, *et al.*, Science **282**, 449 (1998).
13. T. J. Gay, M. A. Khakoo, F. B. Dunning, *et al.*, Rev. Sci. Instrum. **63**, 114 (1992).

Translated by V. Isaakyan

Technical Physics, Vol. 46, No. 12, 2001, p. 1570. Translated from Zhurnal Tekhnicheskoĭ Fiziki, Vol. 71, No. 12, 2001, p. 83.

BRIEF COMMUNICATIONS

On the Length of a Discontinuity in an Acoustically Active Medium

N. E. Molevich

Korolev State Aerospace University, Moskovskoe sh. 34, Samara, 443086 Russia

Received April 11, 2001

Abstract—The discontinuity length is found when a high-frequency gasdynamic perturbation propagates in a thermodynamically nonequilibrium gaseous medium. © *2001 MAIK "Nauka/Interperiodica".*

The gas dynamics of thermodynamically nonequilibrium media, such as vibrationally excited gas, nonisothermal plasma, chemically active mixture, etc., is presently the subject of much experimental and theoretical investigation. It is known that the second (volume) coefficient of viscosity in these media may be inverted, so that the medium becomes acoustically active [1, 2]. The acoustic activity of the media considerably changes the configuration and dynamics of propagating nonlinear waves.

The length of discontinuity L_d is one basic characteristic of nonlinear acoustics. In particular, this parameter specifies the effective length within which plane-wave approximations apply, for examples, to problems like the self-action of sound or the dissipation of acoustic waves by waves of another nature. It has been shown [2] that the discontinuity length in acoustically active media is smaller. In this work, we suggest a simple formula for L_d obtained by the method developed in [3].

Up to quantities of the second order of smallness, the propagation of high-frequency perturbations in a relaxing medium is governed by the Burgers equation with a source given by [1–3]

$$V_Y + \Psi_\infty V V_Z = \mu V_{ZZ} - \alpha_\infty u_\infty V, \qquad (1)$$

where V is a perturbation of the gasdynamic velocity in an acoustic wave (equations for the perturbations of other parameters are similar), $Z = X - u_\infty t$, $y = \Theta t$, $\Theta \ll 1$ is a quantity of the first order of smallness, X and t are coordinate and time, $\Psi_\infty = (\gamma_\infty + 1)/2$ is the hydrodynamic nonlinearity coefficient, γ_∞ is the adiabatic exponent, μ is the dissipation factor due to viscosity and heat conduction,

$$\alpha_\infty = \frac{\xi_0 C_{V0}^2}{2\rho_0 C_{V\infty}^2 u_\infty^3 \tau^2}$$

is the high-frequency dissipation factor due to relaxations with a relaxation time τ in the medium, ρ_0 is the density of the medium, C_{V0} and $C_{V\infty}$ are the equilibrium and frozen heat capacities at constant volume, u_∞ is the frozen speed of sound, and ξ_0 is the low-frequency second coefficient of viscosity. In a nonequilibrium medium, $\xi_0 < 0$ may be negative, hence, the acoustic activity of the medium; i.e., $\alpha_\infty < 0$.

With the initial perturbation represented in the form $V(y = 0, z) = V_0 \sin(\omega Z/u_\infty)$, where ω is frequency, the solution of Eq. (1) at $\mu \longrightarrow 0$ is given by

$$\frac{\omega Z}{u_\infty} = \arcsin\beta - \frac{\beta}{\alpha_\infty L_d^e}[1 - \exp(-\alpha_\infty u_\infty y)], \qquad (2)$$

where $\beta = V\exp(a_\infty u_\infty y)/V_0$ and $L_d^e = u_\infty^2/\Psi_\infty V_0 \omega$ is the well-known expression for the discontinuity length at $\alpha_\infty = 0$ [3].

It is easy to check that expression (2) is the solution of Eq. (1) for both $\alpha_\infty > 0$ and $\alpha_\infty < 0$. According to (2), the discontinuity starts forming at

$$\frac{1}{\alpha_\infty L_d^e}[1 - \exp(-\alpha_\infty u_\infty y)] \approx 1,$$

hence, the discontinuity length

$$L_d \approx -\frac{\ln(1 - \alpha_\infty L_d^2)}{\alpha_\infty}.$$

Thus, knowing the increment α_∞, one can easily find the value of L_d when the initial high-frequency gasdynamic perturbation propagates in an acoustically active medium.

REFERENCES

1. N. E. Molevich and A. N. Oraevskiĭ, Tr. Fiz. Inst. Akad. Nauk **222**, 45 (1992).
2. A. I. Osipov and A. V. Uvarov, Usp. Fiz. Nauk **162** (11), 1 (1992) [Sov. Phys. Usp. **35**, 903 (1992)].
3. R. V. Khokhlov and S. I. Soluyan, Acustica **14**, 241 (1964).

Translated by V. Isaakyan

1063-7842/01/4612-1570$21.00

Technical Physics, Vol. 46, No. 12, 2001, pp. 1571–1574. Translated from Zhurnal Tekhnicheskoĭ Fiziki, Vol. 71, No. 12, 2001, pp. 84–87.

BRIEF COMMUNICATIONS

The Effective Magnetic Permeability of a Two-Phase Fibred Ferromagnetic Composite

V. V. Bakaev*, A. A. Snarskii, and M. V. Shamonin***

** H. ROSEN Engineering GmbH, Am Seitenkanal 8, D-49811 Lingen (Ems), Germany*

*** National Technical University of Ukraine, Kiev, 03056 Ukraine*

e-mail: asnar@phys.carrier.kiev.ua

Received October 30, 2000

Abstract—The magnetic properties of a two-phase fiber composite are theoretically studied. One of the phases is a ferromagnet with a highly nonlinear field dependence of the local magnetic permeability and a negligible hysteresis loop. The dependences of the effective magnetic permeability (both along and across the fibers) on the external magnetic field and on ferromagnetic phase concentration are found. A steep rise in the effective transverse permeability is revealed near the percolation threshold. © *2001 MAIK "Nauka/Interperiodica"*.

Magnetic composites are now attracting considerable interest (see, e. g., [1–5]). This is in great part due to the fact that the potentialities offered by pure (single-phase, uniform in composition, and homogeneous) materials have been substantially exhausted. In many cases, composites acquire properties that are lacking in the initial materials. In the new-material technology, emphasis is currently on the synthesis of macroscopically inhomogeneous media with properties controllable over a wide range (see, e. g., [6]).

Inhomogeneous media are usually characterized by effective coefficients; in our case, the effective magnetic permeability is of interest. For composites with a random structure, the calculation of the effective coefficients is difficult and is possible only in certain approximations. According to the arrangement of the phases, the degree of disorder, etc., the effective coefficients may differently depend on the concentration and external fields. The nonlinearity of the local magnetic permeability, which is (by definition) an inherent characteristic of ferromagnets, presents another problem in the calculations. For example, the direct numerical simulation of a two-phase strongly inhomogeneous nonlinear medium is extremely cumbersome and is made, if possible, only by invoking the grid methods, where the inclusions are specified by the nodes of a regular mesh. Adequate methods that allow the reasonably accurate description of nonlinear composites have been developed only recently [6].

In this study, we consider a composite consisting of circular ferromagnetic filaments (first phase) embedded in a nonmagnetic matrix (second phase). Either phase is characterized by local magnetic properties. The nonlinearity of the ferromagnetic phase permeability is essential and governs the magnetic properties of the medium as a whole. The second phase is paramagnetic or diamagnetic, and its permeability can be set equal to μ_0 with a good accuracy. The effective permeability will be studied in relation to the phase concentration and the external magnetic field. The ferromagnetic phase is considered to have a nearly zero hysteresis loop (see, e.g., [4]). The model of the composite is shown in Fig. 1.

The magnetic properties of the first phase are specified by the dependences $\mu_1 = \mu_1(H)$ (Fig. 2) and

$$\mathbf{B} = \mu_1(H)\mathbf{H}. \quad (1)$$

To characterize the magnetic properties of the material as a whole, one uses the effective values, which relate (by definition) the volume-averaged magnetic field strength and induction:

$$\langle \mathbf{B} \rangle = \mu^e(\langle H \rangle)\langle \mathbf{H} \rangle, \quad (2)$$

where, even in the linear case, μ^e is a tensor whose principal axes are directed along and perpendicular to the cylindrical inclusions.

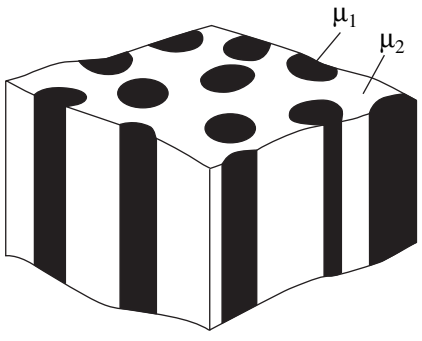

Fig. 1. Fibred two-phase magnetic composite. Fibers are of a circular section, and the circle centers are distributed randomly. The bulk concentration of the ferromagnetic phase (black areas) is *p*.

1063-7842/01/4612-1571$21.00 © 2001 MAIK "Nauka/Interperiodica"

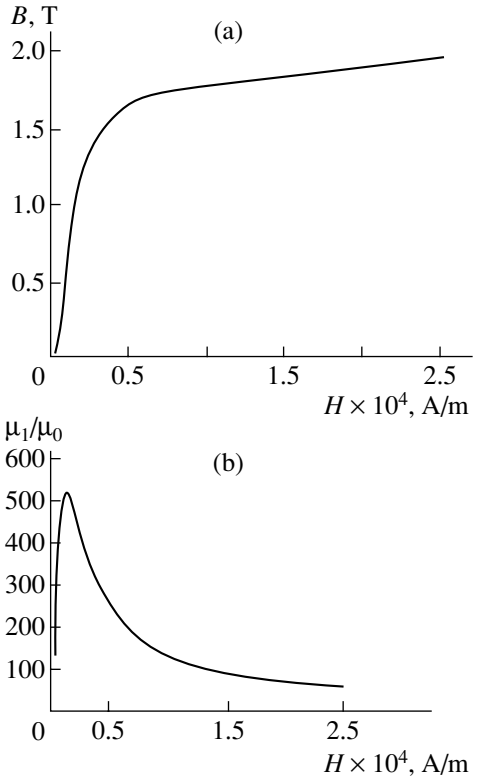

Fig. 2. (a) Magnetic behavior $B = \mu_1(H)H$ and (b) the local permeability of the ferromagnetic phase.

In the principal axes, this tensor is diagonal and has the longitudinal component $\mu_{\parallel}^{e}$ "along" and two equal transverse components $\mu_{\perp}^{e}$ "perpendicular" to the inclusions. In what follows, we will consider the parallel and perpendicular relative orientations of $\langle \mathbf{H} \rangle$ and ferromagnetic fibers.

The composite is assumed to be macroscopically inhomogeneous with the coordinate-dependent local permeability $\mu = \mu(\mathbf{r})$. In our case of the two-phase medium, $\mu(\mathbf{r}) = \mu_1(H(\mathbf{r}))$ in the ferromagnetic phase and $\mu = \mu_2$ in the nonmagnetic one. We also assume that the composite is sufficiently large, so that any randomly occurred parallel arrangement of the ferromagnetic fibers can be considered as the self-averaging of the material properties [7]; in other words, the effective properties of different realizations are indistinguishable. Finally, we restrict our analysis to the stationary case; i.e., we assume that $\mathbf{B}(\mathbf{r})$ and $\mathbf{H}(\mathbf{r})$ obey the Maxwell equations in the form

$$\mathrm{div}\mathbf{B} = 0, \quad \mathrm{curl}\mathbf{H} = 0. \tag{3}$$

The calculation of the longitudinal component $\mu_{\parallel}^{e}$ presents no difficulties. Under the assumption that $\langle H \rangle$ is parallel to the fibers, Eq. (3) gives for the local magnetic field $H_{\parallel 1} = H_{\parallel 2}$; that is, the local magnetic field strength in both phases equals $\langle H \rangle_{\parallel}$. Using this circumstance, one can average the local relation

$$B_{\parallel}(\mathbf{r}) = \mu(\mathbf{r}, H_{\parallel})H_{\parallel} \tag{4}$$

over the volume:

$$\begin{aligned} \langle B_{\parallel} \rangle &= \langle \mu(H_{\parallel})H_{\parallel} \rangle \\ &= (p\mu_1(\langle H_{\parallel} \rangle) + (1-p)\mu_2)\langle H_{\parallel} \rangle, \end{aligned} \tag{5}$$

where p is the concentration of the ferromagnetic phase.

Equation (5) immediately yields the expression for the effective permeability along the fibers:

$$\mu_{\parallel}^{e}(\langle H \rangle) = p\mu_1(\langle H \rangle) + (1-p)\mu_2. \tag{6}$$

The determination of the transverse component is reduced to solving the two-dimensional problem with randomly distributed circular inclusions. For the linear case, such a problem in terms of dielectric permittivity was posed by Maxwell [6, 8] and solved in the approximation of solitary inclusions. In this approximation, the concentration of the inclusions, for instance, of the first phase, is assumed to be so small that they do not interact with each other [9]. It is evident that, in real composites, this approximation generally fails. The interaction between the inclusions in the linear case is best accounted for by the Bruggeman–Landauer (BL) approximation of self-consistent field [8, 10]. This approximation does well for not too high inhomogeneities in the entire range of concentrations except for the vicinity of the percolation threshold (at high inhomogeneities), where the methods of percolation theory should be applied. It is worth noting that the problem of effective values has no general solution: at different concentrations, arrangements, and distributions of inclusions, as well as at different local dependences, various relationships may take place. Only in particular cases (small concentrations of inclusions, concentrations near the percolation threshold, specific arrangements of the phases in the two-dimensional case, etc.), the problem has a general, while approximate, solution that depends on a small number of parameters, e.g., on the dimension of the problem.

To derive the effective transverse permeability $\mu_{\perp}^{e}$, we use the BL approximation modified for the nonlinear case [11, 12]. Following [11, 12], we consider the local field inside the nonlinear inclusions as constant. With this assumption, the nonlinear phase will be characterized by the constant permeability $\tilde{\mu}_1$:

$$\tilde{\mu}_1 = \langle \mu(H_{\perp}) \rangle_1, \tag{7}$$

where averaging $\langle \ldots \rangle_1$ is carried out over the volume of the inclusions.

Since now the medium consists of two "linear" phases with μ_2 and $\tilde{\mu}_1$, the effective permeability can

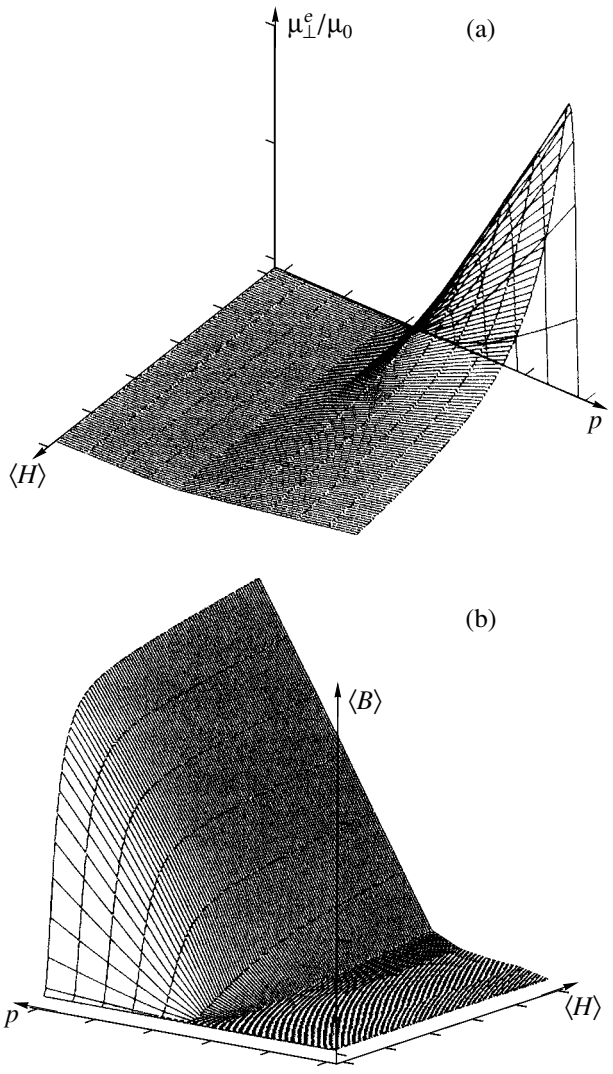

Fig. 3. Volume-averaged magnetic induction and $\mu_\perp^e$ as functions of the volume-averaged magnetic field $\langle H_\perp \rangle$.

be found from the conventional BL formula [8, 10, 13]

$$\mu_\perp^e = \frac{1}{2}(1-2p)(\mu_2 - \tilde{\mu}_1) + \frac{1}{2}\sqrt{(1-2p)^2(\mu_2 - \tilde{\mu}_1)^2 + 4\mu_2\tilde{\mu}_1}. \quad (8)$$

As is well known [7], for samples of a size exceeding the typical self-averaging size (correlation radius), $\langle \mathbf{BH} \rangle = \langle \mathbf{B} \rangle \langle \mathbf{H} \rangle$; hence, with regard for (2) and (7) [11, 12],

$$\langle H^2 \rangle_1 = \frac{\langle H^2 \rangle}{p}\frac{\partial \mu^e}{\partial \tilde{\mu}_1}. \quad (9)$$

After the substitution of $\mu_1 = \mu_1(H_\perp)$ for $\tilde{\mu}_1 = \langle \mu(H_\perp) \rangle_1$, we approximate $\tilde{\mu}_1$ as a function of $\langle H_\perp^2 \rangle_1$:

$$\tilde{\mu}_1 = \langle \mu(H_\perp) \rangle_1 \approx \mu_1(\sqrt{\langle H_\perp^2 \rangle_1}). \quad (10)$$

This approximation has proved to be valid in calculating the effective conductivity of nonlinear two-phase composites [11, 12] with a highly nonlinear *I–V* characteristic [14, 15]. Substituting (10) into (8) and (8) into (9) yields the equation for $\langle H_\perp^2 \rangle_1$:

$$\langle H_\perp^2 \rangle_1 = \frac{\langle H_\perp^2 \rangle}{2p}\left[2p - 1 + \frac{2\mu_2 - (1-2p)^2(\mu_2 - \tilde{\mu}_1)}{\sqrt{(1-2p)^2(\mu_2 - \tilde{\mu}_1)^2 + 4\mu_2\tilde{\mu}_1}}\right]. \quad (11)$$

Substituting $\langle H_\perp^2 \rangle_1$ determined from (11) into (10), we obtain the effective permeability of a nonlinear composite as a function of the concentration, parameters of the local function of the nonlinearity $\mu_1 = \mu_1(H_\perp)$, and external magnetic field $\langle H_\perp \rangle$. The dependence of the effective permeability for the particular local function is plotted in Fig. 3. At $p = 1$ and $p = 0$, the permeability $\mu_\perp^e(\langle H_\perp \rangle)$ becomes, as it must, that of the ferromagnetic and nonmagnetic phases, respectively.

Similar to the conventional BL approximation, its nonlinear generalization leads to the percolation-like behavior of $\mu_\perp^e$. As seen from Fig. 3a, at particular values of $\langle H_\perp \rangle$ (such that $\mu_\perp^e(\langle H \rangle, p = 1)/\mu_0 \gg 1$), the effective permeability abruptly increases as the concentration passes over the threshold. The quantitative description of the near-threshold region, for example, the determination of the critical exponents and their dependences on $\langle H_\perp \rangle$, is possible only within the framework of the percolation theory [16]. Note also that the external field $\langle H_\perp \rangle_{\max}$ at which $\mu_\perp^e$ (p = const) shows a maximum is concentration-dependent, $\langle H_\perp \rangle_{\max} = f(p)$.

ACKNOWLEDGMENTS

We thank P. Rosen, T. Beuker, and J. Rosenmoeller for the fruitful discussion and also Pak-Ming Hui, D. Kalyon, and G. Adachi for sending their preprints.

A. Snarskiĭ thanks H. Rosen Engineering GmbH for the hospitality during the preparation of this article.

REFERENCES

1. T. J. Fiske, H. S. Gokturk, and D. M. Kalyon, J. Mater. Sci. **32**, 5551 (1997).
2. H. S. Gokturk, T. J. Fiske, and D. M. Kalyon, J. Appl. Phys. **73**, 5598 (1993).
3. X. Shui and D. D. L. Chung, J. Electron. Mater. **25**, 930 (1996).
4. R. Arlot, H. Izumi, K. Machida, *et al.*, J. Magn. Magn. Mater. **172**, 119 (1997).

5. S. K. Wong, B. Zhao, T. K. Ng, *et al.*, Eur. J. Phys. B **10**, 481 (1999).
6. *Proceedings of the 4th International Conference on Electron Transport and Optical Properties of Inhomogeneous Media*, Ed. by A. M. Dykhne; Physica A (Amsterdam) **241** (1–2) (1997); *Proceedings of the 5th International Conference on Electron Transport and Optical Properties of Inhomogeneous Media*, Ed. by P.-M. Hui; Physica B (Amsterdam) **279** (1–3) (1999).
7. A. M. Dykhne, Zh. Éksp. Teor. Fiz. **59**, 110 (1970) [Sov. Phys. JETP **32**, 63 (1971)].
8. R. Landauer, J. Appl. Phys. **23**, 779 (1952).
9. L. D. Landau and E. M. Lifshitz, in *Electrodynamics of Continuous Media* (Nauka, Moscow, 1970; Pergamon, Oxford, 1960), p. 620.
10. D. A. Bruggeman, Ann. Phys. (Leipzig) **24**, 636 (1935).
11. P. M. Hui, P. Cheung, and Y. R. Kwong, Physica A **241**, 301 (1997).
12. P. M. Hui, Y. F. Woo, and W. M. V. Wan, J. Phys. C **7**, L593 (1995).
13. J. P. Clerc, G. Giraud, J. M. Laugier, and J. M. Luck, Adv. Phys. **39**, 191 (1990).
14. S. W. Kenkel and J. P. Straley, Phys. Rev. Lett. **49**, 767 (1982).
15. J. P. Straley and S. W. Kenkel, Phys. Rev. B **29**, 6299 (1984).
16. D. Stauffer and A. Aharony, in *Introduction to Percolation Theory* (Taylor & Francis, London, 1992), p. 181.

Translated by A. Sidorova-Biryukova

Technical Physics, Vol. 46, No. 12, 2001, pp. 1575–1578. Translated from Zhurnal Tekhnicheskoĭ Fiziki, Vol. 71, No. 12, 2001, pp. 88–91.

BRIEF COMMUNICATIONS

The Effect of Small Thermal Fluctuations on the Performance of a Single-Contact Interferometer

I. N. Askerzade

Institute of Physics, Academy of Sciences of Azerbaijan, pr. Dzhavida 33, Baku, 370143 Azerbaijan

e-mail: solstphs@lan.ab.az

Received November 13, 2000; in final form, April 26, 2001

Abstract—The effect of small thermal fluctuations on a single-contact interferometer is analyzed. A relationship between the dispersion of magnetic flux fluctuations, geometrical inductance of the interferometer, and external magnetic flux is found. © *2001 MAIK "Nauka/Interperiodica".*

INTRODUCTION

It is known [1] that a single-contact quantum interferometer relies on radically new effects appearing when a Josephson contact is closed to form a superconducting ring. The state of a single-contact interferometer is described by the equation

$$\phi + l\sin\phi = \phi_e, \tag{1}$$

where $\phi_e = 2\pi\Phi_e/\Phi_0$ is the external magnetic flux normalized to the magnetic flux quantum $\Phi_0 = \hbar\pi/e$, $l = L/L_c$ in the geometrical inductance normalized to the Josephson inductance $L_c = \Phi_0/2\pi I_c$, and I_c is the Josephson critical current.

The shape of the $\phi(\phi_e)$ dependence strongly depends on the value of l: at $l \ll 1$, the dependence is nearly linear, while at $l > 1$, it becomes uncertain. At a large inductance, $l \gg 1$, the interferometer has $2N$ ($N = l/\pi$) stationary states and can be used as a basis for constructing memory cells. Several versions of such a memory have already been implemented in experiments [2]. In [3], a reversible data-processing device, parametric quantron, with an extremely low dissipated energy (much smaller than a dissipated thermal energy) has been suggested. Another important application of a single-contact interferometer is a high-sensitivity magnetic sensor incorporated in an rf SQUID. Recent works regarding the use of the interferometers in quantum computers [4] are also worth noting, since these devices are real macroscopic systems that have two quantum states under certain conditions.

The discovery of high-temperature superconductivity [5] has opened new avenues for superconducting electronics. The transition from helium to nitrogen temperatures in cryoelectronics makes it possible to extend the application of superconducting electronic devices (including single-contact interferometers). At the same time, the operation at nitrogen temperatures runs into serious problems, since thermal fluctuations grow with temperature. As is known, the effect of thermal fluctuations on the Josephson device performance can be characterized by the dimensionless parameter

$$\gamma = kT/E_j \tag{2a}$$

(where kT is the thermal fluctuation energy and $E_j = \hbar I_c/2e$ is the Josephson binding energy) or

$$\gamma = I_T/I_c, \quad I_T = 2ekT/\hbar. \tag{2b}$$

Thermal fluctuations are considered to be small if $\gamma \ll 1$. In this case, thermal activation is appreciable near the critical current. Intense fluctuations, which are observed at $\gamma > 1$, will not be considered in this article. For the efficient operation of Josephson devices, the critical current I_c considerably exceed the thermal current I_T; in other words, the parameter γ must lie within some interval. The thermal current is estimated as

$$I_T(\mu\text{A}) = 0.084T\ (\text{K}).$$

At helium temperatures, I_T is small ($I_T = 0.2$ μA), so that the condition $\gamma \ll 1$ is readily fulfilled. At nitrogen temperatures, I_T approaches 3.2 μA and the necessary value of the critical current must grow. However, an increase in the critical current also faces a number of problems. For example, the power

$$P = I_c V_g = I_c 2\Delta(T)/e,$$

dissipated upon switching Josephson tunnel contacts into the resistive state may significantly grow, since the energy gap of high-temperature superconductors is much larger than in the low-temperature material.

Basically, thermal fluctuations at nitrogen temperatures can be suppressed by carefully designing the geometry of both the contacts themselves and their connections to obtain desired properties. This issue calls for special consideration and is beyond the scope of this work. Recently, the effect of intense fluctuations ($\gamma > 1$) on single-contact [6] and double-contact [7] interferometers has been studied. In those works, the theoretical grounds of the interferometer operation under

strong fluctuations have been put forward. We assume that the fluctuations are small and consider the different variations of the magnetic field applied to a single-contact interferometer. Such experiments could also help to elucidate the noise properties of devices based on granulated high-temperature superconducting films, since single-contact interferometers are basic elements in simulating these media.

BASIC EQUATIONS

The effect of fluctuations on a single-contact interferometer can be studied with the Fokker–Planck equation for probability density [1]. For the probability density near the bottom of a potential well, we have

$$\sigma(\phi, v) = \exp(-G(\phi, v)/kT)/\int_{-\infty}^{\infty} d\phi \int_{-\infty}^{\infty} dv \times \exp(-G(\phi, v)/kT), \quad (3)$$

where $G(\phi, v)$ is the energy of a single-contact interferometer [1]:

$$G(\phi, v) = CV_c^2 v^2/2 + \Phi_0 I_c/2\pi(1 - \cos\phi + (\phi - \phi_e)^2/2l); \quad (4)$$

$v = V/V_c$; V is the voltage across the Josephson contact; V_c is the characteristic Josephson voltage: $V_c = I_c R_N$; R_N is the normal resistance of the contact; and C is the contact capacitance.

If the inductance is small, the fluctuations of the critical current of the Josephson contact are neglected, so that only the last term remains. The same approach allows us to calculate the lifetime of the metastable state and fluctuations near the absolute minimum [1]. As a result, the thermal fluctuation factor γ given by (2) and its dependence on the magnetic field are absent in the final expressions. In our analysis, we take into account this disadvantage and calculate the magnetic flux fluctuations. With Eq. (1) for the interferometer state, the dispersion of the magnetic flux fluctuations is expressed as

$$\delta\tilde{\Phi}^2/\Phi_0^2 = (\sin\phi/(\cos\phi + l^{-1}))^2 \delta\tilde{I}_c^2/I_c^2, \quad (5)$$

where the phase ϕ is given by Eq. (1)

It should be noted that the similar equation for the fluctuations has been used in [8]. The dispersion of the fluctuations of the Josephson critical current depends on the McCamber capacitance parameter $\beta = 2\pi I_c R_N^2 C/\Phi_0$ and on the rate of increase of the current through the contact $\alpha = d(I/I_c)/d(t/\Phi_0/2\pi I_c R_N)$.

(1) Small-Inductance Interferometer

For small inductances, the parameter α depends on the rate of change of the external flux by virtue of Eq. (1):

$$\alpha = \cos(\phi_e(t)) d\phi_e/dt. \quad (6)$$

For slowly varying fields (i.e., for a low rate of increase of the current through the contact) and small fluctuations,

$$\alpha < (3\gamma/2)^{2/3} \ll 1, \quad (7)$$

the dispersion of the delay time depends on the rate of increase of current and capacitance parameter only slightly [9, 10]. This is explained by the specific dynamics of the Josephson phase when the rate of increase of the current is low. When deriving these formulas, we assumed that the fluctuations have enough time to thermally activate the system through the slowly lowering energy barrier. Multiplying the formula derived for the dispersion of the delay time by α^2, we obtain the critical current dispersion:

$$F_0 = (\delta\tilde{I}_c^2/I_c^2) \cong (3\gamma \ln C_0/2^{5/2})^{4/3}/6, \quad (8)$$

where C_0 is defined as [9, 10]

$$C_0 = \begin{cases} \gamma/4\pi\alpha & \text{at} \quad \beta \ll 1 \\ (3\gamma/2)^{5/6}/6\pi\alpha & \text{at} \quad \beta \gg 1. \end{cases} \quad (8a)$$

Thus, in view of (5)–(8), the final expression for the magnetic flux dispersion at low rates of increase of the current has the form

$$(\delta\tilde{\Phi}_c^2/\Phi_0^2) = l^2 \sin^2\phi_e F_0. \quad (9)$$

When the rate of increase is high ($\alpha > (3\gamma/2)^{2/3}$) or the fluctuations are small, the switching process is affected insignificantly; in particular, a slight dependence on α arises. Multiplying the associated formulas for the delay time dispersion in the cases of a tunnel contact [11] and a hysteresis-free junction [10] by α^2, we come to the expression for the critical current dispersion:

$$F_1 = (\delta\tilde{I}_c^2/I_c^2) = \begin{cases} 0.03\gamma\beta^{-3/4}\alpha^{3/4} & \text{at} \quad \beta \gg 1, \\ 11.9\gamma\alpha^{7/9} & \text{at} \quad \beta \ll 1. \end{cases} \quad (10)$$

The formula for the magnetic flux dispersion is obtained by substituting F_1 for F_0 in (9).

(2) High-Inductance Interferometer

At high inductances, several stationary states may be observed. Of them, that with the least potential energy is the most stable, while the other are metastable. The lifetimes of the metastable states are estimated by the formulas given in [12]. To estimate the magnetic flux fluctuations near the absolute minimum in formu-

la (5), we must take into account the relationship $\sin\phi \approx \phi_e/l$, which is obtained from the equation for the interferometer state at high inductances. In this case, the rate of increase of the current is given by $\alpha = d\phi_e/dt/l$. At a low rate of increase of the current through the contact and small fluctuations, i.e., when the condition (7) is met, we have for the magnetic flux dispersion:

$$(\delta\tilde{\Phi}^2/\Phi_0^2) = (\phi_e/\sqrt{l^2-\phi_e^2}+1)^2 F_0. \quad (11)$$

When deriving this formula, we used Eq. (5) and Eqs. (1) and (8) for the interferometer state. If the current through the contact grows rapidly, $\alpha > (3\gamma/2)^{2/3}$, the expression for F_1 should be applied instead of that for F_0 in formula (11).

Unlike the low-inductance limit, at large l, switching into the adjacent stationary state takes place as the external magnetic filed increases. Near such switchings, the denominator in the expression $\sin\phi/(\cos\phi + l^{-1})$ tends to zero and the effect of the fluctuations near these threshold points changes. Using the formulas for the threshold values of the phases in Eq. (1), as well as the results obtained in [12], we find in the low-rate limit:

$$(\delta\tilde{\Phi}^2/\Phi_0^2) = (\{l^4 - [(l^2-1)^{1/2}(2\tilde{\phi}_e)^{1/2} - l]^2\}/4l(l^2-1))F_0^{1/2}, \quad (12)$$

where $\tilde{\phi}_e = |\phi_e^{+,-} - \phi_e|$, $\phi_e^{+,-} = \pi n \pm \sqrt{l^2-1} + \arcsin l^{-1} - \pi/2$ (n is the state number).

When deriving this equation, we used the expressions for the barrier height and for the small-amplitude oscillation frequency of a single-contact interferometer near the threshold points (Chapter 6 in [1]). At high rates, formula (12) holds but the rate dependence arises, so that the expression

$$F_1^{1/2} = \begin{cases} 0.17\alpha^{3/8}\beta^{-3/8}\gamma^{1/2} & \text{at} \quad \beta \gg 1, \\ 3.44\alpha^{7/18}\gamma^{1/2} & \text{at} \quad \beta \ll 1 \end{cases} \quad (12a)$$

should be used instead of $F_0^{1/2}$.

DISCUSSION

Comparing formulas (9) and (11), we see that the effect of the fluctuations for a low-inductance interferometer is quadratically small. In this case, the Josephson contact is shunted by the interferometer inductance and the fluctuations turn out to be small, because a major part of the fluctuation current passes through the inductance. This becomes clear if a single-contact interferometer is viewed as parallel-connected contact and inductance that are fed by a current source with a current strength Φ_e/L. For large inductances, the effect of the source is negligible and the interferometer behaves as a single contact with a given current $I_e = \Phi_e/L$. As follows from (12), the effect of the fluctuations is enhanced near the threshold points. At these points, the effect of the Josephson inductance grows and the fluctuation contribution is distributed among the ring and contact inductances. Such a conclusion is in qualitative agreement with the data obtained for the hysteresis-free conditions (Chapter 14 in [1]). In [14], it was noted that the phase jumps near the threshold points enhance the fluctuations.

It is known that the SQUID sensitivity is characterized by the parameter

$$E_V = \delta\Phi^2/2L\Delta f,$$

where $\delta\Phi$ is the external magnetic flux change equivalent to the SQUID intrinsic noise in a band of measurement Δf and L is the inductance of the sensor (single- or double-contact interferometer).

The formulas for $\delta\tilde{\Phi}^2/\Phi_0^2$ derived above can be used for estimating the SQUID energy sensitivity. The careful calculation of the output characteristics of rf SQUIDs is beyond the scope of this work. However, these formulas allow us to make tentative conclusions. For a slowly varying external magnetic flux, the energy sensitivity degrades with decreasing frequency [see (9)], because the logarithm increases when the parameter $\alpha \propto \Omega$ in the denominator decreases ($\Omega \propto d\phi_e/dt$). This statement qualitatively agrees with the formulas in Chapter 14 from [1], as well as with formula (30) in [6] deduced in the small fluctuation approximation. This approximation is obtained at $L/L_F \longrightarrow 0$ and $\gamma \longrightarrow 0$. According to [6], this case corresponds to the adiabatic limit and the output energy sensitivity drops with decreasing pump frequency. To improve the sensitivity, it is advantageous to raise the pump frequency. Because of this, the transition to super-high-frequency SQUIDs seems to be topical. However, the drastic decrease in the energy sensitivity at pump frequencies on the order of the Josephson junction characteristic frequency, $\omega \approx \omega_c$ ($\Omega \approx 1$), is due to the change in the single-contact interferometer dynamics and, consequently, in the magnetic flux dispersion at high rates of increase of the current. This corresponds to the nonadiabatic limit [6]. As follows from (10), the sensitivity drops as $\Omega^{3/4}$ at $\beta \gg 1$ and as $\Omega^{7/9}$ at $\beta \ll 1$. In the nonadiabatic limit, the sensitivity also decreases with increasing $\Omega \geq 1$, according to [6].

Thus, we have analyzed the effect of small thermal fluctuation on the performance of a single-contact interferometer and related the magnetic flux fluctuation dispersion to the geometric inductance and external magnetic field.

ACKNOWLEDGMENTS

The author thanks the reviewer for the valuable remarks.

REFERENCES

1. K. K. Likharev, *Introduction to the Dynamics of Josephson Junctions* (Nauka, Moscow, 1985).
2. W. Y. Lum and T. van Duzer, J. Appl. Phys. **48**, 1693 (1977).
3. K. K. Likharev, G. M. Lapir, and V. K. Semenov, Pis'ma Zh. Tekh. Fiz. **2**, 809 (1976) [Sov. Tech. Phys. Lett. **2**, 316 (1976)].
4. T. Orlando, J. E. Mooij, L. Tian, *et al.*, Phys. Rev. B **60**, 15398 (1999).
5. J. G. Bednorz and K. A. Muller, Z. Phys. B **64**, 189 (1986).
6. B. Chesca, J. Low Temp. Phys. **110**, 963 (1998).
7. B. Chesca, J. Low Temp. Phys. **112**, 165 (1998).
8. Yu. M. Galperin, V. L. Gurevich, and V. I. Kozub, NATO ASI Ser. (1989), pp. 354–360.
9. O. V. Snigirev, Radiotekh. Élektron. (Moscow) **29**, 2216 (1984).
10. I. N. Askerzade, Zh. Tekh. Fiz. **68** (9), 129 (1998) [Tech. Phys. **43**, 1123 (1998)].
11. I. N. Askerzade, Turk. J. Phys. **22**, 811 (1998).
12. J. Kurkijarvi, Phys. Rev. B **6**, 832 (1972).

Translated by V. Isaakyan

Technical Physics, Vol. 46, No. 12, 2001, pp. 1579–1581. Translated from Zhurnal Tekhnicheskoĭ Fiziki, Vol. 71, No. 12, 2001, pp. 92–94.

BRIEF COMMUNICATIONS

Formation of an External Source by a Hard Radiation Pulse in an Electrodynamic Problem

F. F. Valiev

St. Petersburg State University, Universitetskiĭ pr. 2, St. Petersburg, 198504 Russia

e-mail: valiev@snoopy.phys.spbu.ru

Received November 3, 2000; in final form, March 2, 2001

Abstract—A method is proposed for calculating an external source that forms when hard radiation is absorbed by matter. The relevant electrodynamic problem is solved by numerical modeling. It is shown that the current density vector can be localized in space and time. © *2001 MAIK "Nauka/Interperiodica".*

The investigation of electromagnetic waves accompanying the absorption of gamma-ray photons by matter implies a calculation of the macroscopic current density vector, i.e., an external source for the electrodynamic problem. The objective of this paper is to consider the formation of a current pulse during the irradiation of a gas medium by a collimated beam of hard radiation. The method of calculation is described, and the spatiotemporal structure of electromagnetic wave sources moving at the speed of light is calculated. The methods of numerical modeling are applied. The numerical code is devised with the use of the GEANT software package [1], which is widely utilized in nuclear and high-energy physics. Account is taken of the main processes of the interaction of photons with matter (photoabsorption, Compton scattering, and pair production), as well as of the secondary effects of the interaction of delta-electrons with matter and ionization processes induced by the secondary electrons. Electrons with energies lower than ten kiloelectronvolts are not taken into consideration. The input to the code includes the data on the elemental composition of the absorbing region and its geometry, as well as on the spatiotemporal distribution of the primary gamma-ray photons and their momenta. This work is motivated by recent studies on the formation of highly directed, strongly localized (in both space and time) electromagnetic waves by sources propagating at the speed of light [2–8]. Note that, in [2–8], the sources (the current density vectors) were specified heuristically rather than calculated. In calculations of the electromagnetic radiation from nuclear explosions [9, 10], the current density was determined using a simplified model. It was assumed that the electrons produced during absorption of gamma-ray photons by matter keep their initial velocity unchanged along the path of propagation and then stop abruptly. The spread in velocities and ejection angles of the electrons, as well as secondary effects, were neglected. These simplifications had to be made because, at that time, there were no adequate computers and numerical methods.

A schematic of the numerical experiment is shown in Fig. 1. The geometry of the problem is chosen to satisfy the requirements imposed on the spatiotemporal structure of the source by the familiar solutions to the electrodynamic problem of the formation of directed waves [4–8]. A homogeneous absorbing medium is bounded by a cylindrical surface and by two planes that are orthogonal to the cylinder axis, along which a spatiotemporal δ-pulse of primary radiation propagates. The origin of the coordinate system is chosen to be located at the point $O(x = 0, y = 0, z = 0)$, which lies in one of the two planes. The z-axis is assumed to coincide with the cylinder axis. The initial instant is chosen to be the time at which a gamma-ray pulse passes through the boundary of the absorbing region. The results presented below were obtained for 10-MeV gamma-ray photons propagating through air at a pressure of 10 atm. In Fig. 1, the electron trajectories are shown by the solid lines, and the trajectories of gamma-ray photons are represented by the dashed lines. We can see that the electrons are concentrated near the z-axis.

The spatiotemporal distribution of the current density $\mathbf{j}(\mathbf{r}, t)$ is determined by the current density vectors $\mathbf{j}_{\Delta V_i}(\mathbf{r}, t)$ in the volume elements ΔV_i $((x_i, x_i + \Delta x), (y_i, y_i + \Delta y), (z_i, z_i + \Delta z))$ in space. In each of the elements, the current density vectors of individual electrons is summed:

$$\mathbf{j}_{\Delta V_i}(\mathbf{r}, t) = \frac{1}{\Delta V}\sum_{a=1}^{N_i} e\mathbf{v}(\mathbf{r}_a, t),$$

where $\Delta V = \Delta x \Delta y \Delta z$, $\mathbf{v}(\mathbf{r}_a, t)$ and $\mathbf{r}_a(x, y, z, t)$ are the velocities and coordinates of the electrons in an absorbing medium at the time t, and N_i is the number of electrons in the volume element ΔV_i.

1063-7842/01/4612-1579$21.00

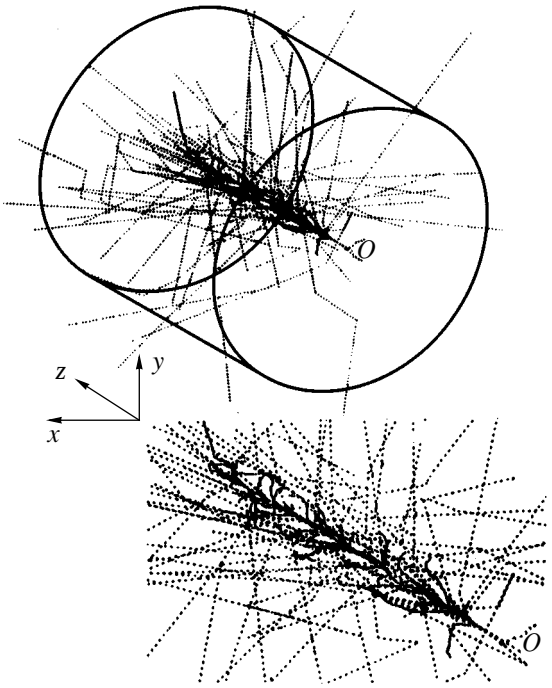

Fig. 1. Schematic of the model experiment. A 20-m long and 20-m-diameter cylindrical region is filled with air at a pressure of 10 atm. The energy of the primary gamma-ray photons is 10 MeV. The solid lines are the electron trajectories, and the dashed lines are the trajectories of gamma-ray photons. The upper frame presents the region around the *z*-axis on an enlarged scale.

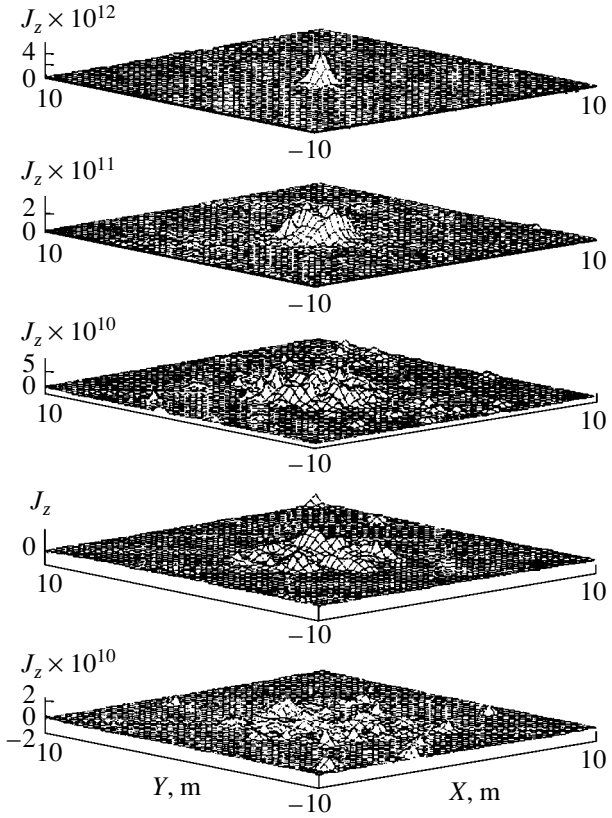

Fig. 2. Histograms of the transverse distributions of the *z*-component $j_z(\mathbf{r}, t)$ of the current density vector at the time $t = 500$ ns in the cross sections separated by a distance of 0.2 m along the *z*-axis.

The centers of the volume element ΔV_i are assigned the vectors $\mathbf{j}_{\Delta V_i}(\mathbf{r}, t)$. The histograms describing transverse distributions of the *z*-component $j_z(\mathbf{r}, t)$ of the current density vector at fixed *t* and *z* are shown in Fig. 2. For the above parameters of the model experiment, the half-width ΔR_1 of the distribution $j_z(\mathbf{r}, t)$ is smaller than 60 cm. This value of ΔR_1 is an estimate of the extent to which the forming source is localized in the transverse direction at the chosen observation time.

Figure 3 shows how the shape of the current pulse changes from cross section to cross section along the absorbing region. For the above parameters of the medium and for the above energy of the primary radiation, the pulse duration *T* at a level of 0.1 of the peak amplitude is shorter than 2 ns, which corresponds to the spatial extension $\Delta Z_2 = cT < 60$ cm (where *c* is the speed of light). This value of ΔZ_2 is an estimate of the spatial localization of the current along the *z*-axis. In Fig. 3, we can also see that the current pulse propagates at the speed of light.

The above estimates of the longitudinal and transverse localization of the pulse enable us to draw the following conclusion: for the chosen parameters of the model experiment, the irradiation of a gas medium by a collimated gamma-ray beam during the time interval under consideration leads to the formation of a spatially localized region that propagates at the speed of light and in which $\mathbf{j}(\mathbf{r}, t) \neq 0$. Hence, a simplified model in which the external source is represented by a delta-pulse of the current propagating at the speed of light along a straight line [7] can be employed in electrodynamic calculations of directed electromagnetic waves.

The method proposed here for calculating the current density vector **j** in electrodynamic problems can be used to model other sources propagating at the speed of light (in particular, the sources that give rise to directed waves [5, 6, 11]) by specifying the required distributions of the coordinates and momenta of the primary gamma-ray photons.

The proposed method for calculating the current density vector **j** can also be used to determine the shape of a current pulse propagating faster than light (a superluminal source of radiation). An example of the formation of a superluminal source was given in [12], in which the front of a hard radiation pulse was assumed to be incident at an angle to the symmetry axis of an extended absorbing region.

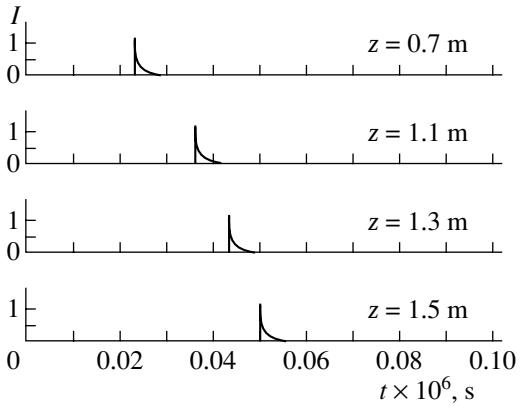

Fig. 3. Waveforms of the current pulse in different cross sections of the absorbing regions for 10-MeV primary gamma-ray photons.

The main results of the present work can be summarized as follows. A method is proposed for simulating an electromagnetic wave source that forms in the interaction of hard radiation with matter and propagates with a speed that is equal to or greater than the speed of light. The transverse and longitudinal localization of the current density vector in a gas medium irradiated by a collimated gamma-ray beam is estimated under the conditions chosen for the numerical experiment. The use of a model in which the external source is represented by a delta-pulse of the current propagating at the speed of light along a straight line is justified.

ACKNOWLEDGMENTS

I am grateful to V.V. Borisov for many useful discussions. This work was supported in part by the Russian Foundation for Basic Research, project no. 99-02-16893.

REFERENCES

1. *GEANT User's Guide*, CERN DD/EE/83-1.
2. P. J. Hillion, J. Math. Phys. **29**, 2219 (1988).
3. P. J. Hillion, J. Math. Phys. **31**, 1939 (1990).
4. P. L. Overfelt, J. Opt. Soc. Am. A **14**, 1087 (1997).
5. P. L. Overfelt and C. S. Kenney, in *Proceedings of the International Symposium on Electron Theory, 1998*, p. 802.
6. V. V. Borisov and A. B. Utkin, J. Phys. A **26**, 4081 (1993).
7. V. V. Borisov and A. B. Utkin, J. Phys. A **27**, 2587 (1994).
8. V. V. Borisov and I. I. Simonenko, Can. J. Phys. **75**, 573 (1997).
9. C. L. Longmire, IEEE Trans. Electromagn. Compat. **20** (1), 3 (1978).
10. W. J. Karzas and R. Letter, Phys. Rev. B **137**, 1369 (1965).
11. N. Brittingham, J. Appl. Phys. **54**, 1179 (1983).
12. F. F. Valiev and V. V. Borisov, in *Proceedings of the International Conference on Nuclear Physics, St. Petersburg, 2000*, p. 379.

Translated by O. Khadin

Technical Physics, Vol. 46, No. 12, 2001, pp. 1582–1584. Translated from Zhurnal Tekhnicheskoĭ Fiziki, Vol. 71, No. 12, 2001, pp. 95–97.

BRIEF COMMUNICATIONS

The Production of Excimer Molecules and Excited Atoms in a Positive Corona Discharge in He/Xe(Kr)/SF_6/CCl_4 Mixtures

A. K. Shuaibov, A. I. Minya, and A. I. Dashchenko

Uzhgorod State University, Podgornaya ul. 46, Uzhgorod, 88000 Ukraine

e-mail: ishev@univ.uzhgorod.ua

Received April 4, 2001

Abstract—Electrical and optical characteristics of a positive corona discharge in He/Xe(Kr)/SF_6/CCl_4 mixtures, which are of interest for the use in multiwavelength excimer radiation sources, are studied in the needle–grid electrode configuration. The length of the discharge, which is usually used to pump repetitive high-pressure multiwavelength radiation sources, is equal to the length of the electrodes of an excimer laser or lamp pumped by a transverse electric discharge. The discharge current–voltage and frequency characteristics, panoramic emission spectra, and the dependences of the relative emission intensity from the halogenides and excited noble gas atoms on the corona discharge current are investigated. The main processes resulting in the production of halogenides, as well as xenon and krypton excited atoms, in the generation regions of a corona discharge are studied. © *2001 MAIK "Nauka/Interperiodica".*

INTRODUCTION

Pulsed corona discharges (CDs) in the mixtures of noble gases with halogen-containing gases are widely used for the UV preionization of electric discharge–pumped excimer (*RX**) lasers [1, 2]. The steady-state or quasi-steady-state CDs in active media of the *RX* lasers are studied less extensively. A CD with a length approximately equal to the length of an *RX* laser active medium can be used to pump the active media of high-pressure gas lasers [3]. The studies carried out with He/Xe(Kr)/HCl mixtures showed that, for negative supply voltage at the needle–grid electrode system, this type of discharge can be used to pump the laser active medium, whereas, for the positive voltage, a streamer corona arises, which makes the discharge unfit for pumping [4]. A multielectrode negative CD in He/Xe(Kr) mixtures, whose composition is similar to those used in multiwavelength radiation sources based on the noble gas chlorides (with low-corrosive CCl_4 as a halogen donor), was studied in [5].

Here, we investigate the production of halogenides and xenon (krypton) excited atoms in the generation regions of a positive CD in He/Xe(Kr)/SF_6/CCl_4 mixtures and its electrical characteristics.

EXPERIMENTAL SETUP

The electrode system consists of 12 needles arranged in a row and a grid made from 0.15-mm-radius nickel wires. A radius of the needle apex is 0.5 mm; the needle–grid distance is 2 cm. The electrode system is mounted on a dielectric flange and set into a high-pressure chamber. A positive dc voltage is applied to the needles. A more detailed description of the experimental facility is presented in [4, 5].

In our experiments, the CD has the form of bright generation regions near the needle apexes, while the bulk of the discharge gap is dark. At elevated voltages, when a breakdown is going to occur, the generation regions near the grid also arise. The increase in the supply voltage results in the onset of a streamer at one of the needles. The optical characteristics of the discharge plasma are studied throughout the entire aperture of the CD. The main emission sources are the generation regions near the needle apexes.

ELECTRICAL CHARACTERISTICS

Figure 1 shows the typical current–voltage characteristics of a positive CD in the mixtures of noble gases with SF_6 and CCl_4. The maximum CD current in the

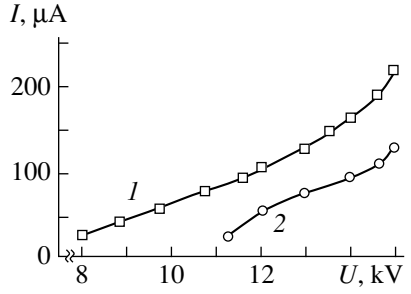

Fig. 1. Averaged current-voltage characteristic of a positive CD in the (*1*) He/Xe/SF_6/CCl_4 = 300/1.6/0.2/0.02-kPa and (*2*) He/Kr/SF_6/CCl_4 = 300/13/0.2/0.02-kPa mixtures.

1063-7842/01/4612-1582$21.00 © 2001 MAIK "Nauka/Interperiodica"

noncontracted stage of the discharge and the minimum discharge ignition voltage are attained with xenon-containing mixtures. The difference of the current–voltage characteristic from the dependence $I = \alpha(U - U_0)^2$, which is characteristic of a CD [6], is related to the significant content of heavy noble gases in the mixture and the resulting nonlinearity of the discharge [7]. Under these conditions, the discharge acquires some properties of a glow discharge.

A hysteresis in the current–voltage characteristic was almost absent, although it occurred in CDs in two-component mixtures like He/Xe(Kr) [8]. This is related to the decrease in the density of the excited heavy noble gas atoms that participate in quenching reactions with SF_6 and CCl_4 molecules (including the production of RCl* and RF* excimer molecules) [9, 10].

Since the pumping rate of a gas mixture in an electric discharge scales as $\nu \sim (I)^{1/2}$ [11], it is maximum in xenon containing mixtures with the lowest content of halogen-containing molecules. In mixtures under study, the maximum CD current is determined by the density of halogen donors and depends only slightly on the ballast resistance in the supply circuit.

A typical waveform of the CD current pulse and dependence of the pulse repetition rate on the power supply voltage are shown in Fig. 2. During almost the entire discharge phase, the CD current is continuous, being superimposed by a set of submicrosecond pulses with a repetition rate of 1–225 kHz. The maximum amplitude of the current pulses (~1 mA) is attained in a CD in $He/Kr/SF_6/CCl_4$ mixture, whereas in the xenon-containing mixtures it no higher than 0.15 mA. Since the mixtures under study only differ by the content of heavy noble gas atoms, the CD current pulses seem to be related to the drift of positive ions (such as Xe^+ or Xe_2^+) through the peripheral zone of the CD toward the metal grid. The ratio between the current amplitudes is approximately equal to the ratio between the krypton and xenon atom densities in the mixture. The maximum repetition rate of the CD current pulses is attained with krypton-containing mixtures. In the entire range of the parameters where the discharge is stable, the repetition rate gradually increases with the power supply voltage.

OPTICAL CHARACTERISTICS AND PLASMA PROCESSES

The studies of the panoramic emission spectra from the CD plasma show that, in the UV spectral region, the most intense are the KrCl* 222-nm, KrF* 249-nm, XeCl* 308-nm, and XeF* 351-nm bands, whereas in the near IR region, these are the spectral lines corresponding to the transitions Kr(5*s*–5*p*) and Xe(6*s*–6*p*). Just a few emission lines from the Xe(6*s*–7*p*) and Kr (5*s*–6*p*) transitions are observed in the visible spectral region. There are no emission lines from the high-lying levels of the Kr and Xe atoms, as well as from their single-charged ions.

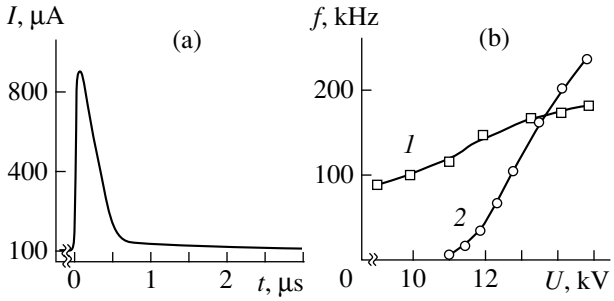

Fig. 2. (a) Waveform of the CD current in the $He/Kr/SF_6/CCl_4$ = 300/13/0.2/0.02-kPa mixture and (b) the repetition rate of the current pulses vs. power supply voltage for (*1*) $He/Xe/SF_6/CCl_4$ and (*2*) $He/Kr/SF_6/CCl_4$ mixtures at U = 13 kV.

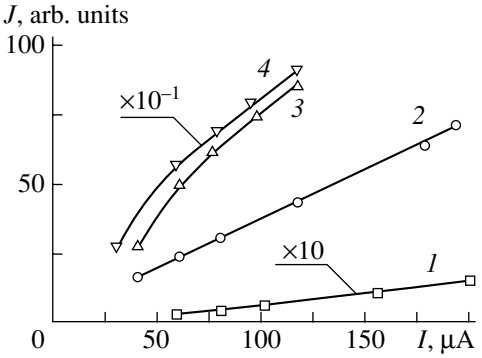

Fig. 3. Average intensities of the excimer molecule emission bands in (*1*, *2*) $He/Xe/SF_6/CCl_4$ and (*3*, *4*) $He/Kr/SF_6/CCl_4$ mixtures vs. average CD current: (*1*) XeF(*B*–*X*) 351-nm, (*2*) XeCl(*B*–*X*) 308-nm, (*3*) KrF(*B*–*X*) 249-nm, and (*4*) KrCl(*B*–*X*) 222-nm bands.

Figure 3 shows the relative intensities of the emission bands from excimer molecules versus the CD current. The dependences are linear for the mixtures with a low content of heavy noble gas atoms and deviate from being linear at a higher content.

The most intense is the KrCl 222-nm emission band. Comparing the production efficiency of the xenon and krypton chlorides and fluorides in the four-component mixtures, we can see that the emission intensity from noble gas chlorides is higher by more than one order of magnitude than that from the noble gas fluorides.

The dependences of the intensities of the emission lines from the excited xenon and krypton atoms on the CD current are shown in Fig. 4. They are linear and correlate with the dependences of the emission intensities from excimer molecules on the discharge current. For the same currents, the ratio between the emission intensities of Kr and Xe atomic spectral lines is approximately equal to the ratio between the atom densities in the CD plasma. In view of such behavior of the emission intensities from the RCl*, RF*, and R(*s*–*p*), we can suppose that, in the CD generation regions, the excimer

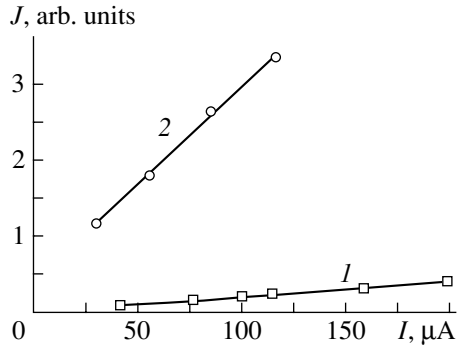

Fig. 4. Intensities of the emission lines from xenon and krypton atoms vs. CD current: (*1*) Xe(6*s*–6*p*) 832-nm line ($He/Xe/SF_6/CCl_4$ mixture) and (*2*) Kr(5*s*–5*p*) 810-nm line ($He/Kr/SF_6/CCl_4$ mixture).

molecules form via the "harpoon" reactions like

$$R(np, ns) + (CCl_4, SF_6) \longrightarrow RCl^*(RF^*) + \text{products}. \quad (1)$$

According to [9, 10], the rate constant for reaction (1) with the participation of SF_6 molecules is almost zero (the corresponding branching ratio for the quenching reaction resulting in the production of an excimer molecule is 0.02); hence, the emission intensity from RF* molecules is much lower than that from RCl* molecules. Under our conditions, RF* molecules can also form in secondary processes with the participation of light radicals that are produced due to either the dissociation of SF_6 molecules in a CD or ion–ion recombination.

In CCl_4-containing mixtures, RCl* molecules can be produced via direct reactions (1) with the participation of CCl_4 molecules, the reactions involving Xe(6*p*) atoms being the most efficient. The branching ratio for the quenching of Xe(6*p*) by CCl_4 molecules with the production of XeCl(*B*) amounts to 0.6–0.7, whereas, for metastable atoms, it is much less (about 0.24) [9].

In producing RX* in the generation regions of a CD, ion–ion recombination is of lesser significance than the "harpoon" reaction due to both the truncating the electron energy distribution function on the high-energy side and the low densities of the positive ions of a noble gas as compared to the density of the excited R (*ns*, *np*) atoms [11, 12]. Moreover, the electron temperature in the CD generation regions can be too high for the recombination of Cl^- (F^-) ions with R^+ (R_2^+) ions to be efficient.

The main process resulting in the production of Xe(6*p*, 7*p*) and Kr(5*p*, 6*p*) atoms can be the direct electron–impact excitation of noble gas atoms, which agrees with both the linear dependence of the R line emission intensities on the discharge current and the values of the effective cross sections for the electron–impact excitation of *np* levels of Xe and Kr [13, 14]. The dissociative recombination of R_2^+ molecular ions with electrons [15] can be another efficient mechanism for populating the R(*np*) levels; however, its efficiency is reduced by the high electron temperature in the hot regions of the CD.

In the discharge under study, the current density and the gas flow rate are limited by the onset of an instability resulting in the formation of a cathode streamer. The streamer arises near one of the needles at an elevated power supply voltage. In the uniform phase of the discharge, the CD current density increases as the concentration of halogen-containing molecules in the gas mixtures decreases.

CONCLUSION

The characteristics of a positive multielectrode CD in the mixtures of noble gases with SF_6 and CCl_4 and the processes resulting in the excitation of atoms and molecules are investigated. It is shown that this discharge is characterized by low energy consumption ($W \le 1$ W) and can be used to pump multiwavelength excimer radiation sources. The excimer molecules and excited noble gas atoms in the generation regions of a corona discharge are produced mainly via harpoon reactions and direct electron impact, respectively.

REFERENCES

1. G. J. Ernst, A. B. Nieuwenhuis, and K. M. Abramski, IEEE J. Quantum Electron. **21**, 1127 (1985).
2. R. S. Taylor and K. E. Leopold, J. Appl. Phys. **65**, 22 (1989).
3. A. I. Baranov, K. V. Gurkov, M. I. Lomaev, *et al.*, Prib. Tekh. Éksp., No. 4, 108 (1994).
4. A. K. Shuaibov, L. L. Shimon, and I. V. Shevera, Kvantovaya Élektron. (Moscow) **24**, 20 (1997).
5. A. K. Shuaibov, Zh. Tekh. Fiz. **68** (5), 48 (1998) [Tech. Phys. **43**, 522 (1998)].
6. P. L. Henson, J. Appl. Phys. **52**, 709 (1981).
7. A. A. Belevtsev and L. M. Biberman, Beitr. Plasmaphys. **23**, 803 (1983).
8. A. K. Shuaibov, A. I. Dashchenko, I. V. Shevera, *et al.*, Fiz. Plazmy **23**, 960 (1997) [Plasma Phys. Rep. **23**, 886 (1997)].
9. J. E. Velasko, J. H. Kolts, and D. W. Setser, J. Chem. Phys. **65**, 3468 (1976).
10. J. K. Ku and D. W. Setser, Appl. Phys. Lett. **48**, 689 (1986).
11. I. P. Vereshchagin, *Corona Discharge in Electronic and Ionic Process Equipment* (Énergoatomizdat, Moscow, 1985).
12. V. D. Peskov, Zh. Tekh. Fiz. **45**, 2544 (1975) [Sov. Phys. Tech. Phys. **20**, 1584 (1975)].
13. P. V. Fel'tsan and I. P. Zapesochnyĭ, Ukr. Fiz. Zh. **13**, 205 (1968).
14. P. V. Fel'tsan, Ukr. Fiz. Zh. **12**, 1405 (1967).
15. V. A. Ivanov, Khim. Fiz. **9**, 1454 (1990).

Translated by N. Ustinovskiĭ

Technical Physics, Vol. 46, No. 12, 2001, pp. 1585–1587. Translated from Zhurnal Tekhnicheskoĭ Fiziki, Vol. 71, No. 12, 2001, pp. 98–100.

BRIEF COMMUNICATIONS

Positioning of the Arc Discharge Channel in Vacuum Arc Facilities

A. V. Voronin and A. A. Semenov

Ioffe Physicotechnical Institute, Russian Academy of Sciences, Politekhnicheskaya ul. 26, St. Petersburg, 194021 Russia

e-mail: voronin.mhd@pop.ioffe.rssi.ru

Received April 9, 2001

Abstract—The behavior of an electric arc in a magnetic field is studied theoretically and experimentally. It is found that the arc behavior can be governed by the ponderomotive interaction of the arc with current-carrying elements. In a nonuniform magnetic field, the behavior of the arc depends on the Hall currents and the diamagnetic properties of its plasma. It is shown that the position of the arc channel between the end faces of cylindrical electrodes can be controlled by nonuniform magnetic fields. The methods and devices considered in this paper allow one, in particular, to control arc heat sources used in the heat treatment of metals. © *2001 MAIK "Nauka/Interperiodica".*

INTRODUCTION

Electric arc finds wide application in many industrial processes. Usually, a free arc chaotically moves between electrodes, and its behavior and characteristics are unpredictable. For example, in vacuum arc furnaces for metal melting, the arc can reach the crucible walls, which may adversely affect the metal quality or even cause an accident. The available ways of arc positioning are inadequate [1, 2], since they either control the arc source parameters that only indirectly specify the arc position or minimize the detrimental effect of the uncontrollable interaction between the arc and the surrounding members. The strict positioning of the arc channel between the electrodes is therefore necessary.

In this paper, we consider the possibility of controlling the position of dc and ac arcs [3]. If an arc is considered as a current-carrying conductor, then the ponderomotive interaction between the arc current and the current leads can be used to stabilize the position of the arc channel. On the other hand, an arc can be viewed as a plasma conductor and plasma properties can be employed for arc control.

THE USE OF PONDEROMOTIVE INTERACTION BETWEEN CURRENT LEADS AND ELECTRIC ARC TO STABILIZE THE ARC POSITION

The use of nonuniform magnetic fields generated by the currents in the electrodes and other external current leads to stabilize the arc channel position seems to be a simplest and most attractive way for arc control [4].

Previously, we considered the ponderomotive interaction between the arc current and the current of the electrodes made in the form of coaxial semi-infinite cylinders separated by the arc gap. The arc was considered as an infinitely thin linear current-carrying conductor perpendicular to the electrode end faces. We derived the expression for the force acting on the unit length of the conductor with the current passing between the semi-infinite cylindrical electrodes. This force is equal to zero if the conductor in the arc gap is coaxial with the electrodes. However, the radial force expulsing the conductor out of the arc gap appears for a distance between the conductor and the axis as small as desired. This force increases with distance to the axis and depends on the length of the gap only slightly.

Thus, the position of the arc between long coaxial cylindrical electrodes has been shown to be unstable. The destabilizing radial force can be diminished, for example, by using a coaxial current lead.

Now, consider the ponderomotive interaction of a current-carrying conductor placed between the bottom of a conducting crucible and the end face of a semi-infinite conducting cylinder (Fig. 1). In this geometry, the cylindrical electrode, the crucible bottom with a conductivity σ_b, and the crucible walls with a conductivity σ_w are current leads. As before, the arc is considered as an infinitely thin current filament perpendicular to the electrode end face and the crucible bottom. It is assumed that the current distribution in the electrode occurs within an infinitely thin layer of its end face. The current distributions across the crucible walls and bottom are neglected; i.e., the currents were assumed to be surface.

In the expression for the radial force F_m acting on the unit length of the conductor with the current passing between the crucible bottom and the electrode face end, the relationship between the bottom and wall conductivities of the crucible is of importance [4]. For a magnetic field produced by coaxial electrodes, one can dis-

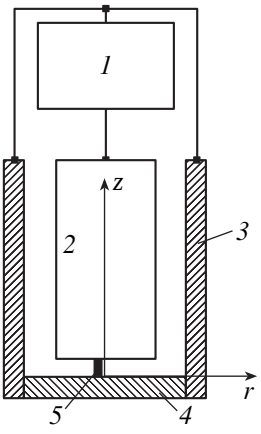

Fig. 1. Coaxial arrangement of the electrodes: *1*, current source; *2*, cylindrical electrode; *3*, crucible wall; *4*, crucible bottom; and *5*, arc channel.

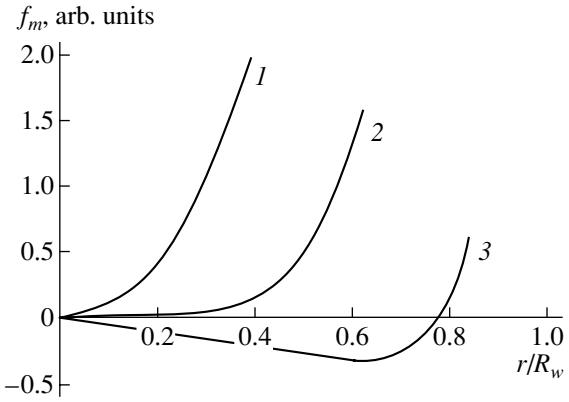

Fig. 2. Radial force f_m acting on the unit length of the current-carrying conductor between the coaxial vs. distance to the electrode axis ($f_m = 10^7 F_m R_e/I^2$, where I is the discharge current in units of A; R_e in m; and F_m in N/m) for the case $\sigma_b \ll \sigma_w$. R_e/R_w = (*1*) 0.5, (*2*) 0.7, and (*3*) 0.9.

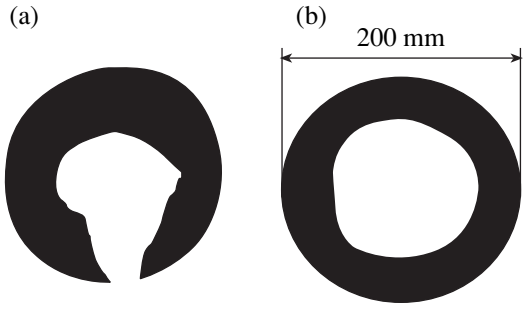

Fig. 3. Foil melted when (a) $\sigma_w = \sigma_b$ and (b) $\sigma_w \ll \sigma_b$.

tinguish three important cases that specify the arc behavior: (i) $\sigma_w \ll \sigma_b$; (ii) $\sigma_w = \sigma_b$; and (iii) $\sigma_b \ll \sigma_w$.

As follows from the calculations, the first two cases are qualitatively similar to the coaxial-electrode problem considered above. For the bottom conductivity much smaller than that of the walls ($\sigma_b \ll \sigma_w$), it was established that, for $R_c/R_w \geq 0.9$ (R_e is the electrode radius and R_w is the inner crucible radius) there is the range $0 \leq R \leq 0.75R_w$, where the force F_m acting on the arc is directed toward the system axis; i.e., the equilibrium position is stable (Fig. 2). In practice, this case is observed, for example, when titanium melts in copper crucibles.

The stabilization of the arc channel position was tested experimentally by melting aluminum foils kept close against the end face of the upper electrode. The foils melted under the conditions when the crucible bottom conductivity was equal (Fig. 3a) and much lower (Fig. 3b) than that of its walls. The experimental data confirmed the calculations. As was expected, in the first case, we observed the traces of the random movement of the arc channel over end face of the electrode up to its periphery. Another picture was observed in the second case. It is seen that the arc channel is confined by the region whose radius is smaller than the upper electrode radius.

THE POSITIONING OF THE DC ARC CHANNEL BY MEANS OF A NONUNIFORM MAGNETIC FIELD

An electric arc is a plasma conductor and, hence, can be controlled by using the plasma properties, in particular, plasma diamagnetism. However, when studying the behavior of plasma conductors in spatially nonuniform magnetic fields, we came across a phenomenon that is paradoxical from the viewpoint of plasma diamagnetism. A plasma column of a dc arc may have a stable position in the region of both the minimum and the maximum magnetic field, depending on the current direction in the plasma column. In this case, the condition of magnetization necessary for diamagnetic interaction may not be satisfied.

The review of papers devoted to electric arcs has revealed experimental evidence for arc stabilization in the region of the maximum magnetic field. However, no satisfactory theoretical explanation has been given [5, 6].

Such behavior of an arc discharge has been explained by taking into account the Hall effect, which shows itself as the appearance of an extra current perpendicular to the electric and magnetic fields applied [7]. It is the interaction of the Hall current with the external magnetic field that governs the arc behavior. The experiment confirming the theoretical prediction has been carried out [8].

THE POSITIONING OF AN AC ARC BY USING THE DIAMAGNETISM OF ITS PLASMA

As has been shown [8], the direction of the force caused by the Hall currents depends on the current direction in the arc. In ac arcs initiated in nonuniform

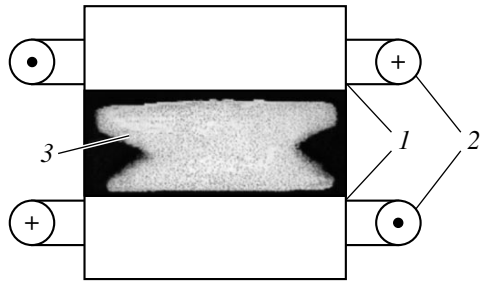

Fig. 4. Arc plasma in the magnetic field of the antiprobkotron: *1*, electrodes; *2*, current-carrying coils; and *3*, arc.

magnetic fields, the Hall force averaged over the arc current period is equal to zero and the diamagnetic effect becomes appreciable. Therefore, it can be used to act upon the arc plasma column [9].

If the magnetic field in the gap increases from the axis of the electrode to its periphery, the arc channel must be within the region where the magnetic field intensity B is minimal. The arc can then be displaced by shifting the minimum of the magnetic field intensity. Arc confinement by plasma diamagnetism is possible if the electronic component of the plasma is magnetized.

The calculations of diamagnetic forces F_d confining the arc, as well as relevant experimental data, showed that arc confinement is effective in the magnetic field of an antiprobkotron. The magnetic field was produced by two short electromagnetic coils with oppositely directed currents that were placed coaxial with the electrodes and symmetrically relative to the arc gap.

The excited plasma of an ac arc in the magnetic field of the antiprobkotron is shown in Fig. 4. One can see the sharp-boundary arc channel, which is coaxial with the electrodes. The region of the maximal pinch corresponds to the position of the maximum magnetic field gradient.

CONCLUSION

It has been found theoretically and experimentally that the arc behavior in a nonuniform magnetic field can be controlled by plasma diamagnetism, Hall currents, and the ponderomotive interaction of the arc with current-carrying elements. The possibility of positioning the arc channel between the end faces of cylindrical electrodes by means of nonuniform magnetic fields has been shown. The current lead arrangement and parameters that allow the ponderomotive interaction of the arc with current-carrying elements to be used for arc stabilization have been suggested. The arc channel can be localized at a given point of the arc gap by using plasma diamagnetism. The position of a dc arc can be controlled by a nonuniform magnetic field in view of Hall currents. The methods and devices considered allow one, in particular, to control arc heat sources during the heat treatment of metals.

REFERENCES

1. L. A. Volokhonskiĭ, *Vacuum Arc Furnaces* (Énergoatomizdat, Moscow, 1985).
2. A. D. Svenchanskiĭ and K. D. Gutterman, *Automatic Control of Furnaces* (Énergiya, Moscow, 1965).
3. A. I. Rusakov, A. A. Semenov, and A. V. Voronin, in *Proceedings of the XVII International Symposium on Discharges and Electrical Insulation in Vacuum, ISDEIV, Berkley, 1996* (IEEE, Piscataway, 1996).
4. A. V. Voronin, A. I. Rusakov, and A. A. Semenov, Preprint of the Ioffe Physicotechnical Institute, USSR Academy of Sciences, Leningrad, 1989, no. 1336.
5. H. Wroe, Br. J. Appl. Phys. **9**, 488 (1958).
6. A. M. Dorodnov, Zh. Tekh. Fiz. **48**, 1858 (1978) [Sov. Phys. Tech. Phys. **23**, 1058 (1978)].
7. L. D. Landau and E. M. Lifshitz, *Course of Theoretical Physics*, Vol. 8: *Electrodynamics of Continuous Media* (Nauka, Moscow, 1982; Pergamon, New York, 1984).
8. A. V. Voronin, A. I. Rusakov, and A. A. Semenov, Zh. Tekh. Fiz. **65** (4), 20 (1995) [Tech. Phys. **40**, 301 (1995)].
9. A. V. Voronin, A. I. Rusakov, and A. A. Semenov, Preprint of the Ioffe Physicotechnical Institute, USSR Academy of Sciences, Leningrad, 1989, no. 1379.

Translated by M. Astrov

Technical Physics, Vol. 46, No. 12, 2001, pp. 1588–1590. Translated from Zhurnal Tekhnicheskoĭ Fiziki, Vol. 71, No. 12, 2001, pp. 101–103.

BRIEF COMMUNICATIONS

Electromagnetic Radiation Induced by the Failure of Piezoelectrics under the Action of Submicrosecond Stress Pulses

Yu. V. Sud'enkov

St. Petersburg State University, Institute of Mathematics and Mechanics, Bibliotechnaya pl. 2, Petrodvorets, St. Petersburg, 198904 Russia

Received May 16, 2001

Abstract—The failure of quartz single crystals and piezoelectric ceramics under the action of ≈80-ns-wide stress pulses is experimentally investigated. Spalling-induced microfailures in the piezoelectrics are found to produce electromagnetic pulses 2–10 ns wide. The occurrences of the electromagnetic radiation and the microfailures correlate. The study of the structure of these electromagnetic pulses in combination with fractography data may gain much real-time information on the failure of brittle materials under impact loads. *© 2001 MAIK "Nauka/Interperiodica".*

The electromagnetic radiation pulses recorded during earthquakes and the geophysical survey of ores with piezoelectric properties, as well as in the laboratories, have a characteristic width, as a rule, of above $(2–3) \times 10^{-6}$ s [1–3]. In these cases, the impact load duration exceeds 10^{-6} s.

At the same time, when the dynamic strength and the elastoplastic properties of the materials are tested by submicrosecond (50–250 ns) impact loading [4–6], individual short (2–10 ns) electric current pulses or trains of these pulses are frequently recorded by piezoelectric transducers along with stress pulses.

Typical signals waveforms upon loading X-cut quartz specimens are presented in Figs. 1a–1c. When the load stress was above ≈150 MPa, the signals arose at different time moments and often their appearance coincided with the edge of the stress pulses. The piezoelectric plates retained their sensitivity and remained macroscopically intact. Upon reloading, the number of the pulses grew (Fig. 1c), the sensitivity of the plates dropped, and microcracks appeared. The electrical signals from the plates and from a loop-shaped antenna arranged around the lateral surface of the plates and terminated by a wave impedance of 50 Ω were studied. The signals detected by the antenna and caused by the magnetic component of the field were found to appear simultaneously with the pulses from the piezoelectric transducer.

The reason for the short electrical pulses is the formation of new surfaces as a result of microfailures. This effect gives rise to local polarization gradients and high local electric fields. Electrical breakdown is apparently the most effective mechanism of electromagnetic pulse generation in piezoelectrics. For these materials, both estimated and measured values of the electric field strength at crack mouths are on the order of $10^6–10^8$ V/m, which suffices to initiate electrical breakdown [6].

In the experiments, the diameter of the loading area exceeded the dimensions of the piezoelectric transducers. Therefore, the appearance of the electromagnetic pulses at the edge of the compression pulse is not a surprise and is due to microfailures near the lateral surface

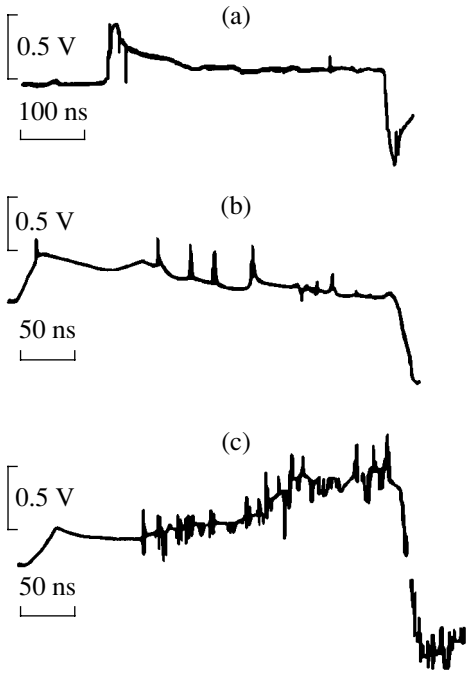

Fig. 1. Waveforms of signals from X-cut SiO_2 piezoelectric transducers (R = 50 Ω) obtained with an S7-10B oscilloscope.

1063-7842/01/4612-1588$21.00

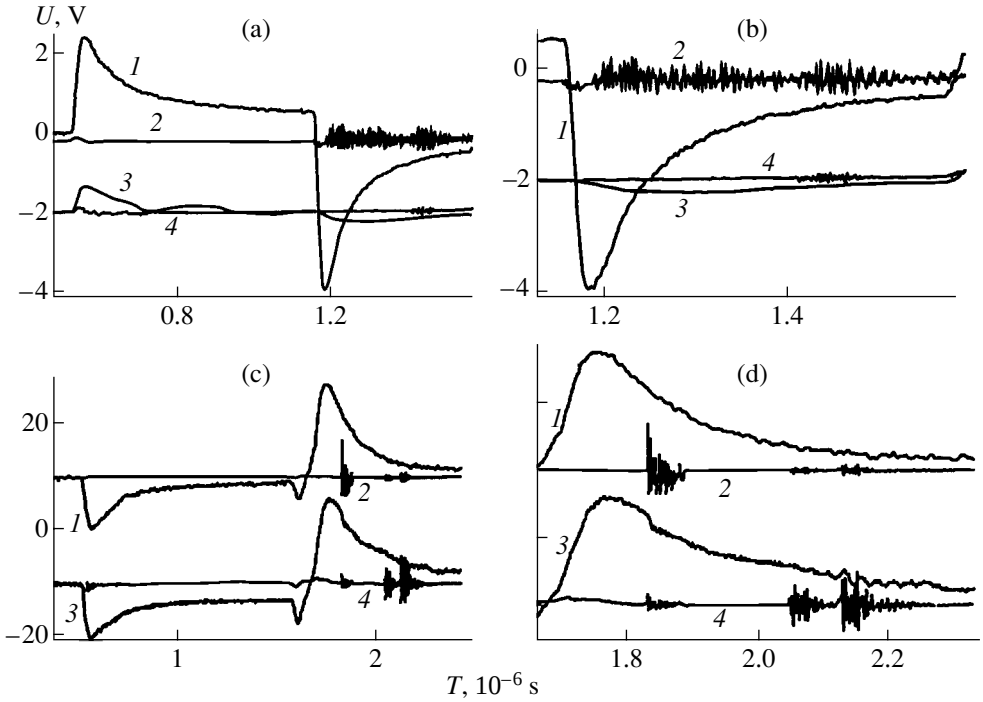

Fig. 2. Waveforms of signals upon spallation obtained with an TDS-754C-type oscilloscope: (a, b) X-cut SiO_2 specimen (24 × 3.65 mm); (c, d) TsTBS-3 piezoelectric ceramic specimen (24 × 5.68 mm); (b, d) magnified fragments of the oscillograms when the pulse reaches the free surface; (*1*, *3*) waveforms of the current for the piezoelectric specimens; and (*2*, *4*) waveforms for the inductive transducer.

of the transducers when the unloading wave passes. Moreover, as is known, the surface strength of brittle materials, such as quartz, becomes much lower than the bulk value after processing.

It would be of interest to correlate the occurrence and the evolution of the electromagnetic pulses with the spalling processes in the case of submicrosecond impact loading.

To separate in time the damage of the lateral surfaces and the spalling, larger diameter specimens were investigated. They were X-cut single-crystal quartz plates 24 mm in diameter and 3.65 mm thick, as well as plates of TsTBS-3 piezoelectric ceramics (24 × 5.68 mm). The diameter of the loading area was 8 mm. For such specimens, the unloading wave originates on the lateral surface more than 10^{-6} s after the longitudinal wave has reached the free surface.

The specimens were stressed by ≈80-ns-wide pulses excited when a pulsed laser irradiated a thin aluminum layer pressed against a titanium acoustic waveguide being in contact with the specimens. To provide plane stressing, the laser energy was uniformly distributed over the irradiated area.

The transducers operated under the short-circuit conditions ($R = 50\ \Omega$). The current from the piezoelectric specimen was determined simultaneously with the signal from the six-turn induction coil of diameter 27 mm wound around it. The temporal resolution of the reception path was 2 ns.

In Figs. 2a and 2b, the waveforms of the currents for the quartz specimen (curves *1*, *3*) and for the induction coil (curves *2*, *4*) are presented in the case when the quartz specimen was stressed at ≈450 MPa. The inductive transducer detects electromagnetic pulses 2–12 ns wide (curve *2*). The appearance of the signals from the inductive transducer coincides with the development of tensile stresses at a depth of ≈85 μm. This phenomenon is apparently associated with microfailures due to near-surface process-induced defects. The electromagnetic radiation intensity peaks at the instant the tensile stresses become maximal at a distance of ≈260 μm from the free surface. This value corresponds to the spallation thickness, as demonstrated by fractography data. The subsequent nonmonotonic behavior of the radiation intensity is apparently due to the development of microfailures because of the reverberation of the voltage pulse in the spallation fragment. Reloading resulted in the macrofailure of the specimens (curves *3*, *4*): they were cleaved along the diameter into three or four parts with the clear-cut spallation area near the free surface.

The signal waveforms for the loaded piezoelectric ceramics specimen are presented in Figs. 2c and 2d. As distinct from the quartz, the instant the electromagnetic radiation anises (curve *2*) coincides with the development of the maximum tensile stress at a depth of ≈430 μm from the free surface. This value agrees with

the measured thickness of the spallation layer. The reloading of the specimen (curves *3*, *4*) also resulted in macrofailures at the lateral surfaces. In this case, the spallation area was even more pronounced than for quartz. Intense oscillations of the electromagnetic radiation that appear upon reloading are due to the failure process because of the reverberation of the pulse voltage in the spallation layer.

Thus, we experimentally demonstrated that the failure of the piezoelectric materials subjected to submicrosecond stress pulses generates electromagnetic pulses three orders of magnitude shorter than the ones observed earlier. The reason for such a discrepancy may be the different characteristic scales of structure levels involved in the failure process at various shock widths.

The investigation of electromagnetic pulses generated by the failure of piezoelectric materials in combination with fractographic analysis provides outstanding possibilities for gaining much real-time information on the development of brittle material failure, as well as on structural levels involved in this process at different durations of shock loading.

REFERENCES

1. V. N. Mineev and A. G. Ivanov, Usp. Fiz. Nauk **119** (1), 75 (1976) [Sov. Phys. Usp. **19**, 400 (1976)].
2. V. V. Viktorov, Yu. V. Kulich, and A. A. Sirotin, Preprint no. 310, IPM AN SSSR (Moscow, 1987).
3. V. M. Demin and G. A. Sobolev, Dokl. Akad. Nauk SSSR **295**, 1337 (1987).
4. Yu. V. Sud'enkov, Cand. Sc. Dissertation (Leningrad, 1986).
5. Yu. B. Nikitin, Cand. Sc. Dissertation (Leningrad, 1993).
6. B. P. Chandra and R. B. Sahu, Cryst. Res. Technol. **18**, 1319 (1983).

Translated by B. Malyukov